

**Thermodynamic investigation of oxidation of  
NiAl-(Cr, Mo) alloys used for manufacturing metal  
matrix composites by directional solidification**

Zur Erlangung des akademischen Grades  
**Doktor der Ingenieurwissenschaften**  
der KIT-Fakultät für Maschinenbau  
Karlsruher Institut für Technologie (KIT)

genehmigte  
**Dissertation**

von

Golnar Geramifard

Tag der mündlichen Prüfung: 11.06.2021  
Referent: Prof. Dr. Hans Jürgen Seifert  
Korreferentin: Prof. Dr. rer. nat. Britta Nestler



This document is licensed under a Creative Commons  
Attribution-ShareAlike 4.0 International License (CC BY-SA 4.0):  
<https://creativecommons.org/licenses/by-sa/4.0/deed.en>

*To my dear parents,  
Vaji and Hadi  
for their perpetual love and support.*

*To my beloved one,  
Iman  
for his immense and everlasting inspiration and love.*



# Abstract

In the past few decades NiAl-based intermetallics have been of interest due to their high temperature engineering applications such as gas turbines. However, pure NiAl with B2 structure shows poor ductility and fracture toughness at room temperature along with inadequate creep resistance and strength at high temperatures.

Therefore, directionally solidified metal-matrix composites of NiAl alloy with embedded chromium or molybdenum fibers, which have enhanced mechanical properties compared to pure NiAl are in the focus of recent research.

In order to design the structural components in the frame of integrated computational materials engineering (ICME), it is essential to acquire the knowledge on materials thermodynamics modeling in the quaternary Ni-Al-Cr-Mo system, including all the relevant intermetallic phases and their heterogeneous reactions. Moreover, investigation of oxidation of the directionally solidified NiAl-Cr and NiAl-Mo is necessary since these alloys will be in contact with high oxygen containing combustion gases at elevated temperature where the corrosion processes are inevitable.

In this work the CALPHAD approach (computer coupling of phase diagrams and thermochemistry) was used to model the Ni-Al-Cr-Mo-O system with focus on NiAl-(Cr, Mo) composites and as a result thermodynamic database is developed. The corresponding ten binary and ten ternary subsystems were taken into account and combined for computed multicomponent extensions. Most of the metallic subsystems have already been assessed and are accepted from the literature. However, deficiencies and lack of data regarding the oxidic

systems exist in the assessments available in the literature. Therefore, the relevant oxide systems were assessed in this work and changes were implemented in the data adapted from the literature when necessary.

In the present work, different oxides which can form during oxidation of NiAl-Cr and NiAl-Mo are included in the database, such as  $\alpha$ -Al<sub>2</sub>O<sub>3</sub>, Cr<sub>2</sub>O<sub>3</sub>, NiO, as well as the spinel phases.

The solution phases are described with sublattice models expressed in the compound energy formalism, while both metallic liquid and oxide melts are described with the ionic two-sublattice model. Spinel within this system like Cr<sub>3</sub>O<sub>4</sub>, NiCr<sub>2</sub>O<sub>4</sub> and NiAl<sub>2</sub>O<sub>4</sub> are also described with four sublattices. Moreover, some application-relevant metastable oxides which can form at lower temperatures or in the initial stages of oxidation, like  $\gamma$ -Al<sub>2</sub>O<sub>3</sub> (with spinel structure),  $\delta$ -Al<sub>2</sub>O<sub>3</sub> and  $\kappa$ -Al<sub>2</sub>O<sub>3</sub>, are included.

The isothermal oxidation of NiAl alloys with embedded Cr bar was studied experimentally, in a thermobalance using argon gas containing 13 vol.% O<sub>2</sub> at temperatures of 800 °C, 1200 °C and 1300 °C in which the formation of a mixed oxide at the interface of NiAl and Cr was investigated using X-ray diffraction (XRD), scanning electron microscopy (SEM) equipped with energy dispersive X-ray analysis (EDX), electron backscatter diffraction (EBSD) and electron probe micro-analyzer (EPMA).

At high temperatures, the oxidation of NiAl-Cr resulted in formation of a continuous solid solution of (Al,Cr)<sub>2</sub>O<sub>3</sub> at the interface of NiAl and Cr in which the composition changed from almost pure Al<sub>2</sub>O<sub>3</sub> near the NiAl matrix to almost pure Cr<sub>2</sub>O<sub>3</sub> in contact with the gas phase while pure Cr<sub>2</sub>O<sub>3</sub> and Al<sub>2</sub>O<sub>3</sub> were formed on Cr region and NiAl region, respectively. This oxide layer was to some extent protective.

The oxidation behavior of the directionally solidified NiAl-34Cr was also investigated similar to the coarse NiAl-Cr composite in which more spallation of the oxide scales was seen during the oxidation process compared to the coarse NiAl-Cr composite. This spallation was mainly caused by Cr-rich region formed between the oxide scale and the substrate surface.

A similar procedure was performed for NiAl with embedded molybdenum wire in which a rapid weight loss was observed during oxidation in the thermobalance already at a relatively low temperature. This was due to the formation of volatile Mo oxides. Most of the formed molybdenum oxides evaporated which made further investigation of the interface of NiAl and Mo impossible.

The computer-readable database resulting from CALPHAD modeling, in which the analytical Gibbs energy functions for each phase are stored, was used with the Thermo-Calc software to determine stability ranges of the formed intermetallic phases and oxides of the engineering alloys. The phase diagrams, such as isothermal sections, isopleths and potential diagrams, as well as property diagrams and thermodynamic properties were calculated and compared with the experimental results and showed a good agreement.



# Kurzfassung

In den letzten Jahrzehnten waren intermetallische Werkstoffe auf NiAl-Basis aufgrund von hochtemperaturtechnischen Anwendungen wie Gasturbinen von Interesse. Jedoch zeigt reines NiAl mit B2-Struktur eine schlechte Duktilität und Bruchzähigkeit bei Raumtemperatur, sowie unzureichende Kriechbeständigkeit und Festigkeit bei hohen Temperaturen.

Dieses Verhalten kann durch eine gerichtete Verfestigung durch Metallmatrix-Verbundwerkstoffe der NiAl-Phase, verstärkt mit in situ gebildeten Chrom- und Molybdänfasern, unterdrückt werden.

Dies ist der Grund, weshalb gerichtet erstarrte Metallmatrix-Kompositwerkstoffe auf Basis von NiAl-Legierungen mit eingebetteten Chrom- oder Molybdänfasern, welche im Vergleich zu reinem NiAl verbesserte mechanische Eigenschaften aufweisen, im Fokus der aktuellen Forschung liegen.

Um Bauteile mithilfe von Integrated Computational Materials Engineering (ICME) zu entwickeln, muss die Materialthermodynamik des quaternären Ni-Al-Cr-Mo-Systems inklusive der relevanten intermetallischen Phasen sowie der heterogenen Phasenreaktionen modelliert werden. Darüber hinaus wird das Oxidationsverhalten der gerichtet erstarrten NiAl-Cr und NiAl-Mo untersucht, da diese Legierungen in ständigem Kontakt mit Verbrennungsgasen mit hohem Sauerstoffgehalt bei hohen Temperaturen stehen, sodass Oxidationsprozesse unvermeidlich sind.

In der vorliegenden Arbeit wird die CALPHAD-Methode (computer coupling of phase diagrams and thermochemistry) verwendet, um das Ni-Al-Cr-Mo-System mit dem Fokus auf die NiAl-(Cr, Mo)-Komposite zu modellieren, als Ergebnis wird eine thermodynamische Datenbank entwickelt.

Die entsprechenden zehn binären und zehn ternären Subsysteme wurden berücksichtigt und für berechnete Mehrkomponenten-Erweiterungen kombiniert. Die meisten der metallischen Subsysteme wurden bereits untersucht und die thermodynamischen Beschreibungen aus der Literatur werden akzeptiert. Allerdings gibt es Mängel und fehlende Daten bezüglich der oxidischen Systeme in den verfügbaren Assessments aus der Literatur. Daher werden in der vorliegenden Arbeit die relevanten Oxid-Systeme untersucht und, wenn nötig, die thermodynamische Beschreibung aus der Literatur angepasst.

In der vorliegenden Arbeit werden verschiedene Oxide, welche sich während der Oxidation von NiAl-Cr und NiAl-Mo bilden können, in der Datenbank berücksichtigt, wie zum Beispiel  $\alpha$ -Al<sub>2</sub>O<sub>3</sub>, Cr<sub>2</sub>O<sub>3</sub>, NiO, sowie die Spinellphasen.

Die Lösungsphasen werden mithilfe des Untergittermodells im Compound Energy Formalism beschrieben, wohingegen beide metallischen Flüssigphasen sowie die Oxidschmelzen mit dem ionischen Zwei-Untergitter-Modell (ionic two-sublattice model) beschrieben werden. Im System auftretende Spinelle wie Cr<sub>3</sub>O<sub>4</sub>, NiCr<sub>2</sub>O<sub>4</sub> und NiAl<sub>2</sub>O<sub>4</sub> werden mithilfe von vier Untergittern beschrieben. Zusätzlich werden manche anwendungsrelevanten metastabilen Oxide, welche sich bei niedrigeren Temperaturen oder in der Anfangsphase des Oxidationsprozesses bilden, wie zum Beispiel  $\gamma$ -Al<sub>2</sub>O<sub>3</sub> (mit Spinellstruktur),  $\delta$ -Al<sub>2</sub>O<sub>3</sub> und  $\kappa$ -Al<sub>2</sub>O<sub>3</sub>, berücksichtigt.

Die isotherme Oxidation einer NiAl-Legierung mit einem darin eingeschlossenen Cr-Stab wurde in einer Thermowaage unter Argon-Atmosphäre mit 13 Vol.% O<sub>2</sub> bei Temperaturen von 800 °C, 1200 °C und 1300 °C experimentell untersucht, wobei die Bildung der Mischoxide in der Grenzfläche von NiAl und Cr mithilfe von Röntgendiffraktometrie (XRD), Rasterelektronenmikroskopie (REM) mit energiedispersiver Röntgenspektroskopie (EDX), Elektronenrückstreubeugung (EBSD), sowie Electron probe micro-analyzer (EPMA) untersucht wurden.

Bei hohen Temperaturen führte die Oxidation von NiAl-Cr zur Bildung eines kontinuierlichen Mischkristalls von (Al,Cr)<sub>2</sub>O<sub>3</sub> an der Grenzfläche von NiAl

und Cr, in dem sich die Zusammensetzung von nahezu reinem  $\text{Al}_2\text{O}_3$  in der Nähe der NiAl-Matrix bis zu fast reinem  $\text{Cr}_2\text{O}_3$  an der Oberfläche veränderte, während reines  $\text{Cr}_2\text{O}_3$  sowie  $\text{Al}_2\text{O}_3$  in der Cr-Region beziehungsweise der NiAl-Region entstand. Die gebildete Oxidschicht war bis zu einem gewissen Maße protektiv.

Das Oxidationsverhalten des gerichtet erstarrten NiAl-34Cr wurde mit den gleichen Methoden wie die einfach NiAl-Cr Legierung untersucht, wobei eine ausgeprägtere Spallation der Oxid-Schuppen während des Oxidationsprozesses im Vergleich zu der NiAl-Cr Legierung festgestellt werden konnte. Die Spallation wurde hauptsächlich durch die Cr-reichen Regionen hervorgerufen, welche sich zwischen den Oxid-Schuppen und der Substratoberfläche gebildet haben.

Eine ähnliche Prozedur wurde ebenfalls an NiAl mit einem eingebetteten Mo-Stab durchgeführt, wobei eine rapide Gewichtsabnahme der Probe während der Oxidation auch schon bei relativ niedrigen Temperaturen gemessen wurde. Dies wurde durch die Bildung von volatilen Mo-Oxiden hervorgerufen. Die meisten der entstandenen Mo-Oxide verdampften, wodurch die weiterführende Untersuchung der Grenzfläche zwischen NiAl und Mo nicht möglich war. Die computerlesbare Datenbank, welche aus der CALPHAD-Modellierung resultiert, in welcher die analytischen Funktionen der freien Energie jeder Phase hinterlegt sind, wurde mithilfe der Thermo-Calc Software genutzt, um die Stabilitätsbereiche der gebildeten intermetallischen Phasen und Oxide der Legierungen zu bestimmen. Die Phasendiagramme wie isotherme Schnitte, Isolethen und Potentialdiagramme, sowie Eigenschaftsdiagramme und thermodynamische Eigenschaften wurden berechnet und mit den experimentellen Ergebnissen verglichen, wobei die Ergebnisse eine gute Übereinstimmung zeigen.



# Acknowledgment

The present work is provided based on my PhD study accomplished in Karlsruhe Institute of Technology (KIT) at the Institute for Applied Materials-Applied Material Physics (IAM-AWP) in Karlsruhe, Germany and is financially supported by the Initiative and Networking Fund of Helmholtz Association (VH-KO-610). Herein, I would like to express my gratitude to all the people whose contributions led to succession of this work.

First and foremost, I would like to profoundly thank Prof. Dr. Hans Jürgen Seifert for his supervision in which he went above and beyond with his patience and support in all aspects of this work. Giving me priceless opportunities for presentation and discussion of the results.

I would also like to sincerely thank Dr. Peter Franke, for his enthusiastic and motivational discussions during this work and for his instructions and support regarding CALPHAD modeling, without him pursuing my PhD would have not been possible.

My special gratitude goes to Dr. Martin Steinbrück for his endless support and help with the oxidation experiments and his instructive advises, Dr. Jan Hoffman for the scientific support with EBSD measurements, Dr. Harald Leiste for performing XRD analysis and Kolja Erbes for his great help with the EPMA measurements.

I would like to acknowledge endless support from Ulrike Stegmaier, Petra Severloh, Alexandra Reif and Daniel Bolich for their great help with the experiments.

My special thanks to Camelia Gombola, for her enduring support and persistent help specifically with the sample preparations.

My deepest appreciation to all members of the Helmholtz Research School on Integrated Materials Development for Novel High-Temperature Alloys, specially Prof. Martin Heilmaier and Dr. Heinz Riesch-Oppermann for their great discussions and guidance.

I am truly thankful of my colleagues Dr. Maximilian Rank, Dr. Jian Peng, Dr. Nicolas Mayer, Joel Fels, Ingo markel, Alexandra Meyer, Judith Jung, Dr. Magnus Rohde, and all colleagues in IAM-AWP and members of Thermophysics and Thermodynamics group.

Furthermore, I am deeply thankful to my friends for their support throughout the difficult times and their enormous encouragement for me to pursue my dreams.

Lastly, I would like to give my special thanks to my beloved one, Iman and my wonderful parents Vaji and Hadi, and my delightful siblings Ordin, Omid and Negar for their everlasting support, encouragement and love.

Karlsruhe, November 2020

*Golnar Geramifard*

# Contents

<b>1</b>	<b>Motivation</b>	<b>1</b>
<b>2</b>	<b>Introduction to CALPHAD method</b>	<b>5</b>
<b>3</b>	<b>Analytical models used for describing the Gibbs energy</b>	<b>11</b>
3.1	Compound energy formalism	12
3.2	Liquid phase description	13
3.3	Pure elements	15
3.4	Stoichiometric phases (compounds)	15
3.5	Corundum	16
3.6	Spinel	17
3.7	Halite	19
<b>4</b>	<b>Experimental characterization of oxidation behavior</b>	<b>21</b>
4.1	Sample preparation	21
4.1.1	Arc melting	21
4.1.2	Directional solidification	22
4.1.3	Sample synthesis and preparation	23
4.2	Thermogravimetric analysis	26
4.3	Oxidation procedure	27
4.4	Characterization methods	27
4.4.1	SEM	27
4.4.2	XRD	28
4.4.3	EPMA	29
4.4.4	EBSD	29

<b>5</b>	<b>Oxidation Kinetics</b>	<b>31</b>
5.1	Fick's first law of diffusion	31
5.2	Oxidation rate equations	32
5.2.1	Linear kinetics	33
5.2.2	Parabolic kinetics	33
5.2.3	Logarithmic kinetics	35
<b>6</b>	<b>Evaluation of literature data for binary and ternary systems</b>	<b>37</b>
6.1	The Ni-Al-Cr system	39
6.1.1	Review of binary systems	39
6.1.1.1	Ni-Al	39
6.1.1.2	Ni-Cr	43
6.1.1.3	Al-Cr	44
6.1.2	Review of Ni-Al-Cr system	48
6.2	The Ni-Cr-O system	49
6.2.1	Review of binary systems	49
6.2.1.1	Ni-O	49
6.2.1.2	Cr-O	50
6.2.2	Review of Ni-Cr-O system	52
6.3	The Al-Cr-O system	53
6.3.1	Review of binary systems	53
6.3.1.1	Al-O	53
6.3.2	Review of Al-Cr-O system	55
6.4	The Al-Cr-Mo system	56
6.4.1	Review of binary systems	56
6.4.1.1	Al-Mo	56
6.4.1.2	Cr-Mo	60
6.4.2	Review of Al-Cr-Mo system	62
6.5	The Ni-Al-Mo system	62
6.5.1	Review of binary systems	62
6.5.1.1	Ni-Mo	62
6.5.2	Review of Ni-Al-Mo system	66

---

6.6	The Ni-Cr-Mo system . . . . .	66
6.6.1	Review of binary systems . . . . .	66
6.6.2	Review of Ni-Cr-Mo system . . . . .	66
<b>7</b>	<b>Optimization results and discussion . . . . .</b>	<b>69</b>
7.1	Mo-O binary system . . . . .	70
7.2	The Ni-Mo-O system . . . . .	86
7.3	The Al-Mo-O system . . . . .	93
7.4	The Cr-Mo-O system . . . . .	96
7.5	The Al-Ni-O system . . . . .	99
<b>8</b>	<b>Experimental results and discussion . . . . .</b>	<b>111</b>
8.1	Oxidation of NiAl, NiAl-Cr coarse composite and DS NiAl-34Cr111	
8.2	Surface and cross section investigation . . . . .	119
8.2.1	Oxidation of NiAl-Cr coarse composite at 800 °C . .	122
8.2.2	Oxidation of NiAl-Cr coarse composite at 1200 °C . .	126
8.2.3	Oxidation of NiAl-Cr coarse composite at 1300 °C . .	128
8.2.4	Oxidation of DS NiAl-34Cr at 1200 °C and 1300 °C .	139
8.3	Oxidation of NiAl-Mo . . . . .	141
<b>9</b>	<b>Conclusion and outlook . . . . .</b>	<b>145</b>
	<b>Bibliography . . . . .</b>	<b>149</b>
	<b>List of Figures . . . . .</b>	<b>179</b>
	<b>List of Tables . . . . .</b>	<b>185</b>
	<b>List of abbreviations and symbols . . . . .</b>	<b>187</b>
	<b>Appendix . . . . .</b>	<b>191</b>
	<b>The thermodynamic dataset of Ni-Al-Cr-Mo-O . . . . .</b>	<b>203</b>

**List of publications . . . . . 253**

# Chapter 1

## Motivation

Ni-based superalloys have received much attention and have been used in the gas turbines in the past few decades. These superalloys can tolerate high gas inlet temperature in the combustion chamber which consequently leads to high operational efficiency. Nevertheless, the operating temperatures in the engines are currently near the solidus temperatures of the implemented materials. As a result, alternative alloys which can withstand higher temperatures are required. NiAl-based intermetallics are proposed and have been investigated in recent decades with promising results [1].

NiAl has a higher melting temperature than the solidus temperature of Ni-based superalloys. However, undesirable mechanical properties of pure NiAl, such as low fracture toughness and poor ductility at room temperature along with an inadequate creep resistance and low strength at high temperatures, necessitates improvements in the manufactured alloys [2].

These issues could be suppressed, by directional solidification of metal-matrix composites of the NiAl phase reinforced with in-situ formed chromium and molybdenum fibers [3–9]. For instance, the fracture toughness at room temperature for the directionally solidified NiAl-9Mo, NiAl-34Cr and NiAl-28Cr-6Mo are 16, 20 and 24  $MPa \cdot \sqrt{m}$ , respectively which are much higher than that of NiAl ( $\sim 6 MPa \cdot \sqrt{m}$ ) [4]. In addition, creep testing of directionally solidified eutectics of NiAl-Mo at 600 °C showed superior creep resistance with minimum creep rates up to 7 orders of magnitude lower than that of pure NiAl.

Therefore, directionally solidified metal-matrix composites are considered as potential candidates for high-temperature applications in turbines since they also exhibit good thermodynamic stability and chemical compatibility between the NiAl matrix and the strengthening fibers.

However, when applied in turbines, these composites will be in contact with oxygen-containing combustion gases where oxidative corrosion processes are inevitable. During oxidation of NiAl, metastable phases such as  $\gamma$ -Al<sub>2</sub>O<sub>3</sub>,  $\theta$ -Al<sub>2</sub>O<sub>3</sub> and  $\delta$ -Al<sub>2</sub>O<sub>3</sub> are formed [10–12] which after further heating are transformed into stable  $\alpha$ -Al<sub>2</sub>O<sub>3</sub> [13, 14].

The oxidation behavior of both NiAl-Cr and NiAl-Mo composites are of concern, due to the fact that rather than the  $\alpha$ -Al<sub>2</sub>O<sub>3</sub> which is formed during oxidation of NiAl at high temperatures, Cr<sub>2</sub>O<sub>3</sub> and various volatile Mo oxides can form, respectively [15].

While the mechanical properties of the aforementioned composites have been investigated thoroughly by many authors, there are only few reports on oxidation behavior of directionally solidified NiAl-based eutectic alloys [15, 16].

This work is part of a project in the Helmholtz Research School on "Integrated Materials Development for Novel High-Temperature Alloys (IMD)". Parallel works in the IMD project provide information regarding the mechanical properties of the directionally solidified NiAl-based composites and the influence of processing conditions, quantitative phase-field simulations of 3D eutectic microstructure formation and thermodynamic modeling of liquid and solid solution phases of the DS eutectic alloys.

This work continues the investigations performed by Peng [17] who mainly focused on thermodynamic modeling of the Ni-Al-Cr-Mo system with the purpose of enhancing the selection of alloy compositions in NiAl-based composites.

In the present work, we continue further with the role of oxygen added to Ni-Al-Cr-Mo and investigate the oxidation of this quaternary system. The oxidation processes for both systems of NiAl-Cr-O and NiAl-Mo-O are investigated using experimental and advanced computational thermodynamics. The

investigations are focused on alloys with equimolar ratio of Ni:Al.



# Chapter 2

## Introduction to CALPHAD method

In materials research and alloy engineering, an equilibrium phase diagram can be used to perceive the interrelation of components, and formation of microstructures. In addition, it can provide information on the required processing conditions such as temperature and pressure prior to production of alloys. Although most binary systems are already investigated thoroughly, there is still lack of experimental information in higher order systems. The experiments which are needed to obtain these information, are time-consuming and cost-intensive. Specifically, as the number of components increase, the traditional experimental method becomes less efficient since various experiments are required.

CALPHAD was originally an abbreviation for CALculation of PHase Diagrams. However, it was later modified to refer to Computer Coupling of Phase Diagrams and Thermochemistry. The major principle in the CALPHAD method is to mathematically describe the Gibbs energy of all the relevant phases in the system to provide a Gibbs energy prospect. Next, a software is used to minimize the total Gibbs energy in order to calculate the equilibrium state. It is worth mentioning that the reason for choosing the Gibbs energy rather than other state energy functions such as internal energy ( $U$ ), enthalpy ( $H$ ) or Helmholtz free energy ( $A$ ), is that the equilibrium can be characterized by minimum of Gibbs energy function at constant temperature, pressure and

composition which can be monitored easily during experiments. Other thermodynamic quantities like enthalpy and entropy can be derived from the Gibbs energy.

$$S = -\left(\frac{\partial G}{\partial T}\right)_{P,N_i} \quad (2.1)$$

$$H = G - T\left(\frac{\partial G}{\partial T}\right)_{P,N_i} \quad (2.2)$$

$$C_p = -T\left(\frac{\partial^2 G}{\partial T^2}\right)_{P,N_i} \quad (2.3)$$

The schematic figure of CALPHAD method is shown in figure 2.1. The main issue in this method is developing the analytical description of the Gibbs energy functions of all phases within a binary, a ternary or a multi-component system.

Different models can be used based on the physical and chemical properties of each phase. Which could be decided based on the crystal structure of the phase, type of bonding between the compounds, the magnetic properties or the order-disorder transition of each phase. Different models applied in this work are explained in details in chapter 3. When an appropriate Gibbs energy model is selected, then by adapting the data the parameters in the models can be optimized.

In this method, the Gibbs energy of each phase is modeled using different parameters. These parameters can be assessed based on thermodynamic data obtained from experiments or ab initio calculations. The experimental data includes: enthalpies of mixing obtained by calorimetry, phase transformation temperature acquired from Differential Thermal Analysis (DTA), vapor pressure measured by Knudsen cell, the oxygen potentials for univariant and bivariant equilibria obtained from EMF measurements, etc. Since any deviation from the reliable data will affect the parameters in higher-order systems, it should be considered that only accurate and reasonable experimental data should be

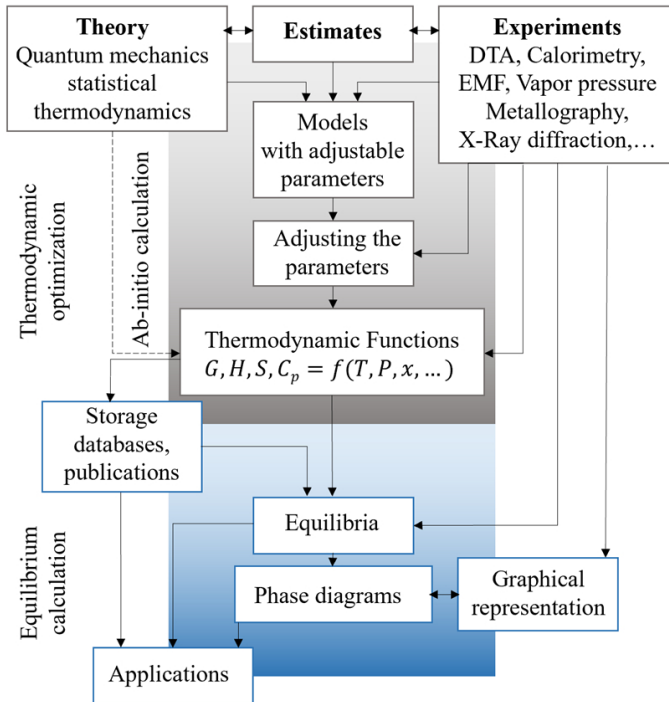


Figure 2.1: Scheme of CALPHAD method, modified from [18].

used for setting the parameters in defining the Gibbs energy functions. Therefore, the purity of the materials used, the experimental procedures and methods should carefully be evaluated.

In addition to the experimental data which need to be implemented in the CALPHAD approach, it is also possible to use ab initio or first-principle calculations to obtain thermodynamic data for different phases. These calculations are particularly convenient when acquiring experimental data is difficult in case of hazardous elements or compounds or due to the extreme conditions needed for the experiments as well as formation of unstable or metastable phases.

Despite of the reliable results from the ab initio calculations which can be used in the CALPHAD models, it still has some limitations. Since in the ab initio calculations only a unit cell of crystal structure is considered, therefore, simulation of the disordered phases with random distribution of atoms in the unit cell is an issue. Nevertheless, new approaches are used to overcome this challenge.

The procedure explained above, would be done for all different phases in the desired system. By gathering all Gibbs energy functions for all different phases in a specific format, a database is established. This database can be further used for calculation of the phase diagrams, thermodynamic properties for each phase and estimate the transformation behavior of multi-phases in multicomponent systems at broad temperature and composition ranges where no experimental data are available or it is difficult to obtain. It can also be used for the modeling of the higher order systems or be used as a source in the phase field simulation. First and second derivatives of the Gibbs energies can be calculated and used in diffusion simulations. In addition, the microstructure evolution which are simulated using the driving forces of phases are used along with the information acquired experimentally on the solid phase fractions and energies of metastable states [19].

One of the most attractive features of CALPHAD is the increasing of predictability which means as the number of component increases, less experimental data is needed to obtain a satisfactory description of the Gibbs energy of the phases [20].

The CALPHAD method has shown results with reasonable accuracy in various fields including virtual casting [21], design and development of lightweight materials [22] and Ni-based superalloys [23], in which it has effectively accelerated the design by optimizing the compositions.

While using CALPHAD method could save lots of effort and time, it still has some constrains one should be aware of. Although extrapolation from lower order systems to higher ones is a great tool, it is only beneficial if no new phases are formed in the higher order system. This means that it is not possible

to predict the stability of a multi-component phase that has not already been described in lower-order systems [20].

Since the descriptions of lower-order systems have direct effect on the higher-order systems, it is necessary to update all the higher-order system assessments if any changes are made in the lower-order systems. As an example if the description of one binary is changed, the assessment for  $n-2$  ternary systems in  $n$ -component system has to be updated.

For this reason all binary and ternary systems in this work are carefully investigated and suitable experimental data are implemented in the relevant selected models. The investigations of the corresponding binary and ternary systems are discussed in chapters 6 and 7.

During optimization of the parameters in Thermo-Calc [24], POP files are used which contain the experimental information to be fitted. These POP files are later used in PARROT work space where the optimization will be run [25]. The information acquired in the POP file could be measurements of any thermodynamic quantities that can be set as conditions in Thermo-Calc. Including enthalpies or activities in single-phase region, or transformation temperatures or solubilities in a multi-phase region. The parameters are optimized in a way to minimize the deviation of the calculated data from the available experimental values. An example of POP file for optimizing parameters of the liquid phase in the Mo-O binary can be found in the appendix B.



# Chapter 3

## Analytical models used for describing the Gibbs energy

The Gibbs energy of a phase  $\Phi$  can be derived by the equation 3.1.

$$G_m^\Phi = {}^{ref}G_m^\Phi + {}^{cnf}G_m^\Phi + {}^{phys}G_m^\Phi + {}^E G_m^\Phi + {}^P G_m^\Phi \quad (3.1)$$

Where  ${}^{ref}G_m^\Phi$  is the surface of reference and describes the Gibbs energy of the virtually not interacting constituents. The contribution to the Gibbs energy due to physical properties such as magnetism is represented by  ${}^{phys}G_m^\Phi$ . The configurational entropy contribution is considered in  ${}^{cnf}G_m^\Phi = -T \cdot {}^{cnf}S_m$ , where  ${}^{cnf}S_m$  is calculated based on the number of possible arrangements of the constituents in the phase. The excess Gibbs energy is denoted by  ${}^E G_m^\Phi$  which shows the deviation from the ideal behavior. The  ${}^P G_m^\Phi$  is the contribution in the Gibbs energy which is pressure dependent. In this work this would only be decisive regarding the gas phase, since the pressure dependency is not of concern for the other phases with working pressure in scale of 1 *bar*. The pressure dependency would be necessary to be considered in condensed phases at pressures of several hundred atmospheres.

### 3.1 Compound energy formalism

The compound-energy formalism (CEF) is a general method to describe the thermodynamics of solid solution phases with multiple sublattices which show a variation in composition [19, 26]. The constituent array was introduced by Sundman and Ågren to provide the analytical expressions for the Gibbs energy of these phases [27]. This concept is used to specify one or more constituents ( $i$ ) on each sublattice which is denoted by  $I$ , the constituents can have a superscript  $s$  to denote the sublattice. These arrays can have different orders. If there is only one constituent on each sublattice it has order of zero denoted by  $I_0$  and it represents a compound. The Gibbs energy expression for CEF is defined as follows:

$${}^{ref}G_m = \sum_{I_0} P_{I_0}(Y) \circ G_{I_0} \quad (3.2)$$

$${}^{cnf}G_m = -T \cdot {}^{cnf}S_m = R \cdot T \sum_{s=1}^n a_s \sum_{i=1}^{n_s} y_i^s \ln(y_i^s) \quad (3.3)$$

$${}^E G_m = \sum_{I_1} P_{I_1}(Y) L_{I_1} + \sum_{I_2} P_{I_2}(Y) L_{I_2} + \dots \quad (3.4)$$

Where  $P_{I_0}(Y)$  is the product of the site fractions specified by  $I_0$ . The Gibbs energy of the compound  $I_0$  is represented by  $\circ G_{I_0}$ . In some cases  $I_0$  does not represent a stable compound and  $\circ G_{I_0}$  should be estimated. In the configurational entropy  $a_s$  represents the number of sites on each sublattice and  $y_i^s$  is used to denote the site fraction of constituent  $i$  on sublattice  $s$ . The excess Gibbs energy is denoted by  ${}^E G_m$  where  $I_1$  is a constituent array of first order which means it has one extra constituent in one sublattice and  $L_{I_1}$  is the interaction parameter defined by  $I_1$ . The Gibbs energy of the compound  $I_0$  is the parameter which is stored in the database and it would be sufficient to include only the  $\circ G_{I_0}$  and the  $L$  parameters where the constituent array is indicated in the index to calculate the  $G_m^\Phi$ . Examples of the  $\circ G_{I_0}$  and the  $L$  parameters can be found in the appendix A.

An example of using the CEF for describing the thermodynamics of a phase is using two-sublattice liquid model which will be discussed in section 3.2

## 3.2 Liquid phase description

In the literature different models are suggested to describe the liquid phase such as associate solution model [28], the cellular model [29, 30] and the modified quasi-chemical model [31, 32]. However, while dealing with systems which have both metallic and non-metallic liquids it is advised to use ionic two-sublattice liquid model since it makes it possible to extend the model from metallic to non-metallic liquids.

Ionic two-sublattice liquid model is a special case of two-sublattice model where the vacancies have variable charges and the site ratios of the sublattices are not fixed. This was developed by Hillert et al. [33]. This model was primarily established for the description of molten salt mixtures where the cations mix on a hypothetical cation sublattice and the anions mix on the second sublattice with each other.

By introduction of negative charged vacancies in the anionic sublattice the model was extended to describe metallic melts as  $(C_i^{v_i^+})_P(A_j^{v_j^-}, Va^{Q-}, B_k^0)_Q$ , in which the first sublattice contains cations which are represented by  $C$  and the second sublattice contains anions ( $A$ ), vacancies ( $Va$ ) and neutral species ( $B$ ).  $i, j$  and  $k$  denote a specific constituent.  $P$  and  $Q$  are the number of sites on the sublattices and vary with the compositions to maintain the electro-neutrality. The values of  $P$  and  $Q$  are calculated by the equations 3.5 and 3.6.

$$P = \sum_j v_j y_{A_j} + Q y_{Va} \quad (3.5)$$

$$Q = \sum_i v_i y_{C_i} \quad (3.6)$$

Examples of constituent arrays  $I_1$  for metallic and oxidic melts are as follows:

Interaction in metallic melt:

$$I_1 = (C_1^+, C_2^+ : Va)$$

Interaction in oxidic melt:

$$I_1 = (C_1^+, C_2^+ : O^{2-})$$

The Gibbs energy of liquid phase is defined as follows:

$$\begin{aligned} G_m = & \sum_i \sum_j y_{C_i} y_{A_j} {}^\circ G_{C_i:A_j} + Q y_{Va} \sum_i y_{C_i} {}^\circ G_{C_i} + Q \sum_k y_{B_k} {}^\circ G_{B_k} \\ & + RTP \sum_i y_{C_i} \ln(y_{C_i}) + RTQ \sum_j y_{A_j} \ln(y_{A_j}) + RTQ y_{Va} \ln(y_{Va}) \\ & + RTQ \sum_k y_{B_k} \ln(y_{B_k}) + {}^E G_m \end{aligned} \quad (3.7)$$

And the excess Gibbs energy is calculated using Redlich-Kister polynomials [34]:

$$\begin{aligned} {}^E G_m = & \sum_{i_1} \sum_{i_2} \sum_j y_{C_{i_1}} y_{C_{i_2}} y_{A_j} L_{C_{i_1}, C_{i_2}:A_j} + Q y_{Va}^2 \sum_{i_1} \sum_{i_2} y_{C_{i_1}} y_{C_{i_2}} L_{C_{i_1}, C_{i_2}:Va} + \\ & y_{Va} \sum_i \sum_j y_{C_i} y_{A_j} L_{C_i:A_j, Va} + \sum_i \sum_j \sum_k y_{C_i} y_{A_j} y_{B_k} L_{C_i:A_j, B_k} + \\ & Q y_{Va} \sum_i \sum_k y_{C_i} y_{B_k} L_{C_i:B_k, Va} \end{aligned} \quad (3.8)$$

Where the species are separated using a comma and different sublattices are distinguished by using a colon. For simplicity only the binary interaction terms using the first order constituent array are included here. In this work, ionic two-sublattice liquid model was used to describe both metallic and oxide liquids, an example for this case is the Mo-O binary which will be discussed in section 7.1. Further details about the changes made in the liquid phase description is given in chapter 6.

### 3.3 Pure elements

The Gibbs energy of element  $i$  in phase  $\Phi$  and at temperature  $T$  is  ${}^\circ G_i^\Phi(T)$  and is expressed relative to its enthalpy in the standard state ( $SE$ R) by a semi-empirical function of the temperature which is valid only within a limited temperature range [19]:

$${}^\circ G_i^{HSE}R(T) = {}^\circ G_i^\Phi(T) - {}^\circ H_i^{SE}R(298.15K) = GHSE R_i(T) = a + bT + cT \ln(T) + dT^2 + eT^{-1} + fT^3 \quad T_1 < T < T_2 \quad (3.9)$$

Where  $a, b, c,$  are adjustable coefficients.  ${}^\circ H_i^{SE}R$  is the enthalpy of pure element  $i$  in its reference state which is usually the stable state at 298.15 K and 1 bar. It is necessary to refer the Gibbs energy of all phases to the same reference point of each element.

In this expression the lower temperature limit ( $T_1$ ) is usually 298.15 K, which is adequately low to be used in equilibrium calculations. In order to avoid using too many coefficients, usually the applied method is using different expressions for various temperature ranges. In this case, it is important that the first and second derivative of Gibbs energy are continuous at the boundaries of the temperature intervals. Here the constituent array has zeroth order which means it has 1 sublattice with 1 constituent  $I_0 = (i)$ , where  $i$  represents the element.

### 3.4 Stoichiometric phases (compounds)

The stoichiometric phase  $A_P B_Q C_R \dots$  with the stoichiometric coefficients  $P, Q, R, \dots$  can be modeled similar to pure elements using the equation 3.9 where the constituent array is zeroth order with only one constituent on each sublattice which is shown as  $I_0 = (A : B : C : \dots)$ . In which  $A, B$  and  $C$  are the elements separated with colon symbol showing various sublattices.

Another possibility is to model the stoichiometric phase  $(A)_P : (B)_Q$  with  $P$  and

$Q$  as the stoichiometric coefficients in which two separate sublattices are used. This model is only temperature dependent and is defined as follows:

$$\begin{aligned} \circ G_m = G_{A:B}^{A_p B_Q}(T) - P \cdot \circ H_A^{SER} - Q \cdot \circ H_B^{SER} = \Delta_f G_{A_p B_Q}(T) \\ + P \cdot GHSER_A(T) + Q \cdot GHSER_B(T) \end{aligned} \quad (3.10)$$

Where  $\Delta_f G_{A_p B_Q}(T)$  is the standard Gibbs energy of formation of the stoichiometric compound formed from pure elements and is expressed as a power series of temperature. If the heat capacity of the compound is approximated by the Neumann-Kopp rule then the energy of formation simplifies to:

$$\Delta_f G_{A_p B_Q}(T) = a + bT \quad (3.11)$$

The coefficients  $a$  and  $b$  correspond to the enthalpy and entropy of formation, respectively.

In the following sections of 3.5, 3.6 and 3.7, the corundum, spinel and halite phases are described, respectively. These are the main phases needed in this work.

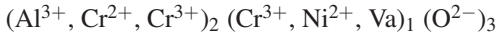
## 3.5 Corundum

Corundum with space group 167:  $R\bar{3}c$ , crystallizes in the hexagonal (rhombohedral) crystal system. The cations occupy 4c Wyckoff positions, while the oxide ions of  $O^{2-}$  occupy the Wyckoff positions 6e.

Chromia ( $Cr_2O_3$ ) and alumina ( $Al_2O_3$ ) with the phase prototype of corundum are described using three sublattices in the work from Saltykov et al. [35, 36].

In this work, the description of Saltykov is accepted and it includes the  $Al^{3+}$ ,  $Cr^{2+}$  and  $Cr^{3+}$  on the first sublattice and an additional interstitial sublattice with  $Cr^{3+}$ ,  $Ni^{2+}$  and vacancies which occupy the Wyckoff positions 2b. The last sublattice corresponds to  $O^{2-}$  sites.  $Ni^{2+}$  is used to describe the solubility

of Ni in the chromia and alumina phase and  $\text{Cr}^{3+}$  is introduced in the second sublattice to keep the electroneutrality. This phase is presented as follows:



In the iron oxide hematite,  $\text{Fe}_2\text{O}_{3-\varepsilon}$  the major dominant ionic defects are anion vacancies [37]. Nevertheless, in this work the interstitial defects are adapted due to compatibility with previous assessments [38–40].

## 3.6 Spinel

$\text{NiCr}_2\text{O}_4$ ,  $\text{NiAl}_2\text{O}_4$  and metastable  $\gamma\text{-Al}_2\text{O}_3$  have the spinel structure which belongs to space group symbol  $\text{Fd}\bar{3}\text{m}$  and number of 227. The spinel structure can be described as a cubic closest packing of oxygen anions where the cations occupy certain tetrahedrally and octahedrally coordinated sites.

Anions which are usually the oxide ions of  $\text{O}^{2-}$  occupy the FCC lattice points. The effective number of ions per unit cell of FCC is 4. Therefore, number of oxygen ions in the spinel unit cell is  $8 \times 4 = 32$ .

In the spinel unit cell the divalent  $\text{A}^{2+}$  cations occupy 1/8 of the tetrahedral sites. As the number of tetrahedral sites per one unit cell of FCC is 8. Therefore, number of divalent  $\text{A}^{2+}$  cations in spinel unit cell is  $8 \times (1/8 \times 8) = 8$ .

Mean while, the trivalent  $\text{B}^{3+}$  cations occupy half of octahedral sites. The number of octahedral sites per one unit cell of FCC is 4. Therefore, number of trivalent  $\text{B}^{3+}$  cations in spinel is  $8 \times (1/2 \times 4) = 16$ .

As a result, 8 cations occupy the Wyckoff positions 8a which are tetrahedrally coordinated, 16 cations occupy the Wyckoff positions 16d which are octahedrally coordinated and 32 oxygen anions in Wyckoff positions 32e. The ratio of ions in spinel is therefore,  $\text{A}^{2+} : \text{B}^{3+} : \text{O}^{2-} = 8 : 16 : 32 = 1 : 2 : 4$ . Hence the normal spinel can be represented as  $(\text{A}^{2+})_{\text{tet}}(\text{B}^{3+})_{\text{oct}}\text{O}_4$ . The spinel unit cell is shown in figure 3.1.

The spinel in which the divalent ions  $\text{A}^{2+}$  are on the tetrahedral sites and the trivalent ions of  $\text{B}^{3+}$  are on the octahedral sites is a normal spinel and denoted

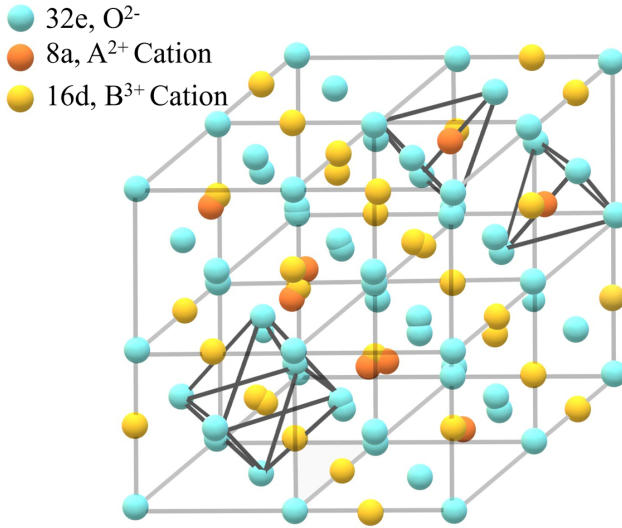


Figure 3.1: The spinel unit cell.

as (A)[B]<sub>2</sub>O<sub>4</sub>. However, if the tetrahedral sites are occupied by trivalent ions of B the term inverse spinel is used and is shown with (B)[AB]<sub>2</sub>O<sub>4</sub>. Any distribution between these two is also possible. The site fraction of B<sup>3+</sup> cations in the tetrahedral site is shown with  $y_{B^{3+}}^t$  and is used as a measure for the degree of intrinsic disorder and is defined in various literature as inversion parameter  $x$ . Therefore, for a perfectly normal spinel  $x$  is zero. NiAl<sub>2</sub>O<sub>4</sub> is reported to be a largely inverse spinel [41–43]. The inversion parameter together with the quasi-binary phase diagram of NiO-Al<sub>2</sub>O<sub>3</sub> was used to assess the spinel phase in the Ni-Al-O system. To extend this model to a higher order system including also Cr, a four-sublattice model was used with Cr<sup>2+</sup> also on the interstitial sublattice, to describe a deviation from stoichiometry towards excess metal. This was done earlier by Kjellqvist et al. [39], while modeling Cr-Fe-Ni-O system in order to reproduce the behavior observed in the experimental work of Töpfer et al. [44] which showed that the diffusion of Cr and Fe in (Cr<sub>*x*</sub>Fe<sub>1-*x*</sub>)<sub>3-*δ*</sub>O<sub>4</sub> is controlled by cation vacancies and cation interstitials at high and low oxygen

activities, respectively. Therefore, the spinel phase is modeled as follows:

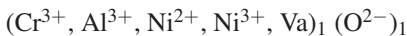


Where the first parenthesis represents the regular tetrahedral sites, while the second parenthesis correspond to the regular octahedral sites. The deviation from stoichiometry towards excess metal could be caused by both, octahedral and tetrahedral interstitial sites. Based on the work of Dieckmann and Schmalzried [45, 46] the predominant defects are the vacancies on Wyckoff positions 16d and also at high temperature the vacancies on 8a. In addition, at high temperatures the octahedral interstitial sites on 16c could be occupied.

In this work, only octahedral interstitial sites (third parenthesis) are included to be compatible with the rest of the assessments performed earlier [39, 40]. The spinel phase of Ni-Al-O is discussed in more details in section 7.5.

## 3.7 Halite

NiO has the NaCl structure which is known as halite. This structure is shown in figure 3.2 which belongs to the space group 225:  $Fm\bar{3}m$  with octahedral  $\text{Ni}^{2+}$  and  $\text{O}^{2-}$  sites. In this work, the halite structure is described using two sublattices model. The first sublattice includes the cations and vacancies, while the second one is occupied with oxygen. Vacancies are introduced to model the homogeneity range and maintaining the electroneutrality. This phase is presented as follows:



As can be noticed,  $\text{Cr}^{3+}$  and  $\text{Al}^{3+}$  are also included in the first sublattice to model the solubility of Cr and Al in NiO.

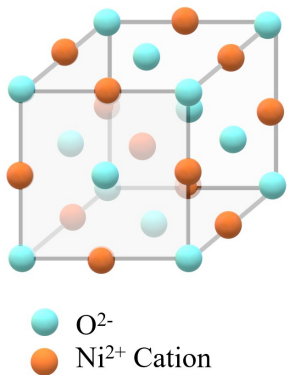


Figure 3.2: The NiO crystal structure.

# Chapter 4

## Experimental characterization of oxidation behavior

In order to investigate the oxidation behavior of NiAl with embedded Cr and Mo fibers, samples were produced in an arc melter and were subsequently cast. In addition, a zone melting device was used to produce directionally solidified NiAl-34Cr. The phase reactions of NiAl alloys with embedded Cr and Mo and the isothermal oxidation behavior were studied in a thermobalance. The oxidized samples were investigated by electron microscopy (SEM), chemical analysis (EDX), electron backscatter diffraction (EBSD) and X-ray diffraction (XRD). The interface reactions and oxide formations were studied in details. In this chapter the devices applied for sample preparation and characterization are introduced.

### 4.1 Sample preparation

#### 4.1.1 Arc melting

Arc melting is a process for melting metals in which electrical energy is used to generate an arc between electrode and materials. This electrode could either be consumable or non-consumable. Both of which can be used for melting of

materials with high melting points. Here, the cathode is a water-cooled copper pole with a tungsten head. The water-cooled copper crucible at the bottom and the metals to be melted work as the anode. The current exchanged between the two electrodes can reach high up to several hundred amperes. The ion plasma is generated due to the electric arc in the argon atmosphere and it can melt the samples. In this work the arc melting furnace (AM/0.5, Edmund Bühler) with a non-consumable tungsten electrode is used for the sample production. This arc melter can reach up to 3500 °C and can melt approximately 500 g of materials.

### 4.1.2 Directional solidification

Directional solidification of materials using floating zone processing have been used for decades in which various methods of heating can be applied such as optical heating [47, 48], induction heating [4] or electron beam heating. These methods are based on the float zone method which is derived from the zone-melting technique of Pfann [49]. In this technique only a small zone in a relatively large rod shape ingot is melted in which this molten zone is transformed along the rod by moving the ingot along its axle. The molten zone is preserved in position by the surface tension between two co-linear rods of the same alloy, and as a result a crucible is not required to retain the melt [50].

In this work, to produce the directionally solidified samples, first the button-shape alloys were produced in the arc melter. Subsequently, each sample was drop cast in a cylindrical shape copper mold with 10 mm in diameter and 180 mm in length. The drop cast ingot was later directionally solidified using a similar method compared to the work of Johnson et al. [4]. A crystal growth system from Systec was used to melt the cylindrical ingots, in which an induction coil heating source and a container-less vertical zone-pulling process

are applied. As shown in figure 4.1, the rod is held at its two ends by water-cooled grips and is derived upwards through the stationary induction coil. The induction coil divides the sample rod into the upper, directionally solidifying region (seed rod) and the lower, polycrystalline part (feed rod). The process is performed in a continuous Ar flow atmosphere. The preparation of the DS samples were performed in the institute of IAM-WK by Camelia Gombola as part of a collaboration in the IMD project of the Helmholtz research school.

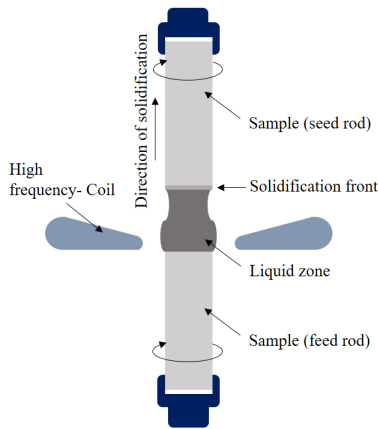


Figure 4.1: Formation of an electromagnetically constrained liquid zone during containerless processing, modified from [51].

### 4.1.3 Sample synthesis and preparation

NiAl with equimolar compositions were produced from high-purity nickel shot (99.95 wt.%) and aluminum shot (99.99 wt.%) employing an electric arc furnace (AM 0.5, Edmund Bühler) under an argon atmosphere with 99.9999% purity. Each alloy button was turned over and re-melted at least five times, to ensure compositional homogeneity. Considering that the weight loss after

melting did not exceed 0.1 mass %, nominal compositions were accepted. NiAl-Cr and NiAl-Mo coarse composites were produced by placing chromium bars or molybdenum wires in a cylindrical mold of the arc-melting device and then casting molten NiAl over them (figure 4.2). Subsequently, the resulting rods of NiAl with embedded Cr or Mo were cut with a diamond saw to samples of approximately 10 mm in diameter and between 1.5 to 3 mm in thickness as shown in figure 4.3-a and b. Figure 4.3-a, shows the NiAl-Cr coarse composite. In order to distinguish these composites from the directionally solidified samples (DS), these specimens are named "coarse composites" of NiAl-Cr and NiAl-Mo. Even though, a good contact between the Cr (the brighter region of the sample) and NiAl (the darker region of the sample) was made, pores could not be avoided completely at the interface of NiAl and the chromium bar.

In figure 4.3-b the NiAl-Mo coarse composite is shown in which the brighter

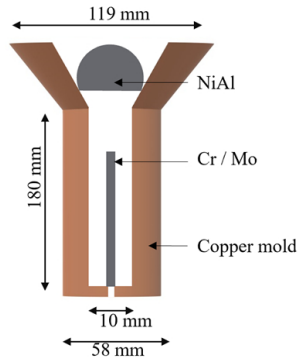


Figure 4.2: Schematic cross section view of the cylindrical mold used for producing NiAl-Cr and NiAl-Mo coarse composites.

region of the sample is the molybdenum wire and the darker region is the solidified NiAl which was cast over the molybdenum wire.

In order to validate the oxidation results in this work, samples of pure NiAl without any embedded materials were also produced and compared with the work by Brumm and Grabke who investigated the oxidation of pure NiAl [52].

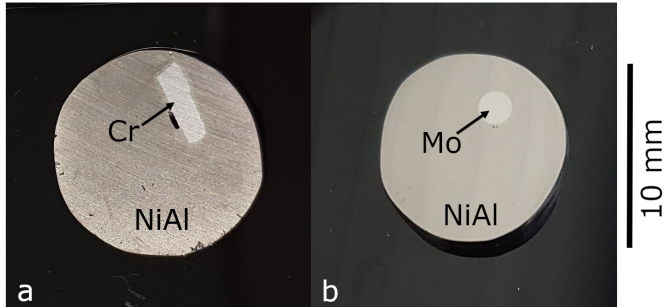


Figure 4.3: Samples from arc melting procedure. a) Junction of NiAl-Cr. b) Junction of NiAl-Mo.

Furthermore, directionally solidified samples of NiAl with 34 *at.%* Cr were prepared using the zone melting device which was discussed in section 4.1.2 with a growth rate of 120 *mm/h* and the clockwise rotation of 60 *rpm*. The cross section SEM image of the as cast DS NiAl-34Cr in perpendicular and parallel direction of the fiber planes are shown in figure 4.4 in which the darker region shows the NiAl matrix and the brighter region indicates to Cr-rich fibers. Prior to the oxidation, all specimens were abraded with SiC abrasive to a max-

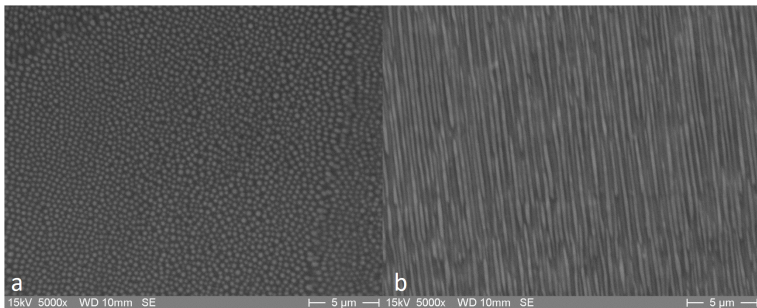


Figure 4.4: Cross section SEM image of as cast DS NiAl-34Cr with a growth rate of 120 *mm/h*: a) Perpendicular to the direction of fiber plane. b) Parallel to the direction of fiber plane.

imum of 1200 grit. Afterwards, they were cleaned in an ultrasonic bath using iso-propanol for 10 minutes. For surface investigations using SEM the samples were coated with graphite to achieve conductivity. Regarding the cross section investigations by SEM and EBSD, specimens were completely embedded in resin or graphite epoxy, respectively. Then, they were abraded at the desired surface to reveal the interface of NiAl and Cr and were further ground to a maximum of 1200 grit and were polished down to 1  $\mu\text{m}$  surface finish. Some samples were also etched with a solution of 80 vol.%  $\text{H}_2\text{O}$ , 10 vol.%  $\text{HCl}$  (37%  $w/w$ ) and 10 vol.%  $\text{H}_2\text{O}_2$  (30%  $w/w$ ) to better reveal the microstructure.

## 4.2 Thermogravimetric analysis

The thermogravimetric analysis (TGA) was performed in Netzsch 449 F3 Jupiter (TG resolution 0.1  $\mu\text{g}$ ) which was used for oxidation. The TGA measures the mass of a sample while it is heated, cooled or held at a constant temperature in a defined atmosphere. The Netzsch 449 is based on the classic concept of a thermobalance and is vertically-arranged instrument where the sample is loaded on top. However this arrangement results in the so called buoyancy effect, which further needs correction.

The buoyancy effect is in fact a combination of different factors which all lead to a deviation from the real mass change. These factors include; 1) the true buoyancy effect where the decrease in density of the gas causes an apparent weight gain of the sample; 2) the convection currents formed on the wall of the furnace which will force the cold gas in the center downwards and increases the apparent weight; 3) gas velocity which increases with the temperature and can have effects on the gas impinging the sample.

The thermobalance is sensitive to heat and any thermal effect can impact the results. Therefore, a blank correction experiment was performed after each measurement to reduce these effects. The results acquired from the TGA are

discussed in depth in section 8.1.

## 4.3 Oxidation procedure

Mass changes of the specimens during oxidation were investigated by thermogravimetric analysis (TGA) (Netzsch STA 449 F3 Jupiter), as samples were oxidized for 50 hours with the total flow of 10 L/h (argon gas containing 13 vol.% O<sub>2</sub>) at temperatures of 800 °C, 1200 °C and 1300 °C. The reason for using Ar/13 vol.% O<sub>2</sub> during oxidation is having similar conditions to the work of Brumm and Grabke [52] in order to use their work as a reference within this investigation. The desired temperatures were reached using the heating rate of 20 °C/min. Al<sub>2</sub>O<sub>3</sub> or ZrO<sub>2</sub>-crowns were used in order not to block the oxygen flow on one side of the sample while placing the specimens in the TGA. The mass change during oxidation was recorded by the microbalance. After oxidation, the oxide layers were investigated both on the surface and in cross sections, using XRD, EDX, EPMA, SEM and EBSD.

## 4.4 Characterization methods

### 4.4.1 SEM

Scanning electron microscope (SEM) is a microscope in which the electron beam is used to scan the surface and produce images. As the focused electron beam irradiates the target surface, it can result in formation of various signals at different depths within the sample.

This includes Auger electrons (AE), secondary electrons (SE), reflected or back-scattered electrons (BSE), characteristic X-rays, continuum X-ray and

light (cathodoluminescence) (CL). The most commonly used signals which are used in the SEM are the secondary electrons, back-scattered electrons and X-rays.

The secondary electrons are generated by the inelastic interaction of the incident electron and the atoms near the surface. Therefore, the secondary electron imaging (SEI) creates the high-resolution image from the sample surface in which details with less than 1 nm in size are visible. The back-scattered electrons (BSE) are the electrons that are reflected due to the elastic collision and are emerged from deeper area below the surface. Hence, the resolution of BSE is less than SEI. The intensity of the BSE depends strongly on the atomic number ( $Z$ ) of the specimen, as a result it can reveal the information about the distribution of composition together with the topographic information. The characteristic X-ray emits when an electron is removed from the inner shell and replaced by a higher-energy electron from the outer-layer shell while releasing X-ray photon. These X-rays can be used to characterize the composition of the sample using the energy dispersion X-ray (EDX) detector. In this work microstructure images are provided using the SEM (FEI XL30S, PHILIPS).

#### 4.4.2 XRD

The X-ray diffraction (XRD) method is used to determine the structures of crystals. A beam of incident X-ray is diffracted in specific patterns according to Bragg's law. These patterns specifically depend on the crystal structure of the specimen. Based on the diffraction directions and the intensities a diffraction pattern is obtained. Since each crystal has a unique crystal structure therefore a specific diffraction pattern is expected for different crystal structures.

In this work, a PADII X-ray diffractometer is used with a Meteor detector. The X-ray diffraction patterns were identified in Bragg-Brentano geometry where

the sample remains fixed while the X-ray tube rotates clockwise and the detector rotates anticlockwise. The measuring range is  $10^\circ$  to  $90^\circ$  with intervals of  $0.01^\circ$  and a counting time of 360 seconds per step using a  $\text{Cu K}\alpha_{1/2}$  source. The obtained patterns were compared with the standard patterns for phase identification. The background subtraction was performed using Rachinger correction [53].

### 4.4.3 EPMA

The electron micro probe analyser (EPMA) is used to determine the chemical composition of solid materials. The principle is similar to SEM where the sample is irradiated with the electron beam. In the EPMA the X-ray wavelength emitted from the targeted surface is corresponding to the specific elements and is used to characterize the composition of the sample. The main advantage of EPMA is the precise and quantitative elemental analyses even at very small spot sizes down to  $1 \mu\text{m}$ . The accuracy is typically  $\sim 1 \text{ at.}\%$  for major element analysis as long as the beam is stable and conditions of operation are optimized.

### 4.4.4 EBSD

Electron backscattered diffraction (EBSD) is a type of SEM in which the microstructural-crystallographic technique is used to study crystalline or polycrystalline materials. This technique can reveal information on the structure, phases, crystal orientations, defects and deformations.

In EBSD the specimen is placed in the SEM chamber in a way that a small angle of about  $20^\circ$  is formed between the incident beam and the surface of the sample. This tactical tilting will result in the reduction of the path length of electrons which back scatter by lattice planes and therefore, a greater fraction

of these electrons scatter from the sample.

Moreover, the contrast in electron backscatter diffraction pattern will increase compared to the situation when the beam irradiates directly over the surface of the sample [54].

The phosphor screen is placed in the specimen chamber and is coupled to a compact lens to focus the image from the phosphor screen on the CCD camera. Based on this design, a fraction of the electrons which have irradiated to the surface will backscatter. While leaving the sample, some of these electrons can fulfill the Bragg's condition corresponding to the spacing of the periodic atomic lattice planes of the crystalline structure and diffract. These diffracted electrons can produce an image on the phosphor screen transforming the backscattered signal to a visible light signal. These diffracted parts of the backscattered electrons are highly anisotropic and can produce a Kikuchi pattern. This pattern is later captured by the CCD camera which is placed behind the phosphor screen and is transferred to a computer where it is analyzed. By applying a well described system geometry, these patterns can be used to reveal the phase distribution map and the orientation distribution map.

However, using either EBSD or EDX analysis alone may not be enough to successfully distinguish between different phases. When the compositions are similar, the application of only EDX is limited, also it would not be possible to identify the structures with the EBSD alone if different phases have similar crystal structures and therefore producing similar patterns. Using integrated EBSD/EDX mapping can improve the results from the both techniques.

In this work, EBSD investigations were performed using a Zeiss Merlin field-emission gun scanning electron microscope (SEM) with GEMINI II electron optics. The acceleration voltage of 20 keV was applied.

# Chapter 5

## Oxidation Kinetics

The oxidation kinetics involves the evolution of the oxide thickness or oxide weight with time. If the density of the oxide scales were constant, these two could have been equivalent. Based on the numerous conditions such as the alloy composition, temperature and oxygen partial pressure, various oxidation mechanisms could be expected.

In this chapter Fick's first law of diffusion is briefly introduced and various oxidation rates based on different circumstances are discussed. These conditions are explained in depth in the work of Young [55].

### 5.1 Fick's first law of diffusion

The simple description of diffusion was first reported by Adolf Fick and was further developed in 19<sup>th</sup> century [56]. The Fick's first law shows that in a one-dimensional system, the flux of particles (ions, molecules, atoms etc.) is caused by concentration gradient and the flux is expressed as follows:

$$J = \frac{dm}{A \cdot dt} = -D \frac{\partial C}{\partial x} \quad (5.1)$$

Where  $J(\text{mol}/\text{m}^2 \cdot \text{s})$  is the flux which is the amount of substance,  $dm(\text{mol})$  that flows through a unit area,  $A(\text{m}^2)$  during a unit time interval,  $dt(\text{seconds})$ .

$D(m^2/s)$  is the diffusion coefficient,  $C(mol/m^3)$  is the concentration of particles and  $x(m)$  is the position parameter.

## 5.2 Oxidation rate equations

Oxidation of metals at high temperature is inevitable which could occur in wide range of conditions. Estimation of the material lifetime and the corrosion resistibility would be possible using the oxidation rate which could be linear, parabolic or logarithmic as shown in figure 5.1. The basic oxidation behaviors are investigated by various authors [55, 57–59] and are briefly introduced in this section.

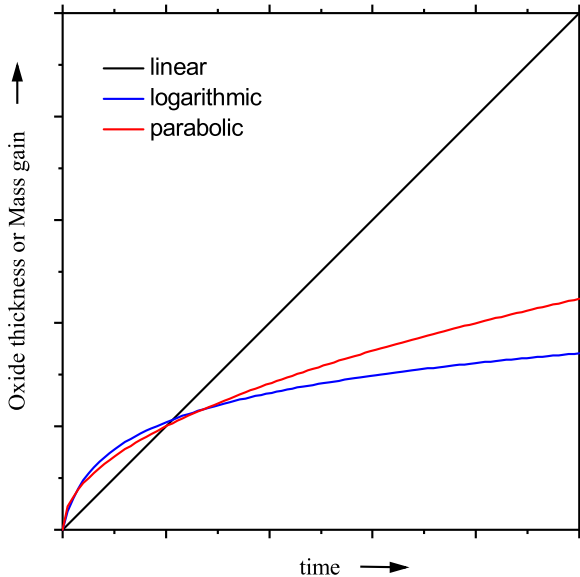


Figure 5.1: Schematic oxidation growth kinetics vs. time.

### 5.2.1 Linear kinetics

The non-protective oxide layers usually show a linear kinetic growth behavior. In this case, the oxide scale formation is directly proportional to time which could be described as follows:

$$\frac{dx}{dt} = K_l \quad (5.2)$$

Therefore:

$$x = K_l \cdot t \quad (5.3)$$

Where  $K_l$  is the linear rate constant. An example of this behavior can be seen in oxidation at high temperature and very low oxygen activities. Under these conditions, the diffusion of oxygen in the oxide scale is fast enough not to be the rate determining step. Meanwhile, the oxygen transfer from the gas to the scale surface is relatively slow and would control the rate. Hence, if the oxygen activity is constant, then the equation 5.3 holds. When a planar phase boundary process controls the rate of oxidation, linear oxidation behavior is expected [55]. Additionally, in cases where the oxide scale is highly porous, the oxygen mass transfer can occur through the pores easily and the oxide scale thickness does not have a determining effect on the diffusion of the gaseous species. Therefore, the linear kinetics is presumed which could indicate catastrophic reaction due to spallation of oxides, scale delamination or formation of cracks in the oxide scale [59].

### 5.2.2 Parabolic kinetics

The parabolic kinetic behavior has been first experimentally found by Tamman [60] and Pilling and Bedworth [61] and was later investigated thoroughly by Wagner [62–69]. The diffusion of species through the oxide scale can control the growth rate of the compact oxide scales. This could be either the

diffusion of metal ions from the substrate to oxide/gas interface, or oxygen ions which diffuse through the oxide scale and reach the oxide/metal interface, which would depend on the defect structure of the oxide.

As the oxide scale grows, longer time is needed for the ions to reach the oxide/gas or the oxygen to reach the metal/oxide interface which means:

$$\frac{dx}{dt} = \frac{K}{x} \quad (5.4)$$

Therefore:

$$x^2 = K_p \cdot t + x_0 \quad (5.5)$$

Where  $x$  is the oxide scale thickness (or mass gain during oxidation, which is proportional to the oxide scale thickness),  $K_p = 2K$  is the parabolic rate constant and is proportional to the diffusivity of the species which is the rate determining step and  $x_0$  is constant. Assuming the diffusion constant is independent of the oxide thickness, would mean that the oxide density, composition and topology should be constant.

Fick's first law (equation 5.1) describes the rate of diffusion in one dimension. The partial derivative in equation 5.1 is approximated by the difference in boundary values as follows:

$$J = -D \frac{\Delta C}{\Delta x} = \frac{-D(C_2 - C_1)}{x} \quad (5.6)$$

$C_1$  and  $C_2$  are the concentrations of the diffusing component at the scale-metal and scale-gas interfaces, respectively. A comparison of equations 5.6 and 5.4 would lead to:

$$K = \Omega \cdot D(C_2 - C_1) \quad (5.7)$$

Where  $\Omega$  is the volume of oxide formed per unit quantity of diffusing species. Using the acquired mass gain data from the thermogravimetric analysis the parabolic rate constant is calculated as follows:

$$\frac{\Delta m^2}{A} = K_p \cdot t \quad (5.8)$$

Where  $\Delta m$  is the mass gain and  $A(\text{cm}^2)$  corresponds to the oxide surface. More details about parabolic oxide growth can be found in work of Young [55], Paul et al. [58] and Pieraggi [70, 71]. In Ref. [70] the author has mathematically explained the difference in the parabolic nature of the oxide growth and how it could be differentiated between two types of plots of kinetics data, comparing  $\Delta m^2$  vs.  $t$  and  $\Delta m$  vs.  $t^{\frac{1}{2}}$ .

If the oxide has poor adhesion with the metal surface or the oxide scale is porous, then the oxygen can diffuse through more diffusion passes such as the grain boundaries, dislocations or stacking faults [72, 73]. In this case, the parabolic growth can no longer describe the oxidation behavior.

### 5.2.3 Logarithmic kinetics

The logarithmic oxidation kinetics relates to fast initial reaction which later slows down as the thickness of the oxide layer increases. This phenomenon is mainly seen during formation of thin oxide layers at low temperature. Therefore, it is not applicable to high temperature oxidation. The oxide scale thickness is logarithmically a function of time as follows:

$$x = K \cdot \log(ct + b) \quad (5.9)$$

Where  $c$  and  $b$  are both constants.

This rate law was suggested empirically. Nevertheless, the mechanism was explained by Cabrera and Mott [74], where the rate of the oxide growth is exponentially related to the electric field along the oxide scale. As the oxide

scale grows, the electric field is reduced and the activation energy for the ion movement decreases, then the oxidation rate follows the Wagner theory with the parabolic rate law.

# Chapter 6

## Evaluation of literature data for binary and ternary systems

In order to establish a reliable thermodynamic description for high component systems it is crucial to implement trustworthy data for the corresponding binary and ternary systems. In this work, as a means to provide the thermodynamic database for Ni-Al-Cr-Mo-O, 10 binary (Ni-Al, Ni-Cr, Al-Cr, Ni-O, Cr-O, Al-O, Al-Mo, Cr-Mo, Ni-Mo and Mo-O) and 10 ternary (Ni-Al-Cr, Ni-Cr-O, Al-Cr-O, Al-Cr-Mo, Ni-Al-Mo, Ni-Cr-Mo, Ni-Mo-O, Al-Mo-O, Cr-Mo-O and Al-Ni-O) systems needed to be described. Several respective systems have already been investigated thoroughly in the literature and are compared to the experimental data which will be briefly reviewed in this chapter. The systems which had to be revised or have been assessed in this work will be discussed in chapter 7.

In the present work, the open source database for the ternary system of Ni-Al-Cr from Dupin et al. [75] was used as the main basis and was further extended. Peng et al. [17, 76] used the assessment of Dupin [75] and improved the description of eutectic point of NiAl-Cr section to better fit to the experimental data. Additionally, in their work molybdenum and its corresponding binary and ternary systems were added to the database which are exploited here.

The compound energy of vacancies in the bcc phase was set to zero ( $G_{Va}^{bcc} = 0$ ) in the work from Dupin. However, as suggested by Franke [77], in the work

from Peng the  $G_{Va}^{bcc} = 0.2 \cdot RT$  was used. In addition, further subtraction of  $0.2 \cdot RT$  from the coefficients of A2/B2 phase was required to reproduce the result from Dupin.

Changes applied by Peng et al. [17, 76] in Ni-Al-Cr system were taken into account in this work.

Keeping the consistency while adding the elements Mo and O was the main challenge during extending of the database. In this regard, a single model had to be applied for the same phases in different ternary or binary systems. To model both metallic liquid and oxide liquid with one single description, the ionic-liquid model was chosen.

In the first step, the metallic liquid model which was used in Ni-Al-Cr assessment was changed to ionic-liquid model.

In the work of Dupin [75], the liquid phase containing two metallic elements such as Ni and Al was previously described using substitutional solution model. This description could now be changed to ionic two-sublattice model. The description is  $(Ni^{2+}, Al^{3+})_Q(Va)_Q$  where only the most stable oxidation states are used. In this case  $P$  and  $Q$  are equal since only vacancies exist in the anion sublattice. By using the hypothetically charged vacancy, the electro-neutrality is achieved.

The liquid parameters assessed in the literature which were used in the substitutional model can be directly used in the ionic two-sublattice model. However, modification in the liquid model description had to be applied in all binary and ternary metallic systems adapted from the literature. In order to avoid repetition, this will not be implied in each review of the metallic systems in the following sections.

In the next step after changing the liquid phase model, oxygen was added to the database. Meaning that three different ternary systems of Ni-Al-O, Al-Cr-O and Ni-Cr-O had to be imported. The work from Saltykov was used [36] for the first two ternaries which are the Al containing systems and the works from Taylor and Dinsdale [38] and also Kjellqvist et al. [39] were used for the Ni-Cr-O ternary.

Ionic-liquid model was used in all of these above-mentioned oxidic systems. Therefore, the liquid phase description remained unaltered in these ternaries. While the metallic liquid model had to be changed to the ionic-liquid model in the adapted metallic databases.

In addition, the Mo-O binary which was the missing link between the two quaternary systems of Ni-Al-Cr-Mo and Ni-Al-Cr-O was added in the next step using the work from Zhang [78]. Nevertheless, in their work the metallic liquid and the oxide liquid were addressed as two different phases and were modeled independently. The ionic two-sublattice liquid model was used in this work to describe both the metallic liquid and the oxide liquid with the same description. This will be discussed further in section 7.1.

In this chapter the binary and ternary systems which are assessed in the literature are reviewed. Different thermodynamic models were used in various adapted data especially regarding the liquid phase and the spinel phase which resulted in inconsistencies. Changes had to be applied in order to acquire a self-consistent database.

## **6.1 The Ni-Al-Cr system**

### **6.1.1 Review of binary systems**

The Ni-Al-Cr system consists of three binary sub-systems of Ni-Al, Ni-Cr and Al-Cr. All these three binaries are studied thoroughly in the literature and have been assessed. In the following sections these binaries are briefly reviewed.

#### **6.1.1.1 Ni-Al**

The Ni-Al was evaluated based on the experimental data available in 1990 by Nash et al. [79]. In 2004 Okamoto [80] updated the phase diagram based on the experimental data available in [81, 82]. The most recent critical evaluation was

established by Saltykov et al. [83] where  $\text{Ni}_3\text{Al}_4$  was considered as a stable phase.

Several authors have thermodynamically assessed the Ni-Al binary system [75, 84–91]. In the early assessment from Kaufman [84] considerable deviation from the available experimental data could be found. Besides, the  $\text{Ni}_2\text{Al}_3$  and  $\text{Ni}_3\text{Al}$  phases were not included in the calculations. Ansara et al. modeled the order-disorder transition of the  $\text{L1}_2$  to fcc phase using the sublattice model. This description was later improved using two and four sublattice model for describing the fcc/ $\text{L1}_2$  ordering [88].

Dupin et al. later used this description to reassess the data and achieve a better agreement with the experimental solvus data [75, 90]. The assessment of Dupin [75] was later refined by Peng et al. [17, 76, 92] regarding the modeling of the Gibbs energy of vacancies, this is discussed more in details in section 6.1.2. The  $\text{Ni}_3\text{Al}_4$  phase was not included in the work of Dupin et al. [75] and Peng et al. [17, 76, 92].

In this work the assessment of Dupin et al. [75] is used in which the refinement from Peng et al. [76] is taken into account. The crystallographic data of the stable solid phases in the Ni-Al system at atmospheric pressure is listed in 6.1. The Ni-Al binary phase diagram is shown in figure 6.1.

Table 6.1: Crystallographic data of stable solid phases in the Ni-Al system at atmospheric pressure [83].

Phases	Prototype	Pearson symbol	Space group
fcc	Cu	cF4	Fm $\bar{3}$ m
NiAl <sub>3</sub>	Al <sub>3</sub> Ni	oP16	Pnma
Ni <sub>2</sub> Al <sub>3</sub>	Al <sub>3</sub> Ni <sub>2</sub>	hP5	P $\bar{3}$ m1
Ni <sub>3</sub> Al <sub>4</sub>	Ga <sub>4</sub> Ni <sub>3</sub>	cI112	Ia $\bar{3}$ d
NiAl	CsCl	cP2	Pm $\bar{3}$ m
Ni <sub>5</sub> Al <sub>3</sub>	Ga <sub>3</sub> Pt <sub>5</sub>	oC16	Cmmm
Ni <sub>3</sub> Al	AuCu <sub>3</sub>	cP4	Pm $\bar{3}$ m

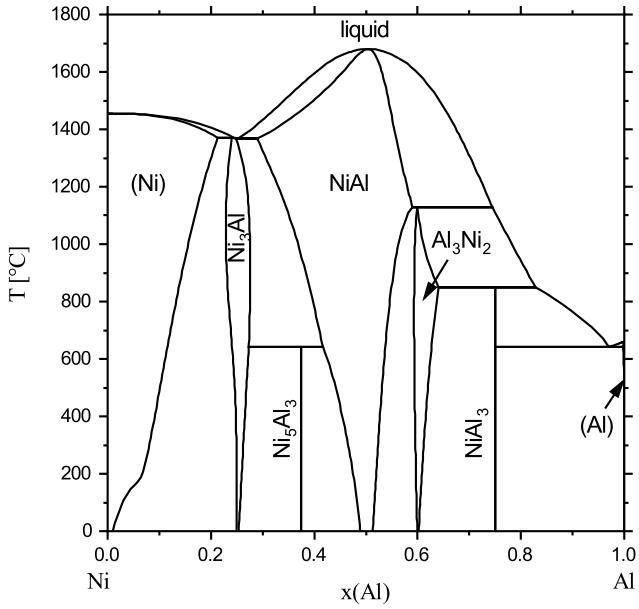


Figure 6.1: Calculated phase diagram of the Ni-Al system from Peng et al. [76].

### 6.1.1.2 Ni-Cr

The phase diagram of Ni-Cr binary was experimentally described by various authors [93–95] which all agree well with each other. The most recent experimental description by Massalski and Okamoto [96] in 1990 is mainly used in the assessments. Several thermodynamic assessments have been established by many authors [97–100] their results are well in agreement with each other. The assessment of Lee [100] was accepted by SGTE (Scientific group Thermodata Europe) SSOL database which does not include the Ni<sub>2</sub>Cr phase. In a more recent work from Turchi et al. [101] the Ni<sub>2</sub>Cr phase was included. However, the homogeneity range of this phase was not considered and the temperature at which the Ni<sub>2</sub>Cr formed peritectoidally was calculated 807 K while the experimental result showed 863 K. In the work of Dupin et al. [75] on Ni-Al-Cr ternary the dataset from Lee [100] and Dinsdale [97] are used for the description of Ni-Cr binary. However, the bcc phase is modified in order to model the disordered bcc and the ordered B2 using a single Gibbs energy function. Similarly, the disordered fcc and ordered L1<sub>2</sub> phases are also modeled by using a single Gibbs energy. The crystallographic data of stable solid phases in the Ni-Cr system is listed in table 6.2. In this work the description of Ni-Cr binary from Dupin [75] is accepted and is shown in figure 6.2. Therefore, Ni<sub>2</sub>Cr is not included in the phase diagram.

Table 6.2: Crystallographic data of stable solid phases in the Ni-Cr system at atmospheric pressure.

Phases	Prototype	Pearson symbol	Space group
bcc(Cr)	W	cI2	Im $\bar{3}$ m
bcc(Ni)	Cu	cF4	Fm $\bar{3}$ m
Ni <sub>2</sub> Cr	Pt <sub>2</sub> Mo	oP6	Immm

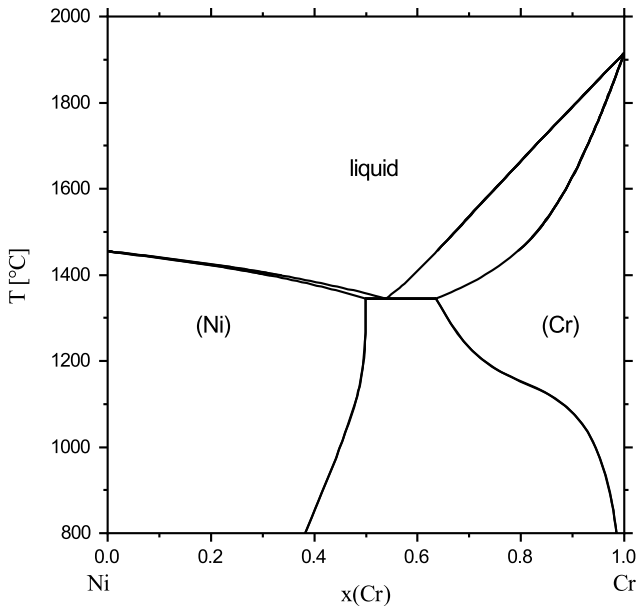


Figure 6.2: Calculated phase diagram of the Ni-Cr system based on work of Dupin [75].

### 6.1.1.3 Al-Cr

The Al-Cr binary system has been investigated and assessed by various authors. It was evaluated based on the experimental data available in 1998 by Murray [102], this evaluation was later updated by Okamoto [103] in 2008. The most recent evaluation was done by Khvan and Watson [104]. Regardless of many experiments performed on this binary, there are still some ambiguities in experimental investigation. Specifically in the region with 30-42 at.% Cr where the structure of the  $\gamma$  phase is still an open discussion. Various thermodynamic assessments were provided by different authors. [75, 105–111]. The assessment work from Dupin and Ansara [75, 107] are mainly based on the work of Saunders and Rivlin [105, 106]. Recently Tokunaga et al. [108] and Liang

et al. [109] have reassessed the Al-Cr system and the results agree well with the experimental data from Grushko et al. [112, 113]. However, the sublattice model used in Ref. [109] was not based on the crystallographic structure of the phases. Moreover, the activities and the enthalpies of mixing for liquid phase calculated in this assessment could not reasonably reproduce the experimental data. Later, Hu et al. [110] reassessed this binary and made some improvements. In the most recent assessment made by Witusiewicz et al. [111] the new experimental data from Stein et al. [114] was taken into account which can reproduce the results well. Nevertheless, the Al-Cr assessed by Dupin et al. [75] is used in this work since the dataset for the Ni-Al-Cr ternary system was adapted as the main basis. Bear it in mind that the main focus of this work is the equimolar ratio of Ni:Al and the assessment of Dupin et al. can reasonably be used in this range. The reliability of Al-Cr assessment based on Dupins work for equimolar ratio of Ni:Al was proved in the work from Peng et al. in which they have assessed the eutectic trough in the system NiAl-Cr-Mo [76]. Crystallographic data of stable solid phases in Al-Cr system are listed in table 6.3. The Al-Cr phase diagram calculated based on work of Dupin [75] is shown in figure 6.3.

Table 6.3: Crystallographic data of stable solid phases in the Al-Cr system at atmospheric pressure [104].

Phases	Prototype	Pearson symbol	Space group
fcc(Al)	Cu	cF4	Fm $\bar{3}$ m
bcc(Cr)	W	cI2	Im $\bar{3}$ m
Al <sub>7</sub> Cr	Al <sub>45</sub> V <sub>7</sub>	mC104	C2/m
Al <sub>11</sub> Cr <sub>2</sub>	Al <sub>5</sub> Cr	mP48	P2 C2/c Cmcm
Al <sub>4</sub> Cr	$\mu$ -Al <sub>4</sub> Mn	hP574	P6 <sub>3</sub> /mmc
$\gamma_1$ -Al <sub>8</sub> Cr <sub>5</sub>	Cu <sub>5</sub> Zn <sub>8</sub>	cI52	I $\bar{4}$ 3m
$\gamma_2$ -Al <sub>8</sub> Cr <sub>5</sub>	Al <sub>8</sub> Cr <sub>5</sub>	hR26	R $\bar{3}$ m
$\gamma'_2$ -Al <sub>8</sub> Cr <sub>5</sub>	-	-	-
$\gamma_3$ -Al <sub>9</sub> Cr <sub>4</sub>	-	-	-
$\gamma_4$ -Al <sub>9</sub> Cr <sub>4</sub>	-	cI52	I $\bar{4}$ 3m
AlCr <sub>2</sub>	MoSi <sub>2</sub>	tI6	I4/mmm
X	Al <sub>3</sub> Cr <sub>5</sub>	-	-

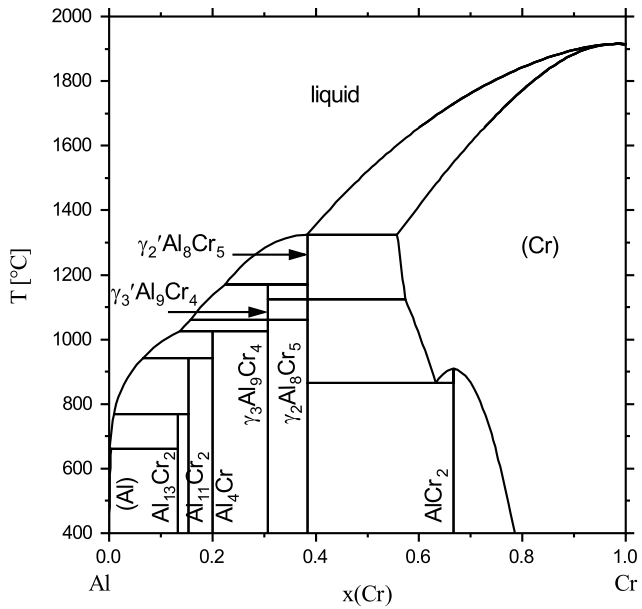


Figure 6.3: Calculated phase diagram of the Al-Cr system based on work of Dupin [75].

## 6.1.2 Review of Ni-Al-Cr system

A detailed review of the Ni-Al-Cr system was given by Velikanova et al. [115] in 2003 in which several ternary phases were reported. These ternary phases were not taken into account in the assessments which were provided earlier. The Ni-Al-Cr was first assessed by Dupin [86] in 1995. Later Huang and Chang [116] reassessed this ternary in order to reproduce the experimental result from Sung and Poirier [117] in which they modeled the disordered fcc and ordered L1<sub>2</sub> phases separately. In addition, two separate Gibbs energy functions for bcc disordered phase of A2 and ordered phase of B2 are used.

However, Dupin et al. [75] stated that "In multicomponent system, a possible competition between stable and metastable disordered phases may occur." Therefore, in their most recent work on Ni-Al-Cr ternary they have modeled the disordered bcc and the ordered B2 using a single Gibbs energy function. Similarly, the disordered fcc and ordered L1<sub>2</sub> phases are also modeled by using a single Gibbs energy. In this revision the new experimental data were also considered [117–119].

This reassessment of Dupin [75] was later used by Peng et al. [17, 76] where further changes were made in order to refine the model for the thermal vacancies in the bcc phase in Ni-Al and to better fit the experimental data regarding the eutectic point of NiAl-Cr section.

In the work of Peng [17] the ternary phases are investigated thoroughly. However, these phases form at relatively low temperatures and in a triangular region between Al<sub>60</sub>Cr<sub>40</sub>, Al<sub>60</sub>Ni<sub>40</sub> and Al (at.%) therefore, they are not considered in the assessment done by Peng. In this work we also focus on the equimolar ratio of Ni:Al and these ternary phases are not included in the assessment.

## 6.2 The Ni-Cr-O system

### 6.2.1 Review of binary systems

The Ni-Cr-O system consists of three binary sub-systems of Ni-Cr, Ni-O and Cr-O. All these three binaries are studied thoroughly in the literature and have been assessed. In the following sections these binaries are reviewed briefly.

#### 6.2.1.1 Ni-O

The Ni-O binary has been reviewed by Lewinsky [120] in 1997. Various experimental studies are available [121–126] and it has been thermodynamically described by different authors [35, 36, 38, 39, 127–132]. In the work from Taylor and Dinsdale [38] the Ni-O phase diagram has been carefully modeled based on the experimental data. Even though the works from Saltykov et al. [36] and Mozaffari [131] are more recent, the melting temperature of NiO is calculated 1976 °C which is 20 °C higher than the experimental results. Therefore, the description from Taylor and Dinsdale [38] is accepted in this work. The calculated Ni-O phase diagram is shown in figure 6.4. The crystallographic data of stable solid phases in Ni-O system are listed in table 6.4.

Table 6.4: Crystallographic data of stable solid phases in the Ni-O system at atmospheric pressure [133].

Phases	Prototype	Pearson symbol	Space group
(Ni)	Cu	cF4	Fm $\bar{3}$ m
NiO	NaCl	cF8	Fm $\bar{3}$ m
Ni <sub>2</sub> O <sub>3</sub>	ZnS	hP4	P6 <sub>3</sub> mc

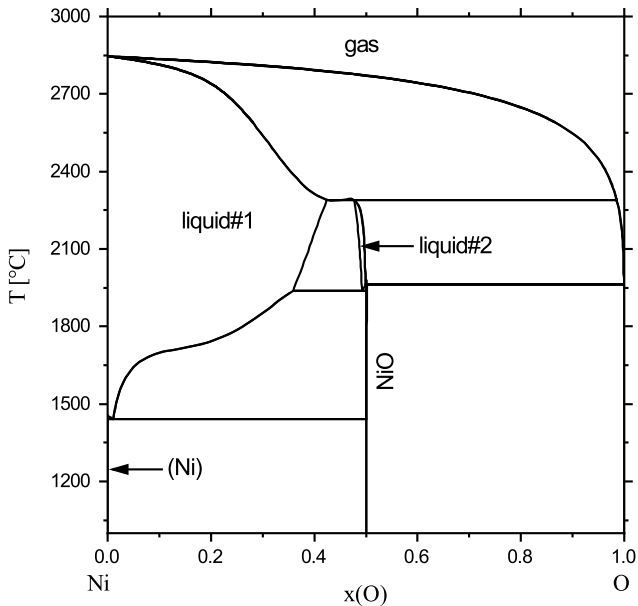


Figure 6.4: Calculated phase diagram of the Ni-O system based on work of Taylor and Dinsdale [38].

### 6.2.1.2 Cr-O

The binary of Cr-O has been reviewed recently in the work of Cornish et al. [134] in 2015. Therefore, only a brief review is given in this work. The Cr-O phase diagram up to 3200 °C was presented by Okamoto in 1997 [135].

Different assessments of this binary system are available from various authors [38–40, 129, 136, 137]. In the work of Povoden et al. [137] similar model to Taylor and Dinsdale work was used.

The determination of lattice parameters of  $\text{Cr}_3\text{O}_4$  has not been reported yet, which is due to the difficulty in retaining the phase while quenching to room temperature. Nevertheless, Toker et al. [138] assumed a tetragonally-distorted

spinel-type structure  $\text{Cr}_3\text{O}_4$  using data from unpublished research on Cr-Mg-O. However, in the work of Taylor and Dinsdale, the  $\text{Cr}_3\text{O}_4$  phase was first modeled as a stoichiometric phase [38], but later, in 1993 in their work with the Cr-Fe-O system,  $\text{Cr}_3\text{O}_4$  was incorporated in the model for the spinel phase [136], thus including  $\text{Cr}^{3+}$  on the tetrahedral sites and vacancies on the octahedral sites. This led to a deviation of melting temperature of  $\text{Cr}_3\text{O}_4$  from the experimental data.

In the most recent assessment of Kjellqvist et al. [39] the miscibility gap in the liquid phases closes with increasing temperature and the melting temperature of  $\text{Cr}_3\text{O}_4$  agrees better with the experimental data. The compound energy model is used in Kjellqvist's work to describe the non-stoichiometric compound of  $\text{Cr}_2\text{O}_3$ . This assessment agrees well with the most consistent experimental data available from Toker et al. [138] and is used in this work. The calculated Cr-O phase diagram is shown in figure 6.5. The crystallographic data of stable solid phases in Cr-O system are listed in table 6.5.

Table 6.5: Crystallographic data of stable solid phases in the Cr-O system at atmospheric pressure [134].

Phases	Prototype	Pearson symbol	Space group
(Cr)	W	cI2	$\text{Im}\bar{3}\text{m}$
$\text{Cr}_3\text{O}_4$	tetragonally distorted spinel-type structure		
$\text{Cr}_2\text{O}_{3-x}$	$\alpha\text{-Al}_2\text{O}_3$	hR30	$\text{R}\bar{3}\text{c}$
$\text{CrO}_2$	$\text{TiO}_2$	tP6	$\text{P}4_2/\text{mmn}$
$\text{CrO}_3$	$\text{CrO}_3$	oC16	ama2

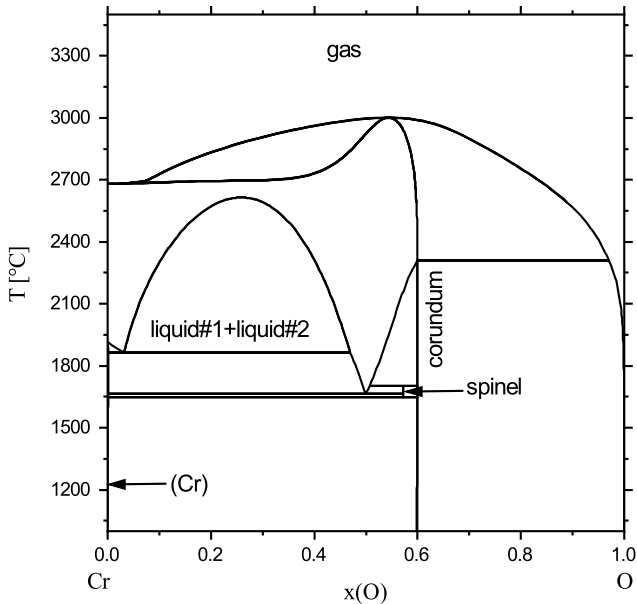


Figure 6.5: Calculated phase diagram of the Cr-O system based on work of Tokar et al. [138].

## 6.2.2 Review of Ni-Cr-O system

The Ni-Cr-O ternary was first assessed by Pelton et al. in 1979 [139] which was later reassessed by Taylor et al. [38] in 1990. The liquid phase was modeled using a two-sublattice ionic liquid model and the solid oxide phases were defined using the compound energy formalism. Using the compound energy formalism will allow the defining of non-stoichiometry and solid solution of NiO and  $\text{Cr}_2\text{O}_3$ -based phases as well as the distribution of cations on different sublattices in spinel phase of  $\text{NiCr}_2\text{O}_4$ . This assessment was later used by Saltykov [35, 36] and Kjellqvist [39, 40] where several changes were made. In the work from Kjellqvist the liquid phase in Ni-Cr-O system is reassessed

due to an unwanted miscibility gap forming in liquid phase at high temperatures. In addition, the description of  $\text{NiCr}_2\text{O}_4$  was modified so that the description is compatible with higher order systems. Due to the reassessment of liquid phase the melting point of  $\text{NiCr}_2\text{O}_4$  was calculated lower compared to what was reported by Taylor et al. [38].

The solubility of Cr in wustite was modeled by Taylor et al. [136] in Cr-Fe-O assessment where they defined the compound energy  $G_{\text{Cr}^{3+},\text{O}^{2-}}$ . However, the value assigned to  $G_{\text{Cr}^{3+},\text{O}^{2-}}$  contradicted with what they used earlier to describe the solubility of Cr in bunsenite. Kjellqvist has introduced an interaction parameter of  $L_{\text{Cr}^{3+},\text{Ni}^{2+},\text{O}^{2-}}$  together with the  $G_{\text{Cr}^{3+},\text{O}^{2-}}$  from Cr-Fe-O assessment to reproduce the solubility of Cr in bunsenite. The recent description of Kjellqvist for Ni-Cr-O [39, 40] is accepted in this work.

## 6.3 The Al-Cr-O system

### 6.3.1 Review of binary systems

The Al-Cr and Cr-O binaries have already been discussed in sections 6.1.1.3 and 6.2.1.2, respectively. The Al-O binary will be reviewed in this chapter.

#### 6.3.1.1 Al-O

The Al-O binary has been reviewed by Fabrichnaya et al. [140] in 2013. Therefore, a brief review of this binary will be given in this work. Wriedt defined the Al-O phase diagram based on the experimental available [141] in 1985 where no solubility of oxygen in the solid Al was observed and the oxygen solubility in the liquid Al was reported to be low. However, the experimental values for oxide-saturated liquid Al deviated from each other and since the preparation conditions were not fully explained, no conclusion was made regarding the solubility of oxygen in liquid Al.

The Al-O phase diagram shows a stable  $\text{Al}_2\text{O}_3$  phase which congruently melts at 2054 °C. This  $\text{Al}_2\text{O}_3$  is the stable corundum structure. Other polymorphic structures of  $\text{Al}_2\text{O}_3$  are also well known and established even though they are metastable including  $\gamma\text{-Al}_2\text{O}_3$  which has a spinel structure,  $\delta\text{-Al}_2\text{O}_3$  and  $\kappa\text{-Al}_2\text{O}_3$ . Several assessments are available [142–146]. The liquid description in the assessment of Taylor et al. [144] was re-evaluated by Hallstedt et al. [145] where  $\text{AlO}_{1.5}$  was introduced as an oxide species in the ionic liquid phase. In the most recent assessment [146] Mao et al. introduced  $\text{AlO}_2^{1-}$  species within the ionic two-sublattice model to describe the tetrahedral network which was used to better fit the experimental information in the  $\text{MgO-Al}_2\text{O}_3$ ,  $\text{CaO-Al}_2\text{O}_3$  and  $\text{SiO}_2\text{-Al}_2\text{O}_3$ . The ionic two-sublattice model was used as  $(\text{Al}^{3+})_P (\text{AlO}_2^{1-}, \text{O}^{2-}, \text{Va})_Q$ . However, in this work the assessment provided by Hallstedt [145] is used which has the liquid description of  $(\text{Al}^{3+})_P (\text{AlO}_{1.5}, \text{O}^{2-}, \text{Va})_Q$ . The calculated Al-O phase diagram is shown in figure 6.6. The crystallographic data of stable solid phases in Al-O system are listed in table 6.6.

Table 6.6: Crystallographic data of stable solid phases in the Al-O system at atmospheric pressure [140].

Phases	Prototype	Pearson symbol	Space group
(Al)	Cu	cF4	$\text{Fm}\bar{3}\text{m}$
$\alpha\text{-Al}_2\text{O}_3$	$\text{Al}_2\text{O}_3$	hR30	$\text{R}\bar{3}\text{c}$

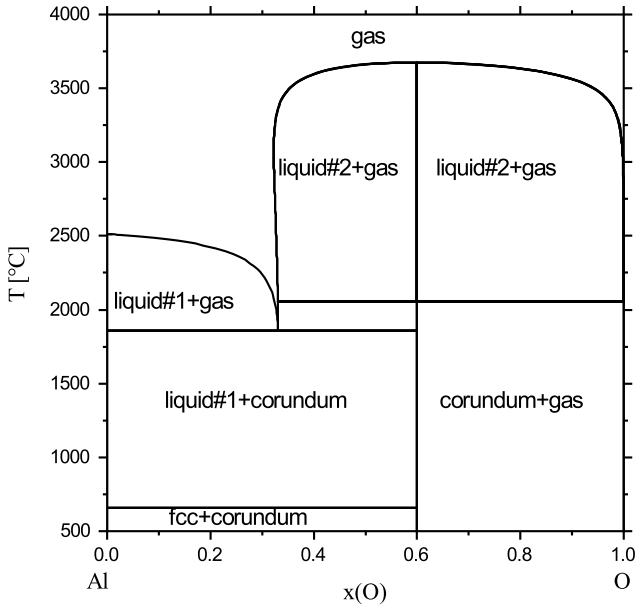


Figure 6.6: Calculated phase diagram of the Al-O system based on work of Hallstedt [145].

### 6.3.2 Review of Al-Cr-O system

The Al-Cr-O ternary system has been recently reviewed in detail by Kumar et al. [147]. Therefore, only a brief description will be given in this section. The studies in this ternary system are mainly focused on  $\text{Al}_2\text{O}_3$ - $\text{Cr}_2\text{O}_3$  quasi-binary section. This is due to the fact that this system is of interest in industrial applications such as catalysis, composites production, ceramic pigments, fiber optics, etc.

The quasi-binary section of  $\text{Al}_2\text{O}_3\text{-Cr}_2\text{O}_3$  is assessed by several authors [148–151]. Degterov et al. [152] used the modified quasi-chemical model for the liquid and subregular model for solid solutions and considered all available thermodynamic and phase equilibrium data to model the quasi-binary. The most recent assessment of this ternary has been done by Saltykov et al. [35, 36] with the same set of data as Degterov in which they have used the two-sublattice ionic liquid model in the compound energy formalism for the solid solution. The assessment of Saltykov et al. [35, 36] is accepted in this work.

## 6.4 The Al-Cr-Mo system

### 6.4.1 Review of binary systems

The Al-Cr-Mo system consists of binaries of Al-Mo, Cr-Mo and Al-Cr. The later has already been reviewed in section 6.1.1.3. Therefore, only Al-Mo and Cr-Mo will be discussed in this chapter.

#### 6.4.1.1 Al-Mo

The Al-Mo binary is recently reviewed by Schuster and Peng [153]. Several thermodynamic assessments are performed by Kaufman and Nesor [154, 155], Saunders [156], Du et al. [157], Cupid et al. [158] and Peng et al. [92]. In the assessment of Kaufman and Nesor [155] only the Mo-rich region of the phase diagram was optimized which deviated considerably from experimental data. Later, Saunders has assessed the Al-Mo phase diagram [156, 159]. However, due to lack of information many intermetallic phases in the Al-rich region were not included. More recently, Eumann et al. [160] re-evaluated the Al-Mo system in Al-rich region which confirmed the investigations of Schuster et al [161], regarding the existence of  $\text{Al}_{17}\text{Mo}_4$ ,  $\text{Al}_{22}\text{Mo}_5$  and  $\text{Al}_3\text{Mo}$  intermetallics.

Du et al. [157] and Cupid et al. [158] later adapted these data in their thermodynamic assessments. The thermodynamic data in the work of Cupid et al. [158] was used by Peng et al. [92] in which the liquid phase was re-optimized. The reason was that the assessment from Cupid et al. [158] led to an artificial inverse miscibility gap in the liquid phase and the stabilization of the bcc phase above the liquidus line. In the work of Peng et al. the congruent melting of AlMo was replaced by a peritectic reaction as the congruent melting point for the AlMo phase was assumed thermodynamically unlikely. However, in a more recent work from Kriegel et al. [162], the experimental results were in line with the assessment of Cupid et al. and at nearly equiatomic composition, the AlMo phase is formed around 2000 K by a congruent type of reaction and exhibits a disordered A2 structure.

Nevertheless, the transformation behavior of AlMo is still an open question. Since no assessment of Al-Mo binary with regards to this transformation AlMo phase is still available, in this work, the assessment performed by Peng et al. [92] is accepted which is in good agreement with experimental data [160, 161, 163–170]. The crystallographic data of stable solid phases in Al-Mo system are listed in table 6.7. The calculated Al-Mo phase diagram based on Peng et al. work is shown in figure 6.7.

Table 6.7: Crystallographic data of stable solid phases in the Al-Mo system at atmospheric pressure [153].

Phases	Prototype	Pearson symbol	Space group
fcc(Al)	Cu	cF4	Fm $\bar{3}$ m
bcc(Mo)	W	cI2	Im $\bar{3}$ m
Al <sub>12</sub> Mo	Al <sub>12</sub> W	cI26	Im $\bar{3}$
Al <sub>5</sub> Mo(r)	Al <sub>5</sub> Mo(r)	hP36	R $\bar{3}$ c
Al <sub>5</sub> Mo(h1)	Al <sub>5</sub> Mo(h1)	hP60	P321
Al <sub>5</sub> Mo(h2)	Al <sub>5</sub> W	hP12	P6 <sub>3</sub> 22
Al <sub>22</sub> Mo <sub>5</sub>	Al <sub>22</sub> Mo <sub>5</sub>	oF216	Fdd2
Al <sub>17</sub> Mo <sub>4</sub>	Al <sub>17</sub> Mo <sub>4</sub>	mC84	C2
Al <sub>4</sub> Mo	Al <sub>4</sub> W	mC30	C2/m
Al <sub>3</sub> Mo	Al <sub>3</sub> Mo	mC32	C2/m
Al <sub>8</sub> Mo <sub>3</sub>	Al <sub>8</sub> Mo <sub>3</sub>	mC22	Cm
Al <sub>63</sub> Mo <sub>37</sub>	-	-	-
AlMo	W	cI2	Im $\bar{3}$ m
AlMo <sub>3</sub>	Cr <sub>3</sub> Si	cP8	Pm $\bar{3}$ n

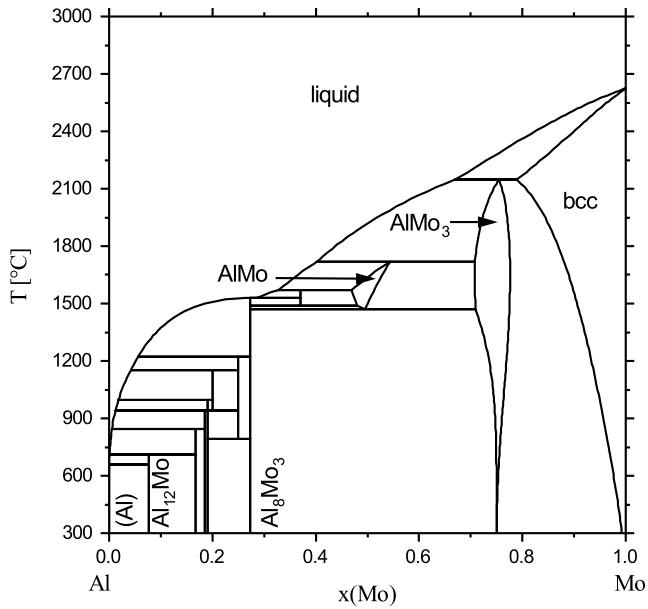


Figure 6.7: Calculated phase diagram of the Al-Mo system based on work of Peng et al. [92].

### 6.4.1.2 Cr-Mo

A detailed review of Cr-Mo is provided by Peng [171]. This binary is known to have a continuous solid solution with a minimum in the liquid and solidus lines at high temperatures as well as a miscibility gap in the solid phase at low temperatures. Venkatraman and Neumann reviewed the experimentally available data on the Cr-Mo system in 1986 [172] where the binary showed a minimum in the liquidus and solidus line at 1820 °C and 12.5 at.% Mo. Kubaschewski and Chart have investigated the miscibility gap [173] and reported a critical point in the range of 900 to 950 °C. As the diffusion rate is too low, it is challenging to experimentally determine the miscibility gap. Therefore, various authors have calculated the miscibility gap using thermodynamic modeling [174–179]. Among these calculations, some showed deviation from the experimental data [174–176] while in the work from Frisk and Gustafson [177] and Jindal et al. [179] a good agreement was seen between the calculated liquidus line and the experimental data. These two mentioned works are also consistent with the data reported by Kubaschewski and Chart [173] regarding the miscibility gap.

In the calculation of Frisk and Gustafson [177] the data from Rudy [180] were excluded as there was no minimum reported in the liquidus line. Instead, the experimental data from Kocherzhinskii and Vasilenko [181] was taken into account in the assessment. In the assessment by Jindal et al. [179], the experimental data from Rudy [180] were taken into account which resulted in lower solidus temperatures compared to the assessment by Frisk and Gustafson [177]. In this work the assessment by Frisk and Gustafson is adapted. The Cr-Mo phase diagram based on their assessment is shown in figure 6.8. The crystallographic data of stable solid phase in Cr-Mo system are listed in table 6.8.

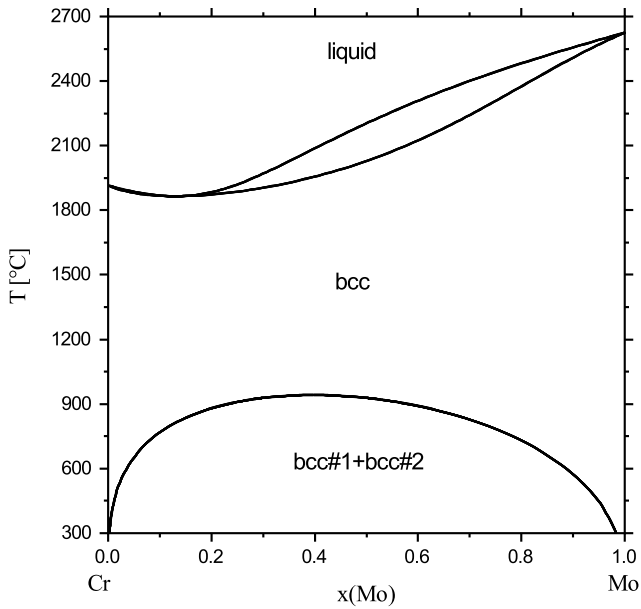


Figure 6.8: Calculated phase diagram of the Cr-Mo system from Frisk and Gustafson [177].

Table 6.8: Crystallographic data of stable solid phases in the Cr-Mo system at atmospheric pressure [171].

Phases	Prototype	Pearson symbol	Space group
(Mo, $\alpha$ Cr) ( $\alpha$ Cr) (Mo)	W	cI2	$\text{Im}\bar{3}\text{m}$

## 6.4.2 Review of Al-Cr-Mo system

Experiments focusing on Al-Cr-Mo systems were performed by different authors, including the work of Raman and Schubert [182], Polesya and Stepina [183], Kaufman and Nesor [154], Sanchez et al. [184, 185], Escorial et al. [186], Akiyama et al. [187] and Natishan et al. [188]. Among these works, Sanchez et al. have investigated the microstructure and the mechanical properties. In the works of Akiyama et al. and Natishan et al. the corrosion behavior of Al-Cr-Mo alloys are investigated. However, phase equilibria in the Al-Cr-Mo system are not studied experimentally.

The isothermal sections at 1000, 1500, 2300 and 2500 *K* were calculated in the work of Kaufman and Nesor [154], using an extrapolation of the binary systems since no experimental data was available at that time. The more recent experimental studies are also too limited to be used for the thermodynamic assessment. However, in the work of Peng et al. [17, 76] a ternary interaction parameter was introduced for the liquid phase in Al-Cr-Mo system to fit the experimental data of the NiAl-Cr-Mo quaternary system. In this work, the assessment of Peng et al. [17, 76] is taken into account.

## 6.5 The Ni-Al-Mo system

### 6.5.1 Review of binary systems

The Ni-Al and Al-Mo binaries have already been discussed in sections 6.1.1.1 and 6.4.1.1, respectively. The Ni-Mo binary will be reviewed in this chapter.

#### 6.5.1.1 Ni-Mo

The thermodynamic properties of Ni-Mo binary was reviewed by Brewer in 1980 [189] where the experimental data had been critically evaluated. Later Singleton and Nash [190] and Okamoto [191] made further corrections in 1991.

Recently, Turchanin et al. [192] have evaluated the Ni-Mo binary. Kaufman and Nesor have first modeled the Ni-Mo binary in 1978 [193] in which the stoichiometry of the  $\sigma$  phase was wrongly determined as  $\text{Ni}_6\text{Mo}_7$ . Further thermodynamic assessments were later carried out [194–197]. The assessment of Frisk et al. [194] could better describe the  $\sigma$  phase which was corrected to be NiMo. Later, Cui et al. [195] modified the dataset using the two-sublattice model to describe the  $\text{Ni}_3\text{Mo}$  phase. Wang et al. [196] indicated that the NiMo is metastable at very low temperatures. The energies of formation for  $\text{Ni}_2\text{Mo}$ ,  $\text{Ni}_3\text{Mo}$ ,  $\text{Ni}_4\text{Mo}$  and  $\text{Ni}_8\text{Mo}$  were calculated using first-principles calculations. Zhou et al. [197] had also investigated the Ni-Mo system using the same approach. Based on the former assessments they predicted the Ni-Mo phase diagram at low temperature and have introduced  $\text{Ni}_2\text{Mo}$  and  $\text{Ni}_8\text{Mo}$  compounds as stable phases in the Ni-Mo phase diagram which resulted the NiMo phase to be unstable at lower temperatures. The crystallographic data of stable solid phases in the Ni-Mo system are listed in table 6.9. The corresponding phase diagram based on the work of Zhou et al. [197] which is accepted in this work is shown in 6.9.

Table 6.9: Crystallographic data of stable solid phases in the Ni-Mo system at atmospheric pressure [192].

<b>Phases</b>	<b>Prototype</b>	<b>Pearson symbol</b>	<b>Space group</b>
bcc(Mo)	W	cI2	$Im\bar{3}m$
fcc(Ni)	Cu	cF4	$Fm\bar{3}m$
NiMo	NiMo	oP56	$P2_12_12_1$
Ni <sub>2</sub> Mo	MoPt <sub>2</sub>	cI8	$Immm$
Ni <sub>3</sub> Mo	CuTi <sub>3</sub>	oP8	$Pmmm$
Ni <sub>4</sub> Mo	MoNi <sub>4</sub>	tI10	$I4/m$
Ni <sub>8</sub> Mo	TiPt <sub>8</sub>	tI18	$I4/mmm$

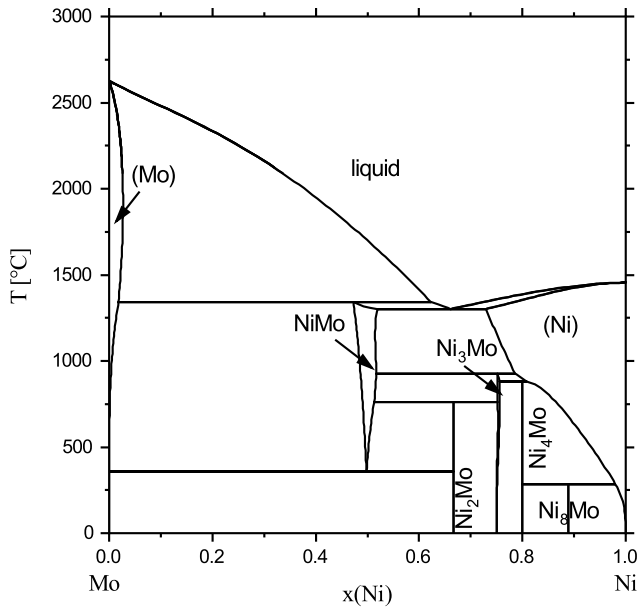


Figure 6.9: Calculated phase diagram of the Ni-Mo system using assessment of Zhou et al. [197].

## 6.5.2 Review of Ni-Al-Mo system

The Ni-Al-Mo system has been recently assessed by Peng et al. [17, 76, 92] and only a brief review of this ternary system is given in this chapter.

Several authors have thermodynamically assessed the Ni-Al-Mo system [154, 198, 199]. However, most of these assessments are focused mainly on the Ni-rich side and as a result the calculation deviates from the experimental data especially in case of the eutectic point in the NiAl-Mo section. Peng et al. used a laser heating-fast pyrometry apparatus to measure the solidus and liquidus temperatures of NiAl-Mo system. Based on these experimental data, a data set was provided in their work where the ordered B2 phase and the disordered A2 phase were also described with a single Gibbs energy function. In this work the assessment of Peng is accepted and is used in the data base.

## 6.6 The Ni-Cr-Mo system

### 6.6.1 Review of binary systems

The Ni-Cr, Cr-Mo and Ni-Mo binaries have been discussed in sections 6.1.1.2, 6.4.1.2 and 6.5.1.1, respectively.

### 6.6.2 Review of Ni-Cr-Mo system

A detailed description of the Ni-Cr-Mo system was given by Gupta [200] in 1990 and Lukas in 2010 [201]. In these works the ternary phases P,  $\sigma$  and  $\mu$  were identified. The ternary interaction parameters for P and  $\sigma$  phases were first introduced by Frisk [202] which were re-optimized in the recent work of Peng et al. [17, 76] and could better describe the experimental data reported by Raghavan et al. [203]. In the work of Peng et al. only P and  $\sigma$  ternary phases were included in the data base as there were some contradictions in the reports

regarding the  $\mu$  phase at lower temperatures [203–205]. In addition, this work is mainly focused on the high temperature phase equilibria. Therefore, the  $\mu$  phase is excluded. The crystallographic data of stable solid phases in Ni-Cr-Mo system are listed in table 6.10.

Table 6.10: Crystallographic data of stable solid phases in the Ni-Cr-Mo system at atmospheric pressure [201, 206].

<b>Phases</b>	<b>Prototype</b>	<b>Pearson symbol</b>	<b>Space group</b>
$\sigma$	CrFe	tP30	P4 <sub>2</sub> /mnm
P	P-CrMoNi	oP56	Pbnm
$\mu$	Fe <sub>7</sub> Mo <sub>6</sub>	hR39	R $\bar{3}$ m



# Chapter 7

## Optimization results and discussion

While establishing a thermodynamic database for a multi-component system, it is mainly necessary to provide binary and ternary assessments using experimental data. If these systems are described properly, reliable extrapolation into higher order systems could also be achieved.

So far most of the binary and ternary systems which were included in this work were already investigated and assessed in the literature and only some modifications had to be made to merge these data and make them compatible and consistent in the higher order systems. However, there were three ternaries which were not covered by any of these mentioned databases and had to be assessed in this work based on the experimental data which were available in the literature. These ternaries are Ni-Mo-O, Al-Mo-O and Cr-Mo-O which will be addressed in this section in more details. In addition, reassessment of Mo-O binary and Ni-Al-O ternary system will also be discussed. A list of references for the existing assessment of binary and ternary systems of Ni-Al-Cr-Mo-O and the further changes which have been applied is shown in table 7.1. A detailed list of parameters evaluated in this work is provided in the appendix A.

Table 7.1: List of modifications made in each binary and ternary systems of Ni-Al-Cr-Mo-O.

Data used directly from literature		Change of liquid phase description		Parameters revised (see text)		Assessed in in this work
Al-O	[36]	Ni-Al	[75]	Mo-O	[78]	Ni-Mo-O
Ni-O	[38, 39]	Ni-Cr	[75]	Al-Ni-O	[36]	Al-Mo-O
Cr-O	[38, 39]	Al-Cr	[75]			Cr-Mo-O
Ni-Cr-O	[38, 39]	Ni-Mo	[17]			
Al-Cr-O	[36]	Cr-Mo	[17]			
		Al-Mo	[17]			
		Ni-Al-Cr	[75]			
		Al-Cr-Mo	[17]			
		Al-Mo-Ni	[17]			
		Ni-Mo-Cr	[17]			

## 7.1 Mo-O binary system

The Mo-O binary system has been investigated by Brewer and Lamoreaux [207] in which the phase diagram is established as shown in figure 7.1.

Various molybdenum oxides are reported in this binary system. The crystallographic data of stable solid phases in Mo-O system are listed in table 7.2. Zhang et al. assessed the Mo-O binary system [78] in 2014. In this work all thermodynamic coefficients are taken from work of Zhang et al. [78] except for the changes which will be discussed in the following.

In the work of Zhang et al. [78] the (Mo, O) solid solution was described as  $(\text{Mo}, \text{O})_1 (\text{O}, \text{Va})_3$ , which means existence of oxygen in the first sublattice is assumed. However, complying with the most common description of oxygen in the metallic phases as interstitially dissolved, in this work the bcc phase is described using a two-sublattice model with metals on the first sublattice and

Table 7.2: Crystallographic data of stable solid phases in the Mo-O system at atmospheric pressure [207].

Phases	Prototype	Pearson symbol	Space group
(Mo)	W	cI2	Im $\bar{3}$ m
Mo <sub>4</sub> O <sub>11</sub>	Mo <sub>4</sub> O <sub>11</sub>	oP60	Pna2 <sub>1</sub>
Mo <sub>9</sub> O <sub>26</sub>	Mo <sub>9</sub> O <sub>26</sub>	mP70	P2/c
Mo <sub>8</sub> O <sub>23</sub>	Mo <sub>8</sub> O <sub>23</sub>	mP62	P2/c
MoO <sub>2</sub>	VO <sub>2</sub>	mP12	P2 <sub>1</sub> /c
MoO <sub>3</sub>	MoO <sub>3</sub>	oP16	Pnma

the oxygen and the vacancies on the second sublattice as suggested by Kjelqvist et al. [39]. Therefore, the solubility of oxygen in Mo is reassessed in the present work using experimental data.

The solubility of oxygen in Mo was investigated by Few and Manning [208] already in 1952 in which they examined the solubility in the range from 1100 to 1650 °C. Later, in 1974 Srivastava and Seigle [209] re-determined the solubility of oxygen in Mo in the range from 1400 to 1900 °C. There is a large difference between these two results.

In the work of Few and Manning they used flowing atmosphere of oxygen on Mo wires which were heated to the desired temperature. The oxygen pressure was increased slowly until an oxide film was formed. Using the known pressure for the formation of oxides, the experiments were repeated this time only reaching 90% of the oxygen pressure recorded. After a specific period of time the samples were rapidly cooled to room temperature. The samples which exhibited no oxide formation were analyzed for oxygen content.

However, the result from Few and Manning still raises some questions. The solubilities are measured in the temperature range from 1100 to 1650 °C. The values are all below 100 ppm in which the solubility curve is linear rather than

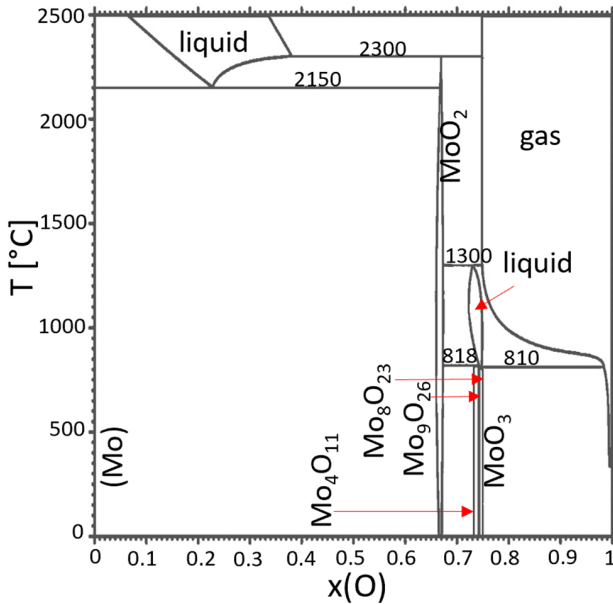


Figure 7.1: Mo-O phase diagram adapted from work of Brewer and Lamoreaux [207].

an exponential function of temperature. Moreover, an extrapolation of their result at zero kelvin, leads to a none zero value. Determination of such low solubility is difficult and it could be possible that the authors have observed higher solubilities due to presence of oxides or oxide-forming impurities in the initial material since the purity of the materials that they used are not determined.

On the other hand, Srivastava and Seigle experimentally investigated the solubility of oxygen in Mo while equilibrating a zone-refined Mo rod with mixtures of powdered Mo and  $MoO_2$  in sealed capsules at high temperatures. Later, the samples were rapidly cooled to room temperature the rods were cleaned thoroughly, and analyzed for oxygen.

The oxygen solubility in the work of Srivastava and Seigle are measured for a wider temperature range and the results from both low and high temperature ranges could be represented with one line in a van't Hoff plot. In addition, Srivastava and Seigle avoided the error caused by impurities by using essentially zone-refined Mo rods. Since the oxygen solubility in the rods annealed for 35 h at 1847 K are similar to the ones annealed at 1846 K for 5.5 h, it is assumed that equilibrium had been achieved in their work.

For this reason, the experimental data from Srivastava and Seigle [209] were used to reassess the solubility of oxygen in Mo. Based on these experimental data the bcc phase is revised using the parameter  $G_{Mo:O}^{bcc}$  with Mo on the first sublattice and oxygen on the second sublattice corresponding to the interstitial sites, to fit the solubility of oxygen in solid molybdenum. The optimized parameters are listed in appendix A and the POP file used for optimizing the solubility is listed in appendix C.

The calculated solubility of oxygen in Mo is shown in figure 7.2 which is in good agreement with the experimental data.

The Mo-O phase diagram described by Brewer and Lamoreaux [207] is shown in figure 7.1 and is used in this work to reassess the liquid phase. As shown in the Mo-O phase diagram, the metallic liquid forms on the Mo-rich side while on the oxygen-rich side the liquid oxide is formed. This was the main reason for using the ionic two-sublattice model in order to have one single description for the two liquids. In the Mo-O binary the ionic-liquid phase is described as follows:  $(Mo^{4+}, Mo^{6+})_p(O^{2-}, Va^Q)_Q$  where  $Mo^{4+}$  and  $Mo^{6+}$  are placed in the cation sublattice and  $O^{2-}$  and Va are placed in the second sublattice. This could describe the metallic liquid where only the cations on the first sublattice and the hypothetical vacancies on the anion sublattice are considered. In addition, this could also describe the oxide liquid formed from  $MoO_2$  and  $MoO_3$ . For this reason, two thermodynamic parameters of  $G_{Mo^{4+}:O^{2-}}^{Liquid}$  and  $G_{Mo^{6+}:O^{2-}}^{Liquid}$  are introduced. In addition two interaction parameters between  $Mo^{4+}$  and  $Mo^{6+}$  on the first sublattice and oxygen on the second sublattice ( $L_{Mo^{4+}, Mo^{6+}:O^{2-}}^{Liquid}$ ) and also between  $Mo^{4+}$  on the first sublattice together with oxygen and vacancies

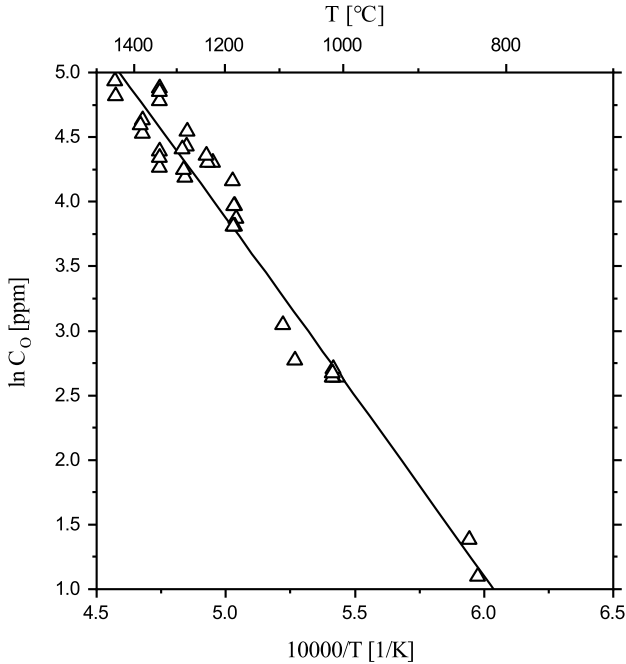


Figure 7.2: Calculated solubility of oxygen in solid molybdenum compared with experimental data from Srivastava and Seigle [209].

on the second sublattice ( $L_{Mo^{4+};O^{2-},Va}^{Liquid}$ ) were introduced to better fit the invariant reactions regarding the oxide liquid in the Mo-O subsystem. The assessed parameters are presented in the appendix A. An example of POP file for optimizing parameters of the liquid phase in the Mo-O binary can be found in the appendix B. The calculated phase diagram in this work is shown in figure 7.3 which shows a good agreement with the experimental phase diagram (figure 7.1). A more detailed Mo-O phase diagram in the range of high oxygen content is shown in figure 7.4.

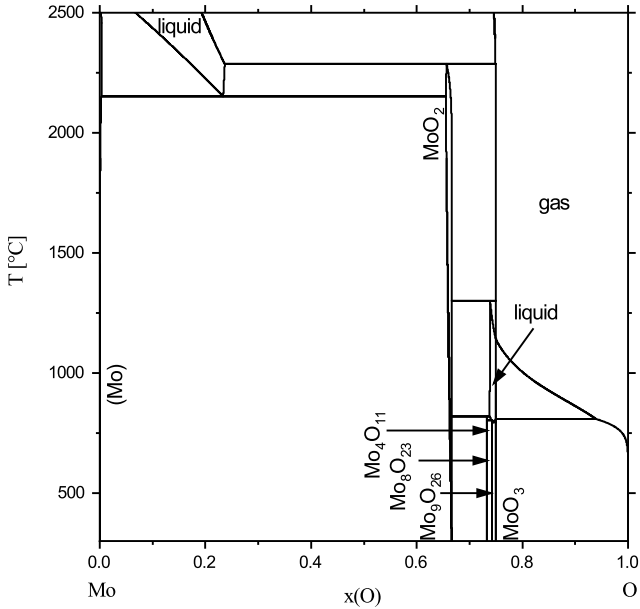


Figure 7.3: Calculated Mo-O phase diagram.

In figure 7.5 the site fraction of  $Mo^{4+}$  and  $Mo^{6+}$  are calculated in the liquid phase at isothermal conditions of 750 °C and 1000 °C as a function of composition. As can be seen, the amount of  $Mo^{4+}$  on the first "sublattice" decreases with increasing of oxygen content while the  $Mo^{6+}$  amount increases. This change corresponds to the formation of  $MoO_2$  and  $MoO_3$  in the Mo-O phase diagram.

The calculated invariant reactions temperature in the Mo-O binary are listed in table 7.3 and are compared with the literature data. As can be seen the results are in a good agreement with the experimental data of Brewer and Lamoreaux [207] and also the calculations of Zhang et al. [78]. The only exception is that in the work of Zhang et al. [78] a peritectic reaction is assumed in which the

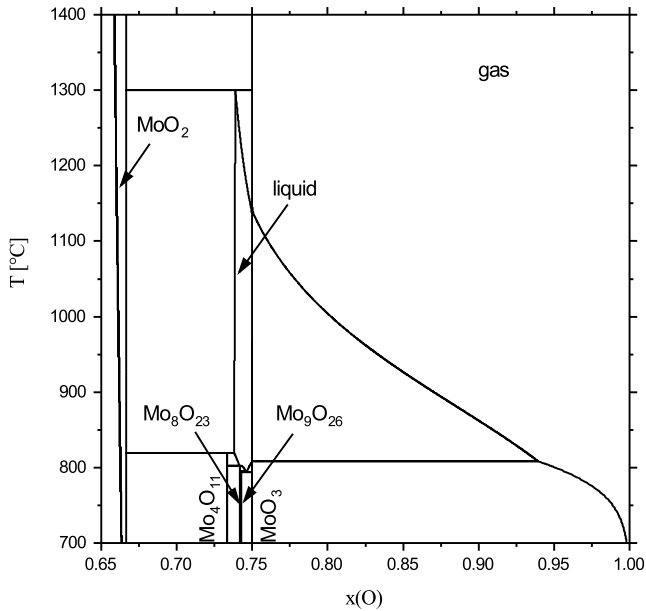
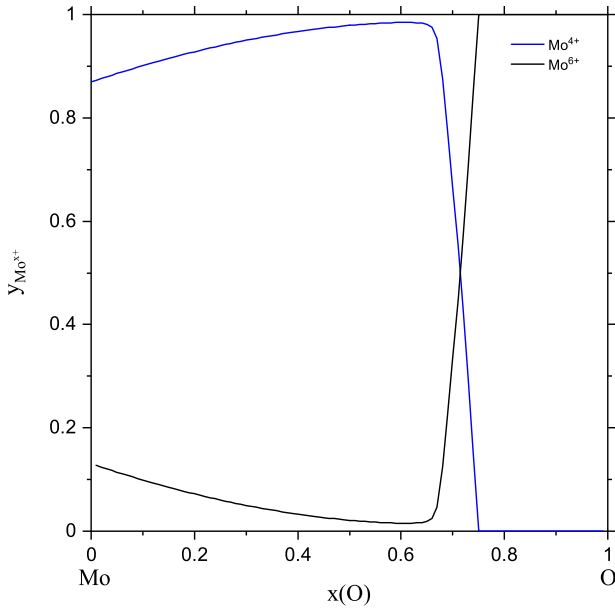


Figure 7.4: Calculated partial Mo-O phase diagram in the range of high oxygen content.

liquid phase and the  $\text{Mo}_4\text{O}_{11}$  form the  $\text{Mo}_8\text{O}_{23}$  at around 797 °C. However, the specific invariant reaction was not indicated in the work of Brewer and Lamoreaux [207]. In this work, eutectic reaction in which the liquid phase forms  $\text{Mo}_4\text{O}_{11}$  and  $\text{Mo}_8\text{O}_{23}$  could better describe the transformation at this temperature range. Consequently, the  $\text{Mo}_8\text{O}_{23}$  melts congruently at 796.1 °C. More accurate experimental data is still needed to better describe the reactions in this composition ranges.

In a more recent work of Corcoran et al. [210] the Mo-O binary was assessed as part of a thermodynamic investigation of the uranium, molybdenum and oxygen system, in which the oxygen solubility in Mo was considered. Similar to this work, the ionic two-sublattice model was used to describe both metallic



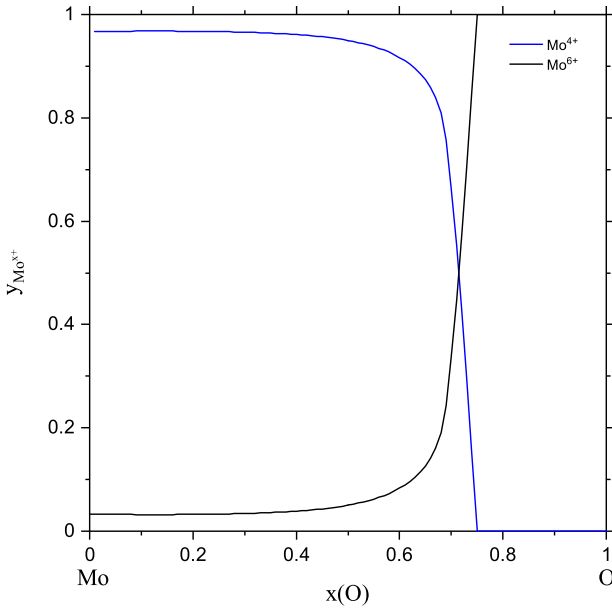
(a) at 750 °C.

Figure 7.5: Calculated site fraction of  $\text{Mo}^{x+}$  in the liquid phase as a function of composition in Mo-O binary system.

and oxidic melts with the same model. However, they described the sublattices as follows:  $(\text{U}^{4+}, \text{Mo}^{4+})_p(\text{O}^{2-}, \text{Va}^{Q-}, \text{MoO}_3, \text{MoO}_4^{2-}, \text{O})_Q$

Both of the descriptions used in this work and in the work of Corcoran et al. are acceptable within the definition of ionic two-sublattice model. Nevertheless, it is conventionally more common to define the cations on the first sublattice and only anions, neutral species and vacancies on the second sublattice as it is performed in the present work.

The heat capacities of  $\text{MoO}_2$  and  $\text{MoO}_3$  are calculated and are compared to the experimental data as shown in figure 7.6. As can be seen in figure 7.6-a



(b) at 1000 °C.

Figure 7.5: Calculated site fraction of  $\text{Mo}^{x+}$  in the liquid phase as a function of composition in Mo-O binary system. (cont.)

the heat capacity of  $\text{MoO}_2$  is in good agreement with the experimental data of King et al. [211]. In figure 7.6-b the calculated  $C_p$  of  $\text{MoO}_3$  in this work is compared with the experimental data in the literature [211–213], the results are in a good agreement for solid  $\text{MoO}_3$ .

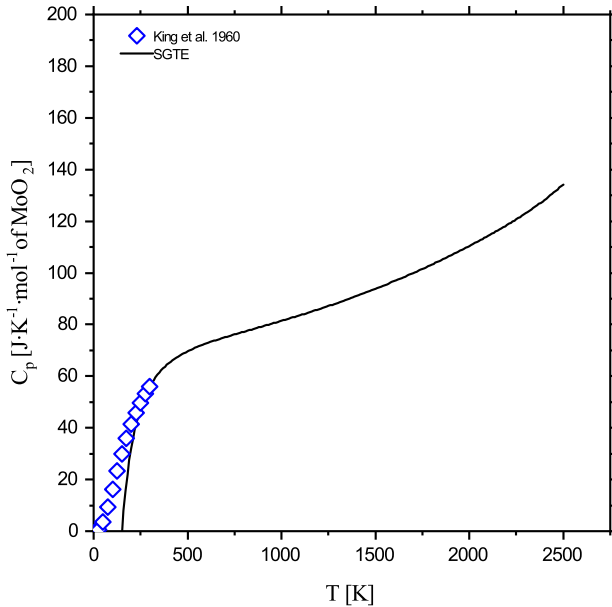
In the work of Cosgrove and Snyder [213] the values are also calculated for the molten  $\text{MoO}_3$  in which different smoothing methods were used below and above the melting point of  $\text{MoO}_3$ . In the work of Corcoran et al. [210] the heat capacity defined for  $\text{MoO}_3$  in SGTE substance database [214] was also extrapolated in higher temperature ranges, in the liquid region in order to avoid

Table 7.3: Calculated invariant reaction temperatures in the Mo-O binary in the present work compared with the literature data [78, 207].

Invariant reactions	Reaction type	Ref. T [°C]		T [°C] (this work)
L $\longleftrightarrow$ (Mo) + MoO <sub>2</sub>	Eutectic	2206	[78]	2151.7
	Eutectic	2150	[207]	
L + MoO <sub>2</sub> $\longleftrightarrow$ Mo <sub>4</sub> O <sub>11</sub>	Peritectic	817	[78]	813.2
		818	[207]	
L + Mo <sub>4</sub> O <sub>11</sub> $\longleftrightarrow$ Mo <sub>8</sub> O <sub>23</sub>	Peritectic	797	[78]	-
	-	-	[207]	-
L $\longleftrightarrow$ Mo <sub>8</sub> O <sub>23</sub>	Congruent melting	-	-	796.1
L $\longleftrightarrow$ Mo <sub>8</sub> O <sub>23</sub> + Mo <sub>4</sub> O <sub>11</sub>	Eutectic	-	-	895
L + Mo <sub>8</sub> O <sub>23</sub> $\longleftrightarrow$ Mo <sub>9</sub> O <sub>26</sub>	Peritectic	788	[78]	788.1
		780.5	[207]	
L $\longleftrightarrow$ Mo <sub>9</sub> O <sub>26</sub> + MoO <sub>3</sub>	Eutectic	786	[78]	787
	Eutectic	778	[207]	

the kink in the  $C_p$  plotted vs. temperature. This would mean that the  $H$  increment in the liquid phase would be lower than what is experimentally expected. In this work, in order to avoid the step in the  $C_p$  plot for the MoO<sub>3</sub> in figure 7.6-b, changes in the data adapted from SGTE substance database are made. At 1075 K, which is the melting point of MoO<sub>3</sub>, the function is split into two new functions. One consists of the data for the lower temperature interval in the SGTE substance database and now is extended to higher temperatures which represents the Gibbs energy function of the solid MoO<sub>3</sub>, including the extrapolation above the melting point. The second function represents the Gibbs energy function for the molten MoO<sub>3</sub> and now the temperature range includes also the supercooled liquid.

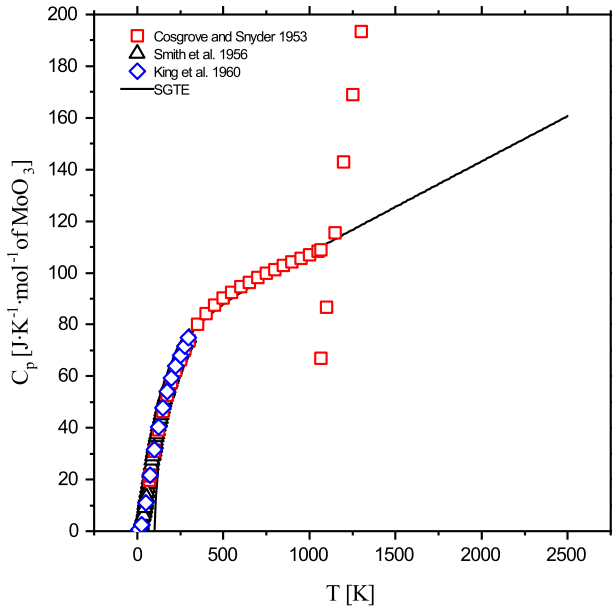
The enthalpy increment as a function of temperature is plotted for MoO<sub>2</sub> and MoO<sub>3</sub> in figures 7.7-a and 7.7-b, respectively. The results show very good agreement with the experimental data from King et al. [211].



(a) for  $\text{MoO}_2$  compared to the experimental data from King et al. [211].

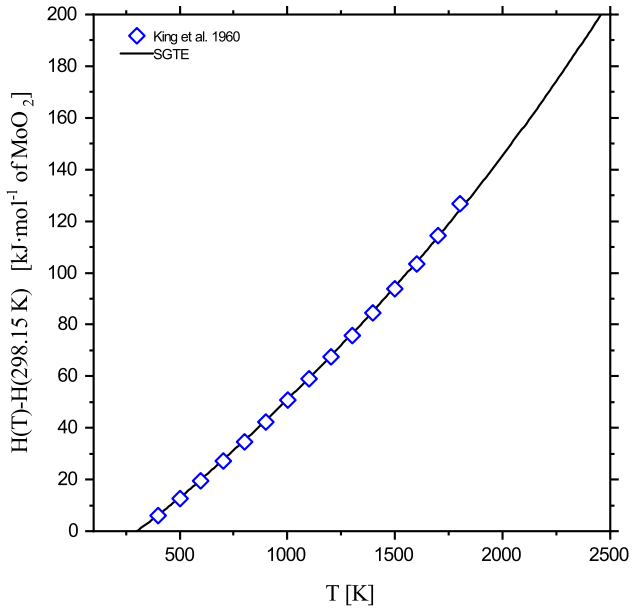
Figure 7.6: Calculated heat capacity for solid  $\text{MoO}_x$ .

Similarly, the entropy of solid  $\text{MoO}_2$  and  $\text{MoO}_3$  are plotted as a function of temperature in figures 7.8-a and 7.8-b, respectively. King et al. [211] have experimentally calculated these values for  $\text{MoO}_2$  and  $\text{MoO}_3$  at 298.15 K as 46.275 and 77.739  $\text{J} \cdot \text{K}^{-1} \cdot \text{mol}^{-1}$ , respectively. The calculated results in this work, agree well with the experimental results from King et al. [211].



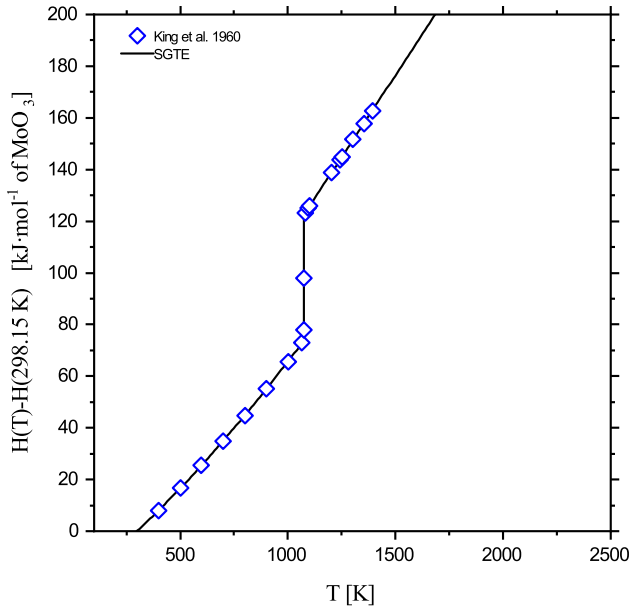
(b) for  $\text{MoO}_3$  compared to the experimental data from literature [211–213].

Figure 7.6: Calculated heat capacity for solid  $\text{MoO}_x$ . (cont.)



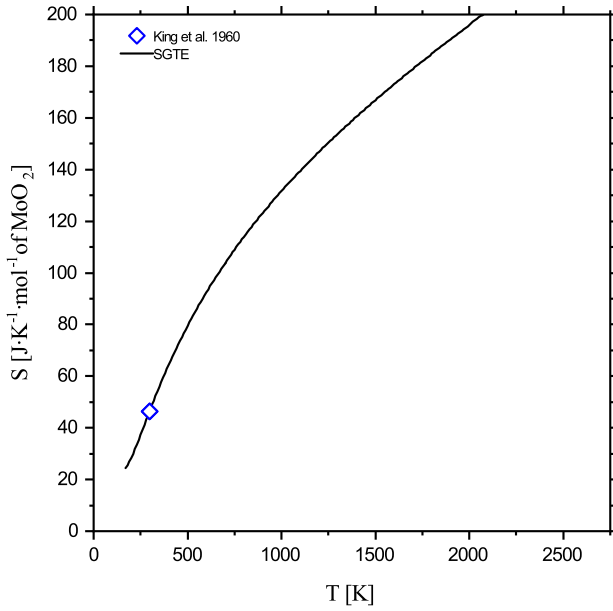
(a) for MoO<sub>2</sub> compared to the experimental data from King et al. [211].

Figure 7.7: Calculated enthalpy increment for solid MoO<sub>x</sub>.



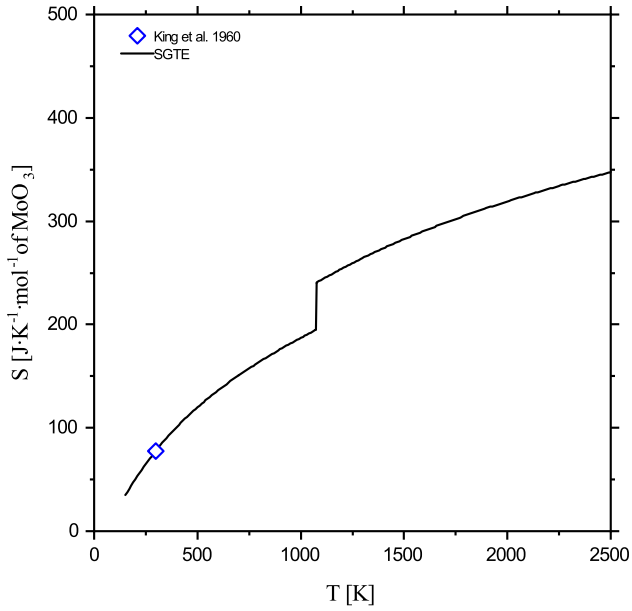
(b) for  $\text{MoO}_3$  compared to the experimental data from King et al. [211].

Figure 7.7: Calculated enthalpy increment for solid  $\text{MoO}_x$ . (cont.)



(a) for MoO<sub>2</sub> compared to the experimental data from King et al. [211].

Figure 7.8: Calculated entropy for solid MoO<sub>x</sub>.



(b) for  $\text{MoO}_3$  compared to the experimental data from King et al. [211].

Figure 7.8: Calculated entropy for solid  $\text{MoO}_x$ . (cont.)

## 7.2 The Ni-Mo-O system

In the Ni-Mo-O ternary system the formation of two ternary phases is suggested in the literature. These two oxides are  $\text{NiMoO}_4$  and  $\text{Ni}_2\text{Mo}_3\text{O}_8$ . Brenner [215] first suggested that oxidation of Ni-Mo alloys leads to formation of the oxide  $\text{NiMoO}_4$ . Later, Smith [216] in 1962 characterized the crystal structure of this phase. However, this characterization was later shown to be the high-temperature modification of  $\text{NiMoO}_4$  which is reported by Sleight and Chamberland [217] with the transformation temperature at  $690^\circ\text{C}$ .

Yanushkevich et al. [218] reported the transformation between the low and high temperature forms to be  $610\pm 10^\circ\text{C}$  for which they used DTA measurements and the transformation of  $\text{NiMoO}_4$  was fluctuating depending on the rate of heating or cooling of the specimen. Later, in 1987 Jacob et al. [219] used electromotive method (EMF) to measure the  $\Delta_f G^\circ$  of  $\text{NiMoO}_4$  in the temperature range from 900 to 1500 K. However, during the transformation of  $\alpha\text{-NiMoO}_4$  to  $\beta\text{-NiMoO}_4$  the expected change in the slope of the  $\Delta_f G^\circ$  could not be detected.

In a more recent work from Morshita and Navrotsky [220], the thermodynamic properties of polymorphs of  $\alpha\text{-NiMoO}_4$  and  $\beta\text{-NiMoO}_4$  were investigated thoroughly using calorimetry. In their work highly pure powders of commercial  $\alpha\text{-NiMoO}_4$ , NiO and  $\text{MoO}_3$  were dried and used.

Next, the standard entropy of formation ( $\Delta_f S^\circ$ ) was evaluated using the molar heat capacity ( $C_{p,m}$ ) which was measured in the temperature range from 2 to 1380 K using relaxation method and differential scanning calorimetry. They have also determined the standard enthalpy of formation ( $\Delta_f H^\circ$ ) for both  $\alpha\text{-NiMoO}_4$  and  $\beta\text{-NiMoO}_4$ , implementing the molar heat capacity and the standard enthalpy of formation at 298 K, which was experimentally obtained using drop solution calorimetry in molten sodium molybdate at  $700^\circ\text{C}$ .

The standard Gibbs energy of formation ( $\Delta_f G^\circ$ ) was determined using the standard enthalpies of formation and the standard entropies of formation, obtained from the experimental results.

In their work, the transition temperature of  $\alpha$ -NiMoO<sub>4</sub> to  $\beta$ -NiMoO<sub>4</sub> is reported as 1000 K (727 °C).

The calorimetric method is more sensitive to the slope change of  $\Delta_f G^\circ$  during the polymorphic phase transformation. As a result, these two polymorphs were added to the database as stoichiometric phases using the measured Gibbs energy of formation acquired by Morishita and Navrotsky [220] which are listed in the appendix A.

The earliest work suggesting the presence of Ni<sub>2</sub>Mo<sub>3</sub>O<sub>8</sub> in the temperature range from 1050 to 1150 °C is from McCarroll et al. [221]. In a more recent work, Ni<sub>2</sub>Mo<sub>3</sub>O<sub>8</sub> was investigated in the work from Steiner and Reichelt [222]. In their work the standard entropy of  $S_{298}^\circ(\text{Ni}_2\text{Mo}_3\text{O}_8) = 231 \text{ (J}\cdot\text{mol}^{-1}\cdot\text{K}^{-1})$  and heat capacity of  $C_{p, 298}(\text{Ni}_2\text{Mo}_3\text{O}_8) = 241 \text{ (J}\cdot\text{mol}^{-1}\cdot\text{K}^{-1})$  were calculated for Ni<sub>2</sub>Mo<sub>3</sub>O<sub>8</sub>. In addition, the decomposition temperature of this oxide was reported to be 1112 °C.

Based on these data, Ni<sub>2</sub>Mo<sub>3</sub>O<sub>8</sub> is added to the database using the stoichiometric description. The calculation results show that Ni<sub>2</sub>Mo<sub>3</sub>O<sub>8</sub> decomposes at 1109 °C and  $S_{298}^\circ$  and  $C_{p, 298}$  are 230.88 and 239.09 J·mol<sup>-1</sup>·K<sup>-1</sup>, respectively. These data are in a good agreement with the reported values. As can be seen in the calculated isothermal section (figure 7.10) at 500 and 1000 °C, the Ni<sub>2</sub>Mo<sub>3</sub>O<sub>8</sub> phase is stable while with increasing the temperature to 1150 °C it decomposes at 1109 °C.

Yanushkevich et al. [218] investigated the quasi-binary phase diagram of MoO<sub>3</sub>-NiO using DTA and visual polythermal methods [223] together with high-temperature X-ray diffraction (HTXRD), and measurements of the electrical resistivity of solid phases. In their work the purity of the starting material was carefully considered. In addition, mixtures of various compositions were made, which were heat treated with the maximum of 650 °C and the total of 10 hours.

According to the work of Yanushkevich et al. [218]  $\beta$ -NiMoO<sub>4</sub> melts incongruently at 1310±10 °C. At 770±5 °C, there should be a eutectic point in the quasi-binary phase diagram of NiO and MoO<sub>3</sub> at 7 mol% of NiO.

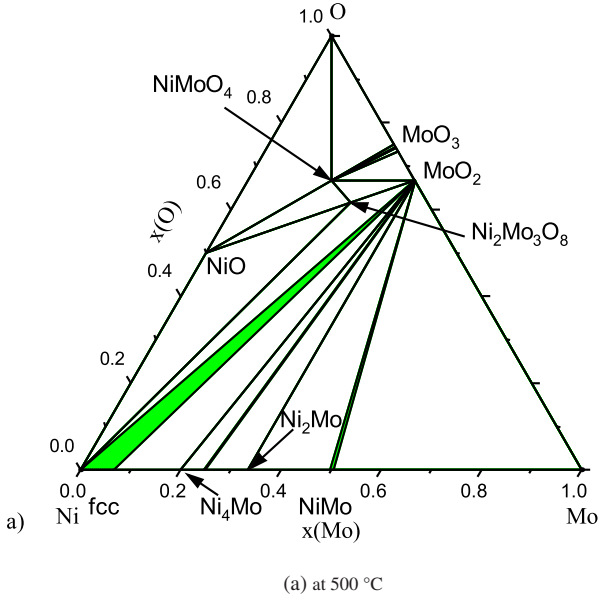


Figure 7.9: Calculated isothermal sections in the Ni-Mo-O system.

These data are taken into account while assessing the Ni-Mo-O system. Therefore, in the liquid phase two interaction parameters are introduced between  $\text{Mo}^{6+}$  and  $\text{Ni}^{2+}$  on the first sublattice and the  $\text{O}^{2-}$  on the second sublattice with which the final phase diagram agrees well with the reported values. The interaction parameters are listed in appendix A.

The calculated quasi-binary phase diagram can be seen in figure 7.11 where the eutectic point exists in 7.88 mol% of NiO and at 769.98 °C. The interaction parameters are listed in the appendix A.

The calculated temperatures for the reactions in the NiO-MoO<sub>3</sub> system are

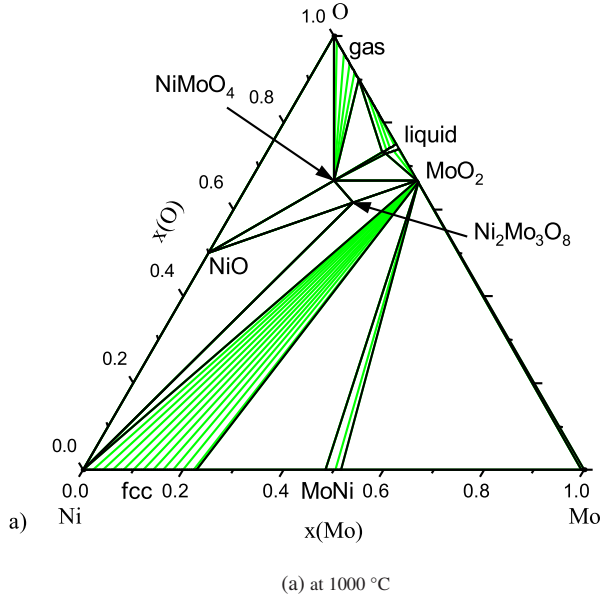


Figure 7.10: Calculated isothermal sections in the Ni-Mo-O system. (cont.)

listed in table 7.4 and are compared to the experimental data from the literature. The calculation shows good agreement with the literature data. In table 7.5 the calculated invariant reactions in this work for the ternary Ni-Mo-O system are listed.

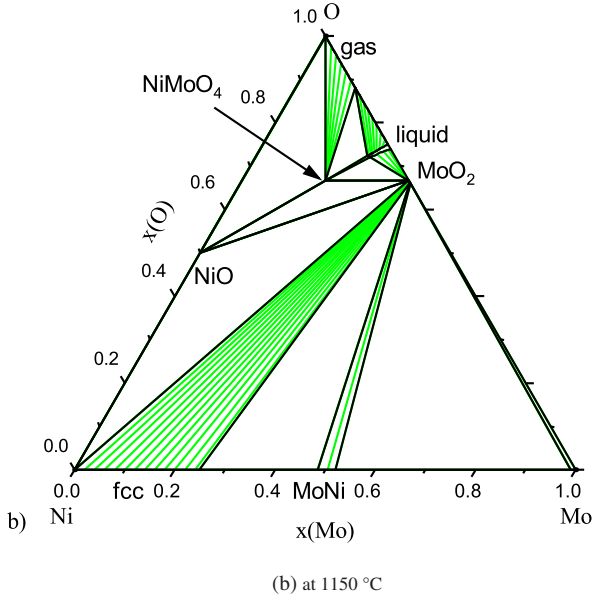


Figure 7.10: Calculated isothermal sections in the Ni-Mo-O system. (cont.)

Table 7.4: Calculated reaction temperatures in the NiO-MoO<sub>3</sub> quasi-binary system in the present work compared with the literature data [218, 222].

Invariant reactions	Reaction type	Ref. T [°C]	T [°C] (this work)
$L + \text{NiO} \longleftrightarrow \beta\text{NiMoO}_4$	Peritectic	1310 ± 10 [218]	1317
$\text{Ni}_2\text{Mo}_3\text{O}_4 \longleftrightarrow \text{MoO}_2 + \text{NiO}$	-	1112 [222]	1109
$L \longleftrightarrow \text{MoO}_3 + \beta\text{NiMoO}_4$	Eutectic	770 ± 5 [218]	769.98

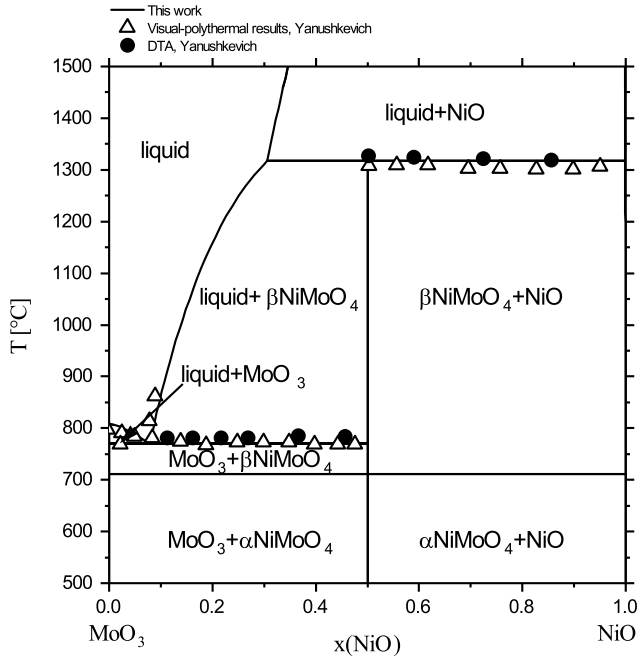


Figure 7.11: Calculated quasi-binary phase diagram for MoO<sub>3</sub>-NiO system compared with the experimental results of Yanushkevich et al. [218] (gas phase suspended).

Table 7.5: Calculated invariant reaction temperatures in the Ni-Mo-O system in the present work.

<b>Invariant reactions</b>	<b>Reaction type</b>	<b>T [°C]</b> (this work)
$L + \text{NiMo} \longleftrightarrow L12 + \text{MoO}_2$	U 1	1983.99
$L + \text{Halite} \longleftrightarrow \text{bcc} + \beta\text{NiMoO}_4$	U 2	1465.20
$L + L12 \longleftrightarrow \text{Halite} + \text{MoO}_2$	U 3	1427.81
$L + \text{Halite} \longleftrightarrow \beta\text{NiMoO}_4 + \text{MoO}_2$	U 4	1295.91
$L + \text{MoO}_2 \longleftrightarrow \beta\text{NiMoO}_4 + \text{Mo}_4\text{O}_{11}$	U 5	801.62
$L + \text{Mo}_4\text{O}_{11} \longleftrightarrow \beta\text{NiMoO}_4 + \text{Mo}_8\text{O}_{23}$	U 6	781.29
$L + \text{Mo}_8\text{O}_{23} \longleftrightarrow \beta\text{NiMoO}_4 + \text{Mo}_9\text{O}_{26}$	U 7	766.77
$L \longleftrightarrow \beta\text{NiMoO}_4 + \text{MoO}_3 + \text{Mo}_9\text{O}_{26}$	E 1	765.00

## 7.3 The Al-Mo-O system

In the literature there are not much experimental thermodynamic data available for the Al-Mo-O system. No mutual solubility was reported in the  $\text{Al}_2\text{O}_3$ -Mo system.

The quasi-binary system  $\text{Al}_2\text{O}_3$ - $\text{MoO}_3$  was experimentally investigated by Dąbrowska et al. [224] for the first time and the phase diagram for this quasi-binary system was constructed based on the results from the temperatures of thermal effects which were recorded on DTA curves taken from the mixture of  $\alpha$ - $\text{Al}_2\text{O}_3$ + $\text{Al}_2(\text{MoO}_4)_3$  and  $\text{MoO}_3$ + $\text{Al}_2(\text{MoO}_4)_3$ .

The solidus lines were determined based on the onset temperatures of the first endothermic effects in DTA and the liquidus curves were identified from the onset temperatures of the last effects recorded in the DTA.

In the work of Dąbrowska et al. [224] the heat treatments for the mixtures prior to the DTA measurements are explained in details. However, only the exact information on the ternary system of  $\text{Al}_2\text{O}_3$ - $\text{V}_2\text{O}_5$ - $\text{MoO}_3$  is given. The  $\text{Al}_2\text{O}_3$ - $\text{MoO}_3$  phase diagram was experimentally measured only as a part of a higher order system and details on the homogenization of the quasi-binary systems are missing. It should be noted that only with the assumption of the high temperature treatments similar to those explained in their work these experimental data could be accepted for which unfortunately no information is implied. Nevertheless, these experimental results are the only data available in the literature and could not be compared to any other values. Therefore, these data are taken into account for the assessment of this work. However, further investigation of this quasi-binary system is still necessary.

The results from Dąbrowska et al. [224] showed formation of aluminum molybdate ( $\text{Al}_2\text{Mo}_3\text{O}_{12}$ ) with the congruent melting at 940 °C. In addition, two eutectic mixtures, one at 820 °C and  $\sim 35$  at.%  $\text{Al}_2\text{O}_3$  and the second one at 740 °C and  $\sim 10$  at.%  $\text{Al}_2\text{O}_3$  are suggested.

Based on the experimental results adapted from their work the Al-Mo-O system is assessed in this work. The stoichiometric description for the  $\text{Al}_2\text{Mo}_3\text{O}_{12}$

phase is used. In addition, two interaction parameters in the liquid phase between the  $\text{Mo}^{6+}$  on the first sublattice and the  $\text{AlO}_{1.5}$  and  $\text{O}^{2-}$  on the second sublattice are defined. These parameters are listed in appendix A. The calculated quasi-binary phase diagram is plotted in figure 7.12 which is in good agreement with the reported experimental data. As an example an isothermal section of Al-O-Mo system at 1000 °C is plotted in figure 7.13 in which gas phase is suspended.

The crystal structure of aluminum molybdate  $\text{Al}_2\text{Mo}_3\text{O}_{12}$  was investigated

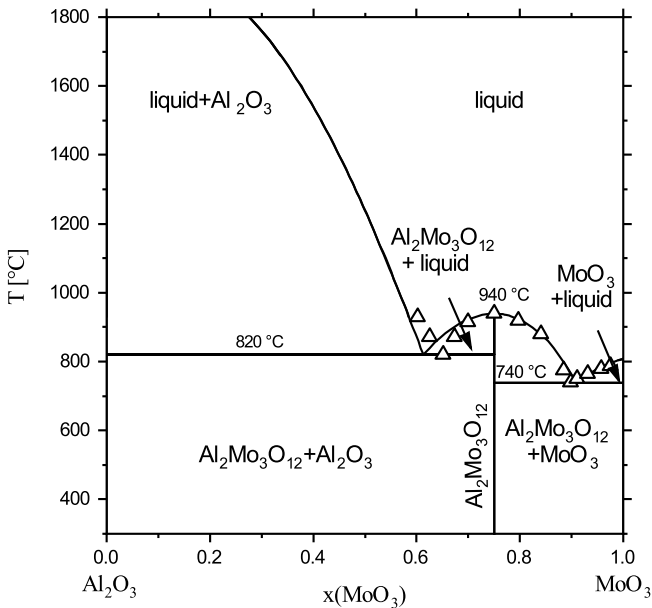


Figure 7.12: Calculated quasi-binary phase diagram for  $\text{Al}_2\text{O}_3$ - $\text{MoO}_3$  system compared with the experimental results from Dąbrowska et al. [224] (gas phase suspended).

by Harrison et al. [225] in 1988 in which transition from monoclinic to orthorhombic form at 200 °C was indicated. A similar transition temperature

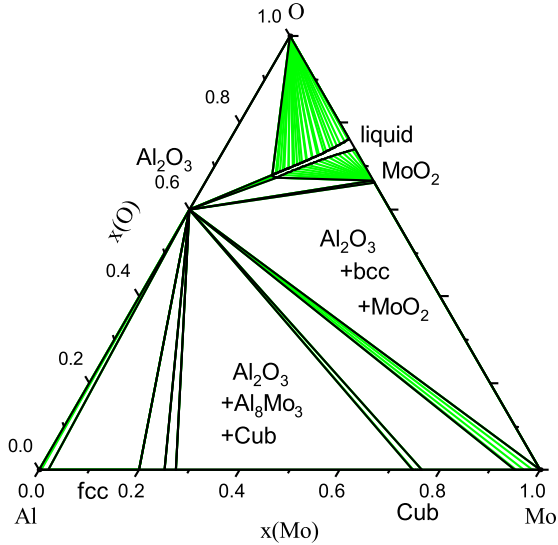


Figure 7.13: Calculated isothermal section for Al-Mo-O at 1000 °C.

was reported later in the work of Tyagi et al. [226]. Recently, in the work of Liu et al. [227] this transformation temperature is reported as 204.8 °C using DSC measurements. However, the transition was not included in this work since higher temperature regions are the main focus of this work.

List of the calculated reaction temperatures in the quasi-binary  $\text{Al}_2\text{O}_3$ - $\text{MoO}_3$  are shown in table 7.6 and is compared with the experimental data from Dąbrowska et al. [224]. The results show a good agreement compared to the experimental data.

In addition, the calculated invariant reactions in the Al-Mo-O ternary are listed in table 7.7.

Table 7.6: Calculated reaction temperatures in the quasi-binary  $\text{Al}_2\text{O}_3$ - $\text{MoO}_3$  system in the present work compared with the literature data from Dąbrowska et al. [224].

Invariant reactions	Reaction type	Ref. T [°C] [224]	T [°C] (this work)
$\text{L} \longleftrightarrow \text{Al}_2\text{Mo}_3\text{O}_{12}$	Congruent melting	940	938
$\text{L} \longleftrightarrow \text{Al}_2\text{Mo}_3\text{O}_{12} + \text{Al}_2\text{O}_3$	Eutectic	820	819.7
$\text{L} \longleftrightarrow \text{Al}_2\text{Mo}_3\text{O}_{12} + \text{MoO}_3$	Eutectic	740	738.8

Table 7.7: Calculated invariant reaction temperatures in the Al-Mo-O system in the present work.

Invariant reactions	Reaction type	T [°C] (this work)
$\text{L} + \text{bcc} \longleftrightarrow \text{CUB} + \text{L}_2$	U 1	2131.23
$\text{L} + \text{L}_2 \longleftrightarrow \text{Corundum} + \text{CUB}$	U 2	1812.34
$\text{L} + \text{CUB} \longleftrightarrow \text{Corundum} + \text{bcc}$	U 3	1717.90
$\text{L} + \text{bcc} \longleftrightarrow \text{Al}_6\text{Mo}_3\text{O}_7 + \text{Corundum}$	U 4	1568.55
$\text{L} \longleftrightarrow \text{Al}_6\text{Mo}_3\text{O}_7 + \text{Al}_8\text{Mo}_3 + \text{Corundum}$	E 1	1528.13
$\text{L} + \text{Al}_8\text{Mo}_3 \longleftrightarrow \text{Al}_3\text{Mo} + \text{Corundum}$	U 5	1221.95
$\text{L} + \text{Al}_3\text{Mo} \longleftrightarrow \text{Al}_4\text{Mo} + \text{Corundum}$	U 6	1151.96
$\text{L} + \text{Al}_4\text{Mo} \longleftrightarrow \text{Al}_{17}\text{Mo}_4 + \text{Corundum}$	U 7	997.32
$\text{L} + \text{Al}_{17}\text{Mo}_4 \longleftrightarrow \text{Al}_{22}\text{Mo}_5 + \text{Corundum}$	U 8	939.99
$\text{L} + \text{Al}_{22}\text{Mo}_5 \longleftrightarrow \text{Al}_5\text{Mo} + \text{Corundum}$	U 9	845.45
$\text{L} + \text{Al}_5\text{Mo} \longleftrightarrow \text{Al}_{12}\text{Mo} + \text{Corundum}$	U10	712.00
$\text{L} + \text{Al}_{12}\text{Mo} \longleftrightarrow \text{Corundum} + \text{L}_{12}$	U11	660.52

## 7.4 The Cr-Mo-O system

Limited information is available on the ternary Cr-Mo-O system. The section of  $\text{Mo-Cr}_2\text{O}_3$  was experimentally investigated in the work from Svoboda et al.

[228] for which they prepared samples from molybdenum metal and  $\text{Cr}_2\text{O}_3$  and also chromium metal and molybdenum oxides. Mixtures of the powders were cold pressed and subsequently sintered under argon atmosphere with annealing up to  $1800\text{ }^\circ\text{C}$  (details on the exact heat treatment can be found in Ref. [228]). A hole was designed in the sintered samples for observation of the incipient melting. The incipient melting of these oxides were investigated in a Pirani-type furnace. For the samples with low conductivity for the DC-heating, including the Cr mixed with molybdenum oxides and also the  $\text{Mo-Cr}_2\text{O}_3$  with high fraction of chromia, specimens were covered with molybdenum foil and heated in a tungsten holder. Mixtures of  $\text{Cr}_2\text{O}_3$  and  $\text{MoO}_2$  were also prepared in order to investigate formations of double oxides. These samples were investigated using XRD, EDX and metallographic analysis.

The Cr-Mo-O system was also recently examined by Tyurin [229] in which the phase diagram at  $25\text{ }^\circ\text{C}$  was constructed. However, their work is limited to low temperature investigation.

In this work the experimental results from Svoboda [228] are considered in which they suggest  $\text{Mo-Cr}_2\text{O}_3$  to be a quasi-binary system with eutectic composition at  $26\text{ mol}\%$  Mo and  $1960\text{ }^\circ\text{C}$ . In their work they have measured the existence of a monotectic reaction at  $2160\pm 20\text{ }^\circ\text{C}$ ,  $88\text{ mol}\%$  Mo.

The interaction parameters between the  $\text{Cr}^{3+}$  and  $\text{Mo}^{4+}$  on the first sublattice and the oxygen and vacancy on the second sublattice, in the liquid phase are introduced. The calculated section through  $\text{Cr}_2\text{O}_3$  and Mo (figure 7.14) shows the eutectic point at  $24.73\text{ mol}\%$  Mo and  $1959.05\text{ }^\circ\text{C}$  which is in good agreement with the reported values.

However, calculation in this work does not show a quasi-binary behavior of  $\text{Mo-Cr}_2\text{O}_3$  section and it shows higher temperature and Mo content for the monotectic reaction ( $2449.59\text{ }^\circ\text{C}$  and  $96.7\text{ mol}\%$  Mo, respectively). This reaction was only suggested in the work of Svoboda and still needs further investigation.

The calculated invariant reaction temperatures for the  $\text{Cr}_2\text{O}_3$ -Mo section are listed in table 7.8 which shows a good agreement with the experimental data

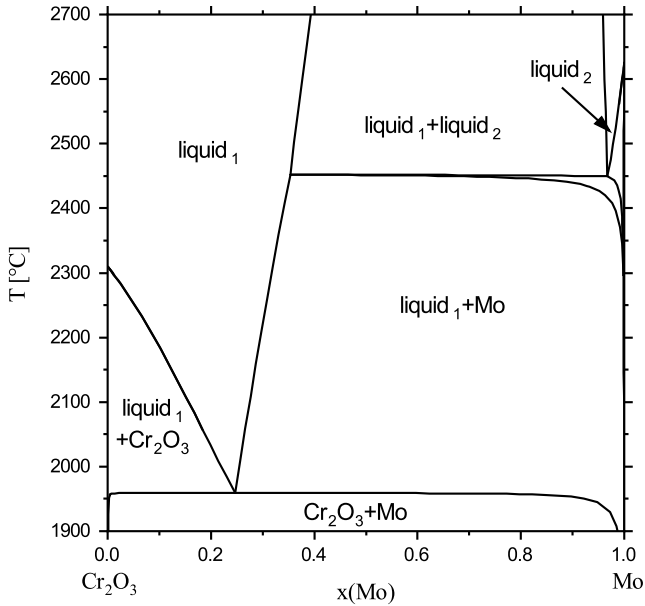


Figure 7.14: Calculated section of  $\text{Cr}_2\text{O}_3$ -Mo (gas phase suspended).

regarding the eutectic reaction. In addition, the calculated invariant reactions for the ternary Cr-Mo-O system are listed in table 7.9.

Table 7.8: Calculated reaction temperatures in  $\text{Cr}_2\text{O}_3$ -Mo section in the present work compared with the literature data from Svoboda [228].

Invariant reactions	Reaction type	Ref. T [°C] [228]	T [°C] (this work)
$L_1 \longleftrightarrow (\text{Mo}) + L_2$	Monotectic	$2160 \pm 20$	2449.59
$L \longleftrightarrow (\text{Mo}) + \text{Cr}_2\text{O}_3$	Eutectic	1960	1959.05

Table 7.9: Calculated invariant reaction temperatures in the Cr-Mo-O system in the present work.

Invariant reactions	Reaction type	T [°C] (this work)
L + Corundum $\longleftrightarrow$ bcc + Spinel	U 1	1685.52
L $\longleftrightarrow$ Corundum + bcc + MoO <sub>2</sub>	E 1	1345.63
L $\longrightarrow$ Corundum + Cr <sub>5</sub> O <sub>12</sub> + MoO <sub>3</sub>	E 2	804.87
L $\longleftrightarrow$ Corundum + MoO <sub>2</sub> + Mo <sub>4</sub> O <sub>11</sub>	E 3	798.86
L $\longleftrightarrow$ Corundum + Mo <sub>4</sub> O <sub>11</sub> + Mo <sub>8</sub> O <sub>23</sub>	E 4	791.72
L + Mo <sub>8</sub> O <sub>23</sub> $\longleftrightarrow$ Corundum + Mo <sub>9</sub> O <sub>26</sub>	U 2	789.61
L $\longleftrightarrow$ Corundum + MoO <sub>3</sub> + Mo <sub>9</sub> O <sub>26</sub>	E 5	788.80
L + Cr <sub>5</sub> O <sub>12</sub> $\longleftrightarrow$ Cr <sub>8</sub> O <sub>21</sub> + MoO <sub>3</sub>	U 3	778.31
L $\longleftrightarrow$ bcc + Cr <sub>8</sub> O <sub>21</sub> + MoO <sub>3</sub>	E 6	771.03

## 7.5 The Al-Ni-O system

Saltykov et al. have already investigated the Al-Ni-O ternary system in their work [36]. However, in the quasi-binary phase diagram of NiO and Al<sub>2</sub>O<sub>3</sub> the homogeneity range of the spinel phase was not included. In the experimental reports [230–236] a homogeneity range is described for the spinel phase. In the presented work, the constitutional model of the spinel phase is proposed as (Al<sup>3+</sup>, Ni<sup>2+</sup>) (Al<sup>3+</sup>, Ni<sup>2+</sup>, Va)<sub>2</sub> (Va)<sub>2</sub> (O<sup>2-</sup>)<sub>4</sub> with four sublattices. The first pair of parenthesis represents the tetrahedral sites and the second one which includes also vacancies corresponds to the octahedral sites, the third sublattice is the vacancies also in the octahedral sites and is only used in the higher order system including Cr to describe the deviation from stoichiometry as mentioned in section 3.6. Using the compound energy formalism, the surface of reference  $^{ref}G_m$  is calculated based on the compound energy of the end members

${}^\circ G_{i,j}$  weighted by site fractions (equation 3.2). Six different end members of  $G_{Al:Al}$ ,  $G_{Al:Ni}$ ,  $G_{Al:Va}$ ,  $G_{Ni:Al}$ ,  $G_{Ni:Ni}$  and  $G_{Ni:Va}$  are defined. Only a few of these end members represent stable compounds. Some of these values have already been defined by different authors describing the spinel phase in other systems which included Ni or Al. The values for  $G_{Ni:Ni}$  and  $G_{Ni:Va}$  have already been defined by Kjellqvist in the spinel phase of ternary of Ni-Cr-O [40]. In addition, the values for  $G_{Al:Al}$  and  $G_{Al:Va}$  were calculated by Hallstedt et al. [143] in the ternary of Al-Mg-O.  $G_{Al:Al}$  was assumed to be zero in their work. However, while combining different descriptions of a phase, a problem of consistency arises, which is caused by different choices of references for charge which are used in various works. One suggestion is using the same reference as in  $Fe_3O_4$  considering  $G(Fe^{2+}:Fe^{3+}:Va:O^{2-}) = G(Fe^{3+}:Fe^{2+}:Va:O^{2-})$  [237] and calculating  $G_{Al:Al}$  end member in the Fe-Al-O system. A diagrammatic view of part of this system is presented in figure 7.15. The values for normal spinels of  $FeAl_2O_4$  and  $Fe_3O_4$  are designated with  $7F$  and  $7G$ , respectively. As can be seen  $G_{Fe^{3+}:Fe^{2+}}$  and  $G_{Fe^{2+}:Fe^{3+}}$  have the equal value of  $7G$  as a reference. The lines connecting the normal spinels of  $Fe_3O_4$  and  $FeAl_2O_4$  to the inverse spinels are the neutral lines. Further discussions of the application of this method for modeling the spinel phase is discussed in work from Taylor and Dinsdale [136] and Barry et al. [238]. When considering simple spinels like  $FeAl_2O_4$  the enthalpy term of disordering can be calculated using the model of O'Neill and Navrotsky [41, 42] as described in equation 7.1:

$$\Delta H_D = Ax + Bx^2 \quad (7.1)$$

Where  $x$  is the site fraction of the trivalent ions on tetrahedral sublattice and  $A$  and  $B$  are calculated for various spinels in which the  $A$  for  $FeAl_2O_4$  is  $31300 J \cdot mol^{-1}$  [239]. As calculated in the work from Barry et al. [238] the  ${}^\circ G_{Al^{3+}:Al^{3+}}$  can be related to  $A$  using equation 7.2:

$$2A = {}^\circ G_{Fe^{2+}:Fe^{2+}} + 2{}^\circ G_{Al^{3+}:Al^{3+}} - 3{}^\circ G_{Fe^{2+}:Al^{3+}} \quad (7.2)$$

Therefore,  ${}^{\circ}G_{Al^{3+}:Al^{3+}}$  can be calculated when  ${}^{\circ}G_{Fe^{2+}:Fe^{2+}}$  and  ${}^{\circ}G_{Fe^{2+}:Al^{3+}}$  are available as shown in figure 7.15.

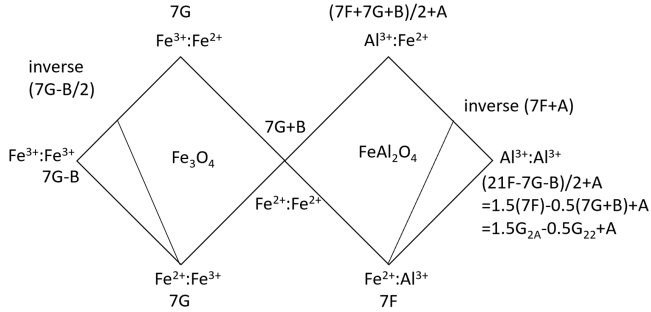


Figure 7.15: Spatial representation of compounds in  $Fe_3O_4$ - $FeAl_2O_4$  spinel system based on work from Taylor and Dinsdale [136].

$${}^{\circ}G_{Al^{3+}:Al^{3+}} = 1.5{}^{\circ}G_{Fe^{2+}:Al^{3+}} - 0.5{}^{\circ}G_{Fe^{2+}:Fe^{2+}} + 31300 \quad (7.3)$$

${}^{\circ}G_{Fe^{2+}:Fe^{2+}}$  is derived from work of Taylor and Dinsdale and is designated with  $(7G + B)$  [136] and  ${}^{\circ}G_{Fe^{2+}:Al^{3+}}$  is calculated as follows:

$${}^{\circ}G_{Fe^{2+}:Al^{3+}} = 7F \quad (7.4)$$

$7F$  is the Gibbs energy of the normal  $FeAl_2O_4$  spinel and is calculated using the coefficient of the normal spinel by Shishin et al. [240]. Using the phase diagram and the inversion parameter for  $NiAl_2O_4$  (the  $Al^{3+}$  distribution on tetrahedral sites) from experimental data provided by O'Neill et al. [43], two end members of  $G_{Al:Ni}$  and  $G_{Ni:Al}$  were assessed. The inversion parameter  $x$  calculated in this work is compared with the experimental data from O'Neill et al. and is shown in figure 7.16.

The results are in a good agreement with the experimental data. The calcu-

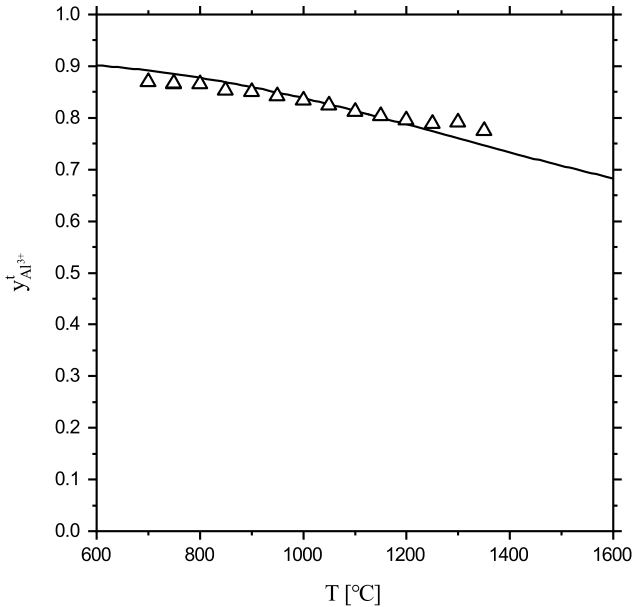


Figure 7.16: Calculated inversion parameter of spinel  $NiAl_2O_4$  compared with the experimental data from O'Neill et al. [43].

lation shows decreasing of  $Al^{3+}$  on the tetrahedral sites while increasing the temperature.

An interaction parameter was also defined between  $Al^{3+}$  in the first sublattice and  $Ni^{2+}$  and Va on the second sublattice to fit the homogeneity range of the spinel phase. There are experimental data available mainly between the range from 1000 to 1650 °C from various authors. Lida calculated the solubility range of  $Al_2O_3$  at 1650 °C as 60 mol%  $Al_2O_3$  using quenching and XRD [230], later Phillips et al. [232] experimentally evaluated this value to be 62 mol%  $Al_2O_3$  and made an approximation of the solubility range at various temperatures. Schmalzried used XRD investigation at temperature range from

1000 to 1500 °C [231, 233]. Elrefaie and Smeltzer [234] also investigated the homogeneity range of the spinel phase in a wide temperature range from 1000 to 1920 °C using XRD and EPMA investigation. More recently Rhamdhani et al. [235] also investigated the solubility of Al<sub>2</sub>O<sub>3</sub> in the spinel phase using equilibration and quenching techniques followed by EPMA in the temperature range from 1200 to 1400 °C. In the most recent work from Prostakova [236] the homogeneity range of spinel phase in NiO-Al<sub>2</sub>O<sub>3</sub> was investigated similar to Rhamdhani et al. [235] at higher temperatures 1500 and 1600 °C.

The majority of these studies are in agreement with each other the data from Schmalzried [231, 233] was used during this assessment. In addition, the melting point of the spinel phase from Phillips et al [232] is taken into account. The quasi-binary phase diagram is shown in figure 7.17 and is in reasonable agreement with literature data.

The reaction temperatures in the quasi-binary NiO-Al<sub>2</sub>O<sub>3</sub> system are listed in table 7.10 which show reasonable agreement compared with the experimental data from Phillips et al. [232] and Revcolevsch [241].

The isothermal section of Ni-Al-O is investigated at 1000 °C and 1390 °C by

Table 7.10: Calculated reaction temperatures in the quasi-binary NiO-Al<sub>2</sub>O<sub>3</sub> in the present work compared with literature data.

Invariant reactions	Reaction type	Ref. T [°C]	T [°C] (this work)
$L \longleftrightarrow \text{NiAl}_2\text{O}_4$	Congruent melting	2110 [232]	2109.9
$L \longleftrightarrow \text{NiAl}_2\text{O}_4 + \text{NiO}$	Eutectic	1900 [241]	1853
$L \longleftrightarrow \text{NiAl}_2\text{O}_4 + \text{Al}_2\text{O}_3$	Eutectic	-	2027

Elrefaie and Smeltzer [242] and Trumble and Rühle [243, 244], respectively. At 1000 °C the calculation shows a good agreement with the experimental data. However, at higher temperatures preliminary calculations revealed the presence of a liquid phase in the range where the two-phase equilibrium between solid Ni

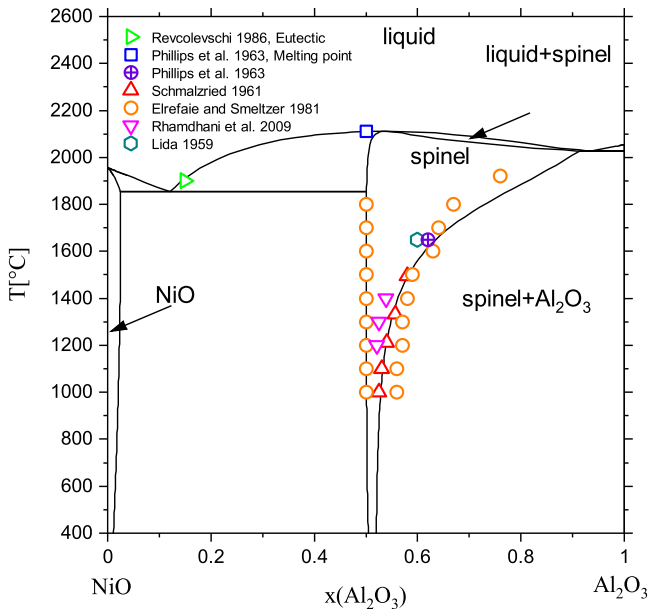


Figure 7.17: Calculated quasi-binary phase diagram of NiO-Al<sub>2</sub>O<sub>3</sub> system compared to the experimental literature data [230–232, 234, 235, 241].

and NiAl<sub>2</sub>O<sub>4</sub> should be, according to Refs [243, 244]. Therefore, a new ternary interaction parameter had to be introduced for the liquid,  ${}^0L_{Ni^{2+};Va,AlO_{1.5}}$ . Giving this parameter a large positive value removes the Ni-rich liquid from the isothermal section at 1390 °C. The result is shown in figure 7.18 which is in good agreement with the literature data from Trumble and Rühle [243, 244].

Furthermore, this parameter can be utilized to fit the deoxidation equilibria in aluminum containing nickel melts at high temperatures. Corresponding experimental data have been provided by Vachet et al. [245] who determined the oxygen concentration in Ni-Al melts in equilibrium with alumina at 1600 °C.

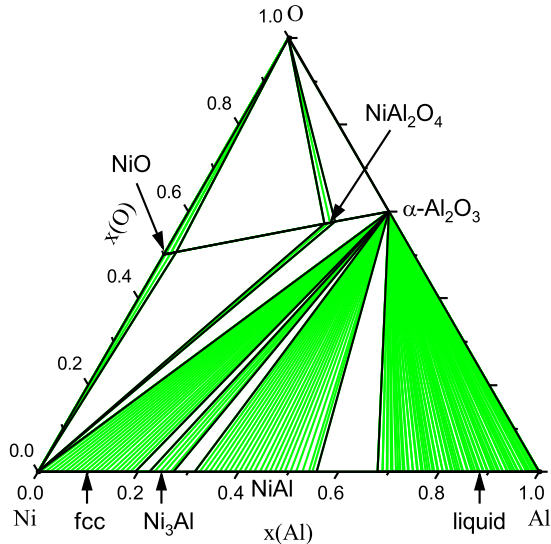


Figure 7.18: Isothermal section of Ni-Al-O at 1390 °C with the interaction parameter [see text].

In figure 7.19, the experimental data are compared with the calculated deoxidation equilibria using this optimized parameter. It can be seen that the data can be very good represented in Ni-rich melts but in Al-rich melts the calculated oxygen concentration is much too low. In order to improve this description, we tried to make the interaction parameter concentration dependent by using higher terms of the Redlich-Kister polynomial. But unfortunately, these higher terms caused impossibly high oxygen solubilities in the calculation of Al-rich melts. Therefore, we remain at this stage with a simplified description of the deoxidation equilibria using only one interaction parameter which is independent of the composition of the Ni-Al melt.

Using the Scheil module in Thermo-Calc software, the solidification simu-

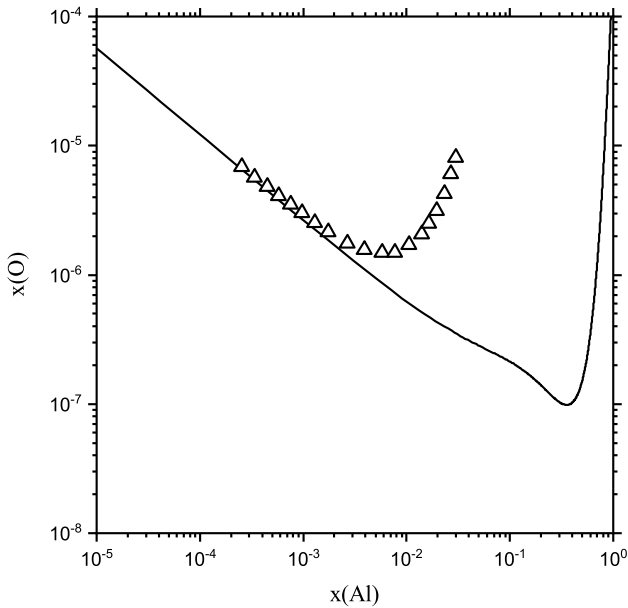


Figure 7.19: Equilibrium between O and Al content in liquid Ni at 1600 °C compared with experimental data from Vachet et al. [245].

lation is performed. Most often in Thermo-Calc equilibrium calculations are used in which a complete diffusion in the liquid and solid states are assumed. However, in reality the diffusion in the solid state is restricted. Therefore, in Scheil simulation instead of an equilibrium calculation, an alternative assumption is used in which the diffusion in liquid phase is infinitely fast and in the solid phases it is assumed zero.

In some cases Ni-containing spinel phases are used in batteries. One method to produce these spinel phases is from melting and quenching and heat treating the mixture.

In figure 7.20 examples of the Scheil solidification simulation which is a non-equilibrium solidification are shown for Ni-Al-O system. The solid lines indicate the temperatures at which various phases start to solidify from liquid. The compositions are chosen in NiO-Al<sub>2</sub>O<sub>3</sub> quasi-binary system one on Al<sub>2</sub>O<sub>3</sub>-rich region in which  $x(\text{Al}_2\text{O}_3)$  is 0.9 (figure 7.20-a) and one on the NiO-rich region in which  $x(\text{Al}_2\text{O}_3)$  is 0.3 (figure 7.20-b). The mole fraction of solid phases are calculated while cooling and the values are compared with the equilibrium condition. As can be seen in figure 7.20-a the first phase which starts to solidify is the spinel phase as also expected from figure 7.17. Approximately at 2038 °C Al<sub>2</sub>O<sub>3</sub> begins forming. The dotted line represents the equilibrium solidification.

As shown in this figure, the equilibrium line and the Scheil solidification line overlap at the beginning of solidification. Below 2160 °C these two lines diverge. Similar observation could be seen in figure 7.20-b on the NiO-rich side. As temperature decreases the equilibrium and non-equilibrium solidification calculation deviates from each other.

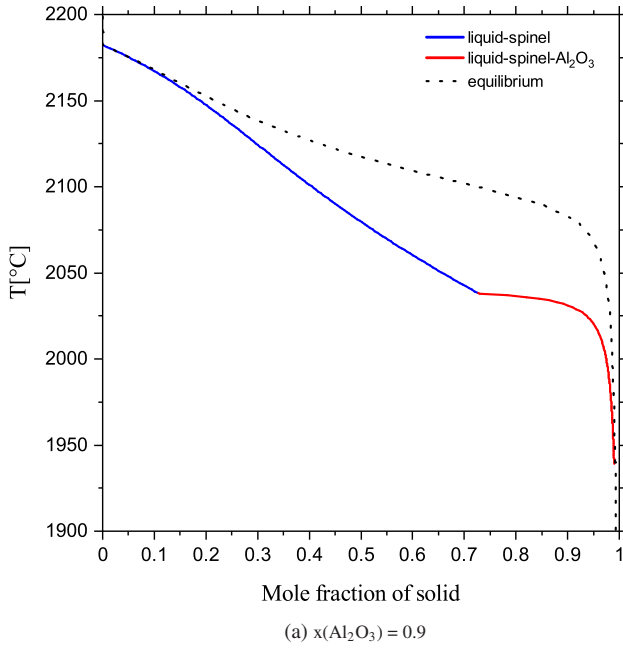


Figure 7.20: Scheil solidification simulation compared to equilibrium for NiO- $\text{Al}_2\text{O}_3$  section.

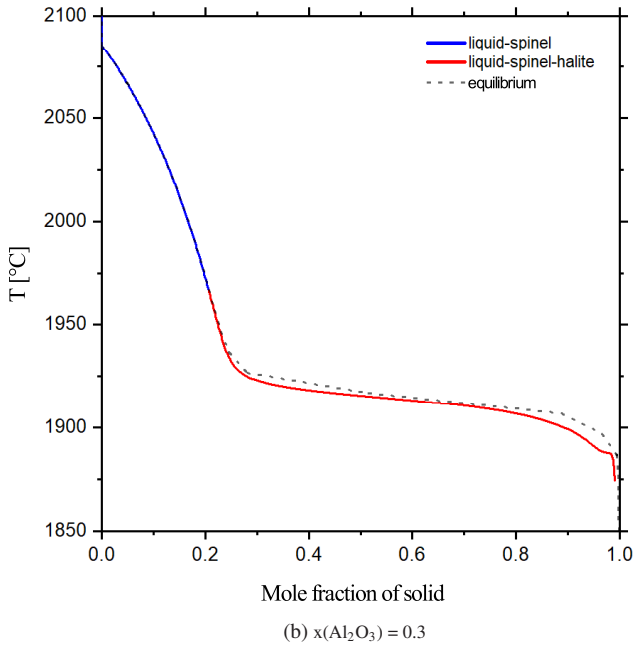


Figure 7.20: Scheil solidification simulation compared to equilibrium for NiO-Al<sub>2</sub>O<sub>3</sub> section.  
(cont.)



# Chapter 8

## Experimental results and discussion

This chapter is based on the publication "[G. Geramifard](#), C. Gombola, P. Franke, and H. J. Seifert. Oxidation behaviour of NiAl intermetallics with embedded Cr and Mo. *Corrosion Science*, 177:108956, 2020." [246] and has been restructured in accordance with the faculty regulations.

### 8.1 Oxidation of NiAl, NiAl-Cr coarse composite and DS NiAl-34Cr

As discussed in chapter 5, when pure metals are oxidized at high temperature, the growth of the oxide layer is governed by the parabolic law [55]. Details of the parabolic kinetics behavior is given in section 5.2.2. Meanwhile, in higher order systems the parabolic law is no longer strictly valid considering that the activities at the phase boundaries are no longer fixed. Nevertheless, the experimental oxidation investigation of the higher order systems, often exhibit an approximate parabolic behavior [55, 58, 67].

In this work, TGA was used to continuously record the mass gains of NiAl, NiAl-Cr coarse composite and DS NiAl-34Cr samples. Figure 8.1 illustrates the mass gain during oxidation at temperatures of 800 °C, 1200 °C and

1300 °C, as can be seen the oxidation rates increased with increasing temperature. At the temperature of 800 °C, the mass gain of NiAl and the coarse

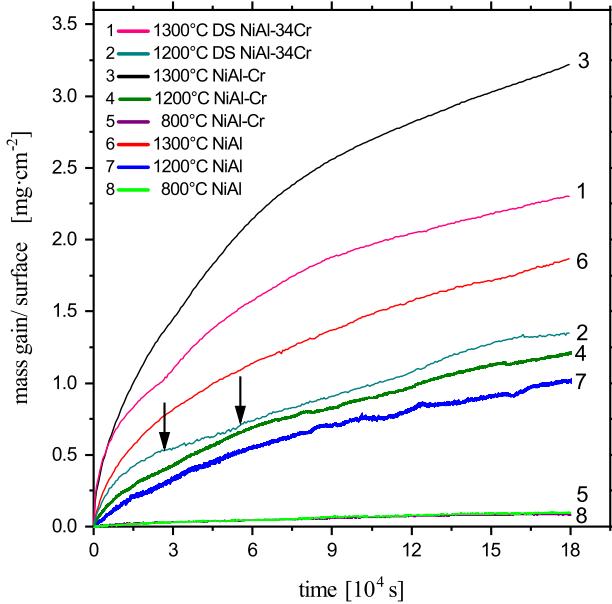


Figure 8.1: Mass gain during oxidation of NiAl-Cr, NiAl and DS NiAl-34Cr at 800 °C, 1200 °C and 1300 °C (arrows show spallation of the oxide layers).

composite of NiAl-Cr show parabolic behavior which indicates that the kinetics of oxide growth is diffusion controlled (curves 8 and 5, overlapping) [55, 58, 67].

As can be seen in 8.1, the curves 2, 4 and 7 show the mass gain at 1200 °C for the samples of DS NiAl-34Cr, NiAl-Cr coarse composite and the pure NiAl, respectively. The DS NiAl-34Cr (curve 2) sample has the highest oxidation rate compared to NiAl-Cr (curve 4) and NiAl (curve 7). The spallation of oxide scales on DS NiAl-34Cr has already started at this temperature as can be

seen in the fluctuation of the mass gain (shown with arrows at curve 2). The reason for this mass gain fluctuation is due to the fact that after formation of oxides for 400 minutes at 1200 °C, the oxides started to spall off and caused weight loss which was followed by further oxidation due to the unprotected surface. This phenomenon was less pronounced for NiAl-Cr (curve 4) and NiAl (curve 7).

All three samples showed higher oxidation rates at 1300 °C compared to 1200 °C and 800 °C. At this temperature NiAl-Cr (curve 3) has a much higher oxidation rate than DS NiAl-34Cr (curve 1) and NiAl (curve 6). The reason could be explained by the fast oxidation of Cr pieces together with spallation of the oxide scales, resulting in unprotected surfaces which were oxidized subsequently.

The SEM images of NiAl-Cr coarse composite after oxidation for 50 hours is shown in figure 8.2 where the quantification of the overall spallation for NiAl-Cr coarse composite at temperatures of 800 °C, 1200 °C, 1300 °C could be compared. The spallation mainly occurred at the interface of NiAl and Cr. More details on this subject will be given in section 8.2.

The square of mass gain for each of the samples was calculated based on the

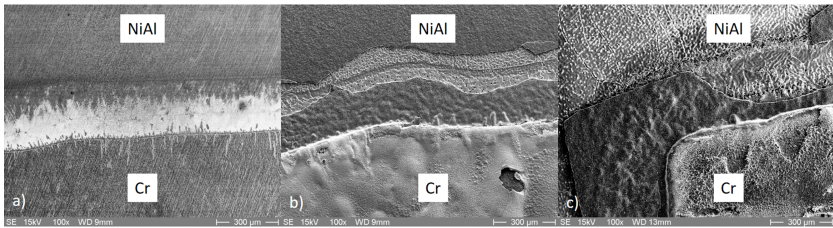


Figure 8.2: SEM images of the oxidized surface of NiAl-Cr coarse composite after reaction in Ar/ 13 vol.% O<sub>2</sub> for 50 hours. The labels denote the corresponding alloy beneath the oxide layer. a) at 800 °C. b) at 1200 °C. c) at 1300 °C.

data in figure 8.1 and plotted as a function of time in figure 8.3. In this plot the slope of each curve is the parabolic rate constant  $K_{p,w}$  (the index "w" refers to the weight measurements). In this figure the dotted lines represent the average

slope for the ideal parabolic behavior for each specimen at a specific temperature. These parabolic rate constants for different samples of NiAl, NiAl-Cr coarse composite and DS NiAl-34Cr are listed in table 8.1. Each measurement lasted 50 hours and the mass gain was recorded with the intervals of 10 minutes, leading to the total of 300 points on which the simple linear regression was performed and squared residuals are calculated for each line. In figure 8.4

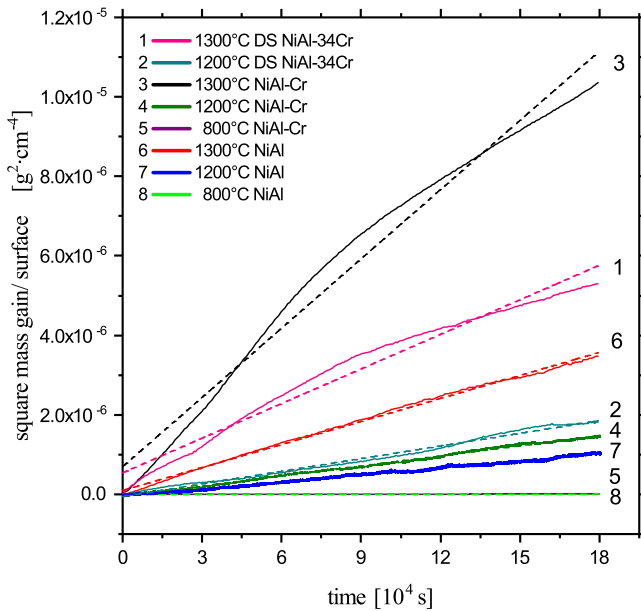


Figure 8.3: Square of mass gain during oxidation of NiAl-Cr, NiAl and DS NiAl-34Cr at 800 °C, 1200 °C and 1300 °C.

the parabolic rate constants ( $K_{p,w}$ ) of oxidation of NiAl, NiAl-Cr coarse composite and DS NiAl-34Cr at various temperatures are plotted in an Arrhenius diagram and are compared with the values reported by Brumm and Grabke in which the oxidation of pure NiAl in the temperature range of 700 °C to 1400 °C

Table 8.1: Parabolic oxidation rate constants for NiAl, NiAl-Cr and DS NiAl-34Cr.

Sample	Temperature	$K_{p,w}$ ( $g^2 \cdot cm^{-4} \cdot s^{-1}$ )	Standard error ( $g^2 \cdot cm^{-4} \cdot s^{-1}$ )	R-squared
DS NiAl-34Cr	1300 °C	$2.90 \times 10^{-11}$	$2.86 \times 10^{-13}$	0.971
DS NiAl-34Cr	1200 °C	$1.06 \times 10^{-11}$	$6.66 \times 10^{-14}$	0.988
NiAl-Cr	1300 °C	$5.81 \times 10^{-11}$	$5.10 \times 10^{-13}$	0.977
NiAl-Cr	1200 °C	$8.48 \times 10^{-12}$	$1.47 \times 10^{-15}$	0.997
NiAl-Cr	800 °C	$4.46 \times 10^{-14}$	$1.29 \times 10^{-17}$	0.985
NiAl	1300 °C	$1.93 \times 10^{-11}$	$6.30 \times 10^{-14}$	0.997
NiAl	1200 °C	$5.90 \times 10^{-12}$	$1.21 \times 10^{-15}$	0.996
NiAl	800 °C	$5.86 \times 10^{-14}$	$2.01 \times 10^{-17}$	0.979

is investigated [52] using argon gas containing 13 vol.% O<sub>2</sub>. The results show similar order of magnitude of the parabolic rate constants for NiAl and even NiAl-Cr samples compared to the reported values.

Brumm and Grabke reported the formation of three oxides  $\gamma$ -Al<sub>2</sub>O<sub>3</sub>,  $\theta$ -Al<sub>2</sub>O<sub>3</sub> and  $\alpha$ -Al<sub>2</sub>O<sub>3</sub> during oxidation of NiAl [52]. Among these oxides, the metastable oxides  $\gamma$ -Al<sub>2</sub>O<sub>3</sub> and  $\theta$ -Al<sub>2</sub>O<sub>3</sub> were formed at lower temperatures or at the early stages of oxidation and the stable  $\alpha$ -Al<sub>2</sub>O<sub>3</sub> oxide was formed at higher temperatures.

In this work, the formation of  $\alpha$ -Al<sub>2</sub>O<sub>3</sub> on NiAl-Cr coarse composite oxidized at 1300 °C was confirmed by XRD analyzing the spalled oxide which is shown in figure 8.5. However, the oxides formed at 1200 °C and 800 °C were too thin and showed a strong texture effect. Therefore, further identification of these oxides with XRD was not feasible. Regardless, EBSD, confirmed the formation of  $\alpha$ -Al<sub>2</sub>O<sub>3</sub> over the NiAl region in the NiAl-Cr coarse composite sample during oxidation at 1200 °C.

The quasi-binary phase diagram of Cr<sub>2</sub>O<sub>3</sub> and  $\alpha$ -Al<sub>2</sub>O<sub>3</sub> is plotted in figure 8.6 which shows that the two components are completely soluble in each other above 909 °C. As a result, it is anticipated that a continuous solid solution of

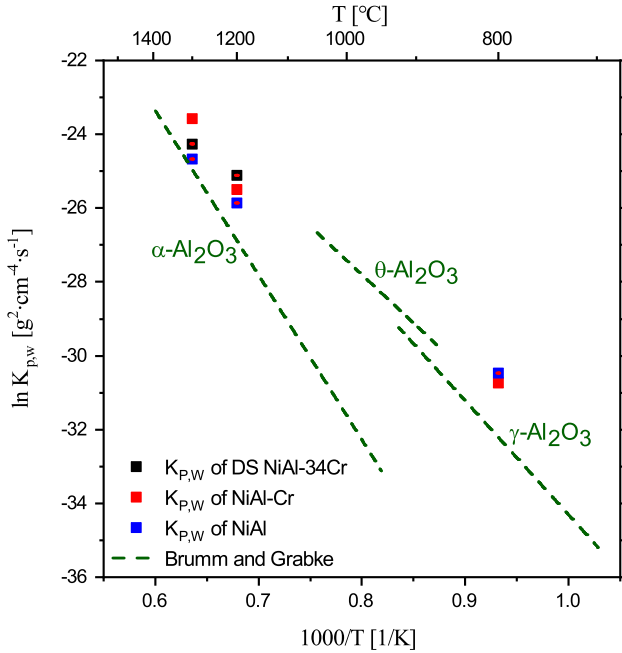


Figure 8.4: Parabolic rate constant of oxidation of NiAl and NiAl-Cr and DS NiAl-34Cr.

Al<sub>2</sub>O<sub>3</sub> and Cr<sub>2</sub>O<sub>3</sub> with corundum structure forms as the oxide scale on the NiAl-Cr coarse composite interface. Further investigations were performed using EDX and EBSD on the cross sections of these samples. The results are discussed in section 8.2.

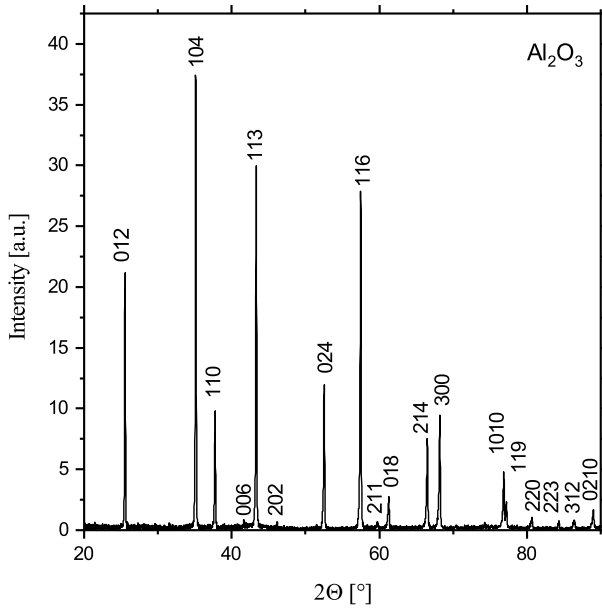


Figure 8.5: XRD pattern of the spalled oxide from the NiAl-Cr oxidized at 1300 °C in Ar/ 13 vol.% O<sub>2</sub> for 50 hours.

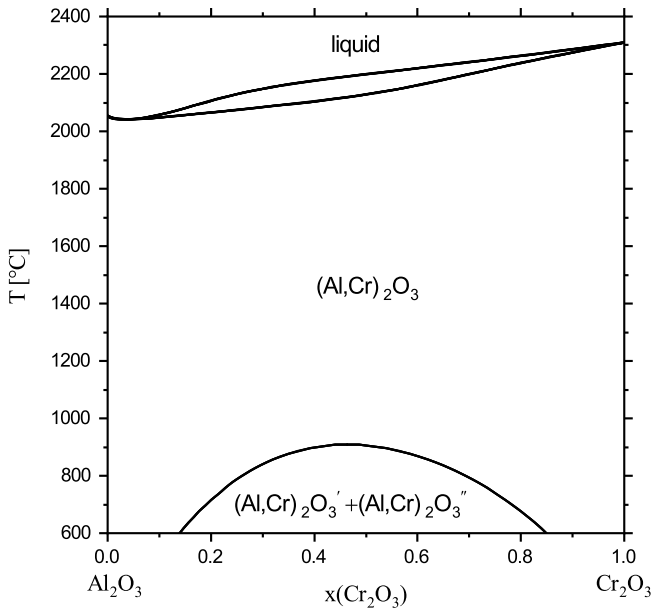


Figure 8.6: Quasi-binary phase diagram of Al<sub>2</sub>O<sub>3</sub> and Cr<sub>2</sub>O<sub>3</sub> [36].

## 8.2 Surface and cross section investigation

Figure 8.7-a shows the surface of the NiAl-Cr coarse composite sample which was oxidized in the thermobalance at 1200 °C under argon gas containing 13 vol.% O<sub>2</sub> for 50 hours. The oxide layer over the NiAl substrate appears to be rather smooth compared to the oxide layer over the Cr region.

Figure 8.7-b is the enlarged image of the figure 8.7-a, as can be seen, spalla-

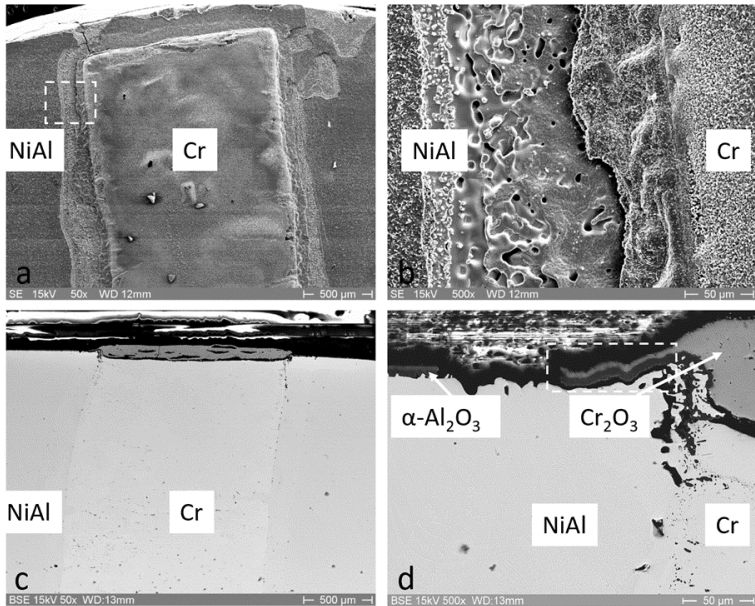


Figure 8.7: NiAl-Cr oxidized at 1200 °C and Ar/ 13 vol.% O<sub>2</sub> for 50 hours. a) Surface image. b) Enlarged image of a: Spallation at the interface of NiAl-Cr. c) Cross section image. d) Enlarged image of c: Interface of NiAl-Cr (for the discussion of the dashed box see section 8.2.2).

tion occurred at the interface between the NiAl and Cr, explained by the fact that the oxidation rate of Cr is much faster compared to the oxidation rate of NiAl. This would cause formation of voids and wrinkles at the interface due to volumetric changes. Formation of these wrinkles will lead to transformation

of biaxial stress in the oxide scale into a normal stress which is perpendicular to the oxide plane and causing spallation of the oxide [247]. Different oxidation rates can also be observed from disparity between the thicknesses of the oxides of  $\alpha$ -Al<sub>2</sub>O<sub>3</sub> and Cr<sub>2</sub>O<sub>3</sub> which are formed on the NiAl and Cr regions, respectively. This could be observed in figures 8.7-c and d.

In addition to TGA investigations, the oxide growth can be examined by determination of the thickness of the oxide layers using SEM images of metallographic cross-sections. These measurements provide parabolic rate constants  $K_{p,t}$  (the index "t" refers to thickness). Table 8.2 provides values of  $K_{p,t}$  for formation of Al<sub>2</sub>O<sub>3</sub> layers on pure NiAl samples, for the formation of Al<sub>2</sub>O<sub>3</sub> over the NiAl region of coarse NiAl-Cr composites as well as for oxides formed on DS NiAl-34Cr samples at temperatures of 800 °C, 1200 °C and 1300 °C. Each value represents an average of 10 measurements at different positions.

In order to compare the parabolic rate constants based on the thickness of

Table 8.2: Parabolic oxidation rate constant  $K_{p,t}$  for NiAl, NiAl-Cr and DS NiAl-34Cr and density of the oxide layers.

Sample	Temperature (°C)	$K_{p,t}$ ( $cm^2 \cdot s^{-1}$ )	$\rho_a$ of Al <sub>2</sub> O <sub>3</sub> ( $g \cdot cm^{-3}$ )
DS NiAl-34Cr	1300	$9.74 \times 10^{-12}$	1.531
DS NiAl-34Cr	1200	$2.33 \times 10^{-12}$	2.146
NiAl-Cr	1300	$1.65 \times 10^{-11}$	1.482
NiAl-Cr	1200	$3.93 \times 10^{-12}$	1.439
NiAl-Cr	800	$1.16 \times 10^{-14}$	1.790
NiAl	1300	$7.09 \times 10^{-12}$	1.649
NiAl	1200	$2.80 \times 10^{-12}$	1.408
NiAl	800	$3.24 \times 10^{-14}$	1.255

the oxides formed ( $K_{p,t}$  ( $cm^2 \cdot s^{-1}$ )) calculated in this work, with the results of Brumm and Grabke [52], which were calculated based on the weight gain of

the oxides  $K_{p,w}$  ( $g^2 \cdot cm^{-4} \cdot s^1$ ), the  $K_{p,t}$  calculated in this work was converted to  $K_{p,w}$  by multiplying it by  $\rho_a^2$  ( $g^2 \cdot cm^{-6}$ ). Where  $\rho_a$  is the apparent density of the oxide layers.

The apparent densities were estimated based on the experimental mass gain, the surface area and the average thickness of the  $Al_2O_3$  layer formed at each isothermal condition on different samples of NiAl, NiAl-Cr coarse composite and DS NiAl-34Cr. The calculated apparent densities are listed in table 8.2. Please note that these apparent density values are smaller compared to the density of a compact  $\alpha-Al_2O_3$  that is  $\rho=3.89 g \cdot cm^{-3}$  which is due to the high porosity of the oxide layers. Moreover, for the simplicity of the approximation, the Cr substrate area in DS NiAl-34Cr and NiAl-Cr coarse composites is not taken into account and the substrate surface is considered as complete NiAl. The Cr substrate included less than 4% of the surface in NiAl-Cr. This procedure can be further justified by the experimental findings during the oxidation of DS NiAl-34Cr in which practically pure  $Al_2O_3$  is formed, as it is discussed in section 8.2.4.

In figure 8.8 the converted  $K_{p,t}$  values are shown on the right axis and they are compared with the parabolic rate constants based on the mass gain ( $K_{p,w}$ ) reported by Brumm and Grabke on the left axis [52]. The results show plausible agreement with the same order of magnitude of the parabolic rate constants. Each oxide thickness was measured 10 times and the standard deviation was calculated based on the average measured values to calculate the error bars.

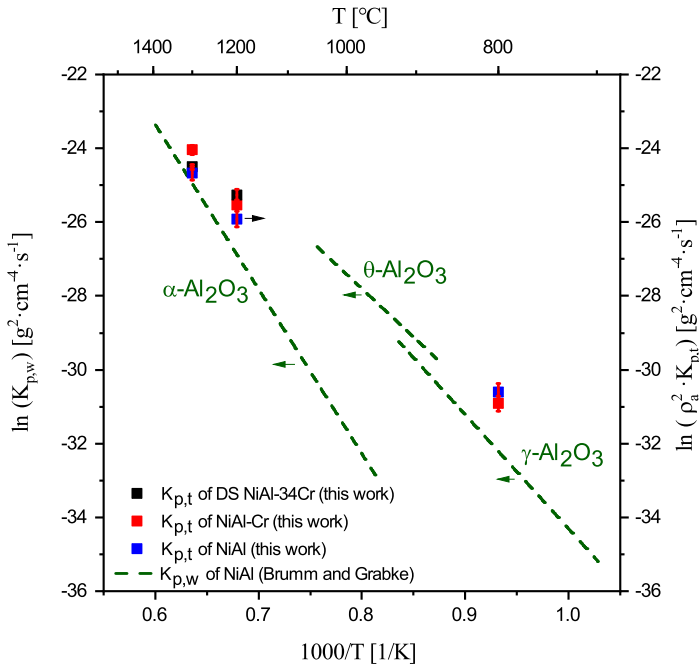


Figure 8.8: Arrhenius diagram of oxidation of NiAl-Cr, DS NiAl-34Cr and NiAl.

## 8.2.1 Oxidation of NiAl-Cr coarse composite at 800 °C

The element maps of O, Cr, Ni and Al are shown, respectively in figure 8.9. This is the EDX map at the vicinity of the interface region between NiAl and Cr in the NiAl-Cr coarse composite after oxidation in the thermobalance at 800 °C under Ar with 13 vol.% O<sub>2</sub> for 50 hours. This image shows NiAl on the left and Cr on the right in all four element maps. The oxide scales which formed above the NiAl region were too thin to be identified with XRD or EBSD. Nevertheless, the oxide scale above the Cr region was identified as Cr<sub>2</sub>O<sub>3</sub> by EBSD.

In figure 8.9, oxygen seems to be detected by EDX in the substrate (shown

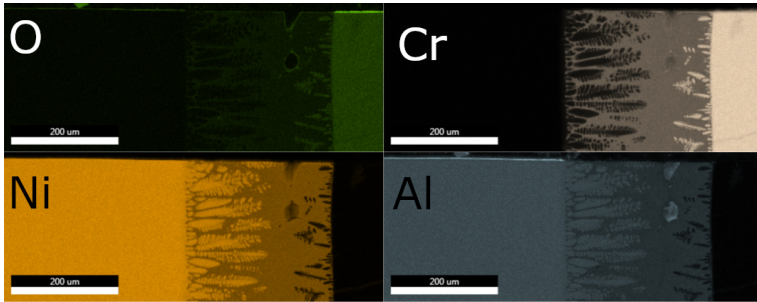


Figure 8.9: EDX map of the region around the joint between NiAl and Cr in NiAl-Cr oxidized at 800 °C in Ar/ 13 vol.% O<sub>2</sub> for 50 hours.

with green) where only pure Cr was expected. Since no internal oxidation was anticipated in this region the enrichment of the Cr region with oxygen due to diffusion is not presumed. The apparent detection of oxygen is probably caused by the overlapping of the chromium  $L_{\alpha}$  line with the oxygen  $K_{\alpha}$  line as they are very close to each other, with energies of 0.572 and 0.525 keV, respectively. Similar observations have been reported by Peng et al. [248].

Dendrites can be observed in the region between NiAl and Cr. These dendrites are formed during the casting process in the arc-melting device, as indicated in section 4.1.3. As molten NiAl is cast over solid chromium, some Cr dissolves in the melt since the temperature is above the melting point of NiAl but below the melting point of Cr, as can be seen from phase diagram in figure 8.10. Due to the short duration of this process, the Cr-enriched melt is restrained in a small region next to the solid Cr. While the temperature decreases below the liquidus line, Cr dendrites are formed and finally when the eutectic temperature is approached a eutectic microstructure is formed in the region of the NiAl-Cr joint, as shown in figure 8.11.

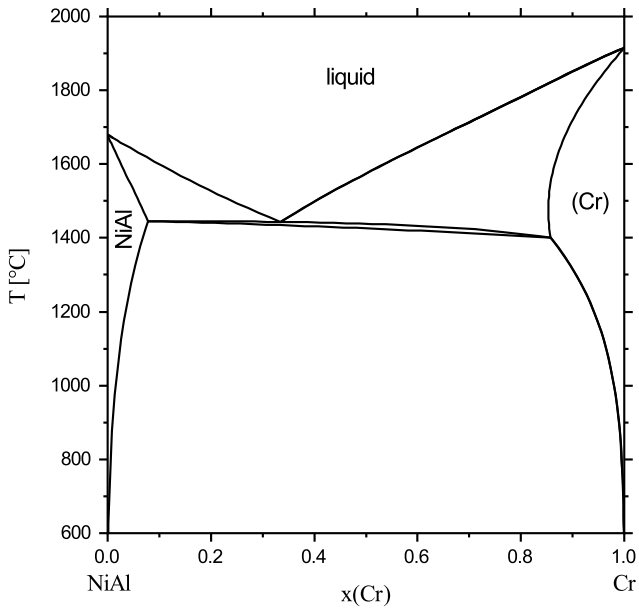


Figure 8.10: Calculated section of NiAl-Cr.

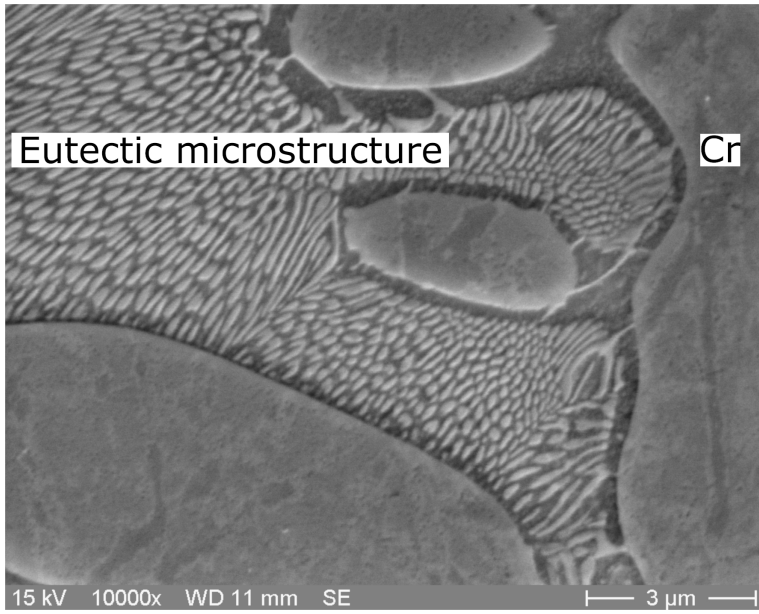


Figure 8.11: Microstructure of the solidified NiAl in the vicinity of Cr rod after annealing at 800 °C for 50 hours.

## 8.2.2 Oxidation of NiAl-Cr coarse composite at 1200 °C

The oxidations at 1200 °C and 1300 °C were performed in the subsolidus region of the NiAl-Cr samples. Nevertheless, the dendrite structures which were observed at 800 °C can coarsen during 50 hours oxidation at 1200 °C and 1300 °C. As a result, the NiAl and Cr interface at these two relatively high temperatures does not show similar dendrites compared to those formed at 800 °C. A dashed box in figure 8.7-d, shows formation of an oxide of  $(Al,Cr)_2O_3$  at the interface between Cr and NiAl. The enlarged image of the dashed box is shown in figure 8.12.

As can be observed in figure 8.12, the oxide in the SEM image brightens from

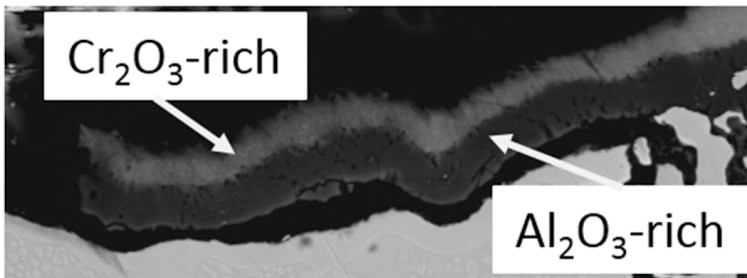


Figure 8.12: Enlarged image of the dashed box shown in figure 8.7-d

the metal surface to the gas surface. This is an indication of a reduction in the amount of Al which has lower atomic number compared to Cr and an increase in Cr content. Note that the  $Al_2O_3$ -rich layer is detached from the substrate and therefore a small gap forms between the oxide and the substrate in figure 8.12.

The identical interface area was further investigated with EDX and EBSD which showed that  $\alpha-Al_2O_3$  was formed on top of the NiAl region and  $Cr_2O_3$  was formed above the Cr region. These oxides were investigated with EDX

mapping and are shown in figure 8.13. At the surface of the sample where oxidation happened, oxygen can be seen and there is a high concentration of Al on the surface at the interface between NiAl and Cr.

The processed image using EDX and EBSD is shown in figure 8.14 which

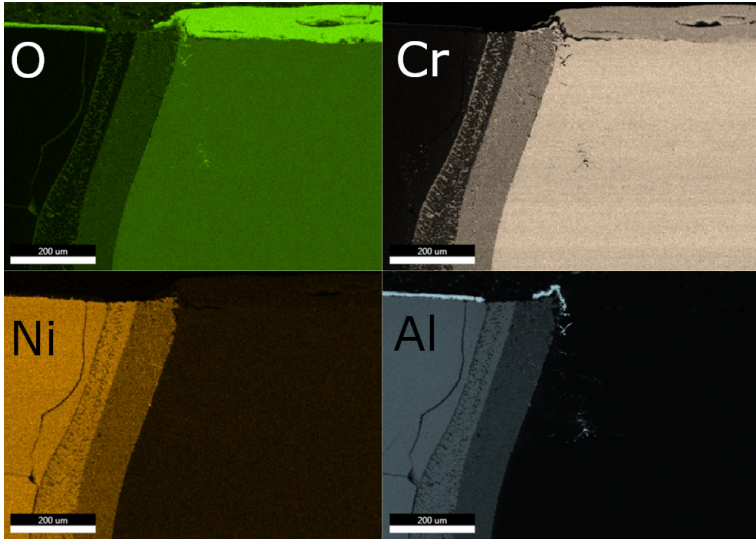


Figure 8.13: EDX map of interface of NiAl and Cr in NiAl-Cr oxidized at 1200 °C.

only confirmed the formation of  $\alpha$ -Al<sub>2</sub>O<sub>3</sub> at the interface of NiAl and Cr after oxidation at 1200 °C. This contradicts the initial assumptions based on the SEM image for formation of a mixed (Al,Cr)<sub>2</sub>O<sub>3</sub> oxide. Further investigations were performed at higher temperatures where the oxide layers are much thicker which allows better investigation of the formed oxides.

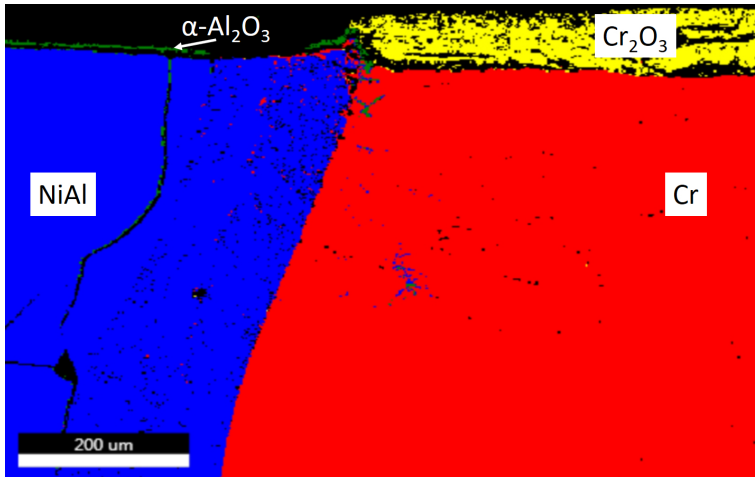


Figure 8.14: Phase image of NiAl-Cr oxidized at 1200 °C.

### 8.2.3 Oxidation of NiAl-Cr coarse composite at 1300 °C

Figure 8.15 shows the EDX analysis for a NiAl-Cr sample oxidized for 50 hours at 1300 °C under Ar with 13 vol.% O<sub>2</sub>. When the NiAl-Cr coarse composite is exposed to high oxygen partial pressures at 1300 °C, then an oxide scale forms on top of the metals which consists of Cr<sub>2</sub>O<sub>3</sub> and α-Al<sub>2</sub>O<sub>3</sub>.

As shown in the processed image from EDX and EBSD in figure 8.16, the results denote the formation of a mixed oxide in which the composition varies from the metal surface to the gas surface. Although, the outer layer of the oxide is mainly Cr<sub>2</sub>O<sub>3</sub>-rich, some Al also exists in the Cr<sub>2</sub>O<sub>3</sub>-rich oxide, which can be seen in the EDX maps of the element distribution in figure 8.15. The same also applies for the existence of Cr in the inner oxide layer which is mainly Al<sub>2</sub>O<sub>3</sub>-rich. Bear in mind that due to methodological reasons, in the combined EBSD and EDX results in figure 8.16, it is not possible to attain an image where the continuous change in Al and Cr content is shown. Rather, it is shown with

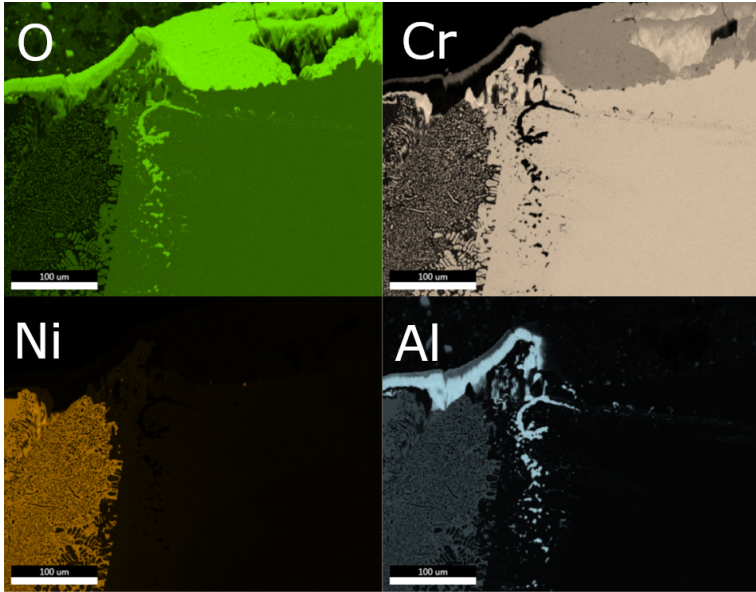


Figure 8.15: EDX map of interface of NiAl and Cr in NiAl-Cr oxidized at 1300 °C.

two different colors. However, it does not indicate to two distinct oxide layers but a continuous solid solution in which the Cr-rich and the Al-rich regions are shown with yellow and blue, respectively.

The reason for formation of the gradient in composition of the oxide can be explained as follows.

The parabolic rate constant of NiAl oxidation at temperatures above 1000 °C is about two orders of magnitude lower than that of Cr oxidation with parabolic oxidation constant in order of  $10^{-9}$  ( $g^2 \cdot cm^{-4} \cdot s^{-1}$ ) at 1300 °C [249–251]. Therefore, the parabolic rate constant for the mixed oxide forming over the region between NiAl and Cr is a continuous function of the composition.

The transport properties of the mixed oxide also change strongly with composition. In the work from Atarashiya et al. [252], the interdiffusion coefficient

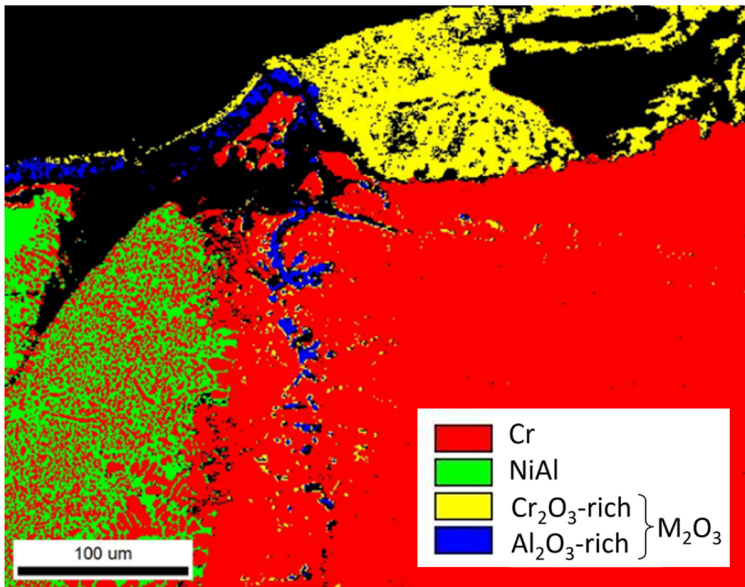


Figure 8.16: Phase image of NiAl-Cr oxidized at 1300 °C.

of Cr<sub>2</sub>O<sub>3</sub>-Al<sub>2</sub>O<sub>3</sub> as a function of composition is investigated in the temperature range from 1400 °C to 1520 °C. The investigation suggests that at high Cr-contents the interdiffusion of aluminum and chromium are by one order of magnitude higher than at high Al-contents. For instance, at 1480 °C this value changes from  $10^{-18.4}$  to  $10^{-17.4}$  ( $m^2 \cdot s^{-1}$ ) from Al-rich towards Cr-rich composition.

As a result, a relatively thick oxide layer is formed over chromium, which consists of almost pure Cr<sub>2</sub>O<sub>3</sub> and is shown in yellow color in figure 8.16. In addition, at an adequate distance from the interface between NiAl and Cr, over the NiAl matrix, only a thin oxide scale is formed which consist of almost pure Al<sub>2</sub>O<sub>3</sub> and is shown in blue color.

Due to the faster diffusion in the high Cr-content region, in the vicinity of the interface of Cr and NiAl, Cr diffuses over the Al<sub>2</sub>O<sub>3</sub> and leading to formation

of an oxide layer in which the composition changes from almost pure  $\text{Cr}_2\text{O}_3$  (yellow) in contact with the gas, to almost pure  $\text{Al}_2\text{O}_3$  (blue) in contact with the metal. The Cr content in this mixed oxide scale also diminishes in the direction from the interface towards the NiAl.

Figure 8.17 shows the Ellingham diagram of  $\text{Al}_2\text{O}_3$ ,  $\text{Cr}_2\text{O}_3$  and NiO. As it is shown, the Gibbs energy of formation of  $\text{Al}_2\text{O}_3$  is much lower than that of  $\text{Cr}_2\text{O}_3$  and NiO which means it is more stable than  $\text{Cr}_2\text{O}_3$  and it would be the first oxide to be formed at the interface. Subsequently, when there is deficiency of Al, then Cr will start oxidizing, as the activity of  $\text{Cr}_2\text{O}_3$  increases. Nevertheless, this diagram only presents the thermodynamic stability of various oxides at different temperature ranges. However, no information regarding the activity of each species could be achieved.

In figure 8.18, a schematic view of the oxide formation near the interface between Cr and NiAl is presented. The concentration of Cr decreases while getting closer to the NiAl region and also it increases in direction of the surface of the oxide. The directions of increasing Cr content in the  $(\text{Al,Cr})_2\text{O}_3$  solid solution are shown by red arrows in this figure.

This suggests that the composition of  $(\text{Al,Cr})_2\text{O}_3$  changes simultaneously in two different directions which makes it challenging to calculate the composition of the oxide at a particular distance from the metallic surface. Without having the exact composition at the interface further calculation of activities and the driving forces for formation of oxides are not possible.

During the process of oxidation, the sample is under a strong oxygen potential gradient. On the surface, the sample is in contact with the gas atmosphere with an oxygen activity of  $a_{\text{O}_2} = 0.13$ , while inside the metallic composite, the oxygen activity is many orders of magnitude lower. These changing local equilibria are discussed below by means of several thermodynamic diagrams which have been calculated with the thermodynamic database from this work. In figure 8.19-a, the potential-composition diagram for the Al-Cr-O system at 1300 °C is plotted. It can be noticed that at any oxygen partial pressure above  $\log(p_{\text{O}_2}) = -16$ , the  $(\text{Al,Cr})_2\text{O}_3$  mixed oxide with the corundum structure is

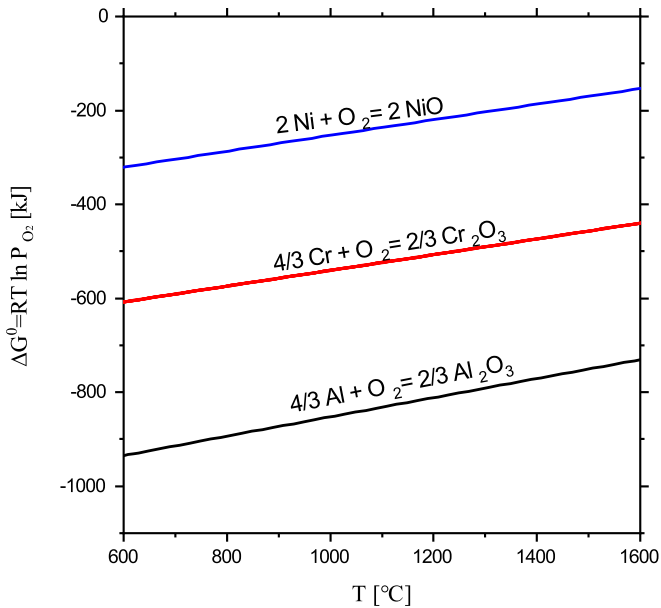


Figure 8.17: Ellingham diagram of  $\text{Al}_2\text{O}_3$  and  $\text{Cr}_2\text{O}_3$  and NiO using data from Saltykov et al. [36].

stable for all compositions.

In equilibrium with Cr-Al alloys the oxide has high chromium concentrations only within a small range where  $\log(p_{\text{O}_2})$  is between  $-16$  and  $-17$ . At even lower oxygen partial pressures the oxide consists of almost pure  $\text{Al}_2\text{O}_3$ . Figure 8.19-b shows the stable phases in the system Ni-Al-O at  $1300^\circ\text{C}$  under various oxygen partial pressures. As can be seen, at high oxygen partial pressures the spinel phase ( $\text{NiAl}_2\text{O}_4$ ), NiO and  $\text{Al}_2\text{O}_3$  are the stable oxides. However, in the oxidation experiments only  $\text{Al}_2\text{O}_3$  was formed as confirmed by EBSD and XRD.

This could be explained by means of figure 8.19-b. As can be seen, the only



Figure 8.18: Schematic view of NiAl-Cr with oxide scales. Arrows show direction of increasing Cr concentration.

oxide which is in equilibrium with NiAl is pure  $\text{Al}_2\text{O}_3$  that is in the range of  $\log(p_{\text{O}_2}) = -25$  to  $\log(p_{\text{O}_2}) = -22$ . Therefore,  $\text{Al}_2\text{O}_3$  forms first and given that nickel is substantially insoluble in  $\text{Al}_2\text{O}_3$ , it cannot diffuse through the oxide layer in order to form spinel or even NiO on the surface of the sample. Similar observations have been reported by Wu et al. [253].

While figure 8.19-a gives information on the oxidation behavior of the Cr-based alloy, and figure 8.19-b provides respective insight into the matrix (NiAl) of our composite material, we now move forward to sections through the quaternary system where the oxidation of the composite can be discussed.

A section through the system Ni-Al-Cr-O at 1300 °C and  $\log(p_{\text{O}_2}) = -24$  is shown in figure 8.20-a. This oxygen partial pressure was selected based on what was shown in figure 8.19-b in order to investigate the region in which  $\text{Al}_2\text{O}_3$  and NiAl are in equilibrium. Depending on the mixing ratio of the metallic components, several phase equilibria are possible under these conditions. The green tie-lines between the NiAl phase and the Cr-rich alloy phase depict the equilibria that exist in the interior of the composite sample at the junction of the corresponding alloys at adequate distance from the surface (and

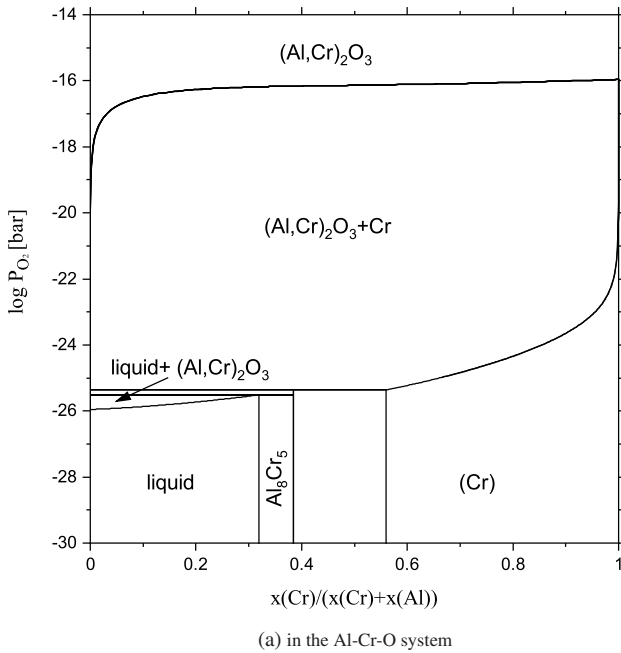


Figure 8.19: Calculated stability diagrams as a function of oxygen partial pressure at 1300 °C.

the oxide layer on it). The tie-triangle between (Cr), NiAl and  $\text{Al}_2\text{O}_3$  corresponds to the equilibrium at the junction between (Cr) and NiAl directly below the oxide layer at the surface of the sample. The narrow two-phase regions  $\text{Al}_2\text{O}_3$ -(Cr) and  $\text{Al}_2\text{O}_3$ -NiAl represent the equilibria between the oxide layer and the corresponding alloys at a certain distance from the NiAl-Cr junction. The section through the quaternary system is given for the same temperature but at a higher oxygen partial pressure,  $\log(p_{\text{O}_2}) = -21$  in figure 8.20-b. It can be noticed that at these conditions the matrix NiAl phase is no longer stable and rather only a Ni-rich and a Cr-rich alloy phase exist. Compared to figure 8.20-a these alloys have less solubility for aluminum. The oxide forming on

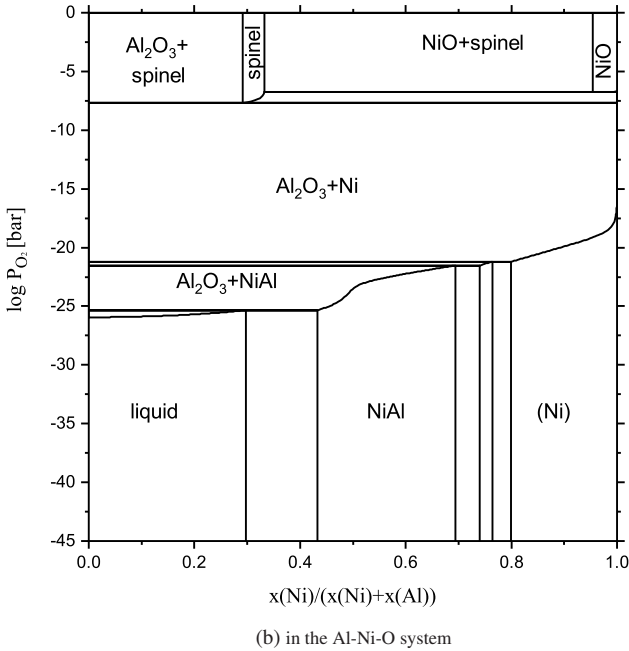


Figure 8.19: Calculated stability diagrams as a function of oxygen partial pressure at 1300 °C.  
(cont.)

these alloys is in both cases almost pure  $\text{Al}_2\text{O}_3$ . While increasing the oxygen partial pressure further towards  $\log(p_{\text{O}_2}) = -16$ , the diagram remains similar to figure 8.20-b except for the mixed oxide  $(\text{Al,Cr})_2\text{O}_3$  which extends from the  $\text{Al}_2\text{O}_3$ -corner along the right axis of the diagram almost down to the Cr-corner (figure 8.20-c).

Finally, another effect which occurs during the oxidation of the NiAl-Cr composite should be explained. A more detailed evaluation of figures 8.15 and 8.16 reveals that oxide particles have formed within the Cr-rich alloy at a short distance from the interface area between the two alloys. The formation of these

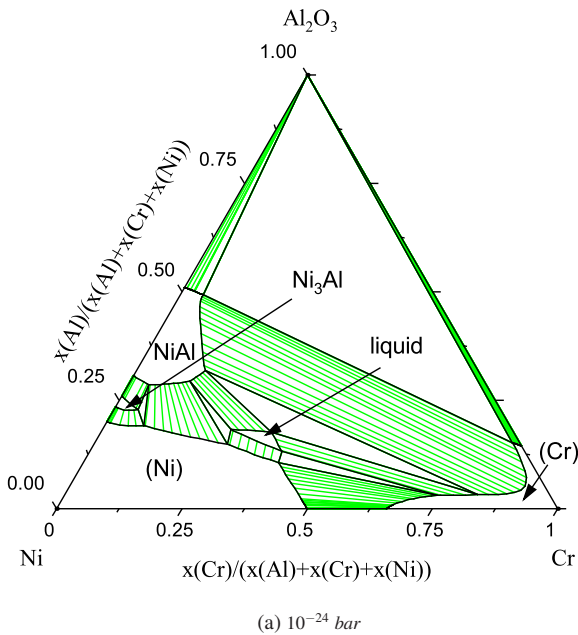


Figure 8.20: Section through the system Ni-Al-Cr-O at 1300 °C.

oxide particles can be assumed to be caused by internal oxidation. In the previous discussion of figure 8.19 and 8.20 it was demonstrated that in the equilibrium between almost pure chromium and its oxide there is a much higher oxygen activity than in the equilibrium between NiAl and  $\text{Al}_2\text{O}_3$ . Therefore, the contact zone between NiAl and Cr is located within an oxygen potential gradient, which causes a (small) oxygen flow from the Cr side to NiAl. Besides, small amounts of NiAl can dissolve in chromium, creating an aluminum stream that diffuses in opposite direction of the oxygen stream. In the region where the concentrations of Al and O exceed the solubility product of  $\text{Al}_2\text{O}_3$  in chromium, the oxide particles are precipitated.

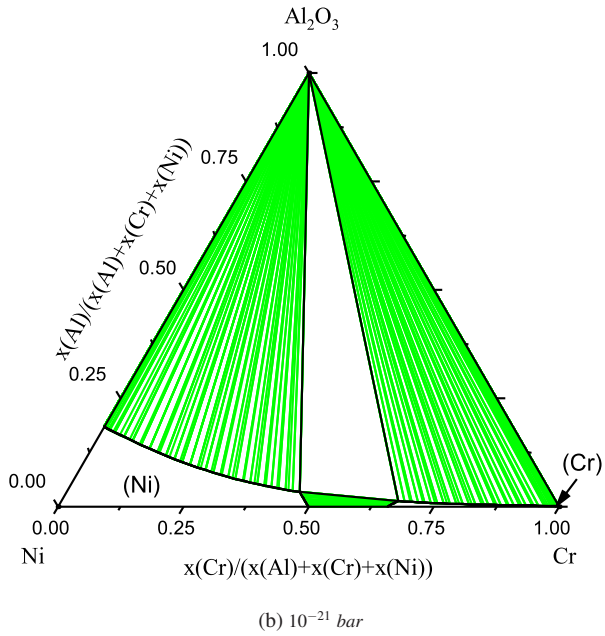


Figure 8.20: Section through the system Ni-Al-Cr-O at 1300 °C. (cont.)

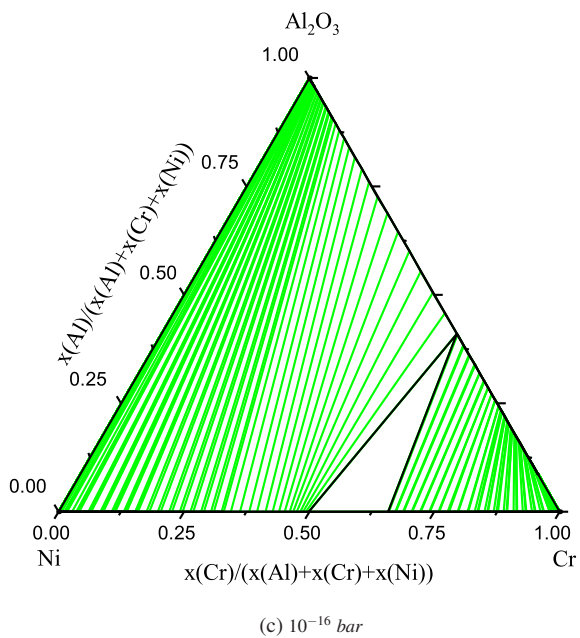


Figure 8.20: Section through the system Ni-Al-Cr-O at 1300 °C. (cont.)

## 8.2.4 Oxidation of DS NiAl-34Cr at 1200 °C and 1300 °C

Figures 8.21-a and b show the cross-section SEM images of DS NiAl-34Cr samples after 50 hours of oxidation in Ar/ 13 vol.% O<sub>2</sub> at 1200 °C and 1300 °C, respectively. An oxide layer of almost pure Al<sub>2</sub>O<sub>3</sub> was formed on the samples in both cases, as found by EPMA. It is evident that the oxide layer is largely detached from the underlying alloys.

During the heat-treatment, the formerly fibrous composite has transformed

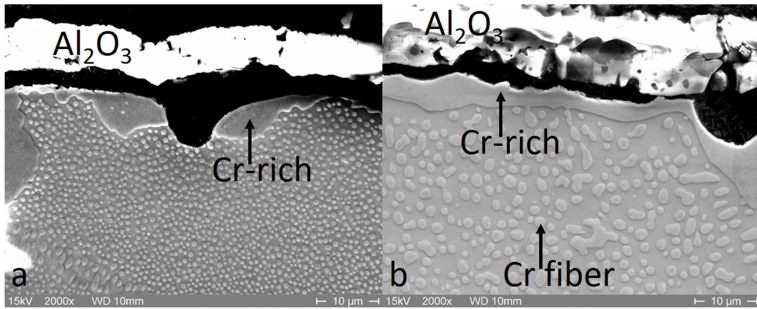


Figure 8.21: Cross section of DS NiAl-Cr oxidized under Ar/13 vol.% O<sub>2</sub> for 50 hours. a) at 1200 °C. b) at 1300 °C.

into a nodular microstructure. This effect is evidenced due to the fact that a section in any direction through the sample reveals the same microstructure within the region of the NiAl+Cr composite as shown in figure 8.21. Moreover, a layer of Cr-rich alloy has formed between the NiAl+Cr composite and the oxide scale.

The EPMA analysis revealed the Cr content of 96.8 at.% and 94.6 at.% at 1200 °C and 1300 °C, respectively. Formation of this Cr-rich region has led to the spallation of the oxide scale resulting from different thermal expansion coefficients (for chromia  $\alpha = 2.75 \times 10^{-5} K^{-1}$  [254] and for alumina  $\alpha = 5 \times 10^{-6}$  to  $9 \times 10^{-6} K^{-1}$  [255]) or deteriorating the adhesion to the Al<sub>2</sub>O<sub>3</sub>

oxide scale.

The composition of the Cr-rich region formed at 1300 °C is shown in table 8.3. Similar observations of formation of the Cr-rich region below the oxide scale were made in the literature. In those reports rejection of Cr from the growing oxide scale and the low solubility of Cr in the NiAl matrix was assumed to be the cause for formation of the Cr-rich region [248, 256, 257].

However, as can be seen in figure 8.20-a the influence of the Ni concentration on the solubility of Cr in NiAl seems to be too small to be accounted for this effect. A better explanation can be given if the alloys came in contact with higher oxygen activities than those of the NiAl/Al<sub>2</sub>O<sub>3</sub> equilibrium. As can be seen in figures 8.21-a and b, the oxide layers are not dense and they are detached from the alloys. This permits contact with the gas which leads to increased oxygen activities in a zone next to the alloy surface. If the oxygen partial pressure approaches a level close to that of figure 8.20-b then the NiAl phase is no longer stable in that zone and a rim of Cr-rich alloy is formed instead. Inside the bulk away from the surface, the oxygen activities are still low enough to keep NiAl stable.

Due to the fact that almost pure Al<sub>2</sub>O<sub>3</sub> is formed during the oxidation, the metallic phases must become enriched with nickel. According to figures 8.20-a and b, some Ni can dissolve in the NiAl matrix but a higher amount can be expected to be seen in the Cr-rich alloy where the solubility is about 35 at.% Ni at 1300 °C. Table 8.3 shows the electron-probe microanalysis results for the composition of the alloy phases shown in figure 8.21-b. Surprisingly, the expected increased Ni concentrations in the Cr-rich alloys were not found. Nevertheless, since the fibers scale are in the range of nano-meters, the EPMA results for the composition of the fibers and the matrix are not precise. The relatively high Cr content (7 at.%) in the matrix indicates the overlapping of results from matrix and the fibers.

Table 8.3: Microprobe analysis of Cr-rich region, fibers and matrix in oxidized DS NiAl-34Cr at 1300 °C after 50 hours.

Element	Element distribution in the Cr-rich region (at.%)	Element distribution in the fibers (at.%)	Element distribution in the matrix (at.%)
Al	2.5	3.3	41.9
Cr	94.6	92.2	7.0
Ni	2.9	4.5	51.1

### 8.3 Oxidation of NiAl-Mo

Brady et al. [15] have studied the oxidation of directionally solidified NiAl-Mo in which the effect of the Mo dispersion size was investigated at 900 °C in both dry and wet conditions. The samples showed better oxidation resistance via Al<sub>2</sub>O<sub>3</sub> formation in dry air.

In the present work, in order to identify the oxides formed at the interface between NiAl and Mo, a NiAl-Mo coarse composite was oxidized for 50 hours at 800 °C under Ar atmosphere with 13 vol.% O<sub>2</sub>. A huge mass loss occurs during the oxidation of NiAl-Mo, as can be seen in figure 8.22. The reason for the mass loss is the formation of volatile Mo oxide species. The Mo wire was oxidized and formed a yellow powder as shown in figure 8.23 which was analyzed by XRD and showed formation of Al<sub>2</sub>Mo<sub>3</sub>O<sub>12</sub> and NiMoO<sub>4</sub> (figure 8.24). These phases form by reaction of MoO<sub>3</sub> with Al<sub>2</sub>O<sub>3</sub> and NiO, respectively. Formation of this powder left a hole in the sample which makes it challenging to further investigate the interface.

The partial pressures of gaseous MoO<sub>x</sub> species over solid (and liquid) molybdenum oxides as a function of the oxygen partial pressure at 800 °C is shown in figure 8.25. As can be seen, under the conditions of the oxidation experiment the total partial pressure of Mo-species is about 0.1 bar which causes a rapid volatilization of the oxides. For further investigation of the interface, the oxygen partial pressure could be decreased down to 10<sup>-20</sup> bar. In that case the

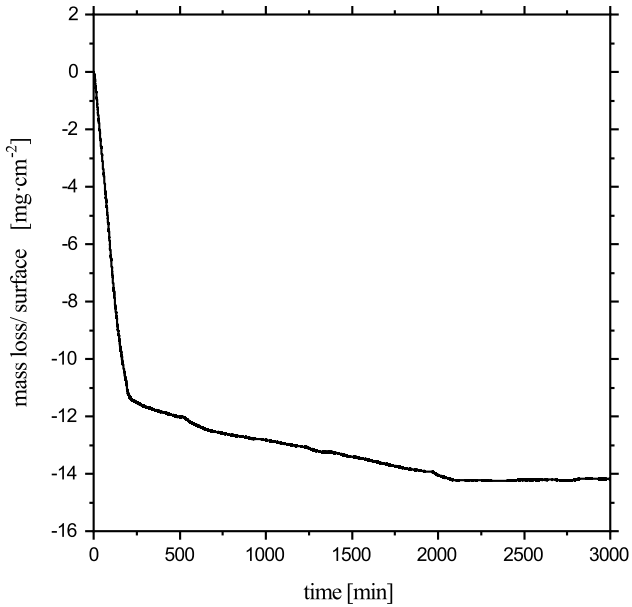


Figure 8.22: Mass loss during oxidation of NiAl-Mo at 800 °C, Ar/ 13 vol.% O<sub>2</sub>.

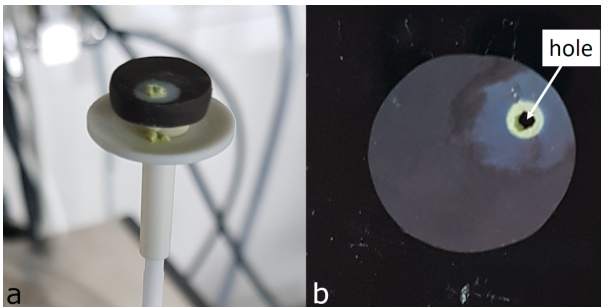


Figure 8.23: NiAl-Mo oxidized at 800 °C for 50 hours.

partial pressure of MoO<sub>2</sub> gets higher than MoO<sub>3</sub> and presumably prevents the

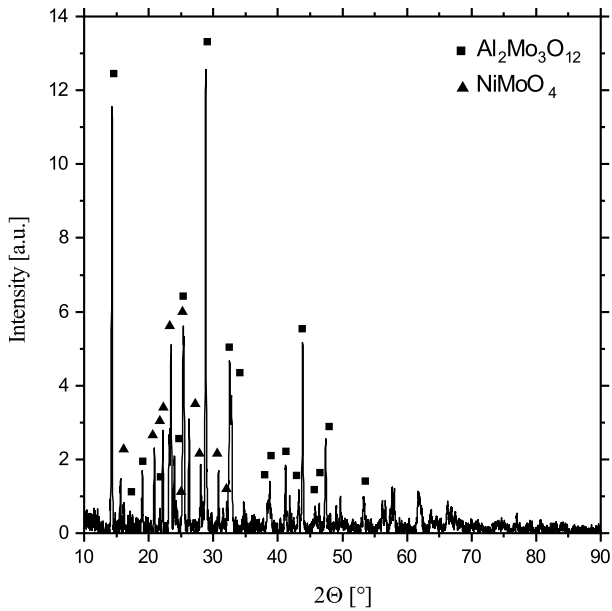


Figure 8.24: XRD pattern of the residuals of oxides at the vicinity of Mo in NiAl-Mo alloy after oxidation at 800 °C for 50 hours in Ar/ 13 vol.%  $\text{O}_2$ .

formation of the powder at the interface.

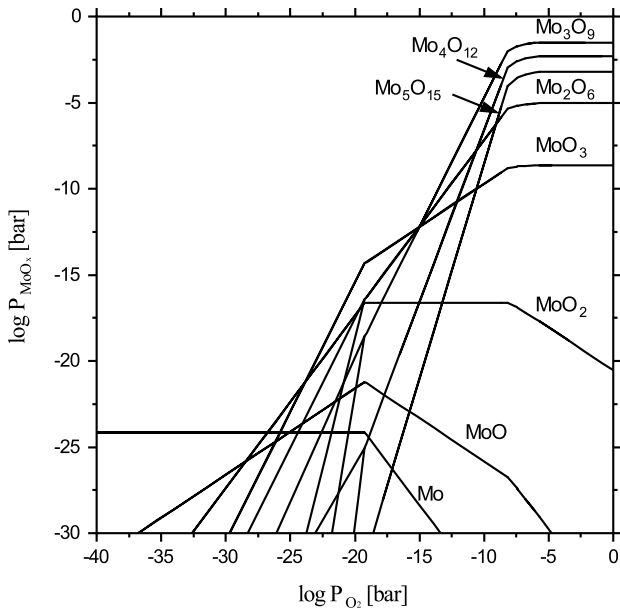


Figure 8.25: Partial pressure of  $MoO_x$  vs. oxygen partial pressure at 800 °C.

# Chapter 9

## Conclusion and outlook

This work gives an insight into the oxidation behavior of specific high temperature NiAl-based alloys reinforced with Cr and Mo.

For this reason, Calphad approach was employed in which combined experimental results from literature together with the experiments performed in the present work were used to optimize the parameters needed in the thermodynamic database.

This database was further applied for determining the stability ranges of the intermetallic phases and the oxides formed during oxidation of the engineered alloys. The phase diagrams, such as isothermal sections, isopleths and potential diagrams, as well as property diagrams and thermodynamic properties were calculated.

The thermodynamic description was provided for Ni-Al-Cr-Mo-O system. All corresponding binary and ternary systems were studied carefully. Evaluating the literature data revealed that most of the metallic sub-systems had already been assessed which were accepted in this work. However, deficiencies and lack of data regarding the oxidic systems were seen in the assessments available in the literature. Consequently, the relevant oxide systems were assessed in the present work. Some changes in the adapted data were still necessary.

The ionic two-sublattice liquid model was used to describe both metallic and oxide liquids. In Mo-O binary system, the solubility of oxygen in Mo was revised based on experimental literature data. In addition, the liquid phase in

the Mo-O system was reassessed using the experimental data available in the literature.

The Cr-Mo-O, Al-Mo-O and Ni-Mo-O systems are assessed based on experimental data available in the literature. The spinel phase in Ni-Al-O system is reassessed to describe the homogeneity range of  $\text{NiAl}_2\text{O}_4$  and keeping the consistency with Ni-Cr-O system as well as the higher order systems.

Isothermal oxidation experiments were performed in which the coarse composites of NiAl-Cr and NiAl-Mo were produced and oxidized at defined oxygen activities and isothermal condition, where a mixed layer of oxides was formed. The composition of this continuous solid solution was dependent on the distance from the interface of the two bulk metal matrix, as well as the distance from the gas/oxide interface.

During oxidation of various samples, mass gain fluctuation and its cause have been investigated. The highly delicate regions, where most of the oxide spallation occurred, are studied.

The spallation of oxide scales followed by further oxidation due to the unprotected surface, together with the difference in the oxidation rates of the pure substrates had an impact on the final disparity between the oxidation rate of various composite samples.

At 1200 °C NiAl has the best oxidation resistance with  $K_{p,w}=5.90 \times 10^{-12}$  ( $g^2 \cdot cm^{-4} \cdot s^{-1}$ ) which is lower compared to the NiAl-Cr coarse composite and DS NiAl-34Cr with  $K_{p,w}$  of  $8.48 \times 10^{-12}$  and  $1.06 \times 10^{-11}$  ( $g^2 \cdot cm^{-4} \cdot s^{-1}$ ), respectively. At this temperature mass gain fluctuation due to spallation of oxide scale is seen during oxidation of DS NiAl-34Cr which led to a higher oxidation rate compared to the NiAl-Cr coarse composite. This spallation is mainly caused by Cr-rich region formed between the oxide scale and the substrate surface. The NiAl-Cr coarse composite does not show huge spallation of oxide scales at 1200 °C.

At 1300 °C the NiAl-Cr coarse composite has the oxidation rate of  $5.81 \times 10^{-11}$   $g^2 \cdot cm^{-4} \cdot s^{-1}$  which is higher compared to DS NiAl-34Cr and pure NiAl with  $K_{p,w}$  of  $2.9 \times 10^{-11}$  and  $1.93 \times 10^{-11}$   $g^2 \cdot cm^{-4} \cdot s^{-1}$ , respectively. This could

have been caused by faster oxidation of Cr pieces and spallation at the interface of NiAl and Cr.

Oxidation of NiAl-Mo on the other hand, was completely corrosive and volatile oxides were formed which evaporated from the surface and left a hole in the sample. The residual of the powder showed formation of  $\text{Al}_2\text{Mo}_3\text{O}_{12}$  and  $\text{NiMoO}_4$ .

Calculation of potential phase diagrams presenting the partial pressure of  $\text{MoO}_x$  species with respect to oxygen partial pressure showed that at oxygen partial pressures above  $10^{-10}$  bar, the oxides which will be formed have high volatilization which is the main reason for the destructive oxidation.

Further investigation of oxidation of DS NiAl-34Cr alloys could be carried out, considering the effects of fiber sizes and their orientation. As it was shown, the oxide spallation mainly occurred at the interface of NiAl and Cr and the oxidation rate escalated as the interface area between NiAl/Cr increased. On the other hand, as it was discussed by Brady et al. [15], if the dispersion of the embedded material is fine enough it would improve the oxidation resistance. Therefore, further investigation is needed in order to achieve an optimum fiber size for the reinforcing material with the aim of formation of more protective oxide layers.

Furthermore, addition of various Mo content would have a huge impact on microstructure of the alloys based on NiAl(Cr,Mo) [258] which would lead to unforeseen oxidation behavior together with consequences on the mechanical properties. Therefore, oxidation of DS NiAl in which Cr and Mo are both embedded as reinforcing materials should be investigated thoroughly.



# Bibliography

- [1] R. D. Noebe, R. R. Bowman, and M. V. Nathal. Physical and mechanical properties of the B2 compound NiAl. *International Materials Reviews*, 38(4):193–232, 1993.
- [2] F. Ebrahimi and S. Shrivastava. Brittle-to-ductile transition in NiAl single crystal. *Acta Materialia*, 46(5):1493–1502, 1998.
- [3] J. L. Walter and H. E. Cline. The effect of solidification rate on structure and high-temperature strength of the eutectic NiAl-Cr. *Metallurgical and Materials Transactions B*, 1(5):1221–1229, 1970.
- [4] D. R. Johnson, X. F. Chen, and B. F. Oliver. Processing and mechanical properties of in-situ composites from the NiAl-Cr and the NiAl-(Cr,Mo) eutectic systems. *Intermetallics*, 3(2):99–113, 1995.
- [5] C. Cui, Y. Chen, J. Guo, D. Li, and H. Ye. Preliminary investigation of directionally solidified NiAl–28Cr–5.5Mo–0.5Hf composite. *Materials Letters*, 43(5-6):303–308, 2000.
- [6] H. Bei and E. P. George. Microstructures and mechanical properties of a directionally solidified NiAl–Mo eutectic alloy. *Acta Materialia*, 53(1):69–77, 2005.
- [7] L. Hu, G. Zhang, W. Hu, G. Gottstein, S. Bogner, and A. Bührig-Polaczek. Tensile creep of directionally solidified NiAl–9Mo in situ composites. *Acta Materialia*, 61(19):7155–7165, 2013.

- [8] C. Seemüller, M. Heilmaier, T. Haenschke, H. Bei, A. Dlouhy, and E. P. George. Influence of fiber alignment on creep in directionally solidified NiAl–10Mo in-situ composites. *Intermetallics*, 35:110–115, 2013.
- [9] Z. Shang, J. Shen, L. Wang, Y. Du, Y. Xiong, and H. Fu. Investigations on the microstructure and room temperature fracture toughness of directionally solidified NiAl–Cr(Mo) eutectic alloy. *Intermetallics*, 57:25–33, 2015.
- [10] K. Wefers and C. Misra. *Oxides and hydroxides of aluminum*. Alcoa Research Laboratories, 1987.
- [11] R. Klumpes, C. Maree, E. Schramm, and Wit J.H.W. de. The influence of chromium on the Oxidation of  $\beta$ -NiAl at 1000 °C. *Materials and Corrosion*, 47:619–624, 1996.
- [12] J. C. Yang, E. Schumann, I. Levin, and M. Rühle. Transient oxidation of NiAl. *Acta Materialia*, 46(6):2195–2201, 1998.
- [13] H. J. Grabke, M. W. Brumm, and B. Wagemann. The oxidation of NiAl. *Materials and Corrosion*, 47(12):675–677, 1996.
- [14] H. Grabke. Oxidation of NiAl and FeAl. *Intermetallics*, 7(10):1153–1158, 1999.
- [15] M. P. Brady, H. Bei, R. A. Meisner, M. J. Lance, and P. F. Tortorelli. Effect of Mo dispersion size and water vapor on oxidation of two-phase directionally solidified NiAl–9Mo in-situ composites. *Scripta Materialia*, 80:33–36, 2014.
- [16] Z. s. Wang, Y. Xie, J. t. Guo, L. z. Zhou, Z. q. Hu, G. Y. Zhang, and Z. g. Chen. High temperature oxidation behavior of directionally solidified NiAl–31Cr–2.9Mo–0.1Hf–0.05Ho eutectic alloy. *Transactions of Nonferrous Metals Society of China*, 22(7):1582–1587, 2012.

- 
- [17] J. Peng. Experimental investigation and thermodynamic modeling of the Al-Cr-Mo-Ni system and its sub-systems. *Dissertation, Karlsruhe Institute of Technology*, 2016.
- [18] H. J. Seifert and F. Aldinger. Applied phase studies. *Zeitschrift für Metallkunde*, 87:841–853, 1996.
- [19] H. L. Lukas, S. G. Fries, and B. Sundman. *Computational thermodynamics: The Calphad method*. Cambridge University Press, Cambridge, 2007.
- [20] G. Cacciamani. An introduction to the CALPHAD method and the Compound Energy Formalism (CEF). *Tecnologia em Metalurgia Materiais e Mineração*, 13(1):16–24, 2016.
- [21] J. Allison, M. Li, C. Wolverton, and X. Su. Virtual aluminum castings: an industrial application of ICME. *Journal of Metals*, 58(11):28–35, 2006.
- [22] R. Shi and A. A. Luo. Applications of CALPHAD modeling and databases in advanced lightweight metallic materials. *Calphad*, 62:1–17, 2018.
- [23] D. U. Furrer and S. L. Semiatin. *Metals Process Simulation*. ASM International, Materials Park, OH, 2010.
- [24] J. O. Andersson, T. Helander, L. Höglund, P. F. Shi, and B. Sundman. Thermo-Calc and DICTRA, Computational tools for materials science. *Calphad*, 2002.
- [25] B. Jansson. *Ph.D thesis, Royal Institute of Technology, Stockholm, Sweden*, 1984.
- [26] N. Saunders and A. P. Miodownik. *Calphad (Calculation of Phase Diagrams): A Comprehensive Guide*. Pergamon Press, New York and London, 1998.

- [27] B. Sundman and J. Ågren. A regular solution model for phases with several components and sublattices, suitable for computer application. *Journal of Physics and Chemistry of Solids*, 42(4):297–301, 1981.
- [28] F. Sommer. Association model for the description of the thermodynamic functions of liquid alloys - 1. basic concepts. *Zeitschrift für Metallkunde*, 73(2):72–76, 1982.
- [29] M. Kapoor and M. Froberg. Chemical metallurgy of iron and steel. *Iron and Steel Institute*, pages 17–21, 1971.
- [30] H. Gaye and J. Welfringer. Modelling of the thermodynamic properties of complex metallurgical slags: Second international symposium on metallurgical slags and fluxes. *TMS-AIME, Lake Tahoe, Nevada*, page 357, 1984.
- [31] A. Pelton and M. Blander. Computer Assisted Analysis of the Thermodynamic Properties and Phase Diagrams of Slags: Proceedings of the second international symposium on metallurgical slags and fluxes. pages 281–294, 1984.
- [32] A. Pelton and M. Blander. Thermodynamic analysis of ordered liquid solutions by a modified quasichemical approach-application to silicate slags. *Metallurgical Transactions B*, 17(4):805–815, 1986.
- [33] M. Hillert, B. Jansson, B. Sundman, and J. Ågren. A two-sublattice model for molten solutions with different tendency for ionization. *Metallurgical and Materials Transactions A*, 16(1):261–266, 1985.
- [34] O. Redlich and A. T. Kister. Algebraic representation of thermodynamic properties and the classification of solutions. *Industrial & Engineering Chemistry*, 40(2):345–348, 1948.
- [35] P. Saltykov. Hochtemperatur-Thermochemie im System Al-Cr-Ni-O: Dissertation an der Universität Stuttgart. *Dissertation, Stuttgart*, 2003.

- [36] P. Saltykov, O. Fabrichnaya, J. Golczewski, and F. Aldinger. Thermodynamic modeling of oxidation of Al–Cr–Ni alloys. *Journal of Alloys and Compounds*, 381(1-2):99–113, 2004.
- [37] R. Dieckmann. Point defects and transport in haematite ( $\text{Fe}_2\text{O}_{3-\epsilon}$ ). *Philosophical Magazine A*, 68(4):725–745, 1993.
- [38] J. R. Taylor and A. T. Dinsdale. A thermodynamic assessment of the Ni–O, Cr–O and Cr–Ni–O systems using the ionic liquid and compound energy models. *Zeitschrift für Metallkunde*, 81:354, 1990.
- [39] L. Kjellqvist, M. Selleby, and B. Sundman. Thermodynamic modelling of the Cr–Fe–Ni–O system. *Calphad*, 32(3):577–592, 2008.
- [40] L. Kjellqvist. Thermodynamic description of the Fe–C–Cr–Mn–Ni–O system. *Ph.D Thesis, KTH industrial engineering and management, Stockholm*, 2009.
- [41] H. O’Neill and A. Navrotsky. Simple spinels: crystallographic parameters, cation radii, lattice energies, and cation distribution. *American Mineralogist*, 68:181–194, 1983.
- [42] H. O’Neill and A. Navrotsky. Cation distributions and thermodynamic properties of binary spinel solid solutions. *American Mineralogist*, 69:733–753, 1984.
- [43] H. O’Neill, W. A. Dollase, and C. R. Ross. Temperature dependence of the cation distribution in nickel aluminate ( $\text{NiAl}_2\text{O}_4$ ) spinel: A powder XRD study. *Physics and Chemistry of Minerals*, 18(5), 1991.
- [44] J. Töpfer, S. Aggarwal, and R. Dieckmann. Point defects and cation tracer diffusion in  $(\text{Cr}_x\text{Fe}_{1-x})_{3-\delta}\text{O}_4$  spinels. *Solid State Ionics*, 81(3-4):251–266, 1995.

- [45] R. Dieckmann. Defects and Cation Diffusion in Magnetite (IV): Nonstoichiometry and Point Defect Structure of Magnetite ( $\text{Fe}_{3-\delta}\text{O}_4$ ). *Berichte der Bunsengesellschaft für physikalische Chemie*, 86:112–118, 1982.
- [46] R. Dieckmann and H. Schmalzried. Defects and cation diffusion in magnetite (VI): point defect relaxation and correlation in cation tracer diffusion. *Berichte der Bunsengesellschaft für physikalische Chemie*, 90(7):546–576, 1986.
- [47] D. P. Pope, D. M. Shah, W. Romanow, and M. Huntley. Directional solidification of refractory intermetallics: Single crystals and composites. *MRS Online Proceedings Library Archive*, 322, 1993.
- [48] D. M. Shah, D. L. Anton, D. P. Pope, and S. Chin. In-situ refractory intermetallic-based composites. *Materials Science and Engineering: A*, 192-193:658–672, 1995.
- [49] W. G. Pfann. Principles of zone-melting. *Journal of Metals*, 4(7):747–753, 1952.
- [50] B. P. Bewlay and M. R. Jackson. High-temperature in situ composites: processing and properties. *Comprehensive composite materials*, 3:579–615, 2000.
- [51] J. Wollweber, T. Duffar, J.-L. Santailier, and V. Chevrier. Growth in solution in a float zone of crystals of a compound or an alloy, December 16 2003. US Patent 6,663,711.
- [52] M. W. Brumm and H. J. Grabke. The oxidation behaviour of NiAl-I. Phase transformations in the alumina scale during oxidation of NiAl and NiAl-Cr alloys. *Corrosion Science*, 33(11):1677–1690, 1992.
- [53] W. Rachinger. A correction for the  $\alpha_1 \alpha_2$  doublet in the measurement of widths of X-ray diffraction lines. *Journal of scientific instruments*, 25(7):254, 1948.

- [54] V. Randle. Texture. In *Encyclopedia of materials: science and technology (Second Edition)*, pages 9119–9129. Elsevier, Amsterdam and London, 2001.
- [55] D. J. Young. *High temperature oxidation and corrosion of metals*, volume 1 of *Elsevier corrosion series*. Elsevier, Amsterdam and Boston and London, 1st ed. edition, 2008.
- [56] A. Fick. Über Diffusion. *Annalen der Physik und Chemie*, 170(1):59–86, 1855.
- [57] A. M. Stoneham. Oxidation kinetics. In K. H. J. Buschow, editor, *Encyclopedia of materials*, pages 6579–6586. Elsevier, Amsterdam and London, 2001.
- [58] A. Paul, T. Laurila, V. Vuorinen, and S. V. Divinski. *Thermodynamics, Diffusion and the Kirkendall Effect in Solids*. Springer International Publishing, Cham, 2014.
- [59] A. S. Khanna. High-temperature oxidation. In M. Kutz, editor, *Handbook of environmental degradation of materials*, pages 117–132. William Andrew, Norwich, 2018.
- [60] G. Tammann. Über Anlauffarben von Metallen. *Zeitschrift für Anorganische und Allgemeine Chemie*, 111:78–89, 1920.
- [61] N. Pilling and R. Bedworth. The oxidation of metals at high temperature. *Journal of the Institute of Metals*, 29:529–582, 1923.
- [62] C. Wagner. Beitrag zur Theorie des Anlaufvorgangs. *Zeitschrift für Physikalische Chemie*, 21B(1):25–41, 1933.
- [63] C. Wagner. Beitrag zur Theorie des Anlaufvorganges. II. *Zeitschrift für Physikalische Chemie*, 32B(1):447–462, 1936.

- [64] C. Wagner and K. Grünewald. Beitrag zur Theorie des Anlauf Vorganges. III. *Zeitschrift für Physikalische Chemie*, 40B(1):455–475, 1938.
- [65] C. Wagner. Atom movements. *ASM, Cleveland*, page 153, 1951.
- [66] C. Wagner. Reaktionstypen bei der Oxydation von Legierungen. *Zeitschrift für Elektrochemie*, 63:772–782, 1959.
- [67] C. Wagner. The evolution of data obtained with diffusion couples of binary single-phase and multiphase systems. *Acta metallurgica*, 17:99–107, 1969.
- [68] C. Wagner. Formation of thin oxide films on metals. *Corrosion Science*, 13(1):23–52, 1973.
- [69] C. Wagner. Equations for transport in solid oxides and sulfides of transition metals. *Progress in Solid State Chemistry*, 10:3–16, 1975.
- [70] B. Pieraggi. Calculations of parabolic reaction rate constants. *Oxidation of Metals*, 27(3-4):177–185, 1987.
- [71] B. Pieraggi. Comments on “Growth rates of alumina scales on Fe–Cr–Al alloys”. *Oxidation of Metals*, 64(5-6):397–403, 2005.
- [72] D. A. Porter and K. E. Easterling. *Phase transformations in metals and alloys*. Chapman & Hall, London and New York, 2<sup>nd</sup> edition, 1992.
- [73] T. Boll, K. A. Unocic, B. A. Pint, A. Mårtensson, and K. Stiller. Grain Boundary chemistry and transport through alumina scales on NiAl alloys. *Oxidation of Metals*, 17:429, 2017.
- [74] N. Cabrera and N. Mott. Theory of the oxidation of metals. *Reports on Progress in Physics*, 12:163–184, 1948.
- [75] N. Dupin, I. Ansara, and B. Sundman. Thermodynamic re-assessment of the ternary system Al–Cr–Ni. *Calphad*, 25(2):279–298, 2001.

- [76] J. Peng, P. Franke, and H. J. Seifert. Experimental investigation and CALPHAD assessment of the eutectic trough in the system NiAl-Cr-Mo. *Journal of Phase Equilibria and Diffusion*, 37(5):592–600, 2016.
- [77] P. Franke. Modeling of thermal vacancies in metals within the framework of the compound energy formalism. *Journal of Phase Equilibria and Diffusion*, 35(6):780–787, 2014.
- [78] C. Zhang, M. C. Gao, Y. Yang, and F. Zhang. Thermodynamic modeling and first-principles calculations of the Mo–O system. *Calphad*, 45:178–187, 2014.
- [79] P. Nash, M. F. Singleton, and J. L. Murray. *Phase Diagrams of Binary Nickel Alloys*. ASM International, Materials Park, Ohio, 1991.
- [80] H. Okamoto. Al-Ni (aluminum-nickel). *Journal of Phase Equilibria and Diffusion*, 25(4):394, 2004.
- [81] H. Okamoto. Al-Ni (aluminum-nickel). *Journal of Phase Equilibria*, 14(2):257–259, 1993.
- [82] Y. Ma and A. J. Ardell. The  $(\gamma + \gamma')/\gamma'$  phase boundary in the Ni–Al phase diagram from 600 to 1200 °C. *Zeitschrift für Metallkunde*, 94(9):972–975, 2003.
- [83] P. Saltykov, L. Cornish, and G. Cacciamani. *Al-Ni binary phase diagram evaluation*. Binary Evaluations. MSI, Materials Science International Services GmbH, Stuttgart, 2004.
- [84] L. Kaufman. Coupled phase diagrams and thermochemical data for transition metal binary systems-III. *Calphad*, 2(2):117–146, 1978.
- [85] I. Ansara, B. Sundman, and P. Willemin. Thermodynamic modeling of ordered phases in the NiAl system. *Acta Metallurgica*, 36(4):977–982, 1988.

- [86] N. Dupin. Contribution à l'évaluation thermodynamique des alliages polyconstitués à base de nickel. *Ph.D thesis, Institut national polytechnique (Grenoble)*, 1995.
- [87] Y. Du and N. Clavaguera. Thermodynamic assessment of the Al-Ni system. *Journal of Alloys and Compounds*, 237(1):20–32, 1996.
- [88] I. Ansara, N. Dupin, H. L. Lukas, and B. Sundman. Thermodynamic assessment of the Al-Ni system. *Journal of Alloys and Compounds*, 247:20–30, 1997.
- [89] W. Huang and Y. A. Chang. A thermodynamic analysis of the Ni-Al system. *Intermetallics*, 6(6):487–498, 1998.
- [90] N. Dupin and I. Ansara. On the sublattice formalism applies to the B2 phase. *Zeitschrift für Metallkunde*, 90(76-85), 1999.
- [91] W. Huang and Y. A. Chang. Corrigendum to “A thermodynamic analysis of the Ni-Al system” [Intermetallics, 6 (1998) 487-498]. *Intermetallics*, 7:625–626, 1999.
- [92] J. Peng, P. Franke, D. Manara, T. Watkins, R. J. Konings, and H. J. Seifert. Experimental investigation and thermodynamic re-assessment of the Al–Mo–Ni system. *Journal of Alloys and Compounds*, 674:305–314, 2016.
- [93] P. Nash. The Cr-Ni (chromium-nickel) system. *Bulletin of Alloy Phase Diagrams*, 7:466–476, 1986.
- [94] A. L. Udovsky and E. A. Kozodaeva. An optimized calculation of phase diagram and thermodynamic properties of the Ni-Cr system. *Calphad*, 17(1):17–34, 1993.
- [95] J. Tomiska, K. Kopecky, M. S. Beleggratis, and C. Myers. Thermodynamic mixing functions and phase equilibria in the nickel-chromium

- system by high-temperature knudsen cell mass spectrometry. *Metalurgical and Materials Transactions A*, 26A:259–265, 1995.
- [96] T. B. Massalski and H. Okamoto. *Binary alloy phase diagrams*. ASM International, Materials Park, Ohio, 2<sup>nd</sup> edition, 1990.
- [97] A. T. Dinsdale and T. G. Chart. MTDS NPL, Unpublished work; Cr-Ni. 1986.
- [98] T. Chart, F. Put land, and A. Dinsdale. Calculated phase equilibria for the Cr-Fe-Ni-Si system-I ternary equilibria. *Calphad*, 4(1):27–46, 1980.
- [99] P. Gustafson. A thermodynamic evaluation of the Cr-Ni-W system. *Calphad*, 12(3):277–292, 1988.
- [100] B.-J. Lee. On the stability of Cr carbides. *Calphad*, 16(2):121–149, 1992.
- [101] P. Turchi, L. Kaufman, and Z.-K. Liu. Modeling of Ni–Cr–Mo based alloys: Part I—phase stability. *Calphad*, 30(1):70–87, 2006.
- [102] J. L. Murray. The Al-Cr (aluminum-chromium) system. *Journal of Phase Equilibria*, 19(4):368–375, 1998.
- [103] H. Okamoto. Al-Cr (aluminum-chromium). *Journal of Phase Equilibria and Diffusion*, 29(1):112–113, 2008.
- [104] A. V. Khvan and A. Watson. *Al-Cr binary phase diagram evaluation*. Binary Evaluations. MSI, Materials Science International Services GmbH, Stuttgart, 2013.
- [105] N. Saunders and V. G. Rivlin. Thermodynamic characterization of Al–Cr, Al–Zr, and Al–Cr–Zr alloy systems. *Materials Science and Technology*, 2(6):520–527, 1986.

- [106] N. Saunders and V. G. Rivlin. A critical-review and thermodynamic calculations for the Al-rich portion of the Al-Cr-Fe phase-diagram. *Zeitschrift für Metallkunde*, 78(11):795–801, 1987.
- [107] I. Ansara, A. T. Dinsdale, and M. H. Rand. Definition of thermochemical and thermophysical properties to provide a database for the development of new light alloys. *Thermochemical database for light metal alloys*, 2, 1998.
- [108] T. Tokunaga, H. Ohtani, and M. Hasebe. Thermodynamic assessment of the Al-Cr system by combining the first principles and CALPHAD methods. In T. Chandra, editor, *THERMEC 2006. Part 2*, Materials science forum, pages 2407–2412, Uetikon-Zuerich, 2007. Trans Tech Publications.
- [109] Y. Liang, C. Guo, C. Li, and Z. Du. Thermodynamic modeling of the Al–Cr system. *Journal of Alloys and Compounds*, 460(1):314–319, 2008.
- [110] B. Hu, W.-W. Zhang, Y. Peng, Y. Du, S. Liu, and Y. Zhang. Thermodynamic reassessment of the Al–Cr–Si system with the refined description of the Al–Cr system. *Thermochimica Acta*, 561:77–90, 2013.
- [111] V. T. Witusiewicz, A. A. Bondar, U. Hecht, and T. Velikanova. Thermodynamic re-modelling of the ternary Al–Cr–Ti system with refined Al–Cr description. *Journal of Alloys and Compounds*, 644:939–958, 2015.
- [112] B. Grushko, E. Kowalska-Strzeciwiłk, B. Przepiorzynski, and M. Surowiec. Investigation of the Al-Cr  $\gamma$ -range. *Journal of alloys and compounds*, 402:98–104, 2005.
- [113] B. Grushko, B. Przepiórzyński, and D. Pavlyuchkov. On the constitution of the high-Al region of the Al–Cr alloy system. *Journal of Alloys and Compounds*, 454(1-2):214–220, 2008.

- [114] F. Stein, C. He, and I. Wossack. The liquidus surface of the Cr–Al–Nb system and re-investigation of the Cr–Nb and Al–Cr phase diagrams. *Journal of Alloys and Compounds*, 598:253–265, 2014.
- [115] T. Velikanova, K. Korniyenko, and V. Sidorko. *Al-Cr-Ni ternary phase diagram evaluation*. Ternary Evaluations. MSI, Materials Science International Services GmbH, Stuttgart, 2004.
- [116] W. Huang and Y. A. Chang. Thermodynamic properties of the Ni–Al–Cr system. *Intermetallics*, 7:863–874, 1999.
- [117] P. K. Sung and D. R. Poirier. Liquid-solid partition ratios in nickel-base alloys. *Metallurgical and Materials Transactions A*, 30(8):2173–2181, 1999.
- [118] W. H. Tian, C. S. Han, and M. Nemoto. Precipitation of  $\alpha$ -Cr in B2-ordered NiAl. *Intermetallics*, 7(1):59–67, 1999.
- [119] P. Saltykov, V. T. Witusiewicz, I. Arpshofen, O. Fabrichanya, H. J. Seifert, and F. Aldinger. Thermodynamics of liquid and undercooled liquid Al–Cr–Ni alloys. *Scandinavian Journal of Metallurgy*, 30:297–301, 2001.
- [120] Y. Lewinsky. *Ni-O p-T-x Phase Diagrams*. p-T-x Diagrams. MSI, Materials Science International Services GmbH, Stuttgart, 1997.
- [121] H. A. Wriedt and J. Chipman. Oxygen in liquid iron-nickel alloys. *Journal of Metals*, 8(9):1195–1199, 1956.
- [122] A. E. Paladino. Phase equilibria in the ferrite region of the system Fe–Ni–O. *Journal of the American Ceramic Society*, 42(4):168–175, 1959.
- [123] E. S. Tankins, N. A. Gokcen, and G. R. Belton. The activity and solubility of oxygen in liquid iron, nickel, and cobalt. *Transactions of The Metallurgical Society of AIME*, 230:820–827, 1964.

- [124] H. Schmalzried and J. D. Tretjakow. Fehlordnung in Ferriten. *Berichte der Bunsengesellschaft für physikalische Chemie*, 70:180–189, 1966.
- [125] S. P. Litvinov, L. S. Cemechman, and B. P. Burylev. The phase diagram of the NiO system and thermodynamic properties of the oxygen solution in the liquid nickel. *Izvestiya Vysshikh Uchebnykh Zavedenii, Chernaya Metallurgiya*, 2:30–34, 1982.
- [126] J.-W. Park and C. J. Altstetter. The diffusion and solubility of oxygen in solid nickel. *Metallurgical Transactions A*, 18(1):43–50, 1987.
- [127] E. Jacobson and E. Rosén. Thermodynamic studies of high temperature equilibria. 25. solid state emf studies of the systems iron-ferrous oxide, nickel-nickelous oxide, and cobalt-cobaltous oxide in the temperature range 1000-1600 K. *Scandinavian Journal of Metallurgy*, 10:39–43, 1981.
- [128] J. P. Neumann, T. Zhong, and Y. A. Chang. The Ni-O (nickel-oxygen) system. *Bulletin of Alloy Phase Diagrams*, 5(2):141–144, 1984.
- [129] M. Kowalski and P. J. Spencer. Thermodynamic reevaluation of the Cr-O, Fe-O and Ni-O systems: remodelling of the liquid, BCC and FCC phases. *Calphad*, 19(3):229–243, 1995.
- [130] R. Luoma. A Thermodynamic analysis of the system Fe-Ni-O. *Calphad*, 19(3):279–295, 1995.
- [131] H. Mozaffari-Jovein. Entwicklung und Einsatz von keramischen Materialien als Wärmedämmschicht für Ni-Basis-Legierungen für Temperaturen größer als 1350 °C. *Dissertation, Stuttgart*, 2003.
- [132] H. Okamoto. Ni-O (nickel-oxygen). *Journal of Phase Equilibria and Diffusion*, 28(4):408, 2007.
- [133] MSI eureka. *Ni-O reference phase diagrams*. Reference Diagrams. MSI, Materials Science International Services GmbH, Stuttgart, 2010.

- [134] L. Cornish, Y. Eichhammer, D. Pavlyuchkov, and E. Semenova. *Cr-O binary phase diagram evaluation*. Binary Evaluations. MSI, Materials Science International Services GmbH, Stuttgart, 2015.
- [135] H. Okamoto. Cr-O (chromium-oxygen). *Journal of Phase Equilibria*, 18(4):402, 1997.
- [136] R. J. Taylor and A. T. Dinsdale. A thermodynamic assessment of the Cr-Fe-O system. *Zeitschrift für Metallkunde*, 84(5):335–345, 1993.
- [137] E. Povoden, A. N. Grundy, and L. J. Gauckler. Thermodynamic re-assessment of the Cr-O system in the framework of solid oxide fuel cell (SOFC) Research. *Journal of Phase Equilibria and Diffusion*, 27(4):353–362, 2006.
- [138] N. Y. Toker, L. S. Darken, and A. Muan. Equilibrium phase relations and thermodynamics of the Cr-O system in the temperature range of 1500 °C to 1825 °C. *Metallurgical Transactions B*, 22(2):225–232, 1991.
- [139] A. D. Pelton, H. Schmalzried, and J. Sticher. Computer-assisted analysis and calculation of phase diagrams of the Fe-Cr-O, Fe-Ni-O and Cr-Ni-O systems. *Journal of Physics and Chemistry of Solids*, 40(12):1103–1122, 1979.
- [140] O. Fabrichnaya, P. Perrot, S. Lakiza, and P. Rogl. *Al-O binary phase diagram evaluation*. Binary Evaluations. MSI, Materials Science International Services GmbH, Stuttgart, 2013.
- [141] H. A. Wriedt. The Al-O (aluminum-oxygen) system. *Bulletin of Alloy Phase Diagrams*, 6(6):548–553, 1985.
- [142] B. Hallstedt. Assessment of the CaO-Al<sub>2</sub>O<sub>3</sub> system. *Journal of the American Ceramic Society*, 73:15–23, 1990.
- [143] B. Hallstedt. Thermodynamic assessment of the system MgO-Al<sub>2</sub>O<sub>3</sub>. *Journal of the American Ceramic Society*, 75(6):1497–1507, 1992.

- [144] J. R. Taylor, A. T. Dinsdale, M. Hillert, and M. Selleby. A critical assessment of thermodynamic and phase diagram data for the Al-O system. *Calphad*, 16(2):173–179, 1992.
- [145] B. Hallstedt. Thermodynamic calculation of some subsystems of the Al-Ca-Mg-Si-O system. *Journal of Phase Equilibria*, 14(6):662–675, 1993.
- [146] H. Mao, M. Selleby, and B. Sundman. A re-evaluation of the liquid phases in the CaO–Al<sub>2</sub>O<sub>3</sub> and MgO–Al<sub>2</sub>O<sub>3</sub> systems. *Calphad*, 28(3):307–312, 2004.
- [147] K. H. Kumar, S. Miran, N. Kovalenko, I. Bajenova, and M. Record. *Al-Cr-O ternary phase diagram evaluation*. Ternary Evaluations. MSI, Materials Science International Services GmbH, Stuttgart, 2016.
- [148] K. T. Jacob. Electrochemical determination of activities in Cr<sub>2</sub>O<sub>3</sub>-Al<sub>2</sub>O<sub>3</sub> solid solution. *Journal of The Electrochemical Society*, 125(2):175, 1978.
- [149] L. Kaufman and H. Nesor. Calculation of quasibinary and quasiternary oxide systems — I. *Calphad*, 2(1):35–53, 1978.
- [150] N. D. Chatterjee, H. Leistner, L. Terhart, K. Abraham, and R. Klaska. Thermodynamic mixing properties of corundum–eskolaite,  $\alpha$ -(Al, Cr<sup>+3</sup>)<sub>2</sub>O<sub>3</sub>, crystalline solutions at high temperatures and pressures. *American Mineralogist*, 67(7-8):725–735, 1982.
- [151] C. A. Handwerker, T. J. Foecke, J. S. Wallace, U. R. Kattner, and R. D. Jiggets. Formation of alumina-chromia-chromium composites by a partial reduction reaction. *Materials Science and Engineering: A*, 195:89–100, 1995.

- [152] S. Degterov and A. D. Pelton. Critical evaluation and optimization of the thermodynamic properties and phase diagrams of the CrO-Cr<sub>2</sub>O<sub>3</sub>, CrO-Cr<sub>2</sub>O<sub>3</sub>-Al<sub>2</sub>O<sub>3</sub>, and CrO-Cr<sub>2</sub>O<sub>3</sub>-CaO systems. *Journal of Phase Equilibria*, 17(6):476–487, 1996.
- [153] J. C. Schuster and J. Peng. *Al-Mo binary phase diagram evaluation*. Binary Evaluations. MSI, Materials Science International Services GmbH, Stuttgart, 2016.
- [154] L. Kaufman and H. Nesor. Calculation of superalloy phase diagrams: Part II. *Metallurgical Transactions*, 5(7):1623–1629, 1974.
- [155] L. Kaufman and H. Nesor. Coupled phase diagrams and thermochemical data for transition metal binary systems — V. *Calphad*, 2(4):325–348, 1978.
- [156] N. Saunders. The Al-Mo system (aluminum-molybdenum). *Journal of Phase Equilibria*, 18(4):370–378, 1997.
- [157] Z. Du, C. Guo, C. Li, and W. Zhang. Thermodynamic description of the Al-Mo and Al-Fe-Mo systems. *Journal of Phase Equilibria and Diffusion*, 30(5):487–501, 2009.
- [158] D. M. Cupid, O. Fabrichnaya, F. Ebrahimi, and H. J. Seifert. Thermodynamic assessment of the Al–Mo system and of the Ti–Al–Mo system from 0 to 20 at.% Ti. *Intermetallics*, 18(6):1185–1196, 2010.
- [159] N. Saunders. System Al-Mo. In I. Ansara, A. T. Dinsdale, and M. H. Rand, editors, *Thermochemical database for light metal alloys*, Definition of thermomechanical and thermophysical properties to provide a database for the development of new light alloys, pages 59–64. Office for Official Publications of the European Communities, Luxembourg, 1998.

- [160] M. Eumann, G. Sauthoff, and M. Palm. Re-evaluation of phase equilibria in the Al–Mo system. *International Journal of Materials Research*, 97(11):1502–1511, 2006.
- [161] J. C. Schuster and H. Ipsier. The Al–Al<sub>8</sub>Mo<sub>3</sub> section of the binary system aluminum-molybdenum. *Metallurgical Transactions A*, 22(8):1729–1736, 1991.
- [162] M. J. Kriegel, A. Walnsch, O. Fabrichnaya, D. Pavlyuchkov, V. Klemm, J. Freudenberger, D. Rafaja, and A. Leineweber. High-temperature phase equilibria with the bcc-type  $\beta$  (AlMo) phase in the binary Al–Mo system. *Intermetallics*, 83:29–37, 2017.
- [163] P. Roentgen and W. Koch. The influence of heavy metals on al alloys. *Zeitschrift für Metallkunde*, 25:182–185, 1930.
- [164] K. Yamaguchi and K. Simizu. The equilibrium diagram of the Al–Mo system. *The Journal of the Japan Institute of Metals*, 4(11):390–392, 1940.
- [165] L. Mondolfo. The Al–Mo system. In L. Mondolfo, editor, *Metallography of aluminium alloys*, pages 30–31. John Wiley & Sons Inc, New York etc, 1943.
- [166] V. Vigdorovich, V. Glazov, and N. Glagoleva. Investigation of the solubility of cr, mo and w in al by the microhardness method. *Izvestiya Vysshikh Uchebnykh Zavedenii, Tsvetnaya Metallurgiya*, 3(2):143–146, 1960.
- [167] J. Rexer. The phase equilibria in the aluminum-molybdenum system at temperatures above 14000C. *Zeitschrift für Metallkunde*, 62(11):844–848, 1971.

- 
- [168] V. N. Yerembnko, Y. Natanzon, and V. I. Dybkov. Interaction of the refractory metals with liquid aluminium. *Journal of the Less Common Metals*, 50(1):29–48, 1976.
- [169] Malinovskii, R.R. Location of the liquidus in the Al–Mo system. *Tekhnologiya Lyogkikh Splavov*, 1:60–61, 1980.
- [170] I. Shilo and H. F. Franzen. High temperature thermodynamic study of the molybdenum–rich regions of the Mo–Al system. *Journal of The Electrochemical Society*, 129(11):2613–2617, 1982.
- [171] J. Peng. *Cr–Mo binary phase diagram evaluation*. Binary Evaluations. MSI, Materials Science International Services GmbH, Stuttgart, 2016.
- [172] M. Venkatraman and J. P. Neumann. The Cr–Mo (chromium–molybdenum) system. *Bulletin of Alloy Phase Diagrams*, 8(3):216–220, 1987.
- [173] K. O and T. Chart. Calculation of metallurgical equilibrium diagrams from thermochemical data. *Journal of the Institute of Metals*, 93:329, 1965.
- [174] L. Kaufman and H. Nesor. Coupled phase diagrams and thermochemical data for transition metal binary systems — I. *Calphad*, 2(1):55–80, 1978.
- [175] A. Lesnik, V. Nemoshkalenko, and A. Ovcharenko. Computer calculation of phase diagrams of some binary alloys in the subregular solution approximation. *Akademiya Nauk Ukrainskai Ssr, Metallofizika*, (75):20–31, 1979.
- [176] S. S. Balakrishna and A. K. Mallik. Synthesis of azeotropic and two terminal solid solution type binary diagrams. *Calphad*, 3(2):109–118, 1979.

- [177] K. Frisk and P. Gustafson. An Assessment of The Cr-Mo-W system. *Calphad*, 12(3):247–254, 1988.
- [178] K. Y. Shunyaev. Calculations of phase diagrams in associated solution model. *Journal of Phase Equilibria and Diffusion*, 26(6):613–615, 2005.
- [179] V. Jindal, B. N. Sarma, and S. Lele. A thermodynamic assessment of the Cr–Mo system using CE-CVM. *Calphad*, 43:80–85, 2013.
- [180] E. Rudy. Ternary phase equilibria in transition metal-boron-carbon-silicon systems. part 5. compendium of phase diagram data. Technical report, Aerojet-general corp sacramento ca materials research lab, 1969.
- [181] Y. Kocherzhinskii. The Mo–Cr fusibility diagram. *Russian Metallurgy*, (4):183–185, 1979.
- [182] A. Raman and K. Schubert. Über die Verbreitung des Zr<sub>2</sub>Cu-Type und Cr<sub>2</sub>Al-Type. *Zeitschrift für Metallkunde*, 55:798–804, 1964.
- [183] A. F. Polesya and A. I. Stepina. Formation of supersaturated ternary solid solutions from melts cooled at high rates. *Physics of Metals and Metallography*, 27:122–126, 1969.
- [184] B. Sanchez, A. G. Escorial, G. Caruana, M. C. Cristina, J. Ibáñez, and M. Torralba. Microstructure and mechanical properties of rapidly solidified Al–3Cr–0.3Mo alloys. *Welding International*, 6(7):539–547, 1992.
- [185] B. Sánchez, A. García-Escorial, M. C. Cristina, G. Caruana, and M. Torralba. Microstructure and thermal stability of Al–Cr–X (X=Ni, Mo, Si) powders obtained by centrifugal atomisation. *Materials Science and Technology*, 12(10):794–801, 1996.

- [186] A. G. Escorial, B. Sánchez, M. C. Cristina, G. Caruana, and M. Torralba. Rapidly solidified Al-3Cr-X (Ni, Mo) ribbons: structure and decomposition behaviour. *Material Science and Engineering*, A134:1204–1207, 1991.
- [187] E. Akiyama, A. Kawashima, K. Asami, and K. Hashimoto. The corrosion behavior of sputter-deposited amorphous Al-Cr-Mo alloys in 1 M HCl. *Corrosion Science*, 38(2):279–292, 1996.
- [188] P. M. Natishan, E. McCafferty, and G. K. Hubler. The corrosion behavior of Mo-Al, Cr-Al and Cr-Mo-Al surface alloys produced by ion beam mixing and ion implantation. *Corrosion Science*, 32(7):721–731, 1991.
- [189] L. Brewer and R. H. Lamoreaux. *Thermochemical properties*. IAEA, International Atomic Energy Agency (IAEA), 1980.
- [190] M. F. Singleton and P. Nash. Phase diagrams of binary nickel alloys. *ASM International, Materials Park, OH*, pages 207–212, 1991.
- [191] H. Okamoto. Mo-Ni (molybdenum-nickel). *Journal of Phase Equilibria*, 12(6):703, 1991.
- [192] M. Turchanin, N. Kolchugina, and D. Smagulov. *Mo-Ni binary phase diagram evaluation*. Binary Evaluations. MSI, Materials Science International Services GmbH, Stuttgart, 2015.
- [193] L. Kaufman and H. Nesor. Coupled phase diagrams and thermochemical data for transition metal binary systems — II. *Calphad*, 2(1):81–108, 1978.
- [194] K. Frisk. A thermodynamic evaluation of the Mo-Ni system. *Calphad*, 14(3):311–320, 1990.
- [195] Y. Cui, Z. Jin, and X. Lu. Experimental study and thermodynamic assessment of the Ni-Mo-Ta ternary system. *Metallurgical and Materials Transactions A*, 30(11):2735–2744, 1999.

- [196] Y. Wang, C. Woodward, S. H. Zhou, Z.-K. Liu, and L.-Q. Chen. Structural stability of Ni–Mo compounds from first-principles calculations. *Scripta Materialia*, 52(1):17–20, 2005.
- [197] S. H. Zhou, Y. Wang, C. Jiang, J. Z. Zhu, L.-Q. Chen, and Z.-K. Liu. First-principles calculations and thermodynamic modeling of the Ni–Mo system. *Materials Science and Engineering: A*, 397(1-2):288–296, 2005.
- [198] P. K. Ray, M. Akinc, and M. J. Kramer. Formation of multilayered scale during the oxidation of NiAl–Mo alloy. *Applied Surface Science*, 301:107–111, 2014.
- [199] S. H. Zhou, Y. Wang, L.-Q. Chen, Z.-K. Liu, and R. E. Napolitano. Solution-based thermodynamic modeling of the Ni–Al–Mo system using first-principles calculations. *Calphad*, 46:124–133, 2014.
- [200] K. P. Gupta. *Phase diagrams of ternary nickel alloys*. Indian Institute of Metals, Calcutta, 1990.
- [201] H. L. Lukas. *Cr-Mo-Ni ternary phase diagram evaluation*. Ternary evaluations. MSI, Materials Science International Services GmbH, Stuttgart, 2010.
- [202] K. Frisk. Report TRITA-MAC 429, Royal Institute of Technology, Stockholm, Sweden. 1990.
- [203] M. Raghavan, R. Mueller, G. A. Vaughn, and S. Floreen. Determination of isothermal sections of nickel rich portion of Ni–Cr–Mo system by analytical electron microscopy. *Metallurgical Transactions A*, 15(5):783–792, 1984.
- [204] I. Class, H. Gräfen, and E. Scheil. Development of a slowly precipitating corrosion resistant nickel-chromium-molybdenum alloy. *Zeitschrift für Metallkunde*, 53(5):283–293, 1962.

- 
- [205] E. Gozlan, M. Bamberger, S. F. Dirnfeld, B. Prinz, and J. Klodt. Topologically close-packed precipitations and phase diagrams of Ni-Mo-Cr and Ni-Mo-Fe and of Ni-Mo-Fe with constant additions of chromium. *Materials Science and Engineering: A*, 141(1):85–95, 1991.
- [206] R. Mathieu, N. Dupin, J.-C. Crivello, K. Yaqoob, A. Breidi, J.-M. Fiorani, N. David, and J.-M. Joubert. CALPHAD description of the Mo–Re system focused on the sigma phase modeling. *Calphad*, 43:18–31, 2013.
- [207] L. Brewer and R. H. Lamoreaux. The Mo-O system (Molybdenum-Oxygen). *Bulletin of Alloy Phase Diagrams*, 1(2):85–89, 1980.
- [208] W. E. Few and G. K. Manning. Solubility of carbon and oxygen in molybdenum. *Journal of Metals*, 4(3):271–274, 1952.
- [209] S. C. Srivastava and L. L. Seigle. Solubility and thermodynamic properties of oxygen in solid molybdenum. *Metallurgical Transactions*, 5:49–52, 1974.
- [210] E. C. Corcoran, J.-L. Flèche, N. Dupin, B. Sundman, and C. Guéneau. Thermodynamic investigations of the uranium-molybdenum-oxygen system by a coupling of density functional theory and CALPHAD methodologies. *Calphad*, 63:196–211, 2018.
- [211] E. G. King, W. W. Weller, and A. Christensen. *Thermodynamics of some oxides of molybdenum and tungsten*, volume 5664. US Department of the Interior, Bureau of Mines, 1960.
- [212] D. F. Smith, D. Brown, A. S. Dworkin, D. J. Sasmor, and E. R. van Artsdalen. Low temperature heat capacity and entropy of molybdenum trioxide and molybdenum disulfide. *Journal of American Chemical Society*, 78(8):1533–1536, 1956.

- [213] L. A. Cosgrove and Snyder, Paul, E. High temperature thermodynamic properties of molybdenum trioxide. *Journal of American Chemical Society*, 75(5):1227–1228, 1953.
- [214] *SGTE substance database*.
- [215] S. S. Brenner. Oxidation of iron–molybdenum and nickel–molybdenum alloys. *Journal of Electrochemical Society*, 102:7–15, 1955.
- [216] G. W. Smith. The crystal structures of cobalt molybdate  $\text{CoMoO}_4$  and nickel molybdate  $\text{NiMoO}_4$ . *Acta Crystallographica*, 15:1065–1057, 1962.
- [217] A. W. Sleight and B. L. Chamberland. Transition metal molybdates of the type  $\text{AMoO}_4$ . *Organic Chemistry*, 7(8):1672–1675, 1968.
- [218] T. M. Yanushkevich, V. M. Zhukovskii, and V. M. Ust'yantsev. Equilibrium Diagram of the  $\text{MoO}_3$ -NiO system. *Russian Journal of Inorganic Chemistry*, 19(7):1056–1058, 1974.
- [219] K. T. Jacob, G. M. Kale, and G. N. K. Iyengar. Phase equilibria and thermodynamic properties in the system Ni-Mo-O. *Journal of Materials Science*, 22(12):4274–4280, 1987.
- [220] M. Morishita and A. Navrotsky. Calorimetric study of nickel molybdate: heat capacity, enthalpy, and Gibbs energy of formation. *Journal of the American Ceramic Society*, 86(11):1927–1932, 2003.
- [221] McCarroll, William, H., L. Katz, and R. Ward. Some ternary oxides of tetravalent molybdenum. *Journal of American Chemical Society*, 79(20):5410–5414, 1957.
- [222] U. Steiner and W. Reichelt. Chemischer Transport ternärer Oxide im System Ni/Mo/O – Experimente und Modellrechnungen. *Zeitschrift für Anorganische und Allgemeine Chemie*, 632(10-11):1781–1791, 2006.

- [223] V. Zhukovskii, T. Yanushkevich, and T. Tel'nykh. Phase diagram of the  $\text{moo}_3\text{-sro}$  system. *Zhurnal Neorganicheskoi Khimii*, 17(10):2827, 1972.
- [224] G. Dąbrowska, P. Tabero, and M. Kurzawa. Phase relations in the  $\text{Al}_2\text{O}_3\text{-V}_2\text{O}_5\text{-MoO}_3$  system in the solid state. The crystal structure of  $\text{AlVO}_4$ . *Journal of Phase Equilibria and Diffusion*, 30(3):220–229, 2009.
- [225] W. Harrison, A. K. Cheetham, and J. Faber Jr. The crystal structure of aluminum molybdate,  $\text{Al}_2(\text{MoO}_4)_3$ , determined by time-of-flight powder neutron diffraction. *Journal of Solid State Chemistry*, 76(2):328–333, 1988.
- [226] A. K. Tyagi, S. N. Achary, and M. D. Mathews. Phase transition and negative thermal expansion in  $\text{A}_2(\text{MoO}_4)_3$  system ( $\text{A}=\text{Fe}^{3+}$ ,  $\text{Cr}^{3+}$  and  $\text{Al}^{3+}$ ). *Journal of Alloys and Compounds*, 339(1):207–210, 2002.
- [227] H. Liu, W. Sun, Z. Zhang, X. Zhang, Y. Zhou, J. Zhu, and X. Zeng. Tailored phase transition temperature and negative thermal expansion of Sc-substituted  $\text{Al}_2\text{Mo}_3\text{O}_{12}$  synthesized by a co-precipitation method. *Inorganic Chemistry Frontiers*, 6(7):1842–1850, 2019.
- [228] A. Svoboda and S. Windisch. Investigations of the ternary system chromium-molybdenum-oxygen. *High Temperatures, High Pressures*, 13:427–434, 1981.
- [229] A. G. Tyurin. Thermodynamic assessment of the effect of chromium and molybdenum on the passivability of nickel-base alloys. *Protection of Metals*, 39(6):568–574, 2003.
- [230] Y. Lida. Formation of  $\text{NiAl}_2\text{O}_4$  spinel by solid reaction. *Journal of the Japan Society of Powder and Powder Metallurgy*, 6(2):55–68, 1959.

- [231] H. Schmalzried. Röntgenographische Untersuchung der Kationenverteilung in Spinellphasen. *Zeitschrift für Physikalische Chemie*, 28:203–219, 1961.
- [232] B. Phillips, J. J. Hutta, and I. Warshaw. Phase equilibria in the system NiO–Al<sub>2</sub>O<sub>3</sub>–SiO<sub>2</sub>. *Journal of the American Ceramic Society*, 46(12):579–583, 1963.
- [233] H. Schmalzried. Point defects in ternary ionic crystals. *Progress in Solid State Chemistry*, 2:265–303, 1965.
- [234] F. A. Elrefaie and W. W. Smeltzer. Phase equilibria in the subsolidus region of the NiO– $\alpha$ -Al<sub>2</sub>O<sub>3</sub> system between 1000 and 1920 °C. *Oxidation of Metals*, 15(5-6):495–500, 1981.
- [235] M. A. Rhamdhani, T. Hidayat, P. C. Hayes, and E. Jak. Subsolidus phase equilibria of Fe–Ni–X–O (X = Mg, Al) systems in air. *Metallurgical and Materials Transactions B*, 40(1):25–38, 2009.
- [236] V. Prostavkova. Development of a thermodynamic database for nickel-containing oxide systems for simulation of Nickel extraction from laterite ores. *Ph.D thesis, Polytechnique Montreal*, 2013.
- [237] B. Sundman. An assessment of the Fe–O system. *Journal of Phase Equilibria*, 12(2):127–140, 1991.
- [238] T. I. Barry, A. T. Dinsdale, J. A. Gisby, B. Hallstedt, M. Hillert, B. Jansson, S. Jonsson, B. Sundman, and J. R. Taylor. The compound energy model for ionic solutions with applications to solid oxides. *Journal of Phase Equilibria*, 13(5):459–475, 1993.
- [239] R. J. Harrison, S. A. T. Redfern, and H. O’Neill. The temperature dependence of the cation distribution in synthetic hercynite (FeAl<sub>2</sub>O<sub>4</sub>) from in-situ neutron structure refinements. *American Mineralogist*, 83:1092–1099, 1998.

- [240] D. Shishin, V. Prostavkova, E. Jak, and S. A. Deckerov. Critical assessment and thermodynamic modeling of the Al-Fe-O system. *Metallurgical and Materials Transactions B*, 47(1):397–424, 2016.
- [241] A. Revcolevschi. Nickel oxide-based aligned eutectics. *Journal of Material Science Research*, 20:115–130, 1986.
- [242] F. A. Elrefaie and W. W. Smeltzer. Thermodynamics of nickel–aluminum–oxygen system between 900 and 1400 K. *Journal of The Electrochemical Society*, 127:2237–2242, 1981.
- [243] K. P. Trumble and M. Rühle. The role of oxygen for the spinel interphase formation at diffusion-bonded Ni/Al<sub>2</sub>O<sub>3</sub> interfaces. *Zeitschrift für Metallkunde*, 81(10):749–755, 1990.
- [244] K. P. Trumble and M. Rühle. The thermodynamics of spinel interphase formation at diffusion-bonded Ni/Al<sub>2</sub>O<sub>3</sub> interfaces. *Acta Metallurgica et Materialia*, 39(8):1915–1924, 1991.
- [245] V. Vachet, P. Desre, and E. Bonnier. Thermodynamics of the liquid systems (Fe, Al, O); (Co, Al, O); (Ni, Al, O) in the Fe, Co or Ni-Rich regions at 1600 °C. *Comptes Rendus de l'Academie des Sciences Paris*, 260(7):1943–1946, 1965.
- [246] G. Geramifard, C. Gombola, P. Franke, and H. J. Seifert. Oxidation behaviour of NiAl intermetallics with embedded Cr and Mo. *Corrosion Science*, 177:108956, 2020.
- [247] V. K. Tolpygo and D. R. Clarke. Wrinkling of  $\alpha$ -alumina films grown by thermal oxidation—I. Quantitative studies on single crystals of Fe–Cr–Al alloy. *Acta Materialia*, 46(14):5153–5166, 1998.
- [248] J. Peng, X. Fang, Z. Qu, and J. Wang. Isothermal oxidation behavior of NiAl and NiAl-(Cr,Mo) eutectic alloys. 151:27–34, 2019.

- [249] L. Cadiou and J. Paidassi. Contribution to the study of the reaction of chromium with oxygen at elevated temperatures. *Mémoires Scientifiques de la Revue de Métallurgie*, 66(3):217–225, 1969.
- [250] K. P. Lillerud and P. Kofstad. On high temperature oxidation of chromium. *Inorganic-Organic Separators*, 127(11):2397–2410, 1980.
- [251] D. Caplan and G. I. Sproule. Effect of oxide grain structure on the high-temperature oxidation of Cr. *Oxidation of Metals*, 9(5):459–472, 1975.
- [252] K. Atarashiya, R. Nagasaki, and K. Nishida. Interdiffusion in  $\text{Al}_2\text{O}_3$ - $\text{Cr}_2\text{O}_3$  quasi-binary system. *Journal of the Japan Institute of Metals*, 51:1018–1022, 1987.
- [253] R. T. Wu, R. Zhu, L. T. Wu, Y. M. Nie, R. C. Reed, K. Kawagishi, and H. Harada. Thermodynamic assessment of ternary NiCrAl alloys: From calculations to experiments. *Canadian Metallurgical Quarterly*, 50(3):291–294, 2013.
- [254] A. M. Dymshits, P. I. Dorogokupets, I. S. Sharygin, K. D. Litasov, A. Shatskiy, S. V. Rashchenko, E. Ohtani, A. Suzuki, and Y. Higo. Thermoelastic properties of chromium oxide  $\text{Cr}_2\text{O}_3$  (eskolaite) at high pressures and temperatures. *Physics and Chemistry of Minerals*, 43(6):447–458, 2016.
- [255] B. Yates, R. F. Cooper, and A. F. Pojur. Thermal expansion at elevated temperatures. II. Aluminium oxide: experimental data between 100 and 800 K and their analysis. *Journal of Physics C: Solid State Physics*, 5(10):1046–1058, 1972.
- [256] B. A. Pint, K. L. More, I. G. Wright, and P. F. Tortorelli. Characterization of thermally cycled alumina scales. *Materials at High Temperatures*, 17(1):165–171, 2000.

- [257] Hu Lei. Microstructure, mechanical properties and oxidation resistance of NiAl in-situ composites. *Dissertation, Aachen*, 2005.
- [258] C. Gombola, A. Kauffmann, G. Geramifard, M. Blankenburg, and M. Heilmaier. Microstructural investigations of novel high temperature alloys based on NiAl-(Cr,Mo). *Metals*, 10(7), 2020.
- [259] A. T. Dinsdale. SGTE data for pure elements. *Calphad*, 15(4):317–425, 1991.



# List of Figures

2.1	Scheme of CALPHAD method. . . . .	7
3.1	The spinel unit cell. . . . .	18
3.2	The NiO crystal structure. . . . .	20
4.1	Formation of an electromagnetically constrained liquid zone during containerless processing. . . . .	23
4.2	Schematic cross section view of the cylindrical mold used for producing NiAl-Cr and NiAl-Mo coarse composites. . . . .	24
4.3	Samples from arc melting procedure. a) Junction of NiAl-Cr. b) Junction of NiAl-Mo. . . . .	25
4.4	Cross section SEM image of as cast DS NiAl-34Cr with a growth rate of 120 mm/h: a) Perpendicular to the direction of fiber plane. b) Parallel to the direction of fiber plane. . . . .	25
5.1	Schematic oxidation growth kinetics vs. time. . . . .	32
6.1	Calculated phase diagram of the Ni-Al system from Peng et al.. . .	42
6.2	Calculated phase diagram of the Ni-Cr system based on work of Dupin. . . . .	44
6.3	Calculated phase diagram of the Al-Cr system based on work of Dupin. . . . .	47
6.4	Calculated phase diagram of the Ni-O system based on work of Taylor and Dinsdale. . . . .	50

6.5	Calculated phase diagram of the Cr-O system based on work of Toker et al.. . . . .	52
6.6	Calculated phase diagram of the Al-O system based on work of Hallstedt. . . . .	55
6.7	Calculated phase diagram of the Al-Mo system based on work of Peng et al.. . . . .	59
6.8	Calculated phase diagram of the Cr-Mo system from Frisk and Gustafson. . . . .	61
6.9	Calculated phase diagram of the Ni-Mo system using assessment of Zhou. et al. . . . .	65
7.1	Mo-O phase diagram adapted from work of Brewer and Lamoreaux.	72
7.2	Calculated solubility of oxygen in solid molybdenum compared with experimental data from Srivastava and Seigle. . . . .	74
7.3	Calculated Mo-O phase diagram. . . . .	75
7.4	Calculated partial Mo-O phase diagram in the range of high oxygen content. . . . .	76
7.5	Calculated site fraction of $\text{Mo}^{x+}$ in the liquid phase as a function of composition in Mo-O binary system. . . . .	77
7.5	Calculated site fraction of $\text{Mo}^{x+}$ in the liquid phase as a function of composition in Mo-O binary system. (cont.) . . . . .	78
7.6	Calculated heat capacity for solid $\text{MoO}_x$ . . . . .	80
7.7	Calculated enthalpy increment for solid $\text{MoO}_x$ . . . . .	82
7.8	Calculated entropy for solid $\text{MoO}_x$ . . . . .	84
7.9	Calculated isothermal sections in the Ni-Mo-O system. . . . .	88
7.10	Calculated isothermal sections in the Ni-Mo-O system. (cont.) . .	89
7.11	Calculated quasi-binary phase diagram for $\text{MoO}_3$ -NiO system compared with the experimental results of Yanushkevich et al. (gas phase suspended). . . . .	91

---

7.12	Calculated quasi-binary phase diagram for $\text{Al}_2\text{O}_3\text{-MoO}_3$ system compared with the experimental results from Dąbrowska et al. (gas phase suspended). . . . .	94
7.13	Calculated isothermal section for Al-Mo-O at 1000 °C. . . . .	95
7.14	Calculated section of $\text{Cr}_2\text{O}_3\text{-Mo}$ (gas phase suspended). . . . .	98
7.15	Spatial representation of compounds in $\text{Fe}_3\text{O}_4\text{-FeAl}_2\text{O}_4$ spinel system based on work from Taylor and Dinsdale. . . . .	101
7.16	Calculated inversion parameter of spinel $\text{NiAl}_2\text{O}_4$ compared with the experimental data from O'Neill et al.. . . . .	102
7.17	Calculated quasi-binary phase diagram of $\text{NiO-Al}_2\text{O}_3$ system compared to the experimental literature data. . . . .	104
7.18	Isothermal section of Ni-Al-O at 1390 °C. . . . .	105
7.19	Equilibrium between O and Al content in liquid Ni at 1600 °C compared with experimental data from Vachet et al.. . . . .	106
7.20	Scheil solidification simulation compared to equilibrium for $\text{NiO-Al}_2\text{O}_3$ section. . . . .	108
7.20	Scheil solidification simulation compared to equilibrium for $\text{NiO-Al}_2\text{O}_3$ section. (cont.) . . . . .	109
8.1	Mass gain during oxidation of NiAl-Cr, NiAl and DS NiAl-34Cr at 800 °C, 1200 °C and 1300 °C (arrows show spallation of the oxide layers). . . . .	112
8.2	SEM images of the oxidized surface of NiAl-Cr coarse composite after reaction in Ar/ 13 vol.% $\text{O}_2$ for 50 hours. The labels denote the corresponding alloy beneath the oxide layer. a) at 800 °C. b) at 1200 °C. c) at 1300 °C. . . . .	113
8.3	Square of mass gain during oxidation of NiAl-Cr, NiAl and DS NiAl-34Cr at 800 °C, 1200 °C and 1300 °C. . . . .	114
8.4	Parabolic rate constant of oxidation of NiAl and NiAl-Cr and DS NiAl-34Cr. . . . .	116

8.5	XRD pattern of the spalled oxide from the NiAl-Cr oxidized at 1300 °C in Ar/ 13 vol.% O <sub>2</sub> for 50 hours. . . . .	117
8.6	Quasi-binary phase diagram of Al <sub>2</sub> O <sub>3</sub> and Cr <sub>2</sub> O <sub>3</sub> . . . . .	118
8.7	NiAl-Cr oxidized at 1200 °C and Ar/ 13 vol.% O <sub>2</sub> for 50 hours. a) Surface image. b) Enlarged image of a: Spallation at the interface of NiAl-Cr. c) Cross section image. d) Enlarged image of c: Interface of NiAl-Cr (for the discussion of the dashed box see section 8.2.2). . . . .	119
8.8	Arrhenius diagram of oxidation of NiAl-Cr, DS NiAl-34Cr and NiAl. . . . .	122
8.9	EDX map of the region around the joint between NiAl and Cr in NiAl-Cr oxidized at 800 °C in Ar/ 13 vol.% O <sub>2</sub> for 50 hours. . . . .	123
8.10	Calculated section of NiAl-Cr. . . . .	124
8.11	Microstructure of the solidified NiAl in the vicinity of Cr rod after annealing at 800 °C for 50 hours. . . . .	125
8.12	Enlarged image of the dashed box shown in figure 8.7-d . . . . .	126
8.13	EDX map of interface of NiAl and Cr in NiAl-Cr oxidized at 1200 °C. . . . .	127
8.14	Phase image of NiAl-Cr oxidized at 1200 °C. . . . .	128
8.15	EDX map of interface of NiAl and Cr in NiAl-Cr oxidized at 1300 °C. . . . .	129
8.16	Phase image of NiAl-Cr oxidized at 1300 °C. . . . .	130
8.17	Ellingham diagram of Al <sub>2</sub> O <sub>3</sub> and Cr <sub>2</sub> O <sub>3</sub> and NiO using data from Saltykov et al. . . . .	132
8.18	Schematic view of NiAl-Cr with oxide scales. Arrows show direction of increasing Cr concentration. . . . .	133
8.19	Calculated stability diagrams as a function of oxygen partial pressure at 1300 °C. . . . .	134
8.20	Section through the system Ni-Al-Cr-O at 1300 °C. . . . .	136
8.21	Cross section of DS NiAl-Cr oxidized under Ar/13 vol.% O <sub>2</sub> for 50 hours. a) at 1200 °C. b) at 1300 °C. . . . .	139

---

8.22	Mass loss during oxidation of NiAl-Mo at 800 °C, Ar/ 13 vol.% O <sub>2</sub> .	142
8.23	NiAl-Mo oxidized at 800 °C for 50 hours. . . . .	142
8.24	XRD pattern of the residuals of oxides at the vicinity of Mo in NiAl-Mo alloy after oxidation at 800 °C for 50 hours in Ar/ 13 vol.% O <sub>2</sub> . . . . .	143
8.25	Partial pressure of MoO <sub>x</sub> vs. oxygen partial pressure at 800 °C. . .	144



# List of Tables

6.1	Crystallographic data of stable solid phases in the Ni-Al system at atmospheric pressure. . . . .	41
6.2	Crystallographic data of stable solid phases in the Ni-Cr system at atmospheric pressure. . . . .	43
6.3	Crystallographic data of stable solid phases in the Al-Cr system at atmospheric pressure. . . . .	46
6.4	Crystallographic data of stable solid phases in the Ni-O system at atmospheric pressure. . . . .	49
6.5	Crystallographic data of stable solid phases in the Cr-O system at atmospheric pressure. . . . .	51
6.6	Crystallographic data of stable solid phases in the Al-O system at atmospheric pressure. . . . .	54
6.7	Crystallographic data of stable solid phases in the Al-Mo system at atmospheric pressure. . . . .	58
6.8	Crystallographic data of stable solid phases in the Cr-Mo system at atmospheric pressure. . . . .	61
6.9	Crystallographic data of stable solid phases in the Ni-Mo system at atmospheric pressure. . . . .	64
6.10	Crystallographic data of stable solid phases in the Ni-Cr-Mo system at atmospheric pressure. . . . .	67
7.1	List of modifications made in each binary and ternary systems of Ni-Al-Cr-Mo-O. . . . .	70

7.2	Crystallographic data of stable solid phases in the Mo-O system at atmospheric pressure. . . . .	71
7.3	Calculated invariant reaction temperatures in the Mo-O binary in the present work compared with the literature data. . . . .	79
7.4	Calculated reaction temperatures in the NiO-MoO <sub>3</sub> quasi-binary system in the present work compared with the literature data. . . .	90
7.5	Calculated invariant reaction temperatures in the Ni-Mo-O system in the present work. . . . .	92
7.6	Calculated reaction temperatures in the quasi-binary Al <sub>2</sub> O <sub>3</sub> -MoO <sub>3</sub> system in the present work compared with the literature data from Dąbrowska et al. . . . .	96
7.7	Calculated invariant reaction temperatures in the Al-Mo-O system in the present work. . . . .	96
7.8	Calculated reaction temperatures in Cr <sub>2</sub> O <sub>3</sub> -Mo section in the present work compared with the literature data from Svoboda. . .	98
7.9	Calculated invariant reaction temperatures in the Cr-Mo-O system in the present work. . . . .	99
7.10	Calculated reaction temperatures in the quasi-binary NiO-Al <sub>2</sub> O <sub>3</sub> in the present work compared with the literature data. . . . .	103
8.1	Parabolic oxidation rate constants for NiAl, NiAl-Cr and DS NiAl-34Cr. . . . .	115
8.2	Parabolic oxidation rate constant $K_{p,t}$ for NiAl, NiAl-Cr and DS NiAl-34Cr and density of the oxide layers. . . . .	120
8.3	Microprobe analysis of Cr-rich region, fibers and matrix in oxidized DS NiAl-34Cr at 1300 °C after 50 hours. . . . .	141

# List of abbreviations and symbols

## Elements

<i>Al</i>	Aluminum
<i>Ar</i>	Argon
<i>Cr</i>	Chromium
<i>Cu</i>	Copper
<i>Fe</i>	Iron
<i>Mo</i>	Molybdenum
<i>Ni</i>	Nickel
<i>O</i>	Oxygen

## Units

$\mu g$	Microgram
$\mu m$	Micrometer
<i>cm</i>	Centimeter
<i>g</i>	Gram
<i>h</i>	Hour
<i>K</i>	Kelvin
<i>keV</i>	kilo-electronvolts
<i>kV</i>	Kilovolt
<i>L</i>	Liter
<i>m</i>	Meter
<i>mA</i>	Milliampere
<i>min</i>	Minute
<i>mm</i>	Millimeter

<i>mol</i>	Mole
<i>nm</i>	Nanometer
<i>s</i>	Second
<i>t</i>	Time
<i>at.%</i>	Atomic percent
<i>vol.%</i>	Volume percent
<i>wt.%</i>	Weight percent
°C	Degree Celsius

### Symbols

$\rho$	Density	$g \cdot cm^{-3}$
$A$	Area	$m^2$
$C$	Concentration	$mol/m^3$
$D$	Diffusion coefficient	$m^2/s$
$G$	Gibbs energy	
$H$	Enthalpy	
$J$	Flux	$mol/m^2 \cdot s$
$P$	Pressure	bar
$S$	Entropy	
$Z$	Atomic number	
$C_p$	Heat capacity	
$K_{p,t}$	Parabolic rate constant based on thickness of the oxide	$cm^2 \cdot s^{-1}$
$K_{p,w}$	Parabolic rate constant based on mass gain	$g^2 \cdot cm^{-4} \cdot s^{-1}$

### Abbreviations and acronyms

BSE	Back-scattered Electrons
CALPHAD	CALculation of PHAse Diagrams: Computer Coupling of Phase Diagrams and Thermochemistry
CCD	Charge-coupled device
CEF	Compound-Energy Formalism

CL	Cathodoluminescence
DS	Directionally Solidified
DSC	Differential Scanning Calorimetry
DTA	Differential Thermal Analysis
EBS	Electron Backscatter Diffraction
EDX	Energy Dispersive X-Ray Analysis
EMF	Electromotive Force
EPMA	Electron Probe Micro Analysis
IMD	Integrated Materials Development for Novel High - Temperature Alloys
rpm	Revolution per minute
SEI	Secondary Electron Imaging
SEM	Secondary Electron Microscopy
SGTE	Scientific group Thermodata Europe
TGA	Thermogravimetric Analysis
XRD	X-ray Diffraction



# Appendix

## Appendix A

Assessed parameters for the Ni-Al-Cr-Mo-O system

(in SI unites: *J*, *mol*, *K*, *Pa*)

\* Parameter assessed in this work.

<b>Mo-O</b>
<p>Ionic-Liquid: <math>(Mo^{4+}, Mo^{6+})_p (O^{2-}, Va^{\varnothing})_Q</math></p> $G_{Mo^{3+};O^{2-}} - 2H_{Mo}^{SER} - 4H_O^{SER} = +2AMoO + 35400 + 34.3T *$ $G_{Mo^{6+};O^{2-}} - 2H_{Mo}^{SER} - 6H_O^{SER} = +2MoO3\_L *$ ${}^0L_{Mo^{4+}, Mo^{6+};O^{2-}} = -63000 *$ ${}^0L_{Mo^{4+};O^{2-}, Va} = -20000 *$ <p>BCC: <math>(Mo, Va)_1 (O, Va)_3</math></p> $G_{Mo:O} - H_{Mo}^{SER} - 3H_O^{SER} = GHSERMO + 3GHSEROO - 146000 + 120T *$
<p>Functions:</p> <p>AMoO (298.15 &lt; T &lt; 3000) =  <math>-617279.692 + 462.340685T - 74.52171T \ln(T) + 0.000468436T^2 - 1.5889975E-6T^3 + 852479T^{-1}</math>  [214]</p> <p>MoO3_S (298.15 &lt; T &lt; 3000) =  <math>-770709.73 + 429.565328T - 73.51818T \ln(T) - 0.01744741T^2 - 8.33756833E-10T^3 + 393450.8T^{-1}</math>  [214]</p> <p>MoO3_L (298.15 &lt; T &lt; 3000) =  <math>-758607.95 + 773.199025T - 127T \ln(T) *</math></p> <p>GHSERMO (298.15 &lt; T &lt; 2896) =  <math>-7746.302 + 131.9197T - 23.56414T \ln(T) - 0.003443396T^2 + 5.66283E-7T^3 + 65812T^{-1}</math>  <math>-1.30927E-10T^4</math> [259]</p> <p>GHSERMO (2896 &lt; T &lt; 5000) =  <math>-30556.41 + 283.559746T - 42.63829T \ln(T) - 4.849315E+33T^{-9}</math> [259]</p> <p>GHSEROO (298.15 &lt; T &lt; 1000) =  <math>-3480.87 - 25.503038T - 11.136T \ln(T) - 0.005098888T^2 + 6.61846E-7T^3 - 38365T^{-1}</math> [259]</p> <p>GHSEROO (1000 &lt; T &lt; 3300) =  <math>-6568.763 + 12.65988T - 16.8138T \ln(T) - 5.95798E-4T^2 + 6.781E-9T^3 + 262905T^{-1}</math> [259]</p> <p>GHSEROO (3300 &lt; T &lt; 6000) =  <math>-13986.728 + 31.259625T - 18.9536T \ln(T) - 4.25243E-4T^2 + 1.0721E-8T^3 + 4383200T^{-1}</math> [259]</p>

<b>Al-Ni-O</b>
<p>Spinel: <math>(Al^{3+}, Ni^{2+}, Va)_1 (Al^{3+}, Ni^{2+}, Va)_2 (Va)_2 (O^{2-})_4</math></p> <p><math>G_{Ni^{2+}: Al^{3+}: Va: O^{2-}} - H_{Ni}^{SER} - 2H_{Al}^{SER} - 4H_O^{SER} = +NSPINEL *</math></p> <p><math>G_{Al^{3+}: Ni^{2+}: Va: O^{2-}} - H_{Al}^{SER} - 2H_{Ni}^{SER} - 4H_O^{SER} = +2ISPINEL + 23.0513T - GALAL [143]</math></p> <p><math>{}^0L_{Al^{3+}: Ni^{2+}: Va: Va: O^{2-}} = -4.08136E5 + 288.3T *</math></p> <p>Ionic-liquid: <math>(Ni^{2+}, Al^{3+})_p (O^{2-}, AlO_{1.5}, Va^Q)_Q</math></p> <p><math>{}^0L_{Ni^{2+}: Va: AlO_{1.5}} = +4E5 *</math></p>
<p>Functions:</p> <p>NSPINEL (298.15&lt;T&lt;6000) = +GBUNSEN+GCORUND+2.3288E4-9.06T *</p> <p>ISPINEL (298.15&lt;T&lt;6000) = +NSPINEL-1.91134E4 *</p> <p>GBUNSEN (298.15&lt;T&lt;1000) =  <math>-254927.2+276.208T-46.03917T\ln(T) -0.0093145T^2+1.29092E-6T^3+382916T^{-1}</math> [38]</p> <p>GBUNSEN (1000&lt;T&lt;1800) =  <math>-256835.2+340.043T-56.36068T\ln(T)+0.00254106T^2-8.11809E-7T^3+1270T^{-1}</math> [38]</p> <p>GBUNSEN (1000&lt;T&lt;2600) =  <math>-259131.4+337.305T-55.75758T\ln(T)+0.00220246T^2-7.80093E-7T^3</math> [38]</p> <p>GCORUND (298.15&lt;T&lt;600) =  <math>-1707351.3+448.021092T-67.4804T\ln(T) -0.06747T^2+1.4205433E-5T^3+938780T^{-1}</math> [36]</p> <p>GCORUND (600&lt;T&lt;1500) =  <math>-1724886.06+754.856573T-116.258T\ln(T) -0.0072257T^2+2.78532E-7T^3+2120700T^{-1}</math> [36]</p> <p>GCORUND (1500&lt;T&lt;3000) =  <math>-1772163.19+1053.4548T-156.058T\ln(T)+0.00709105T^2-6.29402E-7T^3+12366650T^{-1}</math> [36]</p> <p>GALAL (298.15&lt;T&lt;6000) = +1.5G2AV-0.5G22V+A [238]</p> <p>G2AV (298.15&lt;T&lt;6000) = +7 F [136]</p> <p>G22V (298.15&lt;T&lt;6000) = +7G+B [136]</p> <p>A (298.15&lt;T&lt;6000) = +31300 [239]</p> <p>G (298.15&lt;T&lt;6000) = <math>-161731+144.873T-24.9879T\ln(T) -0.0011952256T^2+206520T^{-1}</math> [237]</p> <p>B (298.15&lt;T&lt;6000) = +46826-27.266T [237]</p> <p>F (360&lt;T&lt;6000) =  <math>-291278.9 + 138.0033T - 21.9429T\ln(T) - 0.002905T^2 + 258064.3T^{-1} - 1.7385E-7T^3</math> [240]</p>

<b>Ni-Mo-O</b>
$\alpha$ -NiMoO <sub>4</sub> : (Ni) <sub>1</sub> (Mo) <sub>1</sub> (O) <sub>4</sub> $G_{Ni:Mo:O} - H_{Ni}^{SER} - H_{Mo}^{SER} - 4H_O^{SER} =$ GHSERNI+GHSERMO+4GHSEROO+ GANIMOO4
$\beta$ -NiMoO <sub>4</sub> : (Al) <sub>1</sub> (Mo) <sub>1</sub> (O) <sub>4</sub> $G_{Ni:Mo:O} - H_{Ni}^{SER} - H_{Mo}^{SER} - 4H_O^{SER} =$ GHSERNI+GHSERMO+4GHSEROO+ GBNIMOO4
Ni <sub>2</sub> Mo <sub>3</sub> O <sub>8</sub> : (Ni) <sub>2</sub> (Mo) <sub>3</sub> (O) <sub>8</sub> $G_{Ni:Mo:O} - 2H_{Ni}^{SER} - 3H_{Mo}^{SER} - 8H_O^{SER} =$ 2GHSERNI+3GHSERMO+8GHSEROO - 1.263E6+741T - 1026077.52 *
Ionic-liquid: (Mo <sup>6+</sup> , Ni <sup>2+</sup> ) <sub>p</sub> (O <sup>2-</sup> , Va <sup>Q</sup> ) <sub>Q</sub> ${}^0L_{Mo^{+6}, Ni^{+2}, O^{2-}} = -2.36E4 *$ ${}^1L_{Mo^{+6}, Ni^{+2}, O^{2-}} = -1.2E5 *$
Functions: GANIMOO4 (800<T<1000) = -1052000+371.2T [220] GBNIMOO4 (1000<T<1380) = -993000+311.3T [220]

<b>Al-Mo-O</b>
Al <sub>2</sub> Mo <sub>3</sub> O <sub>12</sub> : (Al) <sub>2</sub> (Mo) <sub>3</sub> (O) <sub>12</sub> $G_{Al:Mo:O} - 2H_{Al}^{SER} - 3H_{Mo}^{SER} - 12H_O^{SER} = 2GHSERAL+3GHSERMO+12GHSEROO - 3860000$ +917T *
Ionic-liquid: (Mo <sup>6+</sup> ) <sub>p</sub> (O <sup>2-</sup> , Al <sub>1.5</sub> , Va <sup>Q</sup> ) <sub>Q</sub> ${}^0L_{Mo^{+6}, AlO_{3/2}, O^{2-}} = -226000 *$ ${}^1L_{Mo^{+6}, AlO_{3/2}, O^{2-}} = -207000 *$
Functions: GHSERAL (298.15<T<700) = -7976.15+137.093038T - 24.3671976Tln(T)0.001884662T <sup>2</sup> - 8.77664E-7T <sup>3</sup> +74092T <sup>-1</sup> [259] GHSERAL (700<T<933.6) = -11276.24+223.048446T - 38.5844296Tln(T)+0.018531982T <sup>2</sup> - 5.764227E-6T <sup>3</sup> +74092T <sup>-1</sup> [259] GHSERAL (933.6<T<2900) = -11278.378+188.684153T - 31.748192Tln(T) - 1.231E+28T <sup>-9</sup> [259]

<b>Cr-Mo-O</b>
Ionic-Liquid : $(Cr^{3+}, Mo^{4+})_P(O^{2-}, Va^{2-})_Q$
${}^0L_{Cr^{3+}, Mo^{4+}; O^{2-}} = -195000 *$
${}^0L_{Cr^{3+}, Mo^{4+}; O^{2-}, Va} = -7E4 *$

## Appendix B

An example of a POP file used in Thermo-Calc software in order to optimize the liquid phase parameters in Mo-O binary system is shown in this section.

In each part, the equilibrium conditions are defined and the experimental data from literature are given. After computing the equilibrium, the calculated values are compared with the experimental ones. Using the PARROT module in Thermo-Calc, the parameters are optimized to minimize the deviation of the calculated data from the available experimental value.

As an example, in the first section, all phases are suspended except for the liquid and gas phases and each of the available phases have the amount of 0.5 mole. The amount of MoO<sub>2</sub> is fixed to zero. The pressure, mole fraction and total amount of phases are defined. Therefore, equilibrium could be computed since the degree of freedom is zero. The calculated equilibrium temperature is compared with the experimental value of 2573 K. Next, the parameters are optimized using the PARROT module.

\$ ionic liquid in Mo-O

\$ p: L+G=MoO2

CREATE\_NEW\_EQ 1,1

CHANGE\_STATUS PHASE \*=SUS

CHANGE\_STATUS PHASE IONIC\_LIQ,GAS=ENTER 0.5

CHANGE\_STATUS PHASE MO1O2=FIX 0

SET\_CONDITION P=1E5 N=1 X(O)=0.6

EXPERIMENT T=2573:1

---

\$ e: L=bcc+MoO2  
CREATE\_NEW\_EQ 2,1  
CHANGE\_STATUS PHASE \*=SUS  
CHANGE\_STATUS PHASE BCC\_A2,MO1O2=ENTER 0.5  
CHANGE\_STATUS PHASE IONIC\_LIQ=FIX 0  
SET\_CONDITION P=1E5 N=1 X(O)=0.2  
EXPERIMENT T=2423:1

\$ p: MoO2+G=L  
CREATE\_NEW\_EQ 3,1  
CHANGE\_STATUS PHASE \*=SUS  
CHANGE\_STATUS PHASE GAS,MO1O2=ENTER 0.5  
CHANGE\_STATUS PHASE IONIC\_LIQ=FIX 0  
SET\_CONDITION P=1E5 N=1 X(O)=0.7  
EXPERIMENT T=1573:1

\$ p: MoO2+L=Mo4O11  
CREATE\_NEW\_EQ 4,1  
CHANGE\_STATUS PHASE \*=SUS  
CHANGE\_STATUS PHASE IONIC\_LIQ,MO1O2=ENTER 0.5  
CHANGE\_STATUS PHASE MO4O11=FIX 0  
SET\_CONDITION P=1E5 N=1 X(O)=0.7  
EXPERIMENT T=1091:1 X(IONIC\_LIQ,O)=0.74:0.0004

```
$ d: MoO3=L(+G)
CREATE_NEW_EQ 5,1
ENTER_SYMBOL VAR HMLT=HM(IONIC_LIQ)-HM(MO1O3);
CHANGE_STATUS PHASE *=SUS
CHANGE_STATUS PHASE IONIC_LIQ,GAS=ENTER 0.5
CHANGE_STATUS PHASE MO1O3=FIX 0
SET_CONDITION P=1E5 N=1 X(O)=0.8
EXPERIMENT T=1083:1 X(IONIC_LIQ,O)=0.75:1E-4 HMLT=12100:500
```

```
$ prevent the ionic-liquid becoming stable where it should not be
CREATE_NEW_EQ 6,1
CHANGE_STATUS PHASE BCC_A2,MO1O2,IONIC_LIQ=ENTER 0.5
SET_CONDITION P=1E5 N=1 X(O)=0.2 T=500
EXPERIMENT DGM(IONIC_LIQ)<-0.1:0.1
```

```
CREATE_NEW_EQ 7,1
CHANGE_STATUS PHASE BCC_A2,MO1O2,IONIC_LIQ=ENTER 0.5
SET_CONDITION P=1E5 N=1 X(O)=0.2 T=100
EXPERIMENT DGM(IONIC_LIQ)<-0.1:0.1
```

```
SAVE
END
```

TABLE\_HEAD 6

CREATE\_NEW\_EQ @@,1

CHANGE\_STATUS PHASE BCC\_A2,MO1O2,IONIC\_LIQ=ENTER 0.5

SET\_CONDITION P=1E5 N=1 X(O)=0.2 T=@1

EXPERIMENT DGM(IONIC\_LIQ)<-0.1:0.1

TABLE\_VALUES

200

500

TABLE\_END

## Appendix C

An example of a POP file used in Thermo-Calc software in order to optimize the solubility of oxygen in Mo.

\$ fit oxygen solubility in Mo

ENTER\_SYMBOL CONSTANT P0=100000

TABLE\_HEAD 1

CREATE\_NEW\_EQ @@,1

ENTER\_SYMBOL VAR LNWO=LOG(W(BCC\_A2,O))+13.81551055;

CHANGE\_STATUS PHASE \*=SUS

CHANGE\_STATUS PHASE BCC\_A2=ENTER 1

CHANGE\_STATUS PHASE MO1O2=FIX 0

SET\_CONDITION P=P0 N=1 T=@ 1

EXPERIMENT LNWO=@2:0.1

TABLE\_VALUES

\$ T/K LNWO

1673 1.098

1683 1.386

1841 2.639

1846 2.708

1846 2.639

1847 2.639

1847 2.674

1898 2.770

1915 3.044

1984 3.871

1986 3.970

1986 3.807  
1987 3.970  
1988 3.807  
1989 4.158  
2020 4.304  
2028 4.304  
2030 4.357  
2061 4.543  
2063 4.431  
2065 4.189  
2067 4.248  
2069 4.407  
2108 4.880  
2108 4.780  
2108 4.852  
2108 4.390  
2108 4.263  
2108 4.344  
2137 4.635  
2138 4.530  
2141 4.595  
2186 4.820  
2188 4.934  
TABLE\_END

SAVE  
END



\$database for Ni-Al-Cr-Mo-O

ELEMENT /-	ELECTRON_GAS	.0000E+00	.0000E+00
.0000E+00!			
ELEMENT VA	VACUUM	.0000E+00	.0000E+00
.0000E+00!			
ELEMENT AL	FCC_A1	2.6982E+01	4.5773E+03
2.8322E+01!			
ELEMENT CR	BCC_A2	5.1996E+01	4.0500E+03
2.3560E+01!			
ELEMENT NI	FCC_A1	5.8690E+01	4.7870E+03
2.9796E+01!			
ELEMENT O	1/2_MOLE_O2 (G)	1.5999E+01	4.3410E+03
1.0252E+02!			
ELEMENT MO	BCC_A2	9.5940E+01	4.5890E+03
2.8560E+01!			
ELEMENT AR	1_MOLE_AR1 (G)	3.9948E+01	0.0000E+00
3.6982E+01!			
SPECIES AL2	AL2!		
SPECIES AL+3	AL1/+3!		
SPECIES ALO3/2	AL1O1.5!		
SPECIES AL1O1	AL1O1!		
SPECIES AL1O2	AL1O2!		
SPECIES AL2O1	AL2O1!		
SPECIES AL2O2	AL2O2!		
SPECIES AL2O3	AL2O3!		
SPECIES CR2	CR2!		
SPECIES CR+2	CR1/+2!		
SPECIES CR+6	CR1/+6!		
SPECIES CR+3	CR1/+3!		
SPECIES CR1O1	CR1O1!		
SPECIES CR1O2	CR1O2!		
SPECIES CR1O3	CR1O3!		
SPECIES CR2O1	CR2O1!		
SPECIES CR2O2	CR2O2!		
SPECIES CR2O3	CR2O3!		
SPECIES CR5O12	CR5O12!		
SPECIES CR8O21	CR8O21!		
SPECIES NI2	NI2!		
SPECIES NI+2	NI1/+2!		
SPECIES NI+3	NI1/+3!		
SPECIES NI1O1	NI1O1!		
SPECIES O-2	O1/-2!		
SPECIES O2	O2!		
SPECIES O3	O3!		
SPECIES MO+4	MO1/+4!		
SPECIES MO+6	MO1/+6!		
Species MO1O1	MO1O1!		
Species MO1O2	MO1O2!		
Species MO1O2.75	MO1O2.75!		
Species MO1O2.875	MO1O2.875!		
Species MO1O2.889	MO1O2.889!		
Species MO1O3	MO1O3!		
Species MO2	MO2!		
Species MO2O6	MO2O6!		
Species MO3O9	MO3O9!		

The thermodynamic dataset of Ni-Al-Cr-Mo-O

---

```

Species MO4O12                      MO4O12!
Species MO5O15                      MO5O15!

FUNCTION UNASS      298.15  0;,,N !

TYPE_DEFINITION % SEQ *!
DEFINE_SYSTEM_DEFAULT ELEMENT 2 !
DEFAULT_COMMAND DEF_SYS_ELEMENT VA /- !

DATABASE_INFO '''
BASE TC-Ni, version 29-09-99'

,
ELEMENTS : Al, Cr, Ni, Mo'
,
ASSESSED SYSTEMS : '
,
BINARIES'
    Al-Cr, Al-Ni, Cr-Ni'
TERNARIES'
    Al-Cr-Ni'
,
MODELLING ORDER/DISORDER: '
,
Al and L12 phases are modelled with a single Gibbs energy curve.'
They are FCC_L12#1 (Al) based on (Ni) and FCC_L12#2 (L12) based on '
Ni3Al, differing by their site occupation.'
The same type of relation exists for the A2 and B2 phases. There are '
several possible sets for the phase named BCC_B2. They are either '
disordered (A2) and correspond to the solid solution based on Cr, '
or ordered based on the B2 compound AlNi.'
!

ASSESSED SYSTEMS
AL-CR(;G5 MAJ:BCC_B2/CR:CR:VA ;P3 STP:.75/1200/1)
AL-NI(;P3 STP:.75/1200/1)
CR-NI(;G5 MAJ:BCC_B2/CR:CR:VA C_S:BCC_B2/NI:NI:VA
;P3 STP:.5/1200/2)
AL-CR-NI(;G5 MAJ:BCC_B2/CR:CR:VA C_S:BCC_B2/AL:NI:VA
;P3 STP:.01/.8/2)
!

PHASE GAS:G % 1 1.0 !
CONST GAS:G :AL,AL2,AL1O1,AL1O2,AL2O1,AL2O2,AL2O3,
CR,CR2,NI,NI2,O2%,O,O3,CR1O1,CR1O2,CR1O3,
CR2O1,CR2O2,CR2O3,NI1O1,MO,MO1O1,MO1O2,MO1O3,
MO2,MO2O6,MO3O9,MO4O12,MO5O15,AR : !

PHASE IONIC_LIQ:Y % 2 1 1 !
CONST IONIC_LIQ:Y :AL+3,CR+3,NI+2,MO+4,MO+6: O-2,VA,ALO3/2,O: !

PHASE FCC_A1 %A 2 1 1 !
CONST FCC_A1 :AL,CR,MO,NI%,O : VA% : !

PHASE BCC_A2 %B 2 1 3 !

```

```

CONST BCC_A2 :AL,CR%,NI,MO,VA : VA,O : !
PHASE BCC_B2 %BCW 3 .5 .5 3 !
CONST BCC_B2 :AL,CR,MO,NI%,VA : AL%,CR,MO,NI,VA : VA,O : !
PHASE FCC_L12 %ADG 3 .75 .25 1 !
CONST FCC_L12 :AL,CR,MO,NI,O : AL,CR,MO,NI,O : VA : !

PHASE CUB_A15 % 2 .75 .25 !
CONSTITUENT CUB_A15 :AL,MO : AL,MO : !

PHASE ALCRO:I %KZ 3 2 1 3 !
CONSTITUENT ALCRO:I :AL+3,CR+2,CR+3% : CR+3,NI+2,VA% : O-2% : !

PHASE CR3O4 % 2 3 4 !
CONSTITUENT CR3O4 :CR : O : !

PHASE ALPHA_NIMOO4 % 3 1 1 4 !
CONSTITUENT ALPHA_NIMOO4 :NI:MO : O : !

PHASE BETA_NIMOO4 % 3 1 1 4 !
CONSTITUENT BETA_NIMOO4 :NI:MO : O : !

PHASE NI2MO3O8 % 3 2 3 8 !
CONSTITUENT NI2MO3O8 :NI:MO : O : !

PHASE AL2MO3O12 % 3 2 3 12 !
CONSTITUENT AL2MO3O12 :AL: MO: O : !

PHASE HALITE:I %+ 2 1 1 !
CONSTITUENT HALITE:I :CR+3,AL+3,NI+2,NI+3,VA : O-2 : !

PHASE HCP_A3 %\ 2 1 .5 !
CONSTITUENT HCP_A3 :AL,MO : VA : !

PHASE AL2O3_DELTA % 1 1.0 !
CONSTITUENT AL2O3_DELTA :AL2O3 : !

PHASE AL2O3_GAMMA % 1 1.0 !
CONSTITUENT AL2O3_GAMMA :AL2O3 : !

PHASE AL2O3_KAPPA % 1 1.0 !
CONSTITUENT AL2O3_KAPPA :AL2O3 : !

TYPE_DEFINITION \ GES A_P_D HCP_A3 MAGNETIC -3.0 2.80000E-01 !
TYPE_DEFINITION + GES A_P_D HALITE MAGNETIC -3.0 2.80000E-01 !
TYPE_DEFINITION K GES A_P_D ALCRO MAGNETIC -3.0 2.80000E-01 !

```

The thermodynamic dataset of Ni-Al-Cr-Mo-O

---

```

TYPE_DEFINITION A GES A_P_D @ MAGNETIC -3.0 .28 !
TYPE_DEFINITION B GES A_P_D @ MAGNETIC -1.0 .40 !
TYPE_DEFINITION - GES A_P_D SPINEL MAGNETIC -3.0 2.80000E-01 !

TYPE_DEFINITION C GES A_P_D BCC_B2 DIS_PART BCC_A2 !
TYPE_DEFINITION D GES A_P_D FCC_L12 DIS_PART FCC_A1 !

TYPE_DEFINITION G IF (AL AND NI) THEN
    GES A_P_D FCC_L12 C_S 2 NI:AL:VA !

TYPE_DEFINITION G IF (NI) THEN
    GES A_P_D FCC_L12 MAJ 1 NI:NI:VA !

TYPE_DEFINITION W IF (CR AND AL AND NI) THEN
    GES A_P_D BCC_B2 C_S,, NI:AL:VA !

TYPE_DEFINITION W IF (CR) THEN
    GES A_P_D BCC_B2 MAJ 1 CR:CR:VA !
TYPE_DEFINITION Z GES A_P_D ALCRO C_S 2 AL+3:VA:O-2 !

FUNCTION ZERO 298.15 0;,,N !
FUNCTION DP 298.15 +P-101325;,,N !
FUNCTION TROIS 298.15 3;,,N !
FUNCTION UNTIER 298.15 TROIS**(-1);,,N !

PARAMETER G(GAS,AR;0) 298.15 +R#*T*LN(1E-05*P);
6000 N !
$*****
$
$ UNARY
PARAMETERS
$
$-----
$
$
$ Al
$
$
FUNCTIONS
$
FUNCTION F154T 298.15
+323947.58-25.1480943*T-20.859*T*LN(T)
+4.5665E-05*T**2-3.942E-09*T**3-24275.5*T**(-1);
4300.0 Y
+342017.233-54.0526109*T-17.7891*T*LN(T)+6.822E-05*T**2
-1.91111667E-08*T**3-14782200*T**(-1);
8200.0 Y
+542396.07-411.214335*T+22.2419*T*LN(T)-.00349619*T**2
+4.0491E-08*T**3-2.0366965E+08*T**(-1); 1.00000E+04 N !
$
FUNCTION F625T 298.15
+496408.232+35.479739*T-41.6397*T*LN(T)

```

```

+ .00249636*T**2-4.90507333E-07*T**3+85390.3*T**(-1);
      900.00 Y
+497613.221+17.368131*T-38.85476*T*LN(T)-2.249805E-04*T**2
-9.49003167E-09*T**3-5287.23*T**(-1); 2.80000E+03 N !
$
FUNCTION GHSERAL 298.15
-7976.15+137.093038*T-24.3671976*T*LN(T)
-.001884662*T**2-8.77664E-07*T**3+74092*T**(-1);
      700.00 Y
-11276.24+223.048446*T-38.5844296*T*LN(T)
+.018531982*T**2-5.764227E-06*T**3+74092*T**(-1);
      933.60 Y
-11278.378+188.684153*T-31.748192*T*LN(T)
-1.231E+28*T**(-9); 2.90000E+03 N !
$
-1.231E+28*T**(-9);,, N !
$
FUNCTION GHCPAL 298.15 +5481-1.8*T+GHSERAL;,, N !
$
FUNCTION GBCCAL 298.15 +10083-4.813*T+GHSERAL;,, N !
$
FUNCTION GLIQAL 298.14
+11005.029-11.841867*T+7.934E-20*T**7+GHSERAL;
      933.59 Y
+10482.282-11.253974*T+1.231E+28*T**(-9)+GHSERAL;,, N !
$
$
GAS PHASE
$
PARAMETER G(GAS,AL;0) 298.15 +F154T+R*T*LN(1E-05*P);,,N REF184 !
PARAMETER G(GAS,AL2;0) 298.15 +F625T+R*T*LN(1E-05*P);,,N REF448 !
$
$
LIQUID PHASE
$
FUNCTION GLIQAL 2.98000E+02
+11005.029-11.841867*T+7.934E-20*T**7
+GHSERAL#; 9.33590E+02 Y
+10482.282-11.253974*T+1.231E+28*T**(-9)+GHSERAL#;
6.00000E+03 N !
PARAMETER G(IONIC_LIQ,AL+3:VA;0) 2.98000E+02 +GLIQAL#;
2.90000E+03 N
91DIN !
$
$
FCC_A1 PHASE
$
PARAMETER G(FCC_A1,AL:VA;0) 298.15 +GHSERAL;,,N 91DIN !
$
$
BCC_A2 PHASE
$
PARAMETER G(BCC_A2,AL:VA;0) 298.15 +GBCCAL;,,N 91DIN !
PARAMETER G(BCC_A2,VA:VA;0) 298.15 +0.2*R*T;,,N 15Fra !
$ the following function had to be amended in order to compensate
the effect
$ of the vacancy parameter on the invariant B2+L=Al3Ni2 and the

```

The thermodynamic dataset of Ni-Al-Cr-Mo-O

---

```

phase diagram
$ P.F., KIT 2015
$ FUNCTION B2ALVA 295.15 10000-T;,,N !
  FUNCTION B2ALVA 295.15 10000-T-0.2*R*T;,,N !
  FUNC LB2ALVA 298.15 150000;,,N !
  PARAMETER L(BCC_A2,AL,VA:VA;0) 298.15 B2ALVA+LB2ALVA;,,N 99DUP !
$
$
BCC_B2 PHASE
$
  PARAMETER G(BCC_B2,AL:VA:VA;0) 298.15 .5*B2ALVA-.5*LB2ALVA;,,N
  99DUP !
  PARAMETER G(BCC_B2,VA:AL:VA;0) 298.15 .5*B2ALVA-.5*LB2ALVA;,,N
  99DUP !
$
HCP_A3 PHASE
  PARAMETER G(HCP_A3,AL:VA;0) 298.15 +5481-1.8*T+GHSERAL; 6000 N
  10Cup !
$
CUB_A15 PHASE
  PARAMETER G(CUB_A15,AL:AL;0) 298.15 +10000+GHSERAL; 6000 N
  10Cup !
$
$-----
$-----
$
$ Cr
$
$
FUNCTIONS
$
FUNCTION F7454T 298.15
+390765.331-31.5192154*T-21.36083*T*LN(T)
+7.253215E-04*T**2-1.588679E-07*T**3+10285.15*T**(-1);
1100.0 Y
+393886.928-44.107465*T-19.96003*T*LN(T)+.001513089*T**2
-4.23648333E-07*T**3-722515*T**(-1);
2000.0 Y
+421372.003-231.888524*T+5.362886*T*LN(T)-.00848877*T**2
+2.984635E-07*T**3-6015405*T**(-1);
3300.0 Y
+305164.698+251.019831*T-55.20304*T*LN(T)+.005324585*T**2
-2.850405E-07*T**3+34951485*T**(-1);
5100.0 Y
+1069921.1-1708.93262*T+175.0508*T*LN(T)-.025574185*T**2
+4.94447E-07*T**3-4.4276355E+08*T**(-1);
7600.0 Y
-871952.838+1686.47356*T-204.5589*T*LN(T)+.007475225*T**2
-4.618745E-08*T**3+1.423504E+09*T**(-1); 1.00000E+04 N !
$
FUNCTION F7735T 298.15 +598511.402+41.5353219*T-40.56798*T*LN(T)
+.004961847*T**2-1.61216717E-06*T**3+154422.85*T**(-1);
800.00 Y
+613345.232-104.20799*T-19.7643*T*LN(T)-.007085085*T**2
-4.69883E-07*T**3-1738066.5*T**(-1);

```

```

1400.0 Y
+642608.843-369.286259*T+17.64743*T*LN(T)-.02767321*T**2
+1.605906E-06*T**3-5831655*T**(-1);
2300.0 Y
+553119.895+159.188556*T-52.07969*T*LN(T)-.004229401*T**2
+1.5939925E-07*T**3+14793625*T**(-1);
3900.0 Y
+347492.339+623.137624*T-105.0428*T*LN(T)+3.9699545E-04*T**2
+1.51783483E-07*T**3+1.4843765E+08*T**(-1);
5800.0 Y
-484185.055+2598.25559*T-334.7145*T*LN(T)+.028597625*T**2
-4.97520167E-07*T**3+7.135805E+08*T**(-1); 6.00000E+03 N !
$
FUNCTION GHSERCR 298.14
-8856.94+157.48*T-26.908*T*LN(T)
+.00189435*T**2-1.47721E-06*T**3+139250*T**(-1);
2180.0 Y
-34869.344+344.18*T-50*T*LN(T)-2.88526E+32*T**(-9);,,N !
$
-23782.344+344.18*T-50*T*LN(T)-2.88526E+32*T**(-9);,,N !
$
FUNCTION GCRLIQ 298.15
+24339.955-11.420225*T+2.37615E-21*T**7+GHSERCR;
2180.0 Y
-16459.984+335.616316*T-50*T*LN(T);,,N !
$ replaced by 08Kje
$ FUNCTION GCRLIQ 298.15 +15483.015+146.059775*T-26.908*T*LN(T)
$
+1.89435E-3*T**2-1.47721E-6*T**3+139250*T**(-1)+237.615E-23*T**7;
2180.0 Y
$ -16459.984+335.616316*T-50*T*LN(T); 6000.0 N 91Din !
$
FUNCTION GFCCCR 298.15 +7284+.163*T+GHSERCR;,,N !
$
FUNCTION GHPCPC 298.15 +4438+GHSERCR;,,N !
$
FUNCTION ACRBCC 298.15 +1.7E-05*T+9.2E-09*T**2;,,N !
FUNCTION BCRBCC 298.15 +1+2.6E-11*P;,,N !
FUNCTION CCRBCC 298.15 2.08E-11;,,N !
FUNCTION DCRBCC 298.15 +1*LN(BCRBCC);,,N !
FUNCTION VCRBCC 298.15 +7.188E-06*EXP(ACRBCC);,,N !
FUNCTION ECRBCC 298.15 +1*LN(CCRBCC);,,N !
FUNCTION XCRBCC 298.15 +1*EXP(.8*DCRBCC)-1;,,N !
FUNCTION YCRBCC 298.15 +VCRBCC*EXP(-ECRBCC);,,N !
FUNCTION ZCRBCC 298.15 +1*LN(XCRBCC);,,N !
FUNCTION GPCRBCC 298.15 +YCRBCC*EXP(ZCRBCC);,,N !
$
FUNCTION ACRLIQ 298.15 +1.7E-05*T+9.2E-09*T**2;,,N !
FUNCTION BCRLIQ 298.15 +1+4.65E-11*P;,,N !
FUNCTION CCRLIQ 298.15 3.72E-11;,,N !
FUNCTION DCRLIQ 298.15 +1*LN(BCRLIQ);,,N !
FUNCTION VCRLIQ 298.15 +7.653E-06*EXP(ACRLIQ);,,N !
FUNCTION ECRLIQ 298.15 +1*LN(CCRLIQ);,,N !
FUNCTION XCRLIQ 298.15 +1*EXP(.8*DCRLIQ)-1;,,N !
FUNCTION YCRLIQ 298.15 +VCRLIQ*EXP(-ECRLIQ);,,N !
FUNCTION ZCRLIQ 298.15 +1*LN(XCRLIQ);,,N !
FUNCTION GPCRLIQ 298.15 +YCRLIQ*EXP(ZCRLIQ);,,N !
$

```

The thermodynamic dataset of Ni-Al-Cr-Mo-O

```

$
GAS PHASE
$
FUNCTION F7491T      298.15 +390765.331-31.5192158*T-21.36083*T*LN(T)
+7.253215E-04*T**2-1.588679E-07*T**3+10285.15*T**(-1); 1100 Y
+393886.928-44.1074654*T-19.96003*T*LN(T)+.001513089*T**2
-4.23648333E-07*T**3-722515*T**(-1); 2000 Y
+421372.003-231.888524*T+5.362886*T*LN(T)-.00848877*T**2
+2.984635E-07*T**3-6015405*T**(-1); 3300 Y
+305164.699+251.019831*T-55.20304*T*LN(T)+.005324585*T**2
-2.850405E-07*T**3+34951485*T**(-1); 5100 Y
+1069921.1-1708.93263*T+175.0508*T*LN(T)-.025574185*T**2
+4.94447E-07*T**3-4.427635E+08*T**(-1); 7600 Y
-871952.837+1686.47356*T-204.5589*T*LN(T)+.007475225*T**2
-4.618745E-08*T**3+1.423504E+09*T**(-1); 10000 N !

FUNCTION F7763T      298.15 +598511.403+41.5353212*T-40.56798*T*LN(T)
+.004961847*T**2-1.61216717E-06*T**3+154422.85*T**(-1); 800 Y
+613345.232-104.207991*T-19.7643*T*LN(T)-.007085085*T**2
-4.69883E-07*T**3-1738066.5*T**(-1); 1400 Y
+642608.843-369.28626*T+17.64743*T*LN(T)-.02767321*T**2
+1.605906E-06*T**3-5831655*T**(-1); 2300 Y
+553119.895+159.188555*T-52.07969*T*LN(T)-.004229401*T**2
+1.5939925E-07*T**3+14793625*T**(-1); 3900 Y
+347492.34+623.137623*T-105.0428*T*LN(T)+3.9699545E-04*T**2
+1.51783483E-07*T**3+1.4843765E+08*T**(-1); 5800 Y
-484185.055+2598.25559*T-334.7145*T*LN(T)+.028597625*T**2
-4.97520167E-07*T**3+7.135805E+08*T**(-1); 6000 N !

$ PARAMETER G(GAS,CR;0) 298.15 +F7454T+R*T*LN(1E-05*P);,, N REF4465
!
PARAMETER G(GAS,CR;0) 298.15 +F7491T+RTLNP; 6000 N 00SUB !
$ PARAMETER G(GAS,CR2;0) 298.15 +F7735T+R*T*LN(1E-05*P);,, N
REF4591 !
PARAMETER G(GAS,CR2;0) 298.15 +F7763T+RTLNP; 6000 N 00SUB !
$
$
LIQUID PHASE
$
PARAMETER G(IONIC LIQ,CR+3:VA;0) 2.98150E+02 +GCRLIQ#;
6.00000E+03 N 91DIN !
$
$
FCC_A1 PHASE
$
PARAMETER G(FCC_A1,CR:VA;0) 298.15 +GFCCCR+GPCRBCC;,,N 89DIN !
PARAMETER TC(FCC_A1,CR:VA;0) 298.15 -1109;,,N 89DIN !
PARAMETER BMAGN(FCC_A1,CR:VA;0) 298.15 -2.46;,,N 89DIN !
$
$
BCC_A2 PHASE
$
$
PARAMETER G(BCC_A2,CR:VA;0) 298.15 +GHSERCR+GPCRBCC;,,N 91DIN !
PARAMETER G(BCC_A2,CR:VA;0) 298.15 +GHSERCR;,,N 91DIN !
PARAMETER TC(BCC_A2,CR:VA;0) 298.15 -311.5;,,N 89DIN !
PARAMETER BMAGN(BCC_A2,CR:VA;0) 298.15 -.008;,,N 89DIN !
$ following parameter amended in order to compensate the vacancy

```

```

contribution
$ P.F., KIT 2015
$ PARAMETER L(BCC_A2,CR,VA:VA;0) 298.15 100000;,,N 01DUP !
PARAMETER L(BCC_A2,CR,VA:VA;0) 298.15 100000-0.2*R*T;,,N 15Fra !
$
$
BCC_B2 PHASE
$
PARAMETER G(BCC_B2,CR:VA:VA;0) 298.15 0;,,N 01DUP !
PARAMETER G(BCC_B2,VA:CR:VA;0) 298.15 0;,,N 01DUP !

$
$-----
-----
$
$
Ni
$
$
FUNCTIONS
$
FUNCTION F13191T 298.15
+417658.868-44.7777921*T-20.056*T*LN(T)
-.0060415*T**2+1.24774E-06*T**3-16320*T**(-1);
800.00 Y
+413885.448+9.41787679*T-28.332*T*LN(T)+.00173115*T**2
-8.399E-08*T**3+289050*T**(-1);
3900.0 Y
+440866.732-62.5810038*T-19.819*T*LN(T)+5.067E-04*T**2
-4.93233333E-08*T**3-15879735*T**(-1);
7600.0 Y
+848806.287-813.398164*T+64.69*T*LN(T)-.00731865*T**2
+8.71833333E-08*T**3-3.875846E+08*T**(-1); 10000. N !
$
FUNCTION F13265T 298.15
+638073.279-68.1901928*T-24.897*T*LN(T)
-.0313584*T**2+5.93355333E-06*T**3-14215*T**(-1);
800.00 Y
+611401.772+268.084821*T-75.25401*T*LN(T)+.01088525*T**2
-7.08741667E-07*T**3+2633835*T**(-1);
2100.0 Y
+637459.339+72.0712678*T-48.587*T*LN(T)-9.09E-05*T**2
+9.12933333E-08*T**3-1191755*T**(-1);
4500.0 Y
+564540.781+329.599011*T-80.11301*T*LN(T)+.00578085*T**2
-1.08841667E-07*T**3+29137900*T**(-1); 6000.0 N !
$
FUNCTION GHSERNI 298.14
-5179.159+117.854*T-22.096*T*LN(T)
-.0048407*T**2;
1728.0 Y
-27840.655+279.135*T-43.1*T*LN(T)+1.12754E+31*T**(-9);,, N !
$
FUNCTION GHCPNI 298.15 +1046+1.2552*T+GHSERNI;,,N !
$
FUNCTION GBCCNI 298.15 +8715.084-3.556*T+GHSERNI;,,, N !
$

```

The thermodynamic dataset of Ni-Al-Cr-Mo-O

---

```

$
GAS PHASE
$
PARAMETER G(GAS,NI;0) 298.15 +F13191T+R*T*LN(1E-05*P);,,N REF7504 !
PARAMETER G(GAS,NI2;0) 298.15 +F13265T+R*T*LN(1E-05*P);,,N REF7553 !
$
LIQUID PHASE
$
FUNCTION GLIQNI 2.98000E+02 +16414.686-9.397*T+GHSERNI#
-3.82318E-21*T**7; 1.72800E+03 Y
+18290.88-10.537*T+GHSERNI#-1.12754E+31*T**(-9); 3.00000E+03
N !

PARAMETER G(IONIC_LIQ,NI+2:VA;0) 2.98150E+02 +GLIQNI#;
6.00000E+03
N 91DIN !
$
$
FCC_A1 PHASE
$
PARAMETER G(FCC_A1,NI:VA;0) 298.15 +GHSERNI;,,N 91DIN !
PARAMETER TC(FCC_A1,NI:VA;0) 298.15 633;,,N 89DIN !
PARAMETER BMAGN(FCC_A1,NI:VA;0) 298.15 .52;,,N 89DIN !
$
$
BCC_A2 PHASE
$
PARAMETER G(BCC_A2,NI:VA;0) 298.15 +GBCCNI;,,N 91DIN !
PARAMETER TC(BCC_A2,NI:VA;0) 298.15 575;,,N 89DIN !
PARAMETER BMAGN(BCC_A2,NI:VA;0) 298.15 .85;,,N 89DIN !
$ the following function had to be amended in order to compensate
the effect
$ of the vacancy parameter on the invariant B2+L=Al3Ni2 and the
phase diagram
$ P.F., KIT 2015
$ FUNCTION B2NIVA 295.15 +162397.3-27.40575*T;,,N !
FUNCTION B2NIVA 295.15 +162397.3-27.40575*T-0.2*R*T;,,N 15Fra !
FUNC LB2NIVA 298.15 -64024.38+26.49419*T;,,N !
PARAMETER L(BCC_A2,NI,VA:VA;0) 298.15 B2NIVA+LB2NIVA;,,N 99DUP !
$
$
BCC_B2 PHASE
$
PARAMETER G(BCC_B2,VA:NI:VA;0) 298.15 .5*B2NIVA-.5*LB2NIVA;,,N
99DUP !
PARAMETER G(BCC_B2,NI:VA:VA;0) 298.15 .5*B2NIVA-.5*LB2NIVA;,,N
99DUP !
$
$
$-----
$
Mo
FUNCTION GHSERMO 2.98150E+02
-7746.302+131.9197*T-23.56414*T*LN(T)

```

```

-.003443396*T**2+5.66283E-07*T**3+65812*T**(-1)-1.30927E-10*T**4;
2.89600E+03 Y
-30556.41+283.559746*T-42.63829*T*LN(T)-4.849315E+33*T**(-9);
5.00000E+03 N !
FUNCTION GFCCMO 298.15 +7453.698+132.5497*T-23.56414*T*LN(T)

-.003443396*T**2+5.66283E-07*T**3+65812*T**(-1)-1.30927E-10*T**4;
2.89600E+03 Y
-15356.41+284.189746*T-42.63829*T*LN(T)-4.849315E+33*T**(-9);
5.00000E+03 N !
FUNCTION GHCPMO 298.15 +3803.698+131.9197*T-23.56414*T*LN(T)

-.003443396*T**2+5.66283E-07*T**3+65812*T**(-1)-1.30927E-10*T**4;
2.89600E+03 Y
-19006.41+283.559746*T-42.63829*T*LN(T)-4.849315E+33*T**(-9);
5.00000E+03 N !

FUNCTION GLIQMO 2.98150E+02
+34085.045+117.224788*T-23.56414*T*LN(T)
-.003443396*T**2+5.66283E-07*T**3+65812*T**(-1)-1.30927E-10*T**4
+4.24519E-22*T**7; 2.89600E+03 Y
+3538.963+271.6697*T-42.63829*T*LN(T); 5.00000E+03 N !
$ following parameter amended in order to compensate the vacancy
contribution
$ FUNC B2MOVA 298.15 10000-T; 6000 N !
FUNC B2MOVA 298.15 10000-T-0.2*R*T; 6000 N !
FUNC LB2MOVA 298.15 150000; 6000 N !
Function F12831T 298.15 651326.983-41.0946081*T-21.0437*T*ln(T)
+0.00027252545*T**2-4.77857833e-008*T**3+5594.93*T**(-1); 1600 Y
633752.125+83.3186552*T-37.98605*T*ln(T)+0.007623775*T**2
-6.52545667e-007*T**3+3471277.5*T**(-1); 3500 Y
1134689.66-1617.69443*T+169.6658*T*ln(T)-0.03080567*T**2
+6.87557667e-007*T**3
-224033800*T**(-1); 5000 Y
1008188.16-1437.30781*T+150.7395*T*ln(T)-0.03086233*T**2
+7.54569333e-007*T**3-106017750*T**(-1); 6200 Y
-929123.768+2587.60477*T-309.2377*T*ln(T)+0.017761425*T**2
-2.10949167e-007*T**3+1426406000*T**(-1); 10000 N !

$
PHASE (Zhang)
Parameter G(GAS,MO;0) 298.15 +F12831T+R*T*ln(1e-005*P);
6000 N 14Zhang!

$
LIQUID PHASE
PARAMETER G(IONIC_LIQ,MO+4;VA;0) 298.14 GLIQMO; 5000 N !

$
BCC_A2 PHASE
PARAMETER G(BCC_A2,MO;VA;0) 298.15 +GHSERMO; 5000 N 14Zhang !
PARAMETER L(BCC_A2,MO,VA;VA;0) 298.15 B2MOVA+LB2MOVA;;,N FRA !
PARAMETER G(BCC_B2,VA;MO;VA;0) 298.15 .5*B2MOVA-.5*LB2MOVA;;,N
FRA !

```

The thermodynamic dataset of Ni-Al-Cr-Mo-O

---

```

PARAMETER G(BCC_B2,MO:VA:VA;0) 298.15 .5*B2MOVA-.5*LB2MOVA;,,N
FRA !
PARAMETER G(BCC_B2,MO:MO:VA;0) 298.15 0; 6000 N!

$
FCC_A1 PHASE
PARAMETER G(FCC_A1,MO:VA;0) 298.15 +GFCCMO; 5.00000E+03 N
REF0 !

$
HCP_A3 PHASE
PARAMETER G(HCP_A3,MO:VA;0) 298.15 +GHCPMO; 5.00000E+03 N 10Cup !

$
CUB_A15 PHASE
PARAMETER G(CUB_A15,MO:MO;0) 298.15 +10000+GHSERMO; 6000 N
10Cup !
$-----
$
$
O
$
FUNCTIONS

FUNCTION GHSEROO 2.98140E+02 -3480.87-25.503038*T-11.136*T*LN(T)
-0.005098888*T**2+6.61846E-07*T**3-38365*T**(-1); 1.00000E+03 Y

-6568.763+12.65988*T-16.8138*T*LN(T)-5.95798E-04*T**2+6.781E-09*
T**3
+262905*T**(-1); 3.30000E+03 Y
-13986.728+31.259625*T-18.9536*T*LN(T)-4.25243E-04*T**2
+1.0721E-08*T**3+4383200*T**(-1); 6.00000E+03 N !

FUNCTION GO2GAS 2.98140E+02 -6961.74451-76729.7484*T**(-1)

-51.0057202*T-22.2710136*T*LN(T)-.01019774469*T**2+1.32369208E-06*
T**3;
1.00000E+03 Y
-13137.5203+525809.556*T**(-1)+25.3200332*T-33.627603*T*LN(T)
-.00119159274*T**2+1.35611111E-08*T**3; 3.30000E+03 Y
-27973.4908+8766421.4*T**(-1)+62.5195726*T-37.9072074*T*LN(T)
-8.50483772E-04*T**2+2.14409777E-08*T**3; 6.00000E+03 N !
FUNCTION F13469T 298.15 +243206.494-20.8612587*T-21.01555*T*LN(T)
+1.2687055E-04*T**2-1.23131283E-08*T**3-42897.09*T**(-1);
2950 Y
+252301.423-52.0847285*T-17.21188*T*LN(T)-5.413565E-04*T**2
+7.64520667E-09*T**3-3973170.5*T**(-1); 6000 N !
FUNCTION F14145T 298.15 +130696.944-37.9096651*T-27.58118*T*LN(T)
-.02763076*T**2+4.60539333E-06*T**3+99530.45*T**(-1); 700 Y
+114760.623+176.626736*T-60.10286*T*LN(T)+.00206456*T**2
-5.17486667E-07*T**3+1572175*T**(-1); 1300 Y
+49468.3958+710.094819*T-134.3696*T*LN(T)+.039707355*T**2
-4.10457667E-06*T**3+12362250*T**(-1); 2100 Y
+866367.075-3566.80563*T+421.2001*T*LN(T)-.1284109*T**2
+5.44768833E-06*T**3-2.1304835E+08*T**(-1); 2800 Y
+409416.384-1950.70834*T+223.4437*T*LN(T)-.0922361*T**2
+4.306855E-06*T**3-21589870*T**(-1); 3500 Y

```



```

PARAMETERS
$
$-----
$
$
$ Al-Cr
$                               Mainly from Saunders (COST507)
$                               Metastable B2 and L12 from revision of
Al-Cr-Ni
$
$
LIQUID PHASE
$
    PARAMETER L(IONIC_LIQ,AL+3,CR+3:VA;0)  2.98150E+02  -29000;
    6.00000E+03  N 91SAU1 !
    PARAMETER L(IONIC_LIQ,AL+3,CR+3:VA;1)  2.98150E+02  -11000;
    6.00000E+03  N 91SAU1 !
$
$
FCC_A1 PHASE
$
    PARAMETER G(FCC_A1,AL,CR:VA;0)  298.15  -45900+6*T;,,N 91SAU1 !
$
$
BCC_A2 PHASE
$
    PARAMETER G(BCC_A2,AL,CR:VA;0)  298.15  -54900+10*T;,,N 91SAU1 !
$
$
BCC_B2 PHASE
$
metastable
$ Present work: july 1999, study of Al-Cr-Ni, revision of NDTH. The B2
$ phase is not stabilized enough to become stable in the Al-Cr. It is
$ thus not in agreement with "T. Helander, and O. Tolochko, J. of
Phase
$ Eq, 20 (1) 1999, 57-60." Further study on the extension of the B2
phase
$ towards AlCr in Al-Cr-Ni would be desirable.
    PARAMETER G(BCC_B2,AL:CR:VA;0)  298.15  -2000;,,N 01DUP !
    PARAMETER G(BCC_B2,CR:AL:VA;0)  298.15  -2000;,,N 01DUP !
$
$
FCC_L12 PHASE
$
metastable
$ Present work: july 1999, study of Al-Cr-Ni, revision of NDTH.
    FUN U1ALCR  298.15  -830;,,N 01DUP !
    FUN U3ALCR  298.15  0.0; 6000.00  01DUP !
    FUN U4ALCR  298.15  0.0; 6000.00  N 01DUP !
    FUNCTION L04ALCR 298.15  U3ALCR;,,N !
    FUNCTION L14ALCR 298.15  U4ALCR;,,N !
    FUNCTION ALCR3  298.15  3*U1ALCR;,,N !
    FUNCTION AL2CR2 298.15  4*U1ALCR;,,N !
    FUNCTION AL3CR  298.15  3*U1ALCR;,,N !
    PARAMETER G(FCC_L12,CR:AL:VA;0)  298.15  +ALCR3;,, N 01DUP !

```

```

PARAMETER G(FCC_L12,AL:CR:VA;0) 298.15 +AL3CR;,, N 01DUP !
PARAMETER L(FCC_L12,AL,CR:AL:VA;0) 298.15
-1.5*ALCR3+1.5*AL2CR2+1.5*AL3CR;,,N 01DUP !
PARAMETER L(FCC_L12,AL,CR:CR:VA;0) 298.15
+1.5*ALCR3+1.5*AL2CR2-1.5*AL3CR;,,N 01DUP !
PARAMETER L(FCC_L12,AL,CR:AL:VA;1) 298.15
+0.5*ALCR3-1.5*AL2CR2+1.5*AL3CR;,,N 01DUP !
PARAMETER L(FCC_L12,AL,CR:CR:VA;1) 298.15
-1.5*ALCR3+1.5*AL2CR2-0.5*AL3CR;,,N 01DUP !
PARAMETER L(FCC_L12,*,AL,CR:VA;0) 298.15 +L04ALCR;,,N 01DUP !
PARAMETER L(FCC_L12,*,AL,CR:VA;1) 298.15 +L14ALCR;,,N 01DUP !
PARAMETER L(FCC_L12,AL,CR:*,VA;0) 298.15 +3*L04ALCR;,,N 01DUP !
PARAMETER L(FCC_L12,AL,CR:*,VA;1) 298.15 +3*L14ALCR;,,N 01DUP !
$
$
AL11CR2 PHASE
$
PHASE AL11CR2 % 3 10 1 2 !
CONST AL11CR2 :AL : CR : !
PARAMETER G(AL11CR2,AL:AL:CR;0) 298.15
+11*GHSERAL+2*GHSERCR-175500+25.805*T;,,N 91SAU1 !
$
$
AL13CR2 PHASE
$
PHASE AL13CR2 % 2 13 2 !
CONST AL13CR2 :AL : CR : !
PARAMETER G(AL13CR2,AL:CR;0) 298.15
+13*GHSERAL+2*GHSERCR-174405+22.2*T;,,N 91SAU1 !
$
$
AL4CR PHASE
$
PHASE AL4CR % 2 4 1 !
CONST AL4CR :AL : CR : !
PARAMETER G(AL4CR,AL:CR;0) 298.15
+4*GHSERAL+GHSERCR-89025+19.05*T;,,N 91SAU1 !
$
$
AL8CR5_H PHASE
$
PHASE AL8CR5_H % 2 8 5 !
CONST AL8CR5_H :AL : CR : !
PARAMETER G(AL8CR5_H,AL:CR;0) 298.15
+8*GHSERAL+5*GHSERCR-147732-58.5*T;,,N 91SAU1 !
$
$
AL8CR5_L PHASE
$
PHASE AL8CR5_L % 2 8 5 !
CONST AL8CR5_L :AL : CR : !
PARAMETER G(AL8CR5_L,AL:CR;0) 298.15
+8*GHSERAL+5*GHSERCR-229515;,,N 91SAU1 !
$
$
AL9CR4_H PHASE
$
PHASE AL9CR4_H % 2 9 4 !

```

The thermodynamic dataset of Ni-Al-Cr-Mo-O

---

```

CONST AL9CR4_H :AL : CR : !
PARAMETER G(AL9CR4_H,AL:CR;0) 298.15
+9*GHSERAL+4*GHSERCR-134433-56.16*T;;;N 91SAU1 !
$
$
AL9CR4_L PHASE
$
PHASE AL9CR4_L % 2 9 4 !
CONST AL9CR4_L :AL : CR : !
PARAMETER G(AL9CR4_L,AL:CR;0) 298.15
+9*GHSERAL+4*GHSERCR-230750+16.094*T;;;N 91SAU1 !
$
$
ALCR2 PHASE
$
PHASE ALCR2 % 2 1 2 !
CONST ALCR2 :AL : CR : !
PARAMETER G(ALCR2,AL:CR;0) 298.15
+GHSERAL+2*GHSERCR-32700-8.79*T;;;N 91SAU1 !
$
$-----
-----
$
$
Al-Ni
$
Mainly from ND thesis,
$
slightly revised to get better solvus at low
temperature
$
$
LIQUID PHASE
$
PARAMETER G(IONIC_LIQ,AL+3,NI+2:VA;0) 2.98150E+02 -207109.28
+41.31501*T; 6.00000E+03 N 95DUP3 !
PARAMETER G(IONIC_LIQ,AL+3,NI+2:VA;1) 2.98150E+02
-10185.79+5.8714*T;
6.00000E+03 N 95DUP3 !
PARAMETER G(IONIC_LIQ,AL+3,NI+2:VA;2) 2.98150E+02
+81204.81-31.95713*T;
6.00000E+03 N 95DUP3 !
PARAMETER G(IONIC_LIQ,AL+3,NI+2:VA;3) 2.98150E+02
+4365.35-2.51632*T;
6.00000E+03 N 95DUP3 !
PARAMETER G(IONIC_LIQ,AL+3,NI+2:VA;4) 2.98150E+02
-22101.64+13.16341*T;
6.00000E+03 N 95DUP3 !
$
$
FCC_A1 PHASE
$
PARAMETER TC(FCC_A1,AL,NI:VA;0) 298.15 -1112;;;N 95DUP3 !
PARAMETER TC(FCC_A1,AL,NI:VA;1) 298.15 1745;;;N 95DUP3 !
PARAMETER G(FCC_A1,AL,NI:VA;0) 298.15 -162407.75+16.212965*T;;;N
95DUP3 !
PARAMETER G(FCC_A1,AL,NI:VA;1) 298.15 +73417.798-34.914168*T;;;N
95DUP3 !
PARAMETER G(FCC_A1,AL,NI:VA;2) 298.15 +33471.014-9.8373558*T;;;N

```

```

95DUP3 !
PARAMETER G(FCC_A1,AL,NI:VA;3) 298.15 -30758.01+10.25267*T;;;N
95DUP3 !
$
$
BCC_A2 PHASE
$
metastable
$
    FUN B2ALNI 295.15 -152397.3+26.40575*T;;;N !
    FUN LB2ALNI 298.15 -52440.88+11.30117*T;;;N !
    PARAMETER L(BCC_A2,AL,NI:VA;0) 298.15 B2ALNI+LB2ALNI;;;N 99DUP!
$
$
BCC_B2 PHASE
$
    PARAMETER G(BCC_B2,AL:NI:VA;0) 298.15 .5*B2ALNI-.5*LB2ALNI;;;N
    99DUP !
    PARAMETER G(BCC_B2,NI:AL:VA;0) 298.15 .5*B2ALNI-.5*LB2ALNI;;;N
    99DUP !
$
$
FCC_L12 PHASE
$
    FUN UALNI 298.15 -22212.8931+4.39570389*T;;;N 01DUP !
    FUN U1ALNI 298.15 2*UNTIER*UALNI;;;N 01DUP !
    FUN U3ALNI 298.15 0;;;N 01DUP !
    FUN U4ALNI 298.15 7203.60609-3.74273030*T;;;N 01DUP !
    FUNCTION L04ALNI 298.15 U3ALNI;;;N 01DUP !
    FUNCTION L14ALNI 298.15 U4ALNI;;;N 01DUP !
    FUNCTION ALNI3 298.15 +3*U1ALNI;;;N 01DUP !
    FUNCTION AL2NI2 298.15 +4*U1ALNI;;;N 01DUP !
    FUNCTION AL3NI 298.15 +3*U1ALNI;;;N 01DUP !
    PARAMETER G(FCC_L12,NI:AL:VA;0) 298.15 +ALNI3;;;N 01DUP !
    PARAMETER G(FCC_L12,AL:NI:VA;0) 298.15 +AL3NI;;;N 01DUP !
    PARAMETER L(FCC_L12,AL,NI:AL:VA;0) 298.15
    -1.5*ALNI3+1.5*AL2NI2+1.5*AL3NI;;;N 01DUP !
    PARAMETER L(FCC_L12,AL,NI:NI:VA;0) 298.15
    +1.5*ALNI3+1.5*AL2NI2-1.5*AL3NI;;;N 01DUP !
    PARAMETER L(FCC_L12,AL,NI:AL:VA;1) 298.15
    +0.5*ALNI3-1.5*AL2NI2+1.5*AL3NI;;;N 01DUP !
    PARAMETER L(FCC_L12,AL,NI:NI:VA;1) 298.15
    -1.5*ALNI3+1.5*AL2NI2-0.5*AL3NI;;;N 01DUP !
    PARAMETER L(FCC_L12,*:AL,NI:VA;0) 298.15 +L04ALNI;;;N 01DUP !
    PARAMETER L(FCC_L12,*:AL,NI:VA;1) 298.15 +L14ALNI;;;N 01DUP !
    PARAMETER L(FCC_L12,AL,NI:*:VA;0) 298.15 +3*L04ALNI;;;N 01DUP !
    PARAMETER L(FCC_L12,AL,NI:*:VA;1) 298.15 +3*L14ALNI;;;N 01DUP !
$
$
AL3NI1 PHASE
$
    PHASE AL3NI1 % 2 .75 .25 !
    CONST AL3NI1 :AL : NI : !
    PARAMETER G(AL3NI1,AL:NI;0) 298.15
    -48483.73+12.29913*T
    +.75*GHSERAL+.25*GHSERNI;;;N 95DUP3 !
$
$

```

```

AL3NI2 PHASE
$
PHASE AL3NI2 % 3 3 2 1 !
CONST AL3NI2 :AL : AL,NI% : NI,VA% : !
PARAMETER G(AL3NI2,AL:AL:NI;0) 298.15 +5*GBCCAL+GBCNCI
-39465.978+7.89525*T;,,N 95DUP3 !
PARAMETER G(AL3NI2,AL:NI:NI;0) 298.15 +3*GBCCAL+3*GBCNCI
-427191.9+79.21725*T;,,N 95DUP3 !
PARAMETER G(AL3NI2,AL:AL:VA;0) 298.15 +5*GBCCAL
+30000-3*T;,,N 95DUP3 !
PARAMETER G(AL3NI2,AL:NI:VA;0) 298.15 +3*GBCCAL+2*GBCNCI
-357725.92+68.322*T;,,N 95DUP3 !
PARAMETER L(AL3NI2,AL:AL,NI:*;0) 298.15
-193484.18+131.79*T;,,N 95DUP3 !
PARAMETER L(AL3NI2,AL:*:NI,VA;0) 298.15
-22001.7+7.0332*T;,,N 95DUP3 !
$
$
AL3NI5 PHASE
$
PHASE AL3NI5 % 2 .375 .625 !
CONST AL3NI5 :AL : NI : !
PARAMETER G(AL3NI5,AL:NI;0) 298.15 +.375*GHSERAL+.625*GHSERNI
-55507.7594+7.2648103*T;,,N 95DUP3 !
$
$-----
$-----
$
$
Cr-Ni
$
Mainly from SSOL
$
Metastable B2 and L12 from revision of
$
Al-Cr-Ni
$
$
LIQUID PHASE
$
PARAMETER G(IONIC_LIQ,CR+3,NI+2:VA;0) 2.98150E+02
+318-7.3318*T;
6.00000E+03 N 91LEE !
PARAMETER G(IONIC_LIQ,CR+3,NI+2:VA;1) 2.98150E+02
+16941-6.3696*T;
6.00000E+03 N 91LEE !
$
$
FCC_A1 PHASE
$
PARAMETER G(FCC_A1,CR,NI:VA;0) 298.15 +8030-12.8801*T;,,N 91LEE !
PARAMETER G(FCC_A1,CR,NI:VA;1) 298.15 +33080-16.0362*T;,,N 91LEE
!
PARAMETER TC(FCC_A1,CR,NI:VA;0) 298.15 -3605;,,N 86DIN !
PARAMETER BMAGN(FCC_A1,CR,NI:VA;0) 298.15 -1.91;,,N 86DIN !
$
$

```

```

BCC_A2 PHASE
$
PARAMETER G(BCC_A2,CR,NI:VA;0) 298.15 +17170-11.8199*T;;;,N 91LEE !
PARAMETER G(BCC_A2,CR,NI:VA;1) 298.15 +34418-11.8577*T;;;,N 91LEE !
PARAMETER TC(BCC_A2,CR,NI:VA;0) 298.15 2373;;;,N 86DIN !
PARAMETER TC(BCC_A2,CR,NI:VA;1) 298.15 617;;;,N 86DIN !
PARAMETER BMAGN(BCC_A2,CR,NI:VA;0) 298.15 4;;;,N 86DIN !
$
$
BCC_B2 PHASE
$
metastable
$
$ Present work: july 1999, study of Al-Cr-Ni, revision of NDTH.
PARAMETER G(BCC_B2,CR:NI:VA;0) 298.15 4000;;;,N 01DUP !
PARAMETER G(BCC_B2,NI:CR:VA;0) 298.15 4000;;;,N 01DUP !
$
$
FCC_L12 PHASE
$
metastable
$ Present work: july 1999, study of Al-Cr-Ni, revision of NDTH.
$ The L12 phase is metastable in the binary Cr-Ni while it was
stable in NDTH.
    FUN U1CRNI 298.15 -1980;;;,N 01DUP !
$    FUN U1CRNI 298.15 -7060+3.63*T;;;,N 01DUP !
    FUN U3CRNI 298.15 0;;;,N 01DUP !
    FUN U4CRNI 298.15 0;;;,N 01DUP !
    FUNCTION L04CRNI 298.15 U3CRNI;;;,N 01DUP !
    FUNCTION L14CRNI 298.15 U4CRNI;;;,N 01DUP !
    FUNCTION CRNI3 298.15 +3*U1CRNI;;;,N 01DUP !
    FUNCTION CR2NI2 298.15 +4*U1CRNI;;;,N 01DUP !
    FUNCTION CR3NI 298.15 +3*U1CRNI;;;,N 01DUP !
PARAMETER G(FCC_L12,NI:CR:VA;0) 298.15 +CRNI3;;;, N 01DUP !
PARAMETER G(FCC_L12,CR:NI:VA;0) 298.15 +CR3NI;;;, N 01DUP !
PARAMETER L(FCC_L12,CR,NI:CR:VA;0) 298.15
-1.5*CRNI3+1.5*CR2NI2+1.5*CR3NI;;;,N 01DUP !
PARAMETER L(FCC_L12,CR,NI:NI:VA;0) 298.15
+1.5*CRNI3+1.5*CR2NI2-1.5*CR3NI;;;,N 01DUP !
PARAMETER L(FCC_L12,CR,NI:CR:VA;1) 298.15
+0.5*CRNI3-1.5*CR2NI2+1.5*CR3NI;;;,N 01DUP !
PARAMETER L(FCC_L12,CR,NI:NI:VA;1) 298.15
-1.5*CRNI3+1.5*CR2NI2-0.5*CR3NI;;;,N 01DUP !
PARAMETER L(FCC_L12,*:CR,NI:VA;0) 298.15 +L04CRNI;;;,N 01DUP !
PARAMETER L(FCC_L12,*:CR,NI:VA;1) 298.15 +L14CRNI;;;,N 01DUP !
PARAMETER L(FCC_L12,CR,NI:*:VA;0) 298.15 +3*L04CRNI;;;,N 01DUP !
PARAMETER L(FCC_L12,CR,NI:*:VA;1) 298.15 +3*L14CRNI;;;,N 01DUP !
$
$-----
$
$
$ Al-O
$
FUNCTIONS
FUNCTION GAL2O3LQ 2.98000E+02
-1607850.8+405.559491*T-67.4804*T*LN(T)

```

```

-0.06747*T**2+1.4205433E-05*T**3+938780*T**(-1); 6.00000E+02 Y
-1625385.57+712.394972*T-116.258*T*LN(T)-.0072257*T**2
+2.78532E-07*T**3+2120700*T**(-1); 1.50000E+03 Y
-1672662.69+1010.9932*T-156.058*T*LN(T)+.00709105*T**2
-6.29402E-07*T**3+12366650*T**(-1); 1.91200E+03 Y
+29178041.6-168360.926*T+21987.1791*T*LN(T)-6.99552951*T**2
+4.10226192E-04*T**3-7.98843618E+09*T**(-1); 2.32700E+03 Y
-1757702.05+1344.84833*T-192.464*T*LN(T); 4.00000E+03 N !
FUNCTION GCORUND 2.98140E+02
-1707351.3+448.021092*T-67.4804*T*LN(T)
-0.06747*T**2+1.4205433E-05*T**3+938780*T**(-1); 6.00000E+02 Y
-1724886.06+754.856573*T-116.258*T*LN(T)-.0072257*T**2
+2.78532E-07*T**3+2120700*T**(-1); 1.50000E+03 Y
-1772163.19+1053.4548*T-156.058*T*LN(T)+.00709105*T**2
-6.29402E-07*T**3+12366650*T**(-1); 3.00000E+03 N !
FUNCTION F577T 298.15 +68468.7356-29.708552*T-27.37717*T*LN(T)
-.008706905*T**2+1.34759667E-06*T**3+42904.83*T**(-1); 800 Y
+70559.2235-26.9045572*T-28.56166*T*LN(T)-.0034503355*T**2
-1.4328805E-07*T**3-437311.7*T**(-1); 1600 Y
+68575.8626-63.4014165*T-22.54674*T*LN(T)-.009242035*T**2
+5.66213667E-07*T**3+1636864.5*T**(-1); 2800 Y
-17076.0658+348.591643*T-75.33292*T*LN(T)+.005011805*T**2
-1.47269833E-07*T**3+27223195*T**(-1); 6000 N !
FUNCTION F587T 298.15 -200250.88+67.6442736*T-45.11105*T*LN(T)
-.016095035*T**2+2.90117167E-06*T**3+212888.2*T**(-1); 800 Y
-208337.344+178.095443*T-61.93533*T*LN(T)-1.05714E-04*T**2
+3.98789667E-09*T**3+970284*T**(-1); 3000 N !
FUNCTION F623T 298.15 +480383.542-1.58706566*T-36.90579*T*LN(T)
-7.56815E-04*T**2-1.31040183E-07*T**3+16498.85*T**(-1); 1600 Y
+484703.82-58.8210679*T-28.53999*T*LN(T)-.00618347*T**2
+4.55704333E-07*T**3; 3100 Y
+399551.917+333.52963*T-78.48514*T*LN(T)+.006619755*T**2
-1.5106045E-07*T**3+26673440*T**(-1); 3800 N !
FUNCTION F768T 298.15 -201660.825+80.9385369*T-49.25823*T*LN(T)
-.012061425*T**2+2.14597333E-06*T**3+130925.75*T**(-1); 800 Y
-208004.473+165.926016*T-62.16169*T*LN(T)-3.72899E-05*T**2
+1.19899483E-09*T**3+738957*T**(-1); 6000 N !
FUNCTION F776T 298.15 -494047.79-72.1054899*T-23.89169*T*LN(T)
-.0621397*T**2+1.29213783E-05*T**3+78100*T**(-1); 600 Y
-514422.654+254.039684*T-74.96724*T*LN(T)-.0042506095*T**2
+4.18842167E-07*T**3+1628653.5*T**(-1); 1500 Y
-521272.731+311.4317*T-82.99675*T*LN(T)-2.4276615E-05*T**2
+7.14432E-10*T**3+2748177*T**(-1); 6000 N !
FUNCTION F802T 298.15 -575903.151+252.49861*T-82.26331*T*LN(T)
-.025448955*T**2+4.17391E-06*T**3+366776.4*T**(-1); 800 Y
-591324.268+447.940009*T-111.611*T*LN(T)-1.2771895E-04*T**2
+4.43587833E-09*T**3+1918382*T**(-1); 6000 N !

FUNCTION F787T 298.15 -1699084.53+463.030133*T-69.46026*T*LN(T)
-.0695571*T**2+1.4647905E-05*T**3+966159*T**(-1); 600 Y
-1717152.63+779.276539*T-119.736*T*LN(T)-.00744798*T**2
+2.87318833E-07*T**3+2183608.5*T**(-1); 1500 Y
-1765472.13+1084.73224*T-160.4551*T*LN(T)+.007211335*T**2
-6.42760667E-07*T**3+12643315*T**(-1); 2308 N !

FUNCTION F792T 298.15 -1689981.34+469.457943*T-70.54517*T*LN(T)
-.0707939*T**2+1.491345E-05*T**3+981167*T**(-1); 600 Y

```

```

-1708394.01+791.595033*T-121.7544*T*LN(T) -.007546725*T**2
+2.89573167E-07*T**3+2222750*T**(-1); 1500 Y
-1758865.4+1110.41949*T-164.253*T*LN(T)+.007753035*T**2
-6.82469667E-07*T**3+13162740*T**(-1); 2290 N !

FUNCTION F797T      298.15 -1694673.42+456.64816*T-69.0088*T*LN(T)
-.0688841*T**2+1.44969317E-05*T**3+960094*T**(-1); 600 Y
-1712611.55+770.32884*T-118.8687*T*LN(T)-.00734585*T**2
+2.796585E-07*T**3+2170324.5*T**(-1); 1500 Y
-1760866.16+1075.07673*T-159.4861*T*LN(T)+.007252735*T**2
-6.44151167E-07*T**3+12625030*T**(-1); 2312 N !

$
PHASE
PARAMETER G(GAS,AL1O1;0)      298.15
+F577T#+R#*T*LN(1E-05*P);
6000 N REF411 !
PARAMETER G(GAS,AL1O2;0)      298.15
+F587T#+R#*T*LN(1E-05*P);
6000 N REF416 !
PARAMETER G(GAS,AL2;0)        298.15
+F623T#+R#*T*LN(1E-05*P);
6000 N REF447 !
PARAMETER G(GAS,AL2O1;0)      298.15
+F768T#+R#*T*LN(1E-05*P);
6000 N REF589 !
PARAMETER G(GAS,AL2O2;0)      298.15
+F776T#+R#*T*LN(1E-05*P);
6000 N REF595 !
PARAMETER G(GAS,AL2O3;0)      298.15
+F802T#+R#*T*LN(1E-05*P);
6000 N REF615 !

$
LIQUID PHASE
PARAMETER G(IONIC_LIQ,AL+3:O-2;0)  2.98150E+02
+GAL2O3LQ#+1000000;
6.00000E+03  N 93hall !
PARAMETER G(IONIC_LIQ,ALO3/2;0)  2.98150E+02  +.5*GAL2O3LQ#;
6.00000E+03  N 93hall !
PARAMETER G(IONIC_LIQ,AL+3:O-2,VA;0)  2.98150E+02
-829000+106*T;
6.00000E+03  N 93hall !
PARAMETER G(IONIC_LIQ,AL+3:VA,ALO3/2;0)  2.98150E+02
+110000+46*T;
6.00000E+03  N 93hall !

$
ALCRO PHASE
PARAMETER G(ALCRO,AL+3:VA:O-2;0)  2.98150E+02  +GCRUND#;
6.00000E+03
N REF51 !

$
HALITE PHASE
PARAMETER G(HALITE,AL+3:O-2;0)  2.98150E+02  +50000+.5*GCRUND#;

```

The thermodynamic dataset of Ni-Al-Cr-Mo-O

---

```

6.00000E+03   N REF51 !

$
AL2O3_DELTA PHASE

    PARAMETER G(AL2O3_DELTA,AL2O3;0)      298.15 +F787T#; 6000 N
    REF602 !

$
AL2O3_GAMMA PHASE

$ this gamma phase is included in spinel description
$ PARAMETER G(AL2O3_GAMMA,AL2O3;0)      298.15 +F792T#; 6000 N
    REF606 !

$
AL2O3_KAPPA PHASE

    PARAMETER G(AL2O3_KAPPA,AL2O3;0)      298.15 +F797T#; 6000 N
    REF611 !

$-----
$
$
$   Cr-O

$
FUNCTIONS

FUNCTION GCR2O3      2.98140E+02
-1177497.8+814.9138*T-132.046*T*LN(T)
+0.005256*T**2-1.38885E-06*T**3+1501761*T**(-1); 1.00000E+03   Y

    -1166947.9+701.5624*T-115.5381*T*LN(T)-.00620492*T**2+1.00698E-0
    7*T**3
+239949*T**(-1); 2.60000E+03   N !

FUNCTION GBUNS      2.98140E+02 -254927.2+276.208*T-46.03917*T*LN(T)
-0.0093145*T**2+1.29092E-06*T**3+382916*T**(-1); 1.00000E+03   Y

    -256835.2+340.043*T-56.36068*T*LN(T)+.00254106*T**2-8.11809E-07*
    T**3
+1270*T**(-1); 1.80000E+03   Y

    -259131.4+337.305*T-55.75758*T*LN(T)+.00220246*T**2-7.80093E-07*
    T**3;
2.60000E+03   N !

FUNCTION F7705T      298.15 +176483.869-31.9513659*T-30.2897*T*LN(T)
-0.0607059*T**2+9.229905E-07*T**3+35263.135*T**(-1); 900   Y
+170853.62+32.1684007*T-39.74749*T*LN(T)+.00119977*T**2
-1.52515733E-07*T**3+682877*T**(-1); 4000   Y
+307209.502-414.237405*T+14.48744*T*LN(T)-.008463125*T**2
+1.722975E-07*T**3-64209900*T**(-1); 8400   Y
-403765.708+805.224944*T-121.5329*T*LN(T)+.003139382*T**2
-1.36845867E-08*T**3+6.35563E+08*T**(-1); 10000   N !

```

```

FUNCTION F7705T      298.15 +176483.869-31.9513659*T-30.2897*T*LN(T)
-.00607059*T**2+9.229905E-07*T**3+35263.135*T**(-1); 900 Y
+170853.62+32.1684007*T-39.74749*T*LN(T)+.00119977*T**2
-1.52515733E-07*T**3+682877*T**(-1); 4000 Y
+307209.502-414.237405*T+14.48744*T*LN(T)-.008463125*T**2
+1.722975E-07*T**3-64209900*T**(-1); 8400 Y
-403765.708+805.224944*T-121.5329*T*LN(T)+.003139382*T**2
-1.36845867E-08*T**3+6.35563E+08*T**(-1); 10000 N !

FUNCTION F7713T      298.15 -121743.409-9.3513573*T-36.29523*T*LN(T)
-.01993456*T**2+3.5091E-06*T**3+193490.75*T**(-1); 700 Y
-130807.622+121.470522*T-56.35306*T*LN(T)-3.3428045E-04*T**2
-6.06589333E-08*T**3+956146*T**(-1); 3400 Y
-110536.941+26.3566562*T-44.22742*T*LN(T)-.003455125*T**2
+8.58097667E-08*T**3-5175510*T**(-1); 6000 N !

FUNCTION F7726T      298.15 -342387.72+103.718924*T-52.84504*T*LN(T)
-.02759153*T**2+4.86524667E-06*T**3+358400*T**(-1); 700 Y
-356869.109+299.291672*T-82.53502*T*LN(T)-7.979305E-05*T**2
-1.88415667E-09*T**3+1702506*T**(-1); 4000 Y
-362423.322+334.459538*T-87.10177*T*LN(T)+.001170557*T**2
-5.86174E-08*T**3+1764429*T**(-1); 6000 N !

FUNCTION F7786T      298.15 +258642.869+18.9762238*T-45.67129*T*LN(T)
-.01091753*T**2+1.82552667E-06*T**3+195214.55*T**(-1); 800 Y
+252339.667+100.708505*T-57.99041*T*LN(T)-4.2445385E-05*T**2
+1.47398017E-09*T**3+811266.5*T**(-1); 6000 N !

FUNCTION F7790T      298.15 -114921.51+90.7837154*T-56.43087*T*LN(T)
-.024901535*T**2+4.46667667E-06*T**3+425434.7*T**(-1); 700 Y
-127421.861+262.909888*T-82.6483*T*LN(T)-1.038465E-04*T**2
+3.69833E-09*T**3+1558529.5*T**(-1); 6000 N !

FUNCTION F7800T      298.15 -356516.314+207.624492*T-81.21114*T*LN(T)
-.02355767*T**2+3.95542E-06*T**3+458816.6*T**(-1); 800 Y
-369964.254+382.961638*T-107.662*T*LN(T)-8.59286E-05*T**2
+2.98778667E-09*T**3+1763567*T**(-1); 6000 N !
FUNCTION RTLNP 298.15 +R*T*LN(1E-05*P); 6000 N !

$
GAS PHASE

PARAMETER G(GAS,CR1O1;0) 298.15 +F7705T+RTLNP; 6000 N 00SUB !
PARAMETER G(GAS,CR1O2;0) 298.15 +F7713T+RTLNP; 6000 N 00SUB !
PARAMETER G(GAS,CR1O3;0) 298.15 +F7726T+RTLNP; 6000 N 00SUB !
PARAMETER G(GAS,CR2O1;0) 298.15 +F7786T+RTLNP; 6000 N 00SUB !
PARAMETER G(GAS,CR2O2;0) 298.15 +F7790T+RTLNP; 6000 N 00SUB !
PARAMETER G(GAS,CR2O3;0) 298.15 +F7800T+RTLNP; 6000 N 00SUB !

$
LIQUID PHASE
$ PARAMETER G(IONIC_LIQ,CR+3:O-2;0) 2.98150E+02 -1047074+260.777*T
$ -3.97112*T*LN(T)+2*GCRLIQ#+1.5*GO2GAS#; 6.00000E+03 N 04salt !
PARAMETER G(IONIC_LIQ,CR+3:O-2;0) 298.15 +2*GCRLIQ+1.5*GO2GAS
-1047074+260.777*T-3.97112*T*LN(T); 6000 N 90DIN!

```

The thermodynamic dataset of Ni-Al-Cr-Mo-O

---

```

$  PARAMETER G (IONIC_LIQ,CR+3:O-2,VA;0)  2.98150E+02
+401677-162.455*T;
$ 6.00000E+03  N 04salt !
  PARAMETER L (IONIC_LIQ,CR+3:O-2,VA;0)      298.15 +280000-99.3*T;
  6000 N 08Kje !

$  PARAMETER G (IONIC_LIQ,CR+3:O-2,VA;1)  2.98150E+02
-231461.2+46.207*T;
$ 6.00000E+03  N 04salt !
  PARAMETER L (IONIC_LIQ,CR+3:O-2,VA;1)      298.15 -146000; 6000 N
  08Kje !

$  PARAMETER G (IONIC_LIQ,CR+3:O-2,VA;2)  2.98150E+02
-419258.8+180.821*T;
$ 6.00000E+03  N 04salt !
  PARAMETER L (IONIC_LIQ,CR+3:O-2,VA;2)      298.15 -65000; 6000 N
  08Kje !

$  PARAMETER G (IONIC_LIQ,CR+3:O-2,O;0)  2.98150E+02  1E+08;
6.00000E+03
$  N 04salt !
$  PARAMETER G (IONIC_LIQ,CR+3:VA,O;0)  2.98150E+02  1E+08;
6.00000E+03
$  N 04salt !

$
ALCRO PHASE
  PARAMETER G (ALCRO,CR+2:CR+3:O-2;0)  2.98150E+02
+665910+GCR2O3#;
6.00000E+03  N 08Kje !
  PARAMETER TC (ALCRO,CR+2:CR+3:O-2;0)  2.98150E+02  306;
6.00000E+03  N
90DIN !
  PARAMETER BMAGN (ALCRO,CR+2:CR+3:O-2;0)  2.98150E+02  1.938;
6.00000E+03
  N REF:0 !
  PARAMETER G (ALCRO,CR+3:CR+3:O-2;0)  2.98150E+02  +GCR2O3#-232227.2
+241.3793*T; 6.00000E+03  N 90DIN!
  PARAMETER TC (ALCRO,CR+3:CR+3:O-2;0)  2.98150E+02  306;
6.00000E+03  N
90DIN !
  PARAMETER BMAGN (ALCRO,CR+3:CR+3:O-2;0)  2.98150E+02  1.938;
6.00000E+03
  N REF:0 !
  PARAMETER G (ALCRO,CR+2:VA:O-2;0)  2.98150E+02  +GCR2O3#;
6.00000E+03
N 08Kje !
  PARAMETER TC (ALCRO,CR+2:VA:O-2;0)  2.98150E+02  306;
6.00000E+03  N
90DIN !
  PARAMETER BMAGN (ALCRO,CR+2:VA:O-2;0)  2.98150E+02  1.938;
6.00000E+03
  N REF:0 !
  PARAMETER G (ALCRO,CR+3:VA:O-2;0)  2.98150E+02  +GCR2O3#;
6.00000E+03
N 08Kje !
  PARAMETER TC (ALCRO,CR+3:VA:O-2;0)  2.98150E+02  306;

```

```

6.00000E+03  N
90DIN !
PARAMETER BMAGN(ALCRO,CR+3:VA:O-2;0) 2.98150E+02 1.938;
6.00000E+03
N REF:0 !

$kjellqwist spinel definition is used instead of cr3o4 from
saltykov
$
CR3O4 PHASE
$ PARAMETER G(CR3O4,CR:O;0) 2.98150E+02 -1511981.4+1038.674*T
$
-174.276*T*LN(T)-.002798521*T**2-3.3145E-07*T**3+1799238*T**(-1);
$ 6.00000E+03 N 04salt !

$
HALITE PHASE

$ PARAMETER G(HALITE,CR+3:O-2;0) 2.98150E+02
+GBUNS#-140288.1-519.3911*T
$ +57.1626*T*LN(T); 6.00000E+03 N !
$ PARAMETER TC(HALITE,CR+3:O-2;0) 2.98150E+02 519;
6.00000E+03 N !
$ PARAMETER BMAGN(HALITE,CR+3:O-2;0) 2.98150E+02 .9873;
6.00000E+03 N!

FUNCTION CWUSTITE 298.15 -563748.9+407.4569*T-66.02315*T*LN(T)
+0.002628*T**2-6.944225E-07*T**3+750881*T**(-1); 1000 Y
-558473.9+350.7812*T-57.76905*T*LN(T)-0.00310246*T**2
+5.034917E-08*T**3+119974.7*T**(-1); 6000 N !
$ parameters are changed to 08Kje
PARAMETER G(HALITE,CR+3:O-2;0) 298.15 +CWUSTITE; 6000 N 93Tayl !
PARAMETER TC(HALITE,CR+3:O-2;0) 298.15 +519; 6000 N 08Kje !
PARAMETER BMAGN(HALITE,CR+3:O-2;0) 298.15 +0.9873; 6000 N 08Kje!

$
BCC_A2 PHASE

PARAMETER G(BCC_A2,CR:O;0) 298.15
+GHSERCR+1.5*GO2GAS+195*T; 6000 N !
PARAMETER L(BCC_A2,CR:O,VA;0) 298.15 -673435+27.86*T; 6000
N 95kowa !

$
Other oxides

FUNCTION F7855T 298.15 -600391.704+281.452816*T-48.5344*T*LN(T)
-.00594128*T**2+569024*T**(-1); 750 N !
FUNCTION F7862T 298.15 -612070.079+453.022241*T-71.7556*T*LN(T)
-.043932*T**2+836800*T**(-1); 470 Y
-620140.958+732.646336*T-117.152*T*LN(T); 600 N !
FUNCTION F7862T 298.15 -612070.079+453.022241*T-71.7556*T*LN(T)
-.043932*T**2+836800*T**(-1); 470 Y
-620140.958+732.646336*T-117.152*T*LN(T); 600 N !
FUNCTION F7951T 298.15 -3105460.92+2323.83748*T-387.02*T*LN(T)
-.0443504*T**2+3556400*T**(-1); 1200 N !

```

## The thermodynamic dataset of Ni-Al-Cr-Mo-O

---

FUNCTION F7958T 298.15 -4951170.76+3648.74788\*T-602.496\*T\*LN(T)  
 -.1740544\*T\*\*2+6066800\*T\*\*(-1); 640 N !

PHASE CR1O2\_S % 1 1.0 !  
 CONSTITUENT CR1O2\_S :CR1O2 : !

PARAMETER G(CR1O2\_S,CR1O2;0) 298.15 +F7855T#; 6000 N  
 REF4682 !

PARAMETER G(IONIC\_LIQ,CR+6:O-2,VA;1) 298.15  
 +F7862T#+14225.6  
 -30.267234\*T; 6000 N REF4687 !

PHASE CR1O3\_S % 1 1.0 !  
 CONSTITUENT CR1O3\_S :CR1O3 : !

PARAMETER G(CR1O3\_S,CR1O3;0) 298.15 +F7862T#; 6000 N  
 REF4687 !

PHASE CR5O12\_S % 1 1.0 !  
 CONSTITUENT CR5O12\_S :CR5O12 : !

PARAMETER G(CR5O12\_S,CR5O12;0) 298.15 +F7951T#; 6000 N  
 REF4749 !

PHASE CR8O21\_S % 1 1.0 !  
 CONSTITUENT CR8O21\_S :CR8O21 : !

PARAMETER G(CR8O21\_S,CR8O21;0) 298.15 +F7958T#; 6000 N  
 REF4755 !

\$-----  
 -----

\$  
 \$  
 Ni-O

\$  
 FUNCTIONS

FUNCTION F13326T 298.15 +275156.639-9.27332589\*T-32.674\*T\*LN(T)  
 -.00254775\*T\*\*2-1.31201667E-07\*T\*\*3+109000\*T\*\*(-1); 700 Y  
 +279389.197-44.5608856\*T-27.903\*T\*LN(T)-.00350505\*T\*\*2  
 -5.10013333E-07\*T\*\*3-458630\*T\*\*(-1); 1300 Y  
 +295728.644-209.722503\*T-4.215\*T\*LN(T)-.0179776\*T\*\*2  
 +1.09025167E-06\*T\*\*3-2390490\*T\*\*(-1); 2400 Y  
  
 +206797.992+271.295114\*T-66.93201\*T\*LN(T)+.0014191\*T\*\*2-2.255E-0  
 8\*T\*\*3  
 +20851205\*T\*\*(-1); 5400 Y

```

+285045.253+50.6214847*T-40.685*T*LN(T)-.0024736*T**2+8.4875E-08
*T**3
-22870970*T**(-1); 6000 N !

FUNCTION GBUNSEN 2.98000E+02 -254927.2+276.208*T-46.03917*T*LN(T)
-.0093145*T**2+1.29092E-06*T**3+382916*T**(-1); 1.00000E+03 Y

-256835.2+340.043*T-56.36068*T*LN(T)+.00254106*T**2-8.11809E-07*
T**3
+1270*T**(-1); 1.80000E+03 Y

-259131.4+337.305*T-55.75758*T*LN(T)+.00220246*T**2-7.80093E-07*
T**3;
2.60000E+03 N !

$
GAS PHASE
PARAMETER G(GAS,NI1O1;0) 298.15 +F13326T+RTLNP; 6000 N 00SUB !

$
LIQUID PHASE

PARAMETER G(IONIC_LIQ,NI+2:O-2;0) 2.98150E+02 -402345.6+176.606*T
-4.35796*T*LN(T)+2*GLIQNI#+2*GHSEROO#; 6.00000E+03 N 90DIN !
PARAMETER G(IONIC_LIQ,NI+2:O-2,O;0) 2.98150E+02 1E+08;
6.00000E+03
N 90DIN !
PARAMETER G(IONIC_LIQ,NI+2:O-2,VA;0) 2.98150E+02
+176711-50.2286*T;
6.00000E+03 N 90DIN !
PARAMETER G(IONIC_LIQ,NI+2:O-2,VA;1) 2.98150E+02 22914.8;
6.00000E+03 N 90DIN !
PARAMETER G(IONIC_LIQ,NI+2:O-2,VA;2) 2.98150E+02 42079.6;
6.00000E+03 N 90DIN !
PARAMETER G(IONIC_LIQ,NI+2:VA,O;0) 2.98150E+02 1E+08;
6.00000E+03
N 90DIN !

$
HALITE PHASE
$ PARAMETER G(HALITE,NI+2:O-2;0) 2.98150E+02 -500+GBUNSEN#;
6.00000E+03
$ N 04salt !
PARAMETER G(HALITE,NI+2:O-2;0) 2.98150E+02 +GBUNSEN#;
6.00000E+03
N 90DIN !
PARAMETER TC(HALITE,NI+2:O-2;0) 2.98150E+02 519;
6.00000E+03 N
90DIN !
PARAMETER BMAGN(HALITE,NI+2:O-2;0) 2.98150E+02 .9873;
6.00000E+03 N
90DIN !
PARAMETER G(HALITE,NI+3:O-2;0) 2.98150E+02
+GBUNSEN#+132919.5-64.8855*T;
6.00000E+03 N 90DIN !
PARAMETER TC(HALITE,NI+3:O-2;0) 2.98150E+02 519;

```



PARAMETER G(CUB\_A15,AL,MO:AL;0) 298.15 +0.455738495\*T; 6000 N  
 10Cup !  
 PARAMETER G(CUB\_A15,MO:AL,MO;0) 298.15 -2.63250337\*T; 6000 N  
 10Cup !

PHASE AL12MO % 2 12 1 !  
 CONSTITUENT AL12MO :AL : MO : !  
 PARAMETER G(AL12MO,AL:MO;0) 298.15 -1.47884522E+05+33\*T  
 +12\*GHSERAL#+GHSERMO#; 6000 N Peng !

PHASE AL17MO4 % 2 17 4 !  
 CONSTITUENT AL17MO4 :AL : MO : !  
 PARAMETER G(AL17MO4,AL:MO;0) 298.15  
 -5.96728081E+05+1.60445888E+02\*T  
 +17\*GHSERAL#+4\*GHSERMO#; 6000 N Peng !

PHASE AL22MO5 % 2 22 5 !  
 CONSTITUENT AL22MO5 :AL : MO : !  
 PARAMETER G(AL22MO5,AL:MO;0) 298.15  
 -7.45899148E+05+1.98500000E+02\*T  
 +22\*GHSERAL#+5\*GHSERMO#; 6000 N Peng !

PHASE AL3MO % 2 3 1 !  
 CONSTITUENT AL3MO :AL : MO : !  
 PARAMETER G(AL3MO,AL:MO;0) 298.15  
 -1.43801421E+05+4.09326635E+01\*T+  
 3\*GHSERAL#+GHSERMO#; 6000 N Peng !

PHASE AL4MO % 2 4 1 !  
 CONSTITUENT AL4MO :AL : MO : !  
 PARAMETER G(AL4MO,AL:MO;0) 298.15  
 -1.42202145E+05+3.54152656E+01\*T  
 +4\*GHSERAL#+GHSERMO#; 6000 N Peng !

PHASE AL5MO % 2 5 1 !  
 CONSTITUENT AL5MO :AL : MO : !  
 PARAMETER G(AL5MO,AL:MO;0) 298.15 -1.48908113E+05+38.3\*T  
 +5\*GHSERAL#+GHSERMO#; 6000 N Peng !

PHASE AL63MO37 % 2 63 37 !  
 CONSTITUENT AL63MO37 :AL : MO : !  
 PARAMETER G(AL63MO37,AL:MO;0) 298.15  
 -1.51552361E+06-1.76057703E+02\*T  
 +63\*GHSERAL#+37\*GHSERMO#; 6000 N Peng !

PHASE AL8MO3 % 2 8 3 !  
 CONSTITUENT AL8MO3 :AL : MO : !  
 PARAMETER G(AL8MO3,AL:MO;0) 2.98150E+02  
 -432300+128.341056\*T+8\*GHSERAL  
 +3\*GHSERMO; 6.00000E+03 N 10Cup !

-----  
 \$  
 \$  
 05Zhou  
 \$

NI-MO

The thermodynamic dataset of Ni-Al-Cr-Mo-O

```

PARAMETER L(IONIC_LIQ,MO+4,NI+2:VA;0) 298.15 -39597+15.935*T;
6000 N 05Zho !
PARAMETER L(IONIC_LIQ,MO+4,NI+2:VA;1) 298.15 -7373+4.102*T;
6000 N 05Zho !
PARAMETER L(IONIC_LIQ,MO+4,NI+2:VA;2) 298.15 -12123+5.551*T;
6000 N 05Zho !

PARAMETER L(BCC_A2,MO,NI:VA;0) 298.15 27691; 6000 N 05Zho !
PARAMETER L(BCC_A2,MO,NI:VA;1) 298.15 18792; 6000 N 05Zho !
PARAMETER L(FCC_A1,MO,NI:VA;0) 298.15 -8916+3.591*T; 6000 N
05Zho !
PARAMETER L(FCC_A1,MO,NI:VA;1) 298.15 5469-0.249*T; 6000 N
05Zho !
PARAMETER L(FCC_A1,MO,NI:VA;2) 298.15 -1549-2.741*T; 6000 N
05Zho !
$MO-Ni metastable
$FUNCTION U1CRNI 298.15 -1980;,,,N 01DUP !
FUNCTION U1MONI 298.15 0;,,,N 01DUP !
$FUNCTION U1CRNI 298.15 -7060+3.63*T;,,,N 01DUP !
FUNCTION U3MONI 298.15 0;,,,N 01DUP !
FUNCTION U4MONI 298.15 0;,,,N 01DUP !
FUNCTION L04MONI 298.15 U3MONI;,,,N 01DUP !
FUNCTION L14MONI 298.15 U4MONI;,,,N 01DUP !
FUNCTION MONI3 298.15 +3*U1MONI;,,,N 01DUP !
FUNCTION MO2NI2 298.15 +4*U1MONI;,,,N 01DUP !
FUNCTION MO3NI 298.15 +3*U1MONI;,,,N 01DUP !
PARAMETER G(FCC_L12,NI:MO:VA;0) 298.15 +MONI3;,,, N 01DUP !
PARAMETER G(FCC_L12,MO:NI:VA;0) 298.15 +MO3NI;,,, N 01DUP !
PARAMETER L(FCC_L12,MO,NI:MO:VA;0) 298.15
-1.5*MONI3+1.5*MO2NI2+1.5*MO3NI;,,,N 01DUP !
PARAMETER L(FCC_L12,MO,NI:NI:VA;0) 298.15
+1.5*MONI3+1.5*MO2NI2-1.5*MO3NI;,,,N 01DUP !
PARAMETER L(FCC_L12,MO,NI:MO:VA;1) 298.15
+0.5*MONI3-1.5*MO2NI2+1.5*MO3NI;,,,N 01DUP !
PARAMETER L(FCC_L12,MO,NI:NI:VA;1) 298.15
-1.5*MONI3+1.5*MO2NI2-0.5*MO3NI;,,,N 01DUP !
PARAMETER L(FCC_L12,*,MO,NI:VA;0) 298.15 +L04MONI;,,,N 01DUP !
PARAMETER L(FCC_L12,*,MO,NI:VA;1) 298.15 +L14MONI;,,,N 01DUP !
PARAMETER L(FCC_L12,MO,NI:*,VA;0) 298.15 +3*L04MONI;,,,N 01DUP !
PARAMETER L(FCC_L12,MO,NI:*,VA;1) 298.15 +3*L14MONI;,,,N 01DUP !

PHASE NIMO % 3 24 20 12 !
CONSTITUENT NIMO :CR,NI : CR,AL,MO,NI : MO : !
PARAMETER G(NIMO,NI:MO:MO;0) 298.15
-169981+1154.981*T-155.484*T*LN(T)
+24*GHSERNI+32*GHSERMO; 6000 N 05Zho !
PARAMETER G(NIMO,NI:NI:MO;0) 298.15
-154106+2855.001*T-394.923*T*LN(T)
+24*GHSERNI+20*GBCCNI+12*GHSERMO; 6000 N 05Zho !
PARAMETER L(NIMO,NI:MO,NI:MO;0) 298.15 -829211+825.923*T; 6000 N
05Zho !
PARAMETER L(NIMO,NI:MO,NI:MO;1) 298.15 -417368+326.504*T; 6000 N
05Zho !

PHASE NI3MO % 3 4 2 2 !
CONSTITUENT NI3MO :MO,NI : NI: MO,NI,AL : !
PARAMETER G(NI3MO,MO:NI:MO;0) 298.15

```



```

+29712.79*T**(-1); 3900 Y
405552.207-231.021687*T-7.917452*T*ln(T)
-0.00561629*T**2+1.15094683e-007*T**3
-21023455*T**(-1); 8600 Y
-32256.1765+515.633032*T-91.14493*T*ln(T)
+0.0014422145*T**2+2.59522333e-009*T**3
+413221300*T**(-1); 10000 N !
Function F12868T 298.15 -29214.2558-18.2585839*T
-36.21138*T*ln(T)-0.02000383*T**2
+3.52112833e-006*T**3+189514.45*T**(-1); 700 Y
-38502.2711+114.501443*T-56.53743*T*ln(T)
-0.0002916212*T**2-5.32984e-008*T**3
+982861.5*T**(-1); 3900 Y
-1708.96675-29.7265541*T-38.59226*T*ln(T)
-0.004131674*T**2+9.85369833e-008*T**3
-13058890*T**(-1); 6000 N !
Function F12881T 298.15 -385452.75+111.238018*T
-55.14262*T*ln(T)-0.025763795*T**2
+4.57728333e-006*T**3+380793.5*T**(-1); 700 Y
-399048.407+295.089953*T-83.06149*T*ln(T)
+0.00016539945*T**2-2.29327833e-008*T**3
+1641495*T**(-1); 3600 Y
-365295.293+210.184114*T-73.23294*T*ln(T)
-0.000800648*T**2-2.14918833e-008*T**3
-17719045*T**(-1); 6000 N !
Function F12904T 298.15 892320.138+5.95304372*T
-37.156*T*ln(T)+3.61e-005*T**2
-1.10858333e-007*T**3+113615*T**(-1); 1000 Y
878307.025+162.383892*T-60.077*T*ln(T)
+0.0165846*T**2-2.3378e-006*T**3
+1706980*T**(-1); 1800 Y
1105100.83-1223.34666*T+124.219*T*ln(T)
-0.05020415*T**2+2.21706167e-006*T**3
-50788800*T**(-1); 3100 Y
641365.422+619.744903*T-105.798*T*ln(T)
+0.00065385*T**2+1.02916667e-007*T**3
+125079000*T**(-1); 6000 N !
Function F12914T 298.15 -1196515.3+475.148267*T
-122.7186*T*ln(T)-0.0555182*T**2
+9.881975e-006*T**3+905237.5*T**(-1); 700 Y
-1224927.81+862.847979*T-181.6815*T*ln(T)
-0.00025878435*T**2+9.21776833e-009*T**3
+3510247*T**(-1); 6000 N !
Function F12921T 298.15 -1973406.71+821.17695*T
-189.5329*T*ln(T)-0.08545285*T**2
+1.514856e-005*T**3+1204267*T**(-1); 700 Y
-2017565.22+1421.04602*T-280.6938*T*ln(T)
-0.0004180418*T**2+1.488785e-008*T**3
+5275200*T**(-1); 6000 N !
Function F12927T 298.15 -2723570.91+1223.62426*T
-261.8078*T*ln(T)-0.1108959*T**2
+1.96875e-005*T**3+1666596*T**(-1); 700 Y
-2780675.44+2000.63179*T-379.9209*T*ln(T)
-0.0005325365*T**2
+1.89757833e-008*T**3+6920375*T**(-1); 6000 N !
Function F12931T 298.15 -3453009.31+1610.12421*T
-331.4199*T*ln(T)-0.13861135*T**2
+2.46066667e-005*T**3+2099000*T**(-1); 700 Y

```

```

-3524391.16+2581.37543*T-479.0592*T*ln(T)
-0.000664948*T**2+2.36668e-008*T**3
+8666450*T**(-1); 6000 N !
Function F12859T 298.15 -737914.48+498.826364*T
-83.772*T*ln(T)+0.00127165*T**2
-3.76915e-006*T**3+661760*T**(-1); 800 Y
-727049.309+357.003784*T-62.391*T*ln(T)
-0.01753945*T**2-6.51193333e-007*T**3
-380915*T**(-1); 1500 N !
Function F12865T 298.15 -759648.196+516.479362*T
-87.136*T*ln(T)+0.00259145*T**2
-4.30271667e-006*T**3+671715*T**(-1); 800 Y
-746850.031+349.150033*T-61.903*T*ln(T)
-0.0196438*T**2-6.12506667e-007*T**3
-553705*T**(-1); 1500 N !
Function F12857T 298.15 -617279.692+462.340685*T
-74.52171*T*ln(T)+0.000468436*T**2
-1.5889975e-006*T**3+852479*T**(-1); 3000 N !
Function F12873T 298.15 -770709.73+429.565328*T
-73.51818*T*ln(T)-0.01744741*T**2
-8.33756833e-010*T**3+393450.8*T**(-1); 1075 Y
-807305.95+818.499025*T-127*T*ln(T); 3000 N !
$ only low-T part of F12873T (solid MoO3)
Function F12874T 298.15 -770709.73+429.565328*T
-73.51818*T*ln(T)-0.01744741*T**2
-8.33756833e-010*T**3+393450.8*T**(-1); 3000 N !
$ only high-T part of F12873T (liquid MoO3)
Function F12875T 298.15 -758607.95+773.199025*T-127*T*ln(T); 3000 N
!
Function GMOFCC 298.15 7453.698+132.5497*T
-23.56414*T*ln(T)-0.003443396*T**2
+5.66283e-007*T**3+65812*T**(-1)-1.30927e-010*T**4; 2896 Y
-15356.41+284.189746*T-42.63829*T*ln(T)
-4.849315e+033*T**(-9); 5000 N !
Function GMOHCP 298.15 3803.698+131.9197*T
-23.56414*T*ln(T)-0.003443396*T**2
+5.66283e-007*T**3+65812*T**(-1)-1.30927e-010*T**4; 2896 Y
-19006.41+283.559746*T-42.63829*T*ln(T)
-4.849315e+033*T**(-9); 5000 N !
Function GHSERSI 298.14 -8162.609+137.236859*T
-22.8317533*T*ln(T)-0.001912904*T**2
-3.552e-009*T**3+176667*T**(-1); 1687 Y
-9457.642+167.281367*T-27.196*T*ln(T)
-4.20369e+030*T**(-9); 3600 N !
$Function GHSERMO 298.14 -7746.302+131.9197*T
$ -23.56414*T*ln(T)-0.003443396*T**2
$ +5.66283e-007*T**3+65812*T**(-1)-1.30927e-010*T**4; 2896 Y
$ -30556.41+283.559746*T-42.63829*T*ln(T)
$ -4.849315e+033*T**(-9); 5000 N !
Function GMO8O23 298.15 -744437+347*T-61.603*T*ln(T)-0.0194438*T**2
-6.12506667e-007*T**3-553705*T**(-1); 1500 N !

Parameter G(GAS,MO1O1;0) 298.15 +F12851T+R*T*ln(1e-005*P); 6000 N !
Parameter G(GAS,MO1O2;0) 298.15 +F12868T+R*T*ln(1e-005*P); 6000 N !
Parameter G(GAS,MO1O3;0) 298.15 +F12881T+R*T*ln(1e-005*P); 6000 N !
Parameter G(GAS,MO2;0) 298.15 +F12904T+R*T*ln(1e-005*P); 6000 N !
Parameter G(GAS,MO2O6;0) 298.15 +F12914T+R*T*ln(1e-005*P); 6000 N !

```

The thermodynamic dataset of Ni-Al-Cr-Mo-O

---

```
Parameter G(GAS,MO3O9;0) 298.15 +F12921T+R*T*ln(1e-005*P)-19000;
6000 N !
Parameter G(GAS,MO4O12;0) 298.15 +F12927T+R*T*ln(1e-005*P); 6000 N !
Parameter G(GAS,MO5O15;0) 298.15 +F12931T+R*T*ln(1e-005*P); 6000 N !
```

```
PARAMETER G(IONIC_LIQ,MO+4:O-2;0)
298.15 +2*F12857T+35400+34.3*T; 6000.0 N 17We !
PARAMETER G(IONIC_LIQ,MO+6:O-2;0)
298.15 +2*F12873T+101000-93.4*T; 6000.0 N 17We !
PARAMETER L(IONIC_LIQ,MO+4,MO+6:O-2;0) 298.15 -63000; 6000.0 N
17We !
PARAMETER L(IONIC_LIQ,MO+4:O-2,VA;0) 298.15 -20000; 6000.0 N
17We !
```

```
$this parameter is redefined in this work based on Srivastava's
PARAMETER G(BCC_A2,MO:O;0)
298.15 +GHSERMO+3*GHSEROO-146000+120*T; 6000 N 17we!
```

```
Phase MO4011 % 2 1 2.75 !
Constituent MO4011 :MO:O:!
Parameter G(MO4011,MO:O;0) 298.15 +F12859T; 6000 N !
```

```
Phase MO9O26 % 2 1 2.889 !
Constituent MO9O26 :MO:O:!
Parameter G(MO9O26,MO:O;0) 298.15 +F12865T; 6000 N !
```

```
Phase MO8O23 % 2 1 2.875 !
Constituent MO8O23 :MO:O:!
Parameter G(MO8O23,MO:O;0) 298.15 +GMO8O23; 6000 N !
```

```
Phase MO1O2 % 2 1 2 !
Constituent MO1O2 :MO,O:MO,O:!
Parameter G(MO1O2,MO:MO;0) 298.15 34486+53*T+3*GHSERMO; 6000 N !
Parameter G(MO1O2,MO:O;0) 298.15 +F12857T; 6000 N !
Parameter G(MO1O2,O:O;0) 298.15 8000+3*GHSEROO; 6000 N !
Parameter G(MO1O2,MO,O:O;0) 298.15 -10000; 6000 N !
```

```
Phase MO1O3 % 2 1 3 !
Constituent MO1O3 :MO:O:!
Parameter G(MO1O3,MO:O;0) 298.15 +F12874T; 6000 N !
```

```
$*****
*****
$
$
PARAMETERS TERNARY
$
$-----
-----
$
```

```

$
Al-Cr-Ni
$
$                                     July 1999, ND
$                                     Revision. Main changes:
$                                     - description of the A2/B2
$                                     - new liquidus data taken into
account
$                                     - simpler ternary interaction
parameters
$
$
LIQUID PHASE
$
PARAMETER L(IONIC_LIQ,AL+3,CR+3,NI+2:VA;0) 298.15 38000;,,N
16peng !
PARAMETER L(IONIC_LIQ,AL+3,CR+3,NI+2:VA;1) 298.15 6000;,,N
16peng !
PARAMETER L(IONIC_LIQ,AL+3,CR+3,NI+2:VA;2) 298.15 16000;,,N
16peng !
$
FCC_A1 PHASE
$
PARAMETER G(FCC_A1,AL,CR,NI:VA;0) 298.15 30300;,,N 01DUP !
$
BCC_A2 PHASE
$
PARAMETER G(BCC_A2,AL,CR,NI:VA;0) 298.15 42500;,,N 01DUP !
$
$
FCC_L12 PHASE
$
FUN U1ALCRNI 298.15 6650;,,N 01DUP !
FUN U2ALCRNI 298.15 0;,,N 01DUP !
FUN U3ALCRNI 298.15 0;,,N 01DUP !
FUN ALCRNI2 298.15 U1ALCR+2*U1ALNI+2*U1CRNI+U1ALCRNI;,,N 01DUP !
FUN ALCR2NI 298.15 2*U1ALCR+U1ALNI+2*U1CRNI+U2ALCRNI;,,N 01DUP !
FUN AL2CRNI 298.15 2*U1ALCR+2*U1ALNI+U1CRNI+U3ALCRNI;,,N 01DUP !
PARA L(FCC_L12,AL,CR,NI:AL:VA;0) 298.15
-1.5*ALCRNI2-1.5*ALCR2NI+ALCR3+ALNI3+6*AL2CRNI
-1.5*AL2CR2-1.5*AL2NI2-1.5*AL3CR-1.5*AL3NI;,,N 01DUP !
PARA L(FCC_L12,AL,CR,NI:CR:VA;0) 298.15
-1.5*ALCRNI2+6*ALCR2NI-1.5*ALCR3-1.5*AL2CRNI
-1.5*AL2CR2+AL3CR+CRNI3-1.5*CR2NI2-1.5*CR3NI;,,N 01DUP !
PARA L(FCC_L12,AL,CR,NI:NI:VA;0) 298.15
+6*ALCRNI2-1.5*ALCR2NI-1.5*ALNI3-1.5*AL2CRNI
-1.5*AL2NI2+AL3NI-1.5*CRNI3-1.5*CR2NI2+CR3NI;,,N 01DUP !
PARA L(FCC_L12,AL,CR:NI:VA;0) 298.15
+1.5*ALCR2NI+1.5*AL2CRNI-1.5*AL3NI-1.5*CR3NI;,,N 01DUP !
PARA L(FCC_L12,AL,NI:CR:VA;0) 298.15
+1.5*ALCRNI2+1.5*AL2CRNI-1.5*AL3CR-1.5*CRNI3;,,N 01DUP !
PARA L(FCC_L12,CR,NI:AL:VA;0) 298.15
+1.5*ALCRNI2+1.5*ALCR2NI-1.5*ALCR3-1.5*ALNI3;,,N 01DUP !
PARA L(FCC_L12,AL,CR:NI:VA;1) 298.15
-1.5*ALCR2NI+1.5*AL2CRNI-0.5*AL3NI+0.5*CR3NI;,,N 01DUP !
PARA L(FCC_L12,AL,NI:CR:VA;1) 298.15

```

The thermodynamic dataset of Ni-Al-Cr-Mo-O

```

-1.5*ALCRNI2+1.5*AL2CRNI-0.5*AL3CR+0.5*CRNI3;,,N 01DUP !
PARAM L(FCC_L12,CR,NI:AL:VA;1) 298.15
-1.5*ALCRNI2+1.5*ALCR2NI-0.5*ALCR3+0.5*ALNI3;,,N 01DUP !
$
$-----
-----
$
$
Al-MO-Ni

PARAMETER L(IONIC_LIQ ,AL+3,MO+4,NI+2:VA;0) 298.15 0; 6000 N Peng !
PARAMETER L(IONIC_LIQ ,AL+3,MO+4,NI+2:VA;1) 298.15 0; 6000 N Peng !
PARAMETER L(IONIC_LIQ ,AL+3,MO+4,NI+2:VA;2) 298.15 144400; 6000 N
Peng !

PARAMETER L(BCC_A2,AL,MO,NI:VA;0) 298.15 280000;,,N Peng !

$ AL-NI-MO
$FUNCTION U1ALCRNI 298.15 6650;,,N 01DUP !
FUNCTION U1ALMONI 298.15 13000;,,N Peng !
FUNCTION U2ALMONI 298.15 0;,,N 01DUP !
FUNCTION U3ALMONI 298.15 5000;,,N Peng !
FUNCTION ALMONI2 298.15 U1ALMO+2*U1ALNI+2*U1MONI+U1ALMONI;,,N 01DUP !
FUNCTION ALMO2NI 298.15 2*U1ALMO+U1ALNI+2*U1MONI+U2ALMONI;,,N 01DUP !
FUNCTION AL2MONI 298.15 2*U1ALMO+2*U1ALNI+U1MONI+U3ALMONI;,,N 01DUP !
PARAMETER L(FCC_L12,AL,MO,NI:AL:VA;0) 298.15
-1.5*ALMONI2-1.5*ALMO2NI+ALMO3+ALNI3+6*AL2MONI
-1.5*AL2MO2-1.5*AL2NI2-1.5*AL3MO-1.5*AL3NI;,,N 01DUP !
PARAMETER L(FCC_L12,AL,MO,NI:MO:VA;0) 298.15
-1.5*ALMONI2+6*ALMO2NI-1.5*ALMO3-1.5*AL2MONI
-1.5*AL2MO2+AL3MO+MONI3-1.5*MO2NI2-1.5*MO3NI;,,N 01DUP !
PARAMETER L(FCC_L12,AL,MO,NI:NI:VA;0) 298.15
+6*ALMONI2-1.5*ALMO2NI-1.5*ALNI3-1.5*AL2MONI
-1.5*AL2NI2+AL3NI-1.5*MONI3-1.5*MO2NI2+MO3NI;,,N 01DUP !
PARAMETER L(FCC_L12,AL,MO:NI:VA;0) 298.15
+1.5*ALMO2NI+1.5*AL2MONI-1.5*AL3NI-1.5*MO3NI;,,N 01DUP !
PARAMETER L(FCC_L12,AL,NI:MO:VA;0) 298.15
+1.5*ALMONI2+1.5*AL2MONI-1.5*AL3MO-1.5*MONI3;,,N 01DUP !
PARAMETER L(FCC_L12,MO,NI:AL:VA;0) 298.15
+1.5*ALMONI2+1.5*ALMO2NI-1.5*ALMO3-1.5*ALNI3;,,N 01DUP !
PARAMETER L(FCC_L12,AL,MO:NI:VA;1) 298.15
-1.5*ALMO2NI+1.5*AL2MONI-0.5*AL3NI+0.5*MO3NI;,,N 01DUP !
PARAMETER L(FCC_L12,AL,NI:MO:VA;1) 298.15
-1.5*ALMONI2+1.5*AL2MONI-0.5*AL3MO+0.5*MONI3;,,N 01DUP !
PARAMETER L(FCC_L12,MO,NI:AL:VA;1) 298.15
-1.5*ALMONI2+1.5*ALMO2NI-0.5*ALMO3+0.5*ALNI3;,,N 01DUP !

PARAM L(FCC_A1,AL,MO,NI:VA;0) 298.15 8543-13.5*T; 6000 N !
PARAM L(FCC_A1,AL,MO,NI:VA;1) 298.15 81408-44.64*T; 6000 N !
PARAM L(FCC_A1,AL,MO,NI:VA;2) 298.15 173588-32.53*T; 6000 N !

PARAM G(NIMO,NI:AL:MO;0) 298.15 -3140000+895*T

```

```

+24*GHSEJNI+20*GBCCAL+12*GHSEMO; 6000 N Peng!

PARAM G(NI3MO,NI:NI:AL;0) 298.15 -309000+31.2*T
+4*GHSEJNI+2*GHSEJNI+2*GBCCAL; 6000 N Peng !

PARAM G(NI4MO,NI:AL;0) 298.15 -161200+19.7*T+4*GHSEJNI+GBCCAL; 6000
N Peng!

PHASE X % 3 .75 .11 .14 !
CONSTITUENT X :AL : MO : NI : !
PARAMETER G(X,AL:MO:NI;0) 298.15 -39464.2+6.521*T
+.75*GHSEAL#+.14*GHSEJNI#+.11*GHSEMO#; 6000 N 14Zhou !

PHASE N % 3 2 1 1 !
CONSTITUENT N :AL,NI : AL,NI : MO : !
PARAMETER G(N,AL:AL:MO;0) 298.15
-108760+22.128*T+3*GHSEAL#
+GHSEMO#; 6000 N 14Zhou !
PARA G(N,NI:AL:MO;0) 298.15 +0; 6000 N!
PARAMETER G(N,AL:NI:MO;0) 298.15
-119040+2*GHSEAL#+GHSEJNI#
+GHSEMO#; 6000 N 14Zhou !
PARAMETER G(N,NI:NI:MO;0) 298.15
-29600+32.028*T+3*GHSEJNI#
+GHSEMO#; 6000 N 14Zhou !
PARAMETER G(N,AL:AL,NI:MO;0) 298.15 -140870; 6000 N
14Zhou !
PARAMETER G(N,AL:AL,NI:MO;1) 298.15 -60570; 6000 N
14Zhou !
$-----
$
$
Al-Cr-O
$
LIQUID PHASE

PARAMETER G(IONIC_LIQ,CR+3:O-2,ALO3/2;0) 2.98150E+02 90686.3571
-1.02149238*T ;
6.00000E+03 N 04salt !

$
ALCRO PHASE

PARAMETER G(ALCRO,AL+3:CR+3:O-2;0) 298.15 0; 6000 N!
PARAMETER G(ALCRO,AL+3,CR+3:VA:O-2;0) 2.98150E+02 +2.82488153E+04
+9.18913289*T; 6.00000E+03 N 04salt !
PARAMETER G(ALCRO,AL+3,CR+3:VA:O-2;1) 2.98150E+02 -3493.30143
+4.58638227*T; 6.00000E+03 N 04salt !
$-----
$
$
Cr-Ni-O

FUNCTION GNICR204 2.98140E+02
-1442728.78+1005.1*T-167.1508*T*LN(T)

```

The thermodynamic dataset of Ni-Al-Cr-Mo-O

---

```

-0.00893284*T**2+1052276*T**(-1); 2.60000E+03 N !

$
LIQUID PHASE

PARAMETER L(IONIC_LIQ,CR+3,NI+2:O-2;0) 298.15 +60000-49.1*T;
6000 N 08Kje !
PARAMETER L(IONIC_LIQ,CR+3,NI+2:O-2,VA;0) 2.98150E+02 -340000;
6000 N 08Kje !
PARAMETER L(IONIC_LIQ,CR+3,NI+2:O-2,VA;0) 298.15 -340000; 6000 N
08Kje !
PARAMETER L(IONIC_LIQ,CR+3,NI+2:O-2,VA;2) 298.15 +240000; 6000 N
08Kje !

$
ALCRO PHASE
PARAMETER G(ALCRO,CR+2:NI+2:O-2;0) 2.98150E+02
+665910+GCR2O3#;
6.00000E+03 N 04salt !
PARAMETER TC(ALCRO,CR+2:NI+2:O-2;0) 2.98150E+02 306;
6.00000E+03 N
90DIN !
PARAMETER BMAGN(ALCRO,CR+2:NI+2:O-2;0) 2.98150E+02 1.938;
6.00000E+03
N REF:0 !
PARAMETER G(ALCRO,CR+3:NI+2:O-2;0) 2.98150E+02
+GCR2O3#+28048.1+54.4*T;
6.00000E+03 N 90DIN !
PARAMETER TC(ALCRO,CR+3:NI+2:O-2;0) 2.98150E+02 306;
6.00000E+03 N
90DIN !
PARAMETER BMAGN(ALCRO,CR+3:NI+2:O-2;0) 2.98150E+02 1.938;
6.00000E+03
N REF:0 !

$
SPINEL PHASE

PHASE SPINEL:I %- 4 1 2 2 4 !
CONSTITUENT SPINEL:I
:AL+3,CR+3,NI+2,CR+2,VA:AL+3%,CR+3,NI+2,VA:VA%,CR+2: O-2 : !

$ data base 08Kje is used:

FUNCTION AS 298.15 +142000; 6000 N !
FUNCTION BS 298.15 +46826-27.266*T; 6000 N !
FUNCTION CS 298.15 +120730-20.102*T; 6000 N !
FUNCTION DS 298.15 +402520-30.529*T; 6000 N !
FUNCTION ES 298.15 -153200+173.55*T-28.259*T*LN(T)
-3.2E-04*T**2+29100*T**(-1); 6000 N !
FUNCTION FS 298.15 -214607.7+138.83*T-23.28714*T*LN(T)
-0.001595929*T**2+227729.3*T**(-1); 6000 N !
FUNCTION GS 298.15 -161731+144.873*T-24.9879*T*LN(T)
-0.0011952256*T**2+206520*T**(-1); 6000 N !
FUNCTION HS 298.15 -1442728.78+1005.1*T-167.1508*T*LN(T)

```

```

-0.00893284*T**2+1052276*T**(-1); 6000 N !
FUNCTION RS 298.15 +156000-3.37*T; 6000 N !
FUNCTION SS 298.15 +46028.95+38.73173*T-11.58574*T*LN(T)
+0.006411774*T**2; 6000 N !
FUNCTION DG 298.15 +1.5*HS-10.5*ES+0.5*AS+10.5*GS-0.5*BS-10.5*FS-RS
+71546; 6000 N !

PARAMETER G (SPINEL,CR+2:CR+3:CR+2:O-2;0) 298.15
+10.5*FS-1.5*GS-1.5*BS+DS+RS+SS; 6000 N !
PARAMETER G (SPINEL,CR+3:CR+3:CR+2:O-2;0) 298.15
+10.5*FS-1.5*GS-1.5*BS+DS+RS; 6000 N !

$this line was missing
PARAMETER G (SPINEL,NI+2:CR+3:CR+2:O-2;0) 298.15 +HS+2*GS-BS+DS;
6000 N !

PARAMETER G (SPINEL,CR+2:NI+2:CR+2:O-2;0) 298.15
+14*ES-AS+3.5*FS-8.5*GS+0.5*BS+DS+RS+SS; 6000 N !
PARAMETER G (SPINEL,CR+3:NI+2:CR+2:O-2;0) 298.15
+HS+2*GS-BS+DS+71546; 6000 N !

PARAMETER G (SPINEL,NI+2:NI+2:CR+2:O-2;0) 298.15
+21*ES-AS-12*GS+BS+DS; 6000 N !
PARAMETER G (SPINEL,CR+2:VA:CR+2:O-2;0) 298.15
+3.5*FS+3.5*GS-1.5*BS+CS+DS+RS+SS; 6000 N !
PARAMETER G (SPINEL,CR+3:VA:CR+2:O-2;0) 298.15
+3.5*FS+3.5*GS-1.5*BS+CS+DS+RS; 6000 N !

PARAMETER G (SPINEL,NI+2:VA:CR+2:O-2;0) 298.15 +7*ES-BS+CS+DS; 6000
N !
PARAMETER G (SPINEL,CR+2:CR+3:VA:O-2;0) 298.15
+10.5*FS-3.5*GS-0.5*BS+RS+SS; 6000 N !
PARAMETER G (SPINEL,CR+3:CR+3:VA:O-2;0) 298.15
+10.5*FS-3.5*GS-0.5*BS+RS; 6000 N !

PARAMETER G (SPINEL,NI+2:CR+3:VA:O-2;0) 298.15 +HS; 6000 N !

PARAMETER G (SPINEL,CR+2:NI+2:VA:O-2;0) 298.15
+14*ES-AS+3.5*FS-10.5*GS+1.5*BS+RS+SS; 6000 N !
PARAMETER G (SPINEL,CR+3:NI+2:VA:O-2;0) 298.15
+2*HS-10.5*FS+3.5*GS+0.5*BS-RS+143092; 6000 N !

PARAMETER G (SPINEL,NI+2:NI+2:VA:O-2;0) 298.15
+21*ES-AS-14*GS+2*BS; 6000 N !

PARAMETER G (SPINEL,CR+2:VA:VA:O-2;0) 298.15
+3.5*FS+1.5*GS-0.5*BS+CS+RS+SS; 6000 N !
PARAMETER G (SPINEL,CR+3:VA:VA:O-2;0) 298.15
+3.5*FS+1.5*GS-0.5*BS+CS+RS; 6000 N !

PARAMETER G (SPINEL,NI+2:VA:VA:O-2;0) 298.15 +7*ES-2*GS+CS; 6000
N !

```

```

PARAMETER TC (SPINEL,CR+2:CR+3:VA:O-2;0) 298.15 +100; 6000 N !
PARAMETER BMAGN (SPINEL,CR+2:CR+3:VA:O-2;0) 298.15 +0.9; 6000 N !
PARAMETER TC (SPINEL,CR+3:CR+3:VA:O-2;0) 298.15 +100; 6000 N !
PARAMETER BMAGN (SPINEL,CR+3:CR+3:VA:O-2;0) 298.15 +0.9; 6000 N !
PARAMETER TC (SPINEL,NI+2:NI+2:VA:O-2;0) 298.15 +858; 6000 N
08Kje !
PARAMETER BMAGN (SPINEL,NI+2:NI+2:VA:O-2;0) 298.15 +0.0; 6000 N
08Kje !
PARAMETER L (SPINEL,CR+3,NI+2:NI+2:VA:O-2;0) 298.15 +DG; 6000 N !
PARAMETER L (SPINEL,CR+3,NI+2:CR+3:VA:O-2;0) 298.15 +DG; 6000 N !

```

```

$
HALITE PHASE

```

```

PARAMETER L (HALITE,CR+3,NI+2:O-2;0) 298.15 +61000-26*T; 6000 N
08Kje !

```

```

$-----
-----

```

```

$
$
Al-Ni-O

```

```

$
LIQUID PHASE

```

```

PARAMETER G (IONIC_LIQ,NI+2:O-2,ALO3/2;0) 2.98150E+02 35000;
6.00000E+03 N 04salt !
PARAMETER G (IONIC_LIQ,NI+2:O-2,ALO3/2;1) 2.98150E+02 -2000;
6.00000E+03 N 04salt !

```

```

$this parameter was added to fit the o and al solubility in liquid
Ni at 1873

```

```

$based on data from Vachet 1965

```

```

PARAMETER G (IONIC_LIQ,NI+2:ALO3/2,VA;0) 2.98150E+02 4e5;
6.00000E+03 N we !

```

```

$
ALCRO PHASE

```

```

PARAMETER G (ALCRO,AL+3:NI+2:O-2;0) 298.15 0; 6000 N!

```

```

$
HALITE PHASE

```

```

PARAMETER G (HALITE,AL+3,NI+2:O-2;0) 2.98150E+02 -40000+32*T;
6.00000E+03 N 04salt !

```

```

FUNCTION NSPINEL 298 +GBUNSEN+GCRUND+2.32880000E+04-9.06*T;

```

```

6000 N !
FUNCTION ISPINEL      298 +NSPINEL-1.91134000E+04; 6000 N !

FUNCTION GGAMMA      2.98140E+02
-1689977.34+469.458181*T-70.5452*T*LN(T)
  -0.070794*T**2+1.491345E-05*T**3+981165*T**(-1); 6.00000E+02 Y
  -1708389.72+791.591946*T-121.754*T*LN(T)-.0075467*T**2
  +2.89573E-07*T**3+2222750*T**(-1); 1.50000E+03 Y
  -1758861.74+1110.41976*T-164.253*T*LN(T)+.00775305*T**2
  -6.8247E-07*T**3+13162750*T**(-1); 3.00000E+03 N !
FUNCTION ISPIN_CF    2.98150E+02 +11.526358*T; 6.00000E+03 N !
FUNCTION ISP         2.98150E+02 +ISPINEL#+ISPIN_CF#+22000;
6.00000E+03
N !
FUNCTION SPALNI      2.98150E+02 +2*ISP#-1.5*GGAMMA#-3*G_CF#;
6.00000E+03
N !

FUNCTION G_CF        2.98150E+02 +2.80965*T+.015*T*LN(T);
6.00000E+03 N !

FUNCTION G2AV        298.15 +7*NSPFEEAL#; 6000 N 93Tayl!
FUNCTION G22V        298.15 +7*GS#+BS#; 6000 N 93Tayl!
FUNCTION SPJ2A       298.15 31300; 6000 N 98Harri!
$ FUNCTION NSPFEEAL  298.15
-287500+136*T-22.1991*T*LN(T)-.001867857*T**2
$ +223844*T**(-1); 6000 N!
FUNCTION NSPFEEAL   360 -291278.9 +
138.0033*T-21.9429*T*ln(T)-0.002905*T**2
+258064.3*T**(-1)-1.73859E-07*T**3; 6000 N 16Shish!
FUNCTION RSFA       298.15 +32000; 6000 N !

FUNCTION SPALVA      2.98150E+02 +GHSERAL#+2*GHSEROO#;
6.00000E+03 N !
FUNCTION GALAL       2.98150E+02 +1.5*G2AV#-.5*G22V#+SPJ2A#; 6000 N
93Barry!

$
PHASE
SPINEL

PARAMETER G (SPINEL,AL+3:AL+3:VA:O-2;0) 2.98150E+02
+GALAL#; 6.00000E+03 N REF51 !

PARAMETER G (SPINEL,AL+3:VA:VA:O-2;0) 2.98150E+02
+44.952*T+8*GGAMMA#-5*GALAL#; 6.00000E+03 N REF51 !

```

The thermodynamic dataset of Ni-Al-Cr-Mo-O

---

```

PARAMETER G(SPINEL,NI+2:AL+3:VA:O-2;0) 2.98150E+02 +NSPINEL#;
6.00000E+03 N 17we!

PARAMETER G(SPINEL,AL+3:NI+2:VA:O-2;0) 2.98150E+02
2*ISPINEL#+23.0513*T-GALAL#; 6.00000E+03 N 17we !

$ this interaction parameter was added by me using experimental data
$ from Schmalzried 1965
parameter L(SPINEL,AL+3:NI+2,VA:VA:O-2;0) 298.15
-4.08136000E+05+288.3*T;
6000 N 17we!

$these parameters are defined in kjell's work
$ PARAMETER G(SPINEL,NI+2:NI+2:VA:O-2;0) 2.98150E+02
$ +NSPINEL#+2*ISPINEL#+23.0513*T; 6.00000E+03 N REF: 0 !

$ PARAMETER G(SPINEL,NI+2:VA:VA:O-2;0) 2.98150E+02
$ +44.952*T+8*GGAMMA#+NSPINEL#; 6.00000E+03 N REF: 0 !

$-----
-----
$
$
$
Al-Cr-MO
$
Liquid
PARAMETER L(IONIC_LIQ,AL+3,Cr+3,MO+4:VA;0) 298.15 27000; 6000 N
Peng !
$-----
-----
$
$
Ni-Mo-O
FUNCTION GANIMOO4 800 -1052000+371.2*T; 1000 N !
FUNCTION GBNIMOO4 1000 -993000+311.3*T; 1380 N !

PARAMETER G(ALPHA_NIMOO4,NI:MO:O;0) 2.98150E+02 GANIMOO4#
+GHSERNI#+GHSERMO#+4*GHSEROO; 6000
N navr03!
PARAMETER G(BETA_NIMOO4,NI:MO:O;0) 2.98150E+02 GBNIMOO4#
+GHSERNI#+GHSERMO#+4*GHSEROO; 6000
N navr03!

$ using S=231 and cp=241 at RT and decomposition T=1385 from steiner
2005
PARAMETER G(NI2MO3O8,NI:MO:O;0) 2.98150E+02
-1.2618E6+741*T-1026077.52
+2*GHSERNI#+3*GHSERMO#+8*GHSEROO; 6000
N 17we!

$interaction parameter added for NiO-MoO3 T. M. Yanushkevich 1974

PARAM L(IONIC_LIQ,MO+6,NI+2:O-2;0) 298.15 -2.36e4; 6000 N 17we!
PARAM L(IONIC_LIQ,MO+6,NI+2:O-2;1) 298.15 -1.2e5; 6000 N 17we!

```

```

$-----
$
$
Al-Mo-O

PARAM L(IONIC_LIQ,MO+6:ALO3/2,O-2;0) 298.15 -226000; 6000 N 17we!
PARAM L(IONIC_LIQ,MO+6:ALO3/2,O-2;1) 298.15 -207000; 6000 N 17we!

PARAM G(AL2MO3O12,AL:MO:O;0) 298.15
      2*GHSERAL#+3*GHSERMO#+12*GHSEROO#-3860000+917*T; 6000 N 17we!

$-----
$
$
Cr-Mo-Ni

$ PHASE OP6 % 2 1 2 !
$ CONSTITUENT OP6 :CR,MO:MO,NI : !

$ PARAMETER G(OP6,CR:MO;0) 298.15 0; 6000 N 06tur!
$ PARAMETER G(OP6,CR:NI;0) 298.15 -7095-5.6*T+GHSERCR#
$ +2*GHSERNI#; 6000 N 06tur!
$ PARAMETER G(OP6,MO:NI;0) 298.15 +1000+GHSERMO#
$ +2*GHSERNI#; 6000 N 06tur!
$ PARAMETER G(OP6,CR:MO,NI;0) 298.15 -80000; 6000 N 06tur!
$ PARAMETER G(OP6,CR,MO:NI;0) 298.15 -11000; 6000 N 06tur!

PHASE Sigma % 3 8 4 18 !
CONSTITUENT Sigma :NI :CR,MO : CR,MO,NI : !

PARAMETER G(Sigma,NI:CR:CR;0) 298.15 173460-188*T
+8*GHSERNI+4*GHSERCR+18*GHSERCR; 6000 N 90Fri !
PARAMETER G(Sigma,NI:MO:CR;0) 298.15 386423
+8*GHSERNI+4*GHSERMO+18*GHSERCR; 6000 N 90Fri !
PARAMETER G(Sigma,NI:CR:MO;0) 298.15 -110000
+8*GHSERNI+4*GHSERCR+18*GHSERMO; 6000 N Peng !
PARAMETER G(Sigma,NI:MO:MO;0) 298.15 85662
+8*GHSERNI+4*GHSERMO+18*GHSERMO; 6000 N 90Fri !
PARAMETER G(Sigma,NI:CR:NI;0) 298.15 100000
+8*GHSERNI+4*GHSERCR+18*GBCCNI; 6000 N Peng !
PARAMETER G(Sigma,NI:MO:NI;0) 298.15 -16385
+8*GHSERNI+4*GHSERMO+18*GBCCNI; 6000 N 90Fri !

PHASE P %C 3 24 20 12 !
CONSTITUENT P :CR,NI :CR,NI,MO : MO : !

PARAMETER G(P,CR:CR:MO;0) 298.15 252300-100*T
+24*GFCCCR+20*GHSERCR+12*GHSERMO; 6000 N 90Fri !
PARAMETER G(P,NI:CR:MO;0) 298.15 -341858
+24*GHSERNI+20*GHSERCR+12*GHSERMO; 6000 N 90Fri !
PARAMETER G(P,CR:MO:MO;0) 298.15 95573-200*T
+24*GFCCCR+20*GHSERMO+12*GHSERMO; 6000 N 90Fri !
PARAMETER G(P,NI:MO:MO;0) 298.15 26739-90*T

```

```

+24*GHSEJNI+20*GHSEMO+12*GHSEMO; 6000 N Peng !
PARAMETER G(P,CR:NI:MO;0) 298.15 0
+24*GFCCCR+20*GBCCNI+12*GHSEMO; 6000 N Peng !
PARAMETER G(P,NI:NI:MO;0) 298.15 208845-60*T
+24*GHSEJNI+20*GBCCNI+12*GHSEMO; 6000 N Peng !

PARAM G(NIMO,NI:CR:MO;0) 298.15 -200000
+24*GHSEJNI+20*GHSECR+12*GHSEMO; 6000 N 90Fri!
PARAM G(NIMO,CR:NI:MO;0) 298.15 -200000
+24*GFCCCR+20*GBCCNI+12*GHSEMO; 6000 N 90Fri!
PARAM G(NIMO,CR:CR:MO;0) 298.15 50000
+24*GFCCCR+20*GHSECR+12*GHSEMO; 6000 N 90Fri!
PARAM G(NIMO,CR:MO:MO;0) 298.15 100000
+24*GFCCCR+20*GHSEMO+12*GHSEMO; 6000 N 90Fri!

PARAM L(FCC_Al,Mo,CR,NI:VA;0) 298.15 6*T; 6000 N Peng !

$*****
*
$ To make fcc phase correctly disordered in quaterbary system,
$ constraints were added for Cr-Mo, Al-Cr-Mo, Cr-Mo-Ni and AL-Ni-Cr-Mo
$*****
*
$
Cr-MO

FUNCTION U1CRMO 298.15 0;;;,N Peng !
FUNCTION U3CRMO 298.15 0;;;,N Peng !
FUNCTION U4CRMO 298.15 0;;;,N Peng !
FUNCTION L04CRMO 298.15 U3CRMO;;;,N Peng !
FUNCTION L14CRMO 298.15 U4CRMO;;;,N Peng !
FUNCTION CRMO3 298.15 +3*U1CRMO;;;,N Peng!
FUNCTION CR2MO2 298.15 +4*U1CRMO;;;,N Peng !
FUNCTION CR3MO 298.15 +3*U1CRMO;;;,N Peng !
PARAM G(FCC_L12,MO:CR:VA;0) 298.15 CRMO3; 6000 N Peng !
PARAM G(FCC_L12,CR:MO:VA;0) 298.15 CR3MO; 6000 N Peng !

PARAM L(FCC_L12,CR,MO:CR:VA;0) 298.15
-1.5*CRMO3+1.5*CR2MO2+1.5*CR3MO
; 6000 N Peng !
PARAM L(FCC_L12,CR,MO:CR:VA;1) 298.15 +.5*CRMO3-1.5*CR2MO2+1.5*CR3MO
; 6000 N Peng !
PARAM L(FCC_L12,CR,MO:MO:VA;0) 298.15
+1.5*CRMO3+1.5*CR2MO2-1.5*CR3MO
; 6000 N Peng !
PARAM L(FCC_L12,CR,MO:MO:VA;1) 298.15 -1.5*CRMO3+1.5*CR2MO2-.5*CR3MO
; 6000 N Peng !
PARAM L(FCC_L12,*,CR,MO:VA;0) 298.15 +L04CRMO ; 6000 N Peng !
PARAM L(FCC_L12,*,CR,MO:VA;1) 298.15 +L14CRMO ; 6000 N Peng !
PARAM L(FCC_L12,CR,MO:*,VA;0) 298.15 +3*L04CRMO ; 6000 N Peng !
PARAM L(FCC_L12,CR,MO:*,VA;1) 298.15 +3*L14CRMO ; 6000 N Peng !

$*****
*
$
Al-Cr-MO
FUNCTION U1ALCRMO 298.15 0;;;,N Peng !

```

```

FUNCTION U2ALCRMO 298.15 0;,,N Peng !
FUNCTION U3ALCRMO 298.15 0;,,N Peng !
FUNCTION ALCRMO2 298.15 U1ALCR+2*U1ALMO+2*U1CRMO+U1ALCRMO;,,N Peng !
FUNCTION ALCR2MO 298.15 2*U1ALCR+U1ALMO+2*U1CRMO+U2ALCRMO;,,N Peng !
FUNCTION AL2CRMO 298.15 2*U1ALCR+2*U1ALMO+U1CRMO+U3ALCRMO;,,N Peng !
PARAM L(FCC_L12,AL,CR,MO:AL:VA;0) 298.15
-1.5*ALCRMO2-1.5*ALCR2MO+ALCR3+ALMO3
+6*AL2CRMO-1.5*AL2CR2-1.5*AL2MO2-1.5*AL3CR-1.5*AL3MO; 6000 N Peng !
PARAM L(FCC_L12,AL,CR,MO:CR:VA;0) 298.15
-1.5*ALCRMO2+6*ALCR2MO-1.5*ALCR3
-1.5*AL2CRMO-1.5*AL2CR2+AL3CR+CRMO3-1.5*CR2MO2-1.5*CR3MO; 6000 N
Peng !
PARAM L(FCC_L12,AL,CR,MO:MO:VA;0) 298.15
+6*ALCRMO2-1.5*ALCR2MO-1.5*ALMO3
-1.5*AL2CRMO-1.5*AL2MO2+AL3MO-1.5*CRMO3-1.5*CR2MO2+CR3MO; 6000 N
Peng !
PARAM L(FCC_L12,CR,MO:AL:VA;0) 298.15
+1.5*ALCRMO2+1.5*ALCR2MO-1.5*ALCR3
-1.5*ALMO3; 6000 N Peng !
PARAM L(FCC_L12,CR,MO:AL:VA;1) 298.15
-1.5*ALCRMO2+1.5*ALCR2MO-.5*ALCR3
+.5*ALMO3; 6000 N Peng !
PARAM L(FCC_L12,AL,MO:CR:VA;0) 298.15
+1.5*ALCRMO2+1.5*AL2CRMO-1.5*AL3CR
-1.5*CRMO3; 6000 N Peng !
PARAM L(FCC_L12,AL,MO:CR:VA;1) 298.15
-1.5*ALCRMO2+1.5*AL2CRMO-.5*AL3CR
+.5*CRMO3; 6000 N Peng !
PARAM L(FCC_L12,AL,CR:MO:VA;0) 298.15
+1.5*ALCR2MO+1.5*AL2CRMO-1.5*AL3MO
-1.5*CR3MO; 6000 N Peng !
PARAM L(FCC_L12,AL,CR:MO:VA;1) 298.15
-1.5*ALCR2MO+1.5*AL2CRMO-.5*AL3MO
+.5*CR3MO; 6000 N Peng !
$*****
*
$
Cr-MO-NI

FUNCTION U1CRMONI 298.15 0;,,N Peng !
FUNCTION U2CRMONI 298.15 0;,,N Peng !
FUNCTION U3CRMONI 298.15 0;,,N Peng !
FUNCTION CRMONI2 298.15 U1CRMO+2*U1CRNI+2*U1MONI+U1CRMONI;,,N Peng !
FUNCTION CRMO2NI 298.15 2*U1CRMO+U1CRNI+2*U1MONI+U2CRMONI;,,N Peng !
FUNCTION CR2MONI 298.15 2*U1CRMO+2*U1CRNI+U1MONI+U3CRMONI;,,N Peng !

PARAM L(FCC_L12,CR,MO,NI:CR:VA;0) 298.15
-1.5*CRMONI2-1.5*CRMO2NI+CRMO3+CRNI3
+6*CR2MONI-1.5*CR2MO2-1.5*CR2NI2-1.5*CR3MO-1.5*CR3NI; 6000 N Peng !
PARAM L(FCC_L12,CR,MO,NI:MO:VA;0) 298.15
-1.5*CRMONI2+6*CRMO2NI-1.5*CRMO3
-1.5*CR2MONI-1.5*CR2MO2+CR3MO+MONI3-1.5*MO2NI2-1.5*MO3NI; 6000 N
Peng !
PARAM L(FCC_L12,CR,MO,NI:NI:VA;0) 298.15
+6*CRMONI2-1.5*CRMO2NI-1.5*CRNI3
-1.5*CR2MONI-1.5*CR2NI2+CR3NI-1.5*MONI3-1.5*MO2NI2+MO3NI; 6000 N
Peng !

```

```

PARAM L (FCC_L12,MO,NI:CR:VA;0) 298.15
+1.5*CRMONI2+1.5*CRMO2NI-1.5*CRMO3
-1.5*CRNI3; 6000 N Peng !
PARAM L (FCC_L12,MO,NI:CR:VA;1) 298.15
-1.5*CRMONI2+1.5*CRMO2NI-.5*CRMO3
+.5*CRNI3; 6000 N Peng !
PARAM L (FCC_L12,CR,NI:MO:VA;0) 298.15
+1.5*CRMONI2+1.5*CR2MONI-1.5*CR3MO
-1.5*MONI3; 6000 N Peng !
PARAM L (FCC_L12,CR,NI:MO:VA;1) 298.15
-1.5*CRMONI2+1.5*CR2MONI-.5*CR3MO
+.5*MONI3; 6000 N Peng !
PARAM L (FCC_L12,CR,MO:NI:VA;0) 298.15
+1.5*CRMO2NI+1.5*CR2MONI-1.5*CR3NI
-1.5*MO3NI; 6000 N Peng !
PARAM L (FCC_L12,CR,MO:NI:VA;1) 298.15
-1.5*CRMO2NI+1.5*CR2MONI-.5*CR3NI
+.5*MO3NI; 6000 N Peng !

```

```

$*****
*
$
Cr-MO-O

```

```

PARAMETER L (IONIC_LIQ,CR+3,MO+4:O-2;0) 298.15 -195000; 4000 N we !
PARAMETER L (IONIC_LIQ,CR+3,MO+4:O-2,VA;0) 298.15 -7e4; 4000 N we !
$*****
*****
$
$
PARAMETERS quaternary
$

```

```

$*****
*
$
Al-Cr-MO-NI
FUNCTION ALCRMONI 298.15
U1ALNI+U1ALCR+U1ALMO+U1CRMO+U1CRNI+U1MONI;,,N Peng !

```

```

PARAM L (FCC_L12,AL,CR,MO:NI:VA;0) 298.15
AL3NI+CR3NI+MO3NI-1.5*ALCR2NI
-1.5*ALMO2NI-1.5*AL2CRNI-1.5*AL2MONI
-1.5*CRMO2NI-1.5*CR2MONI+6*ALCRMONI; 6000 N Peng !
PARAM L (FCC_L12,AL,CR,NI:MO:VA;0) 298.15
AL3MO+CR3MO+MONI3-1.5*ALCR2MO
-1.5*ALMONI2-1.5*AL2CRMO-1.5*AL2MONI
-1.5*CRMONI2-1.5*CR2MONI+6*ALCRMONI; 6000 N Peng !
PARAM L (FCC_L12,AL,MO,NI:CR:VA;0) 298.15
AL3CR+CRMO3+CRNI3-1.5*ALCRMO2
-1.5*ALCRNI2-1.5*AL2CRMO-1.5*AL2CRNI
-1.5*CRMONI2-1.5*CRMO2NI+6*ALCRMONI; 6000 N Peng !
PARAM L (FCC_L12,CR,MO,NI:AL:VA;0) 298.15
ALCR3+ALMO3+ALNI3-1.5*ALCRMO2
-1.5*ALCRNI2-1.5*ALCR2MO-1.5*ALCR2NI
-1.5*ALMONI2-1.5*ALMO2NI+6*ALCRMONI; 6000 N Peng !

```

§\*\*\*\*\*  
\*\*\*\*\*

## LIST\_OF\_REFERENCES

NUMBER	SOURCE
86DIN	'A. Dinsdale, T. Chart, MTDS NPL, Unpublished work (1986); CR-NI'
87jacob	'K.T. Jacob, G.M. Kale, G.N.K. Iyengar, Phase equilibria and thermodynamic properties in the system Ni-Mo-O, J Mater Sci 22 (12) (1987) 4274-4280.'
89DIN	'Alan Dinsdale, SGTE Data for Pure Elements, NPL Report DMA(A)195 September 1989'
90DIN	'J. Taylor, A. Dinsdale, Z. Metallkde. 81 (1990) 354-366.'
91DIN	'Alan Dinsdale, SGTE Data for Pure Elements, NPL Report DMA(A)195 Rev. August 1990'
91LEE	'Byeong-Joo Lee, unpublished revision (1991); C-Cr-Fe-Ni'
91SAU1	'Nigel Saunders, 1991, based on N. Saunders, V.G. Rivlin Z. metallkde, 78 (11), 795-801 (1987); Al-Cr'
91DIN	'Alan Dinsdale, SGTE Data for Pure Elements, Calphad Vol 15(1991) p 317-425, also in NPL Report DMA(A)195 Rev. August 1990'
93hall	'Hallstedt B (1993) Thermodynamic calculation of some subsystems of the Al-Ca-Mg-Si-O system. JPE. Doi:10.1007/BF02667878'
93Tayl	'J.R Taylor, A thermodynamic Assessment of Cr-Fe-O System Z. metallkde, 84 (5), 335-345 (1993)'
93Barry	'T. Barry, A. Dinsdale, The compound energy model for ionic solutions with applications to solid oxides, Journal of Phase Equilibria, vol 13(5) 1993, 459-475'
95DUP3	'N. Dupin, Thesis, LTPCM, France, 1995; Al-Ni, also in I. Ansara, N. Dupin, H.L. Lukas, B. Sundman J. Alloys Compds, 247 (1-2), 20-30 (1997)'
95kowa	'Kowalski M, Spencer PJ (1995) TEERMODYNA&IIC REEVALUATION OF THE 0-0, Fe-0 AND Ni-0 SYSTEMS: REMODELLING OF THE LIQUID,
98Harri	'R. Harrison, S. Redfern, H.S.C. O'Niell, The temperature dependence of the cation distribution insynthetic hercynite (FeAl2O4) from in-situ neutron structure refinements, American mineralogist, vol 83(1998), p 1092-1099'
99DUP	'N. Dupin, I. Ansara, Z. metallkd., Vol 90 (1999) p 76-85; Al-Ni'
00SUB	'SGTE Substance Database, 2000.'
01DUP	' N. Dupin, I. Ansara, B. Sundman Thermodynamic Re-Assessment of the Ternary System Al-Cr-Ni, Calphad, 25 (2), 279-298 (2001); Al-Cr-Ni'



REF411 'AL1O1<G> THERMODATA 01/93  
ALUMINIUM MONOXIDE <GAS>  
28/01/93'

REF416 ' AL1O2<G> THERMODATA 01/93  
ALUMINIUM DIOXIDE <GAS>  
28/01/93'

REF447 'AL2<G> THERMODATA  
New Assessment'

REF589 'AL2O1<G> THERMODATA 01/93  
ALUMINIUM SUBOXIDE <GAS>  
28/01/93'

REF595 ' AL2O2<G> THERMODATA 01/93  
ALUMINIUM MONOXIDE <GAS>  
28/01/93'

REF602 'AL2O3<AL2O3\_DELTA> JANAF THERMOCHEMICAL TABLES SGTE  
DELTA-AL2O3  
PUB. BY JANAF AT 6/75 \*\*.AL2O3(Delta) ALWAYS METASTABLE  
COMPARED  
TO ALPHA. HEAT OF FUSION CALCULATED :2308K . 1978 SUPPL.'

REF606 'AL2O3<AL2O3\_GAMMA> JANAF THERMOCHEMICAL TABLES SGTE  
GAMMA-AL2O3  
PUBLISHED BY JANAF AT 6/75 \*\*  
AL2O3(GAMMA) EST TOUJOURS METASTABLE PAR RAPPORT A ALPHA  
T FUSION CALCULEE : 2290K. 1978 SUPPL.'

REF611 'AL2O3<AL2O3\_KAPPA> JANAF THERMOCHEMICAL TABLES SGTE \*\*  
KAPPA-AL2O3  
PUBL. BY JANAF AT 6/75 \*\*.AL2O3(KAPPA) ALWAYS METASTABLE  
COMPARED  
TO ALPHA. HEAT OF FUSION CALCULATED :2312K .'

REF615 'AL2O3<G> T.C.R.A.S. Class: 7  
ALPHA-ALUMINIUM OXIDE <GAS>'

04SGTE ' SGTE substance database, Provided by  
Thermo-Calc Software v3.2.'

05SGTE 'SGTE Substances Database v4.1  
2002/2004.'

REF4682 'CR1O2 S.G.T.E. SGTE \*\* CHROMIUM DIOXIDE  
O.KUBASCHEWSKI'S REASSESSMENT 1979'

REF4687 'CR1O3 S.G.T.E. SGTE \*\* CHROMIUM TRIOXIDE  
O.KUBASCHEWSKI'S REASSESSMENT 1979'

REF4749 'CR5O12 S.G.T.E. SGTE \*\* 5-CHROMIUM 12-OXIDE  
CR5O12: 5-CHROMIUM 12-OXIDE \*\*DECOMPOSITION (643 -->705 K)  
O.KUBASCHEWSKI'S REASSESSMENT 1979.'

REF4755 'CR8O21 S.G.T.E. SGTE \*\* 8-CHROMIUM 21-OXIDE  
O.KUBASCHEWSKI'S REASSESSMENT 1971  
CR8O21 8-CHROMIUM 21-OXIDE,DECOMPOSITION (600 --> 640K.)'

REF51 'B. Hallstedt, J. Am. Ceram. Soc. 75 (1992) 1497-1507;  
Al2O3-MgO'

!



## List of publications

### Peer-reviewed articles

1. Golnar Geramifard, Camelia Gombola, Peter Franke, and Hans J. Seifert. Oxidation behaviour of NiAl intermetallics with embedded Cr and Mo. Corrosion Science, 177:108956, 2020.
2. Camelia Gombola, Alexander Kauffmann, Golnar Geramifard, Malte Blankenburg, and Martin Heilmaier. Microstructural Investigations of Novel High Temperature Alloys Based on NiAl-(Cr,Mo). Metals, 10(7), 2020.

### MSIT (Materials Science International Team) database

1. Amy Van den Bulck, Golnar Geramifard, Maren Lepple, Ingo Markel, Ivan Saenko, O-Ta-Zr Ternary Phase Diagram Evaluation, in MSI Eureka, G. Effenberg (Ed.), MSI, Materials Science International, Stuttgart (2017), Document ID: 10.11426.1.5
2. Ivan Saenko, Golnar Geramifard, Frank Stein, Co-Ti-Zr Ternary Phase Diagram Evaluation, in MSI Eureka, G. Effenberg (Ed.), MSI, Materials Science International, Stuttgart (2018), Document ID: 10.15651.1.8

## Conference presentations

1. G. Geramifard, P. Franke, H. J. Seifert , Thermodynamic investigation of the oxidation of NiAl-(Cr, Mo) alloys used for manufacturing metal matrix composites by directional solidification, MSE 2018- Materials Science and Engineering, 26-28 September 2018, Darmstadt, Germany.
2. G. Geramifard, P. Franke, H. J. Seifert , Thermodynamic investigation of the oxidation of NiAl-(Cr, Mo) alloys used for manufacturing metal matrix composites (Poster), CALPHAD 2019, 2-8 June 2019, Singapore.
3. G. Geramifard, P. Franke, H. J. Seifert, Thermodynamic investigation of the oxidation of NiAl-(Cr, Mo) alloys, Beyond Nickel-Based Superalloys III, 11-14 June 2019, Nara, Japan.
4. G. Geramifard, P. Franke, H. J. Seifert, Oxidation of directionally solidified NiAl-(Cr, Mo) alloys, Intermetallics 2019, 30 Sep - 4 Oct 2019, Bad Staffelstein, Germany.
5. G. Geramifard, P. Franke, H. J. Seifert, Thermodynamic investigation of oxidation behavior of NiAl intermetallics with embedded Cr and Mo, MSE 2020, 22-25 September 2020, Virtual congress. (Best Poster Award Winner)
6. H. J. Seifert, G. Geramifard, P. Franke, Thermodynamic database for the Ni-Al-Cr-Mo-O system, MSE 2020, 22-25 September 2020, Virtual congress.
7. H. J. Seifert, G. Geramifard, P. Franke, Thermodynamic database and experimental studies of NiAl-Cr and NiAl-Mo composites, TOFA 2020, 28 September-2 October 2020, Bad Staffelstein, Germany.